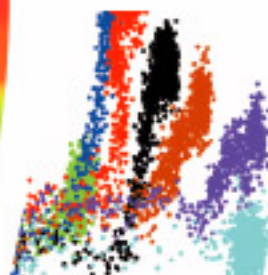
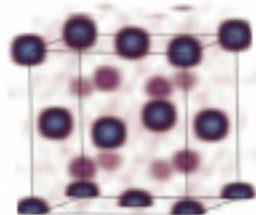
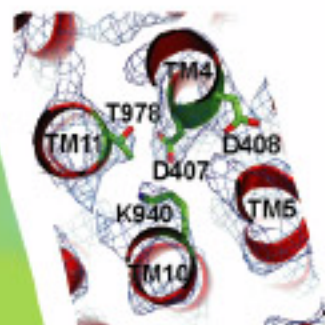
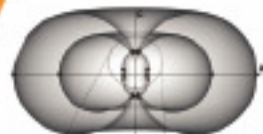




European Synchrotron Radiation Facility

# Highlights

2006





# Highlights

## 2006

<i>Contents</i>	<i>Pages</i>
<b>Introduction</b>	<b>2</b>
<b>Scientific Highlights</b>	<b>4</b>
<i>High Resolution and Resonance Scattering</i>	4
<i>Materials Science</i>	16
<i>Soft Condensed Matter</i>	32
<i>Structural Biology</i>	48
<i>Surface and Interface Science</i>	63
<i>X-ray Absorption and Magnetic Scattering</i>	77
<i>X-ray Imaging and Optics</i>	96
<b>The X-ray Source</b>	<b>112</b>
<b>Facts and Figures</b>	<b>120</b>

## Introduction

The success of the ESRF's scientific programme is the result of the ideas and actions of many people - our large and widely-spread user community (some 5500 scientists visited the ESRF in 2006 to carry out their research projects), the many colleagues who contribute to the ESRF through their work on the proposal review committees as well as the Council, SAC and AFC, and almost 600 staff of the ESRF. Science at the ESRF is underpinned by the work of all of our Divisions and Services: much of this is invisible to our scientific user community but is, nevertheless, of crucial importance for the successful operation of our Machine and beamlines. We open this Introduction to the *Highlights 2006* with some important news and events that marked 2006 for our various Divisions.

The **Machine**, the set of accelerators providing the X-ray beams, operated very successfully in 2006. X-ray beam availability was 98.7% (97.6% in 2005) and the mean time between failures reached a new record of 61.5 hours (44.4 hours in 2005). A new magnetic lattice was developed and tested during the year. This lattice has an effectively unchanged performance and is operated without two quadrupoles in each cell; these may subsequently be removed to provide more space (~ 1 metre) for new insertion devices. Routine upgrades and maintenance continued with, for example, the installation of new high power crotch absorbers and front-ends and several new "revolver" and in-vacuum undulators.

Where the **Experiments Division** is concerned, progress has been achieved in many areas of materials science and in the development of techniques. The high pressure programme has seen the commissioning of ID27, a new high pressure beamline, with much improved performance (flux and focussing capabilities) compared to that of ID30 (now phased-out). The experimental programme of this new beamline has already achieved very significant results such as the first crystallographic data on phase III of solid hydrogen and the discovery of carbonia, a carbon dioxide based glass with a structure similar to vitreous silica. Plans to develop a large volume press programme are progressing well. The year 2006 has also witnessed the commissioning of

two other key beamlines: ID03, the new surface diffraction beamline which has been equipped with an instrument dedicated to the investigation of surfaces under "real" catalytic conditions, and ID26, for high-throughput resonant inelastic X-ray scattering, allowing a powerful and ambitious experimental programme in both inorganic chemistry and bioscience. A novel technique, X-ray-detected magnetic resonance, has been successfully demonstrated on ID12, opening a new avenue by which to study very subtle magnetic processes, such as site-selective time-resolved magnetism down to the picosecond timescale, using X-ray magnetic dichroism techniques in combination with microwave pumping of the sample under investigation. Finally, the new ID06, ID11 and ID13 projects are on schedule to start delivering beam in 2007, thereby increasing the opportunities at the ESRF in the fields of micro- and nano-diffraction in materials science, pulsed magnetic fields up to about 30 T, and instrument developments using high brightness undulator radiation.

The automation of the ESRF macromolecular crystallography (MX) beamlines continues to be of real benefit to the large European structural biology community: MX makes up around 40% of the user visits to the ESRF. Fast screening of a large number of crystals is now possible. This is of great value for biologically challenging projects where it is often difficult to get good quality (diffracting) crystals. Many biological projects also profit from the implementation of techniques complementary to X-ray diffraction such as Raman and UV-VIS spectroscopy, now available on the MX beamlines. A noteworthy and valuable cross-fertilisation between structural biology and soft condensed matter science is growing, of mutual benefit to both research areas. By the use of the coherence in holotomographic mapping, and nano-chemical imaging of the cellular distribution of heavy metals, X-ray imaging has demonstrated its great potential in providing completely new knowledge on biological samples. These X-ray imaging techniques are attracting new user communities. For example, the non-destructive nature of X-ray imaging gives unique opportunities to "see" inside fossils and to unravel the chemical composition of cultural heritage samples. The use of nanometre-sized X-ray beams has been the foundation for many of the exciting results obtained in 2006, and the need for smaller and

smaller X-ray beams is increasing and is an important component of the ESRF upgrade programme. Three pilot projects are preparing the ground for the future developments of beamlines with nanosized beams: the nanoimaging side-station at ID22, and the extension projects of ID11, the materials science beamline and ID13, the microfocus beamline, enabling ID11 and ID13 to operate routinely with nanometre-sized beams. However, nanobeams require developments in nanoengineering and nanomanipulation and so a nanotechnology platform has been established to coordinate all the nanoscale developments.

The year 2006 was a remarkable year for computing-related activities. The beamlines again produced a record amount of data, pushing much of the computing infrastructure to its limits and encouraging the **Computing Services Division** to explore new technologies and techniques. The data network is being constantly enhanced to maintain its high reliability while substantially increasing the available bandwidth. Many experiments now require parallel processing for fast analysis and many users are routinely using the Linux clusters with batch submission software to stay abreast of the data deluge. Other developments concern new database applications and the continuous development of the control system software, two areas where collaborative efforts with other laboratories allow synergy.

Staff of the **Technical Services Division** contribute to science at the ESRF in many ways, from conventional building construction and maintenance to very specific infrastructure for the Machine and beamlines. For example, in 2006 TSD delivered Sectors 10-6 and 14-5 to accommodate the new long (about 100 m) beamlines ID11 and ID13 which have remarkable vibrational and thermal stability.

The **Administration Division**, working closely with the Director General, has very wide responsibilities, including interaction with the ESRF's partner countries. In 2006, the first steps were taken towards the possible participation of Russia in the ESRF. In addition, the Central European countries are demonstrating an increased interest. In line with the intensified use of the ESRF by scientists from Poland and the Czech Republic, these countries increased their contributions as Scientific Associates to 1%

The Director General with the members of the Upgrade Programme Project Group.  
From left to right:  
C. Detlefs,  
J.L. Revol,  
W.G. Stirling,  
T. Bouvet and  
E. Mitchell.



(Poland) and 0.47% (Czech Republic). Contacts with the Slovak Republic have been initiated. Technology transfer is increasingly important for Europe's science-based industries. The rules on the remuneration of inventors were modified last year to give a boost to technology transfer at the ESRF. The *Convention d'Entreprise* governs our working environment and is currently under revision in negotiation with the Unions. These discussions, which focus on shiftwork, time management, and the expatriation allowance, will continue well into 2007.

Following the enthusiastic support of the SAC and Council for the ESRF's ten year **Upgrade Programme** (<http://www.esrf.eu/AboutUs/Upgrade>), the Director General set up a Project Group to prepare the detailed project documentation to be submitted to the Council for approval (see the photo). This major task is well underway with the aim of producing the "Purple Book" by early 2007, after in-depth consultation with SAC members and representatives of the user community. We are looking forward to a "green light" in 2007 from the ESRF Council to start work on our programme of renewal and upgrade, designed to keep the ESRF at the forefront of scientific research.

The *Highlights 2006* presents some of the best science from the ESRF over the last year. We hope that you enjoy reading about some of the remarkable research carried out by our users and staff. In 2007 and the following years we will work together to make the ESRF an even more exciting centre for world science.

**W.G. Stirling, M. Rodriguez Castellano,  
P. Elleaume, R. Dimper, H. Krech, S. Larsen,  
F. Sette, P. Thiry**  
(January 2007)



Highlights 2006

# Scientific Highlights

## High Resolution and Resonance Scattering

### Introduction

This year's contribution again shows the complementarities of research at the beamlines, covering very fundamental aspects of science as well as the development of novel applications.

The first three contributions deal with those fundamental aspects. A hard X-ray photoemission experiment, using the electron analyser developed within the VOLPE collaboration (FP5 project), nicely shows the importance of bulk sensitivity in order to compare theoretical and experimental data in the case of  $V_2O_3$ . The other two examples are related to glasses, still one of the important research areas for the group. Using inelastic X-ray scattering and nuclear inelastic scattering, new insights could be gained in the high-frequency limit

of sound waves and in the understanding of the Boson peak, respectively.

The application part deals this time with phonons and electronic structures. Within the framework of the DYNASYNC collaboration (FP6 project), the phonon density of states from a monolayer iron on W(110) up to bulk iron could be measured *in situ*. Very small high-quality single crystals of molybdenum and hexagonal boron nitride (BN) could be prepared thanks to advanced preparation techniques. The pressure dependence of phonon anomalies in molybdenum and the elasticity of hexagonal BN could thus be determined. Resonant and non-resonant emission spectroscopy are becoming valuable techniques in the applied sciences for the study of local coordination and electronic structure. In the two examples presented

here, dealing with catalysis and electrochemistry, only the emission spectroscopy was sensitive enough to answer the questions on high valence of iron and the ligand environment of nanocrystalline Cr deposits.

As usual, technical developments rank very highly at our beamlines. Before the summer shut-down ID26 took first beam in order to verify the X-ray optics after the refurbishment closure. The successful tests assured the re-opening of the beamline for the second half of 2006. Stable operation for absorption and especially emission spectroscopy allowed a smooth users' programme. The refurbishment programme will continue in parallel with beamline operation: the installation of a new high-performance emission spectrometer in a dedicated hutch is planned for 2007.

Another important activity concerned the preparation of the conceptual design reports for the ESRF upgrade programme. We foresee ambitious scientific and technical developments on all of our beamlines, which will open new possibilities in several fields of research. With this goal in mind, recent tests together with the Machine Group have been highly valuable. For example, the ramping up of the electron current from 0 to 200 mA confirmed the good performance of the high heat-load monochromators, which mastered brilliantly the corresponding power from the undulators. ID18 was allowed to go further to 250 mA and forced a value of 1300 W absorbed power in the first crystal of the monochromator without posing any real problems for the optics. However, best performance was reached at 200 mA. Extrapolation suggests that stable operation for the present scheme is possible up to a 300 mA stored electron beam, corresponding to about 600 W in the central cone at ID18.

**R. Rüffer**

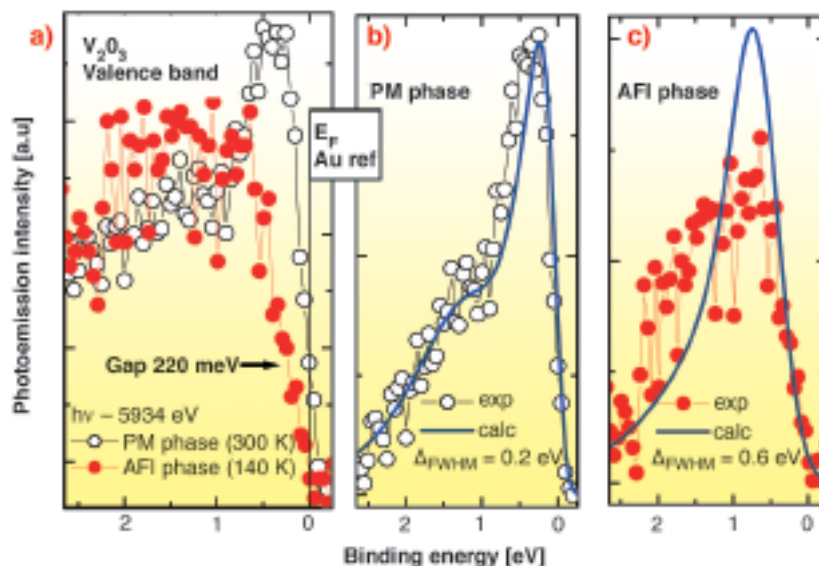
## Coherent peaks and minimal probing depth in photoemission spectroscopy of Mott-Hubbard systems

Transition metal oxides (TMO) form a series of compounds with a uniquely wide range of electronic properties, mostly driven by electron correlation effects. One remarkable example of the competition between itinerancy and correlation is the metal to insulator Mott transition (MIT).  $V_2O_3$  undergoes a Mott transition as a function of both temperature and pressure, thus representing a paradigmatic case in TMO. Over the last decade, the dynamical mean field theory (DMFT) has successfully described the MIT in a unified approach [1]. However, one of its foremost predictions, the presence of coherent features at the Fermi energy  $E_F$ , has only been identified very recently thanks to the increased bulk sensitivity obtained by photoemission spectroscopy (PES) in the soft X-ray regime [2]. In general, reliable comparisons between DMFT and PES data across the MIT are rare: this is mainly due to the lack of truly bulk-sensitive PES experiments.

We have performed hard X-ray PES (HAXPES,  $\hbar\omega \approx 5.95$  keV) experiments on pure  $V_2O_3$  single crystals using the VOLPE setup installed on beamline ID16 [3]. Thanks to the enhanced bulk sensitivity, we: i) obtained a quantitative measure of the electron correlation energy  $U$ , via comparison with LDA+DMFT calculations; ii) observed a clear relationship between the coherent peak measured near  $E_F$  and the satellite features observed in the vanadium 2p core level spectra.

In **Figure 1** we present valence band spectra compared to DMFT calculations. Raw data in panel a) show a well defined coherent peak at  $E_F$  in the paramagnetic metallic (PM) phase, together with an incoherent band centred at

**Fig. 1:** Valence band spectra in the PM (white circles) and AFI (filled red circles) phase: **a)** Raw data with no background subtraction. The spectra reveal the complete disappearance of the coherent peak and the opening of a gap of  $220 \pm 20$  meV in the AFI phase. Comparison with DMFT calculations for: **b)** the PM phase; and **c)** the AFI phase. Calculated lineshapes are convoluted with a Gaussian to match the leading edge of the experimental data.



around 1.5 eV binding energy. When crossing the MIT (140 K, antiferromagnetic insulating (AFI) phase), the coherent peak disappears and one observes the opening of a gap of  $220 \pm 20$  meV. Calculations performed for various values of the parameter  $U$ , find that  $U = 4.2$  eV provides the best simultaneous description of the various phases observed in  $V_2O_3$ . Large values of  $U$  result in the opening of another gap for the structure corresponding to the metallic phase. Panel (b) and (c) show PES spectra compared to LDA+DMFT calculations. In the metallic phase (panel b) the agreement is remarkably good, where the calculation matches simultaneously the ratio between coherent and incoherent parts as well as their location on the energy scale. In the insulating phase (panel c), calculations give the correct energy position of the intensity maximum but, even using an increased broadening (0.6 eV), the agreement remains qualitative. The experimental intensity spreads over a larger bandwidth than in the calculations. At present, we have no explanation for such difference.

**Figure 2** compares the intensity of the coherent quasiparticle peaks at  $E_F$  (inset) and of the  $V 2p_{3/2}$  shake down satellite for two sample preparations (flat surface area and rough surface). We observe that the presence of the core level satellites is directly related to the

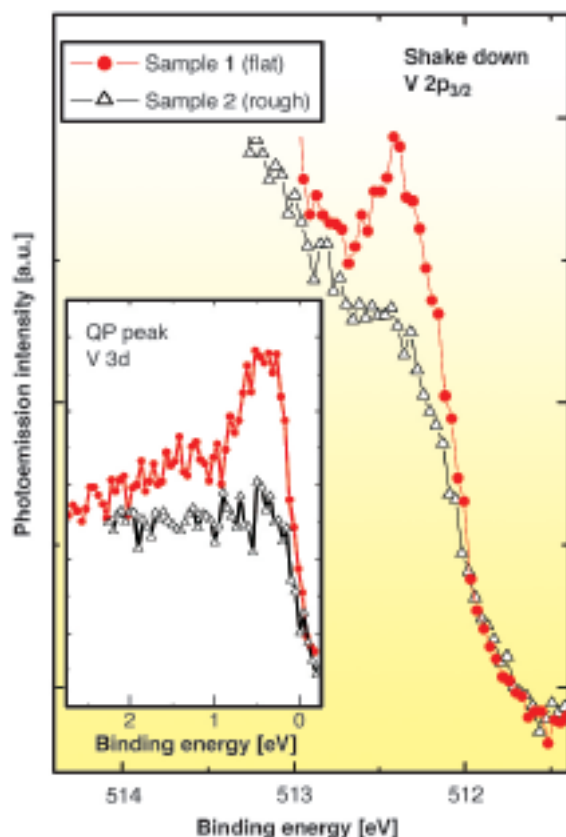


**Fig. 2:** Room temperature  $V 2p_{3/2}$  core-level and (inset) valence band for two different samples preparations: cleaved flat surface (red circles) and mechanically polished rough surface (open triangles). The spectra have been arbitrarily scaled by a multiplication factor for better comparison.

valence band coherent peaks, and that macroscopic imperfections (sample 2) depress both the satellite intensity and the coherent intensity at  $E_F$ .

Our results not only confirm the remarkable change of the screening properties in TMO when going from the surface to the volume, but open the way to the determination of important parameters such as the on-site Coulomb interaction via the combined analysis of core level and valence band PES spectra.

## References

- [1] A. Georges *et al.*, *Rev. Mod. Phys.* **68**, 13 (1996).
- [2] S.-K. Mo *et al.*, *Phys. Rev. Lett.* **90**, 186403 (2003).
- [3] P. Torelli *et al.*, *Rev. Sci. Instr.* **76**, 023909 (2005); M. Sacchi *et al.*, *Phys. Rev.* **B71** 155117 (2005).

## Principal Publication and Authors

G. Panaccione (a), M. Altarelli (b), A. Fondacaro (c), A. Georges (d), S. Huotari (c), P. Lacovig (e), A. Lichtenstein (f), P. Metcalf (g), G. Monaco (c), F. Offi (h), L. Paolasini (c), A. Poteryaev (d), O. Tjernberg (k), M. Sacchi (i), *Phys. Rev. Lett.* **97**, 116401 (2006).

(a) TASC Laboratory, INFN - CNR, Trieste (Italy)

(b) European XFEL Project c/o DESY, Hamburg (Germany)

(c) ESRF

(d) Ecole Polytechnique, Palaiseau (France)

(e) Sincrotrone Trieste (Italy)

(f) Inst. für Theoretische Physik, Univ. Hamburg (Germany)

(g) Dep. of Chemistry, Purdue University, West Lafayette (USA)

(h) Dip. di Fisica Univ. Roma III (Italy)

(k) LMSP, Royal Institute of Technology, Kista (Sweden)

(i) LCP-MR, Univ. P. et M. Curie, Paris, and Synchrotron SOLEIL, Gif-sur-Yvette (France)

## Observing the high-frequency limit of sound waves in glasses

Glasses, like all condensed phases, essentially behave as elastic continua for sound waves of sufficiently low frequencies. These can be described by plane waves with well defined wave vector  $q$ , related to the angular frequency  $\Omega$  by  $\Omega = vq$ , where  $v$  is the phase velocity of sound. These waves propagate with an energy mean free path  $l$ . Two principal mechanisms produce a finite  $l$  in insulating glasses: the relaxation of defects and the anharmonic coupling with modes of the thermal bath, as recently reanalysed in [1]. The question of interest here is what happens at frequencies sufficiently high to probe

the intrinsic structural or dynamical inhomogeneities of glasses. Can these produce such a high attenuation that acoustic excitations lose their wavelike character, as suggested by observations of low-temperature thermal conductivities?

The corresponding frequencies became accessible thanks to Brillouin X-ray scattering on **ID16**. **Figure 3** shows Brillouin linewidths,  $\Gamma = \nu/l$ , obtained on two oxide glasses, permanently densified silica ( $d$ -SiO<sub>2</sub>) [2] and lithium diborate (LB2), Li<sub>2</sub>O-2B<sub>2</sub>O<sub>3</sub>. In both cases, a dramatic increase of  $\Gamma$ , approximately  $\propto \Omega^4$ , is observed up to the frequencies  $\Omega_{IR}$  shown by arrows at  $\Gamma = \Omega/\pi$ . The latter implies that  $l$  decreased to half the sound wavelength. Thus,  $\Omega_{IR}$  corresponds to the Ioffe-Regel (IR) crossover beyond which plane waves cease to be a useful concept. One should remark that although similar onsets of crossover are observed for these two glasses at  $\Omega/2\pi$  in the THz range, the linewidths behave quite differently at lower frequencies. LB2 reveals a  $\Gamma \propto \Omega^1$  dependence in Brillouin light scattering, characteristic of the thermal relaxation of defects, while  $d$ -SiO<sub>2</sub> is dominated by anharmonicity, leading to  $\Gamma \propto \Omega^2$  [1].

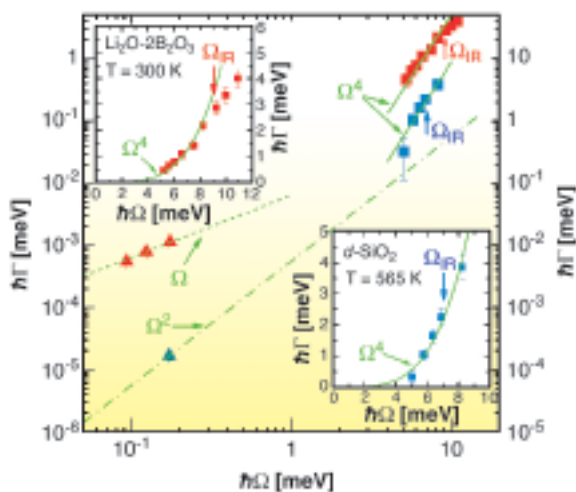


**Fig. 3:** Brillouin scattering linewidths observed with visible light (▲) and X-rays (■). Note that for clarity the two ordinate scales are distinct as indicated by colours. The insets show the same X-ray data on linear scales, emphasising the rapid onset and the smallness of the error bars, where blue symbols are for  $d$ -SiO<sub>2</sub> and red symbols for lithium diborate. The lines are explained in the text.

It is well known that most glasses also exhibit an excess of modes in their reduced vibrational density of states,  $Z(\omega)/\omega^2$ , peaking at a relatively low frequency  $\Omega_{BP}$ , called the boson peak. It is remarkable that  $\Omega_{IR} \approx \Omega_{BP}$  for the two glasses of **Figure 3**. This is presumably not an accident. It suggests that the IR-crossover indeed results from the hybridisation of acoustic excitations with excess ones, as recently described in [3]. As shown there, this hybridisation should lead to  $\Gamma \propto \Omega^4$  below  $\Omega_{IR}$ . However, for most glasses,  $\Omega_{BP}$  is lower than in the

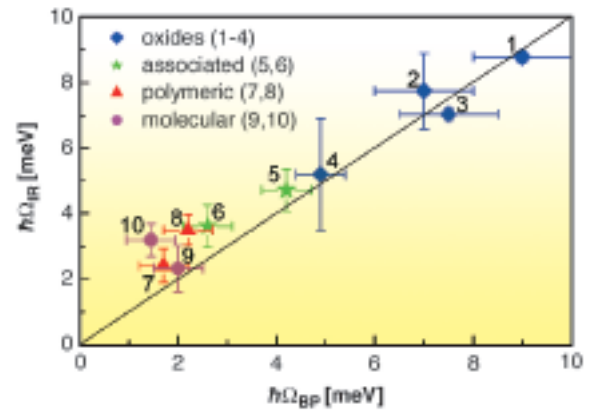


**Fig. 4:** Relation between  $\Omega_{IR}$  and  $\Omega_{BP}$  from literature data. The points are: (1) LB2 at 573 K; (2) lithium tetraborate Li<sub>2</sub>O-4B<sub>2</sub>O<sub>3</sub> at 600 K; (3) densified silica at 565 K; (4) vitreous silica at 1050 K; (5) glycerol at 175 K; (6) ethanol at 86 K; (7) selenium at 295 K; (8) polybutadiene at 140 K; (9) propylene carbonate at 167 K ( $T_g + 7$  K); (10) orthoterphenyl at 156 K. The line is a guide to the eye. See the principal publication for references to the experimental data.

experimentally favourable cases of  $d$ -SiO<sub>2</sub> and LB2. This generally leads to scattering vectors at the IR-crossover that fall near the lower limit attainable with the current spectrometers. It is thus understandable that the onset region  $\Gamma \propto \Omega^4$  was so far not observed in other glasses. However, there is now sufficient information in the literature to extract good estimates and error bars for  $\Omega_{IR}$  in a number of cases. These are shown in **Figure 4** as a function of  $\Omega_{BP}$ . Values of  $\Omega_{BP}$  are available from various spectroscopy methods, which unfortunately, do not necessarily probe the full  $Z(\omega)$ . Hence, average values of  $\Omega_{BP}$  have been used in **Figure 4**. It is remarkable that **Figure 4** suggests a relation between  $\Omega_{IR}$  and  $\Omega_{BP}$  for all these various glasses, and that those glasses having a strong to intermediate excess of modes seem to obey  $\Omega_{IR} \approx \Omega_{BP}$ , in agreement with [3].

## References

- [1] R. Vacher, E. Courtens, and M. Foret, *Phys. Rev. B* **72**, 214205 (2005).
- [2] B. Rufflé, M. Foret, E. Courtens, R. Vacher, and G. Monaco, *Phys. Rev. Lett.* **90**, 095502 (2003).
- [3] V.L. Gurevich, D.A. Parshin, and H.R. Schober, *Phys. Rev. B* **67**, 094203 (2003).

## Principal Publication and Authors

B. Rufflé (a), G. Guimbretière (a), E. Courtens (a), R. Vacher (a) and G. Monaco (b), *Phys. Rev. Lett.* **96**, 045502 (2006).

(a) LCVN, Université Montpellier 2 and CNRS (France)

(b) ESRF

# Density of vibrational states of hyperquenched and densified glasses

Vibrational dynamics of glasses remains a point of controversial discussions. The application of nuclear inelastic scattering of synchrotron radiation provides a new and consistent picture of the subject.

We have studied the vibrational dynamics of the iron-enriched sodium-silicate glasses with (i) different thermal history and (ii) different density. The iron-partial density of vibrational states (DOS)  $g(E)$  was measured with nuclear inelastic scattering at ID18. The reduced DOS  $g(E)/E^2$  (Figure 5) reveals an excess of vibrational states above the Debye level called the boson peak. The peak of the reduced DOS decreases in height and moves to higher energy for the annealed (Figure 5a) and densified (Figure 5b) glasses. This behaviour is usually related to a modification of the short-range or intermediate-range structure. For instance, fast quenching and slow annealing provide a glass with a structure that corresponds to “fictive” temperatures above or below the glass transition, respectively. The change of the structure with densification is usually related to the evolution of the first sharp diffraction peak in the static structure factor.

The properties of the glasses were characterised with various techniques. Calorimetry confirmed high efficiency of quenching (Figure 5c): the calculated fictive temperatures for the quenched and annealed glass are 19% above and 2% below the glass transition, respectively. However, Mössbauer spectroscopy and X-ray scattering did not reveal any relevant effect of quenching on the microscopic or intermediate-range structure. On the other hand, quenching affected the

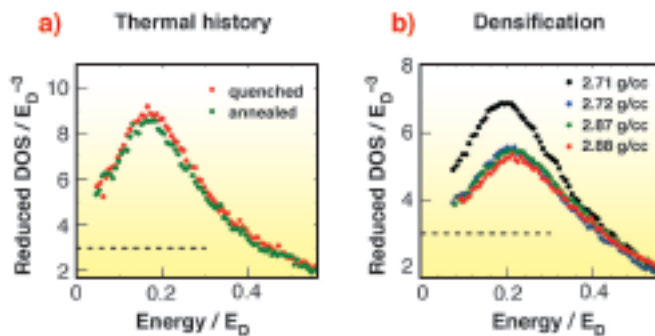


**Fig. 6:** Reduced density of vibrational states of glasses with (a) different thermal history and (b) different density after rescaling the energy axes in Debye energy units and the renormalisation of the DOS area. The horizontal lines show the Debye levels.

macroscopic parameters: the density and the sound velocity for the quenched glass are smaller than for the annealed one. The changes in density and sound velocity suggest that the observed transformation of the reduced DOS (Figure 5a) could be described by the transformation of the elastic medium. In order to evaluate the role of elastic medium, the densities of states were rescaled in Debye energy units and renormalised. After this correction for the macroscopic parameters, the reduced densities of states become identical (Figure 6a).

For the densified samples, the transformation of the glass follows a slightly more complicated path. On the first step of densification, the macroscopic parameters do not change much: the density shows only a slight increase from 2.71 to 2.72 g/cc. The sound velocity does not change significantly either. On the other hand, Mössbauer spectroscopy reveals that the initial step is accompanied by a notable transformation of the local environment of the iron atoms, which is much less pronounced upon further densification. The intermediate-range order seems to change continuously with densification: X-ray scattering

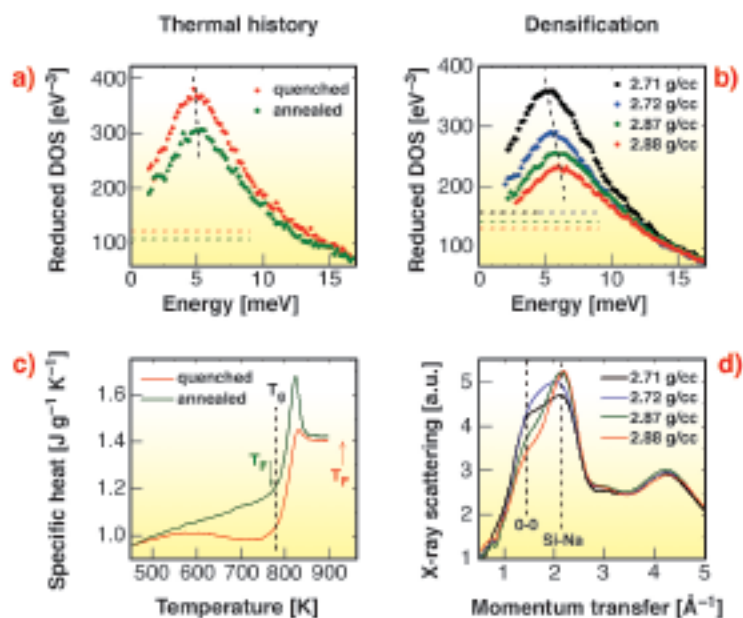


**Fig. 5:** Reduced density of vibrational states of glasses with (a) different thermal history and (b) different density. The horizontal lines show the calculated Debye levels. The black dashed lines emphasise the shift in the peak position. (c) Calorimetry data for the glasses with different thermal history. The vertical dashed line shows the glass transition temperature. The arrows indicate the corresponding fictive temperatures  $T_F$ . (d) X-ray scattering data for the densified glasses. The dashed lines indicate the positions corresponding to the characteristic oxygen-oxygen and silicon-sodium atoms distances.

reveals monotonous transformation of the first sharp diffraction peak (Figure 5d). After correction for the transformation of the elastic medium, the reduced densities of states for all densified glasses except for the initial one become identical (Figure 6b). Thus, the change of the microscopic structure on the initial step of densification causes changes in the density of vibrational states which cannot be accounted for by corresponding transformation of the elastic medium. On the other hand, if the microscopic structure does not change, the transformation of the DOS is entirely described by the transformation of the elastic medium.

The results suggest that for a glass with a given microscopic structure the transformation of atomic vibrations is sufficiently described by the corresponding transformation of the elastic medium. Other parameters such as the fictive temperature or the shape of the first sharp diffraction peak do not appear to be correlated to the density of vibrational states. Furthermore, neither density nor thermal history change the boson peak defined as the excess of the vibrational states above the Debye level: the changes in the number of states are compensated by the changes of the Debye level.

#### Principal publications and authors

A. Monaco (a), A.I. Chumakov (a), G. Monaco (a), W.A. Crichton (a), R. Rüffer (a), D. Fioretto (b), L. Comez (b), Y.-Z. Yue (c), A. Meyer (d), and J. Korecki (e,f), *Phys. Rev. Lett.* **96**, 205502 (2006), *Phys. Rev. Lett.* **97**, 135501 (2006).

(a) ESRF

(b) Univ. Perugia (Italy)

(c) Univ. Aalborg (Denmark)

(d) TUM Physik-E13, Garching (Germany)

(e) AGH Univ. of Science and Technology, Kraków (Poland)

(f) Institute of Catalysis and Surface Chemistry, Polish Academy of Science, Krakow (Poland)

## Phonons in iron: from the bulk to a strained epitaxial monolayer

In general, lattice-expanded states are often found near solid/solid boundaries, like in thin films and nanostructures, where the atomic environment abruptly changes. A classical example is the interface between the Fe and the W(110) surface, for which it is well known that the first iron layer grows in pseudomorphic manner, i.e. the Fe film adopts the periodicity of the substrate [1]. This results in a relative stretching of the Fe lattice by about 10% compared to its bulk value, implying significant changes of the elastic properties in this and the adjacent layers. Increasing the number of iron layers relaxes the lattice strain via a network of misfit

dislocations and re-establishes the bulk Fe-Fe coordination distances. Consequently the vibrational properties of the Fe films are expected to differ remarkably from the corresponding bulk behaviour.

In order to study systematically the lattice vibrations of the iron films deposited on W(110) upon transition from the bulk to a single iron monolayer we have measured the density of phonon states (DOS) as a function of the film thickness applying nuclear inelastic scattering (NIS) of synchrotron radiation. From the measured DOS, a number of relevant parameters (mean specific heat, vibrational entropy, average force constant, sound velocity, etc.) can be calculated.

The experiment was performed at the Nuclear Resonance Beamline ID18 using a recently commissioned ultra-high vacuum (UHV) system, which allows for sample preparation by molecular beam epitaxy, characterisation by low energy electron diffraction and Auger electron spectroscopy, and *in situ* NIS experiments.

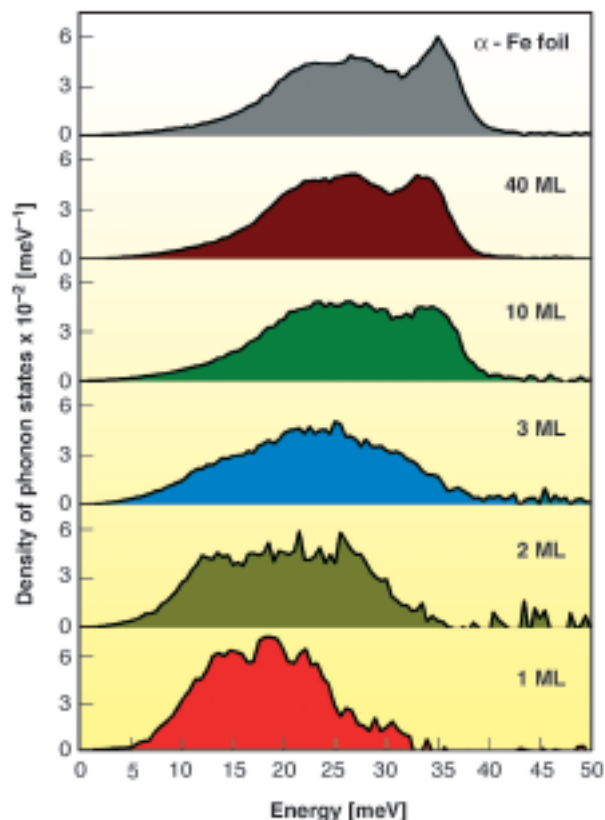


**Fig. 7:** The DOS of single-crystalline Fe films on W(110) for coverages ranging from 1 ML to a 40 ML thick film (1 ML = 0.22 nm). The DOS of polycrystalline bulk  $\alpha$  - iron foil is shown for comparison.

The DOS extracted from the measured NIS spectra are shown in Figure 7 in comparison with the DOS of polycrystalline  $\alpha$  - Fe foil. The DOS of the 40 ML film resembles closely the DOS of the bulk Fe but the spectral features are shifted by about 1 meV to lower values. This is a consequence of the expanded state of the film that results from the mismatch of the W and Fe lattices and

goes along with a lattice volume expansion of about 2%. Relating the observed energy shift to the pressure dependence of the Fe DOS and its spectral features [2], one arrives at a negative pressure of 2 GPa to which the film is effectively subjected. For the 10 ML film one observes a pronounced suppression of the peak at 34 meV and an increase of the modes at low energies. Decreasing the coverage results in a further enhancement of the low-energy modes while spectral features at high energies are significantly reduced. Qualitatively, the observed softening is caused by a decrease in the coordination number at the surface and is typical for surface phonons, but certainly also mirrors the coupling of the adsorbed iron atoms to the softer crystal lattice of the tungsten substrate.

The presented results could be obtained because the high penetration depth of the X-rays is combined with the isotopic selectivity of the nuclear resonant absorption process. While the former aspect renders the technique sensitive to the full volume of the film, the latter aspect assures that the experimental data are practically free of contributions from non-relevant elements, like for example the substrate itself or the residual gases, always present in the UHV system. The method can be extended to many other isotopes. Moreover, the experiment has shown that nuclear inelastic scattering at third-generation synchrotron radiation sources such as the ESRF is well suited to extremely small quantities of material. The lattice dynamics of epitaxial nanostructures on surfaces can be studied via this “state-of-the-art” technique, correlating structural, electronic and dynamical properties of low-dimensional systems. In particular, the use of ultrathin isotopic probe layers allows one to establish ‘phonon microscopy’ for the spatially resolved study of vibrational properties with atomic resolution.

## References

- [1] U. Gradmann, G. Waller, *Surf. Sci.* **116**, 539 (1982).  
 [2] H.K. Mao *et al.*, *Science* **292**, 914 (2001).

## Principle Publication and Authors

S. Stankov (a,b), R. Röhlberger (c), T. Slezak (d,e), M. Sladeczek (b), B. Sepiol (b), G. Vogl (b), A. I. Chumakov (a), R. Rüffer (a), N. Spiridis (e), J. Lazewski (f), K. Parlinski (f,g), and J. Korecki (d,e), *to be submitted*.

(a) ESRF

(b) Faculty of Physics, Institute of Materials Physics, University of Vienna (Austria)

(c) DESY, Hamburg (Germany)

(d) Faculty of Physics and Applied Computer Science, AGH University of Science and Technology, Krakow (Poland)

(e) Institute of Catalysis and Surface Chemistry, Polish Academy of Science, Krakow (Poland)

(f) Institute of Nuclear Physics, Polish Academy of Science, Krakow (Poland)

(g) Institute of Techniques, Pedagogical University, Krakow (Poland)

# Unequivocal detection of the 3d<sup>4</sup> high-spin system by resonant inelastic X-ray scattering

The electronic structure of 3d transition metals is subject to intense studies. Chemists classify transition metal compounds by means of their oxidation states. The most common oxidation states for Fe are II and III. In a purely ionic picture this corresponds to 3d<sup>6</sup> and 3d<sup>5</sup> valence shell configurations, respectively. A higher oxidation state means that the half-filled 3d shell opens up, which significantly changes the Fe chemistry. High oxidation states of iron play an important role in biological systems. Oxoiron(IV) species are found in heme enzymes and Fe(IV) intermediates are important parts of the catalytic cycles of methane monooxygenase, an enzyme capable of oxidising the C-H bond in methane as well as other alkanes. In solid state chemistry high oxidation states of iron are less common. The most well known examples for a material with formal oxidation state Fe(IV) are the perovskite FeSrO<sub>3-x</sub> and related materials with similar composition [1]. They play an important role in catalysis, in gas-sensors, electrochemistry and in solid state physics.

One strongly debated scientific case is Fe in a zeolite framework system (Fe-ZSM-5). The involvement of Fe(IV) species was invoked to explain the high activity and selectivity of Fe-ZSM-5 catalysts in the oxidation of benzene to phenol [2]. The reaction of N<sub>2</sub>O with Fe(II) sites in ZSM-5, generated by autoreduction at high temperatures, creates a highly reactive surface oxygen species, which selectively oxidises benzene at moderate temperatures. Experimental proof of the existence of Fe(IV) in Fe-ZSM-5 has not yet been given because one has to rely on a phenomenological interpretation of the line shifts in Mössbauer and XANES spectra, which is often ambiguous for heterogeneous and strongly covalent systems. Hence, the identification of the oxidation state of iron in Fe-ZSM-5 requires an alternative solution.

Spin-selective absorption spectroscopy takes advantage of the strong (3p,3d) exchange interaction in the final states of 1s3p resonant inelastic X-ray scattering (RIXS) spectroscopy [3]. This interaction splits the K $\beta$  emission lines into the K $\beta$ <sub>1,3</sub> (spin-down) and K $\beta$ ' (spin-up) features. Using an emission spectrometer with an instrumental energy bandwidth of ~1 eV, it is possible to distinguish between final states that correspond to a spin-up or spin-down orientation of the unpaired 3p electron with respect to the valence electrons. This translates directly into the spin orientation of the photoexcited 1s electron thus allowing detection of the spin-up and spin-down density of unoccupied electronic states, respectively.

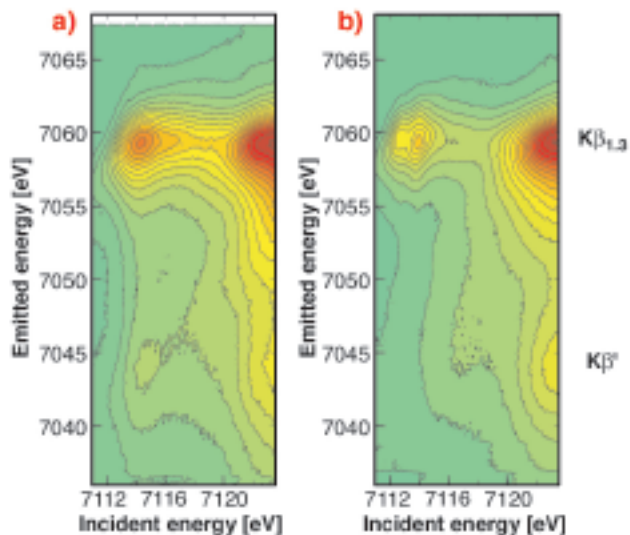


**Fig. 8:** 1s3p RIXS planes of a)  $\text{FeSrO}_{2.89}$  and b)  $\text{Fe}_2\text{O}_3$ . The spectra were taken at ID26.

A high-spin  $3d^5$  (Fe (III)) configuration only allows spin-down resonant (1s-3d) excitations while a further oxidation of the Fe 3d shell will open up vacancies in the spin-up density of states. This is immediately detectable in spin-selective absorption spectroscopy which thus serves as a “smoking gun” technique to detect Fe(IV) species. **Figure 8** shows the full 1s3p RIXS plane of  $\text{Fe}_2\text{O}_3$  as an example for a  $3d^5$  system and of Fe in  $\text{SrFeO}_{2.89}$  as an example for an Fe(IV) containing compound. The weak feature at 7114.5 eV incident and 7045 eV emitted energy is a signature of a  $3d^4$  configuration in  $\text{SrFeO}_{2.89}$  (cf. **Figure 9**).

Based on this proof of principle we applied 1s3p RIXS spectroscopy to Fe in a working catalyst. A Fe-ZSM-5 sample with an iron loading of 0.36 wt% was treated in steam at 873 K and finally in He at 1218 K. After this treatment, the majority of the iron sites should react with  $\text{N}_2\text{O}$  either to the postulated Fe(IV) species or the oxidation process stops at Fe(III) species. **Figure 9**

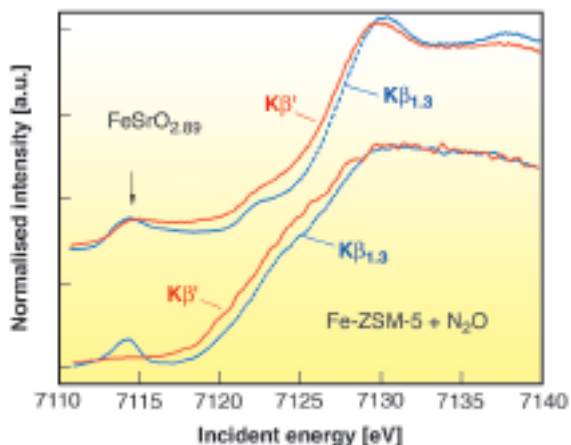


**Fig. 9:** XANES spectra of the Fe K-edge of  $\text{FeSrO}_{2.89}$  and of Fe-ZSM-5 after reaction with  $\text{N}_2\text{O}$  (bottom), recorded on the  $\text{K}\beta_{1,3}$  and the  $\text{K}\beta'$  fluorescence channel. The peak at 7114.5 eV incident energy in the  $\text{K}\beta'$  channel indicates a  $3d^4$  configuration.

compares the spin-selective absorption scans for  $\text{SrFeO}_{2.89}$  and Fe-ZSM-5 under  $\text{N}_2\text{O}$ . We do not find any indication for a  $3d^4$  configuration in Fe-ZSM-5 and thus reject the proposed formation of Fe(IV) species.

RIXS unequivocally proves that Fe(IV) species with a  $3d^4$  spin configuration are not formed during the catalytic reaction of Fe-ZSM-5 with  $\text{N}_2\text{O}$ . On the other hand, the partial  $3d^4$  configuration of the perovskite  $\text{FeSrO}_{2.89}$  is clearly detected. The technique is applicable to all Fe containing systems where Fe(IV) systems are believed to exist and can be extended to some other 3d transition metal systems.

## References

- [1] A.E. Bocquet, A. Fujimori, T. Mizokawa, T. Saitoh, H. Namatame, S. Suga, N. Kimizuka, Y. Takeda, and M. Takano, *Phys. Rev. B* **45**, 1561 (1992).
- [2] L. Kiwi-Minsker, D.A. Bulushev, and A. Renken, *J. Catal.* **219**, 273 (2003).
- [3] G. Peng, F.M.F. Degroot, K. Hämäläinen, J.A. Moore, X. Wang, M.M. Grush, J.B. Hastings, D.P. Siddons, W.H. Armstrong, O.C. Mullins, and S.P. Cramer, *J. Am. Chem. Soc.* **116**, 2914 (1994).

## Principal Publication and Authors

G.D. Pirngruber (a), J.D. Grunwaldt (a), J.A. van Bokhoven (a), A. Kalytta (b), A. Reller(b), O.V. Safonova (c), and P. Glatzel (c), *J. Phys. Chem. B* **110**, 18104 (2006).  
 (a) Eidgenössische Technische Hochschule, Zürich (Switzerland)  
 (b) University of Augsburg (Germany)  
 (c) ESRF

## Identification of carbide compounds in nanocrystalline Cr deposits by valence-to-core X-ray emission spectroscopy

Valence-to-core X-ray emission spectroscopy enables the retrieval of information on the formation of nanocrystalline materials that cannot be accessed by any other technique. Here we report on an application to study the composition of chromium coatings electrodeposited from Cr(III) sulfate electrolytes.

Chromium electroplates exhibit substantial hardness, wear and erosion resistance and are known for their high corrosion-resistant and decorative characteristics. However, due to the toxicity and the difficulties associated with waste utilisation, the conventional



## References

- [1] A.A. Edigaryan, V.A. Safonov, E.N. Lubnin, L.N. Vykhodtseva, G.E. Chusova, Yu.M. Polukarov, *Electrochim. Acta.* **47**, 2775 (2002).  
 [2] P. Glatzel, U. Bergmann, *Coordination Chemistry Reviews* **249** (1-2), 65 (2005).

## Principal Publication and Authors

V.A. Safonov (a), L.N. Vykhodtseva (a), Yu.M. Polukarov (b), O.V. Safonova (c,d), G. Smolentsev (e), M. Sikora (d), S. Eeckhout (d), P. Glatzel (d), *J. Phys. Chem. B*, **110**, 23192-23196 (2006).

(a) Chemistry Department, Moscow State University (Russia)

(b) A.N. Frumkin Institute of Physical Chemistry and Electrochemistry (Russia)

(c) SNBL, ESRF

(d) ESRF

(e) Rostov State University (Russia)

## Pressure dependence of phonon anomalies in molybdenum

The 4d transition elements exhibit a wide variety of phonon dispersion effects and thus provide a fertile testing ground for modern theoretical descriptions of lattice dynamics. Molybdenum, which is a bcc 4d transition metal, has been the focus of numerous theoretical and experimental studies of electronic structure, lattice dynamics, elasticity and strength. While the theoretical treatments of the lattice dynamics have been successful at describing many of the experimental observations, the large softening near the H-point has remained an open problem. Studies by neutron scattering at room conditions and as a function of temperature to 1203 K have shown that the H-point phonon displays anomalous stiffening with increasing temperature, which has been proposed to arise from either intrinsic anharmonicity of the inter-atomic potential or electron phonon coupling. While lattice compression provides a very convenient way to probe the interatomic potential, the requirement of relatively large samples for neutron scattering experiments has generally limited the range of pressures over which direct lattice dynamical information could be gathered. With the advent of inelastic X-ray scattering (IXS) techniques, these difficulties have to a great degree been overcome. Thus, in order to address the nature of these phonon anomalies, we performed both a high-pressure experimental study on beamline ID28 probing the lattice dynamics of molybdenum, as well as a new theoretical treatment of the phonon dispersions.

IXS experiments on single crystals at high pressure are quite unforgiving with respect to the sample quality and the high pressure hydrostatic environment. Thus, we have developed new techniques for preparing extremely small single crystals (45 micrometres in diameter by 20 micrometres thick) of high crystalline quality (**Figure 12**) [1]. The crystals were loaded into diamond anvil cells (DAC), using helium as a pressure-transmitting medium to ensure hydrostatic pressure conditions and the preservation of the crystal quality to pressures as high as 40 GPa.

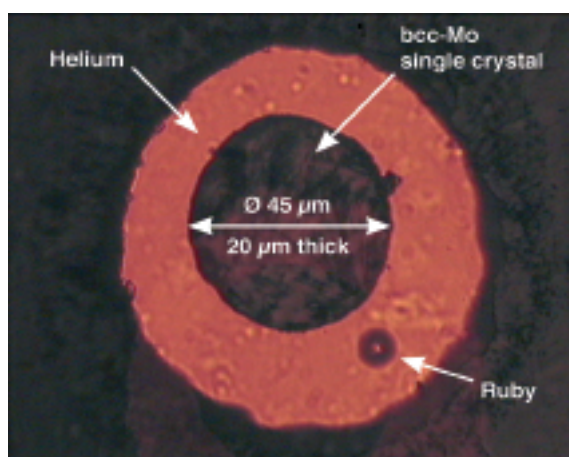


**Fig. 12:** Mo single crystal loaded in helium pressure medium. Photomicrograph was taken of the sample *in situ* at high pressure in the DAC.

We collected the complete phonon dispersion of Mo to 37 GPa, but here we will only focus on the observed decrease in the relative magnitude of the H-point phonon anomaly upon compression (**Figure 13**). This collapse in molybdenum is possibly best illustrated by the

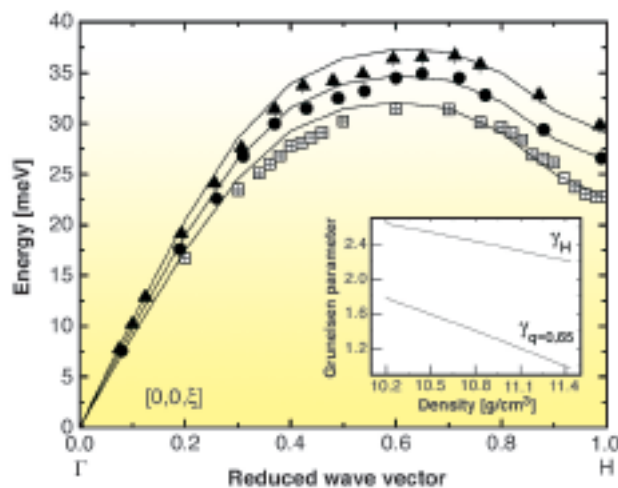


**Fig. 13:** Phonon dispersion in Mo along the [100] directions at high pressure. Filled symbols are IXS data (circle: 17 GPa; triangles: 37 GPa); the unfilled squares are inelastic neutron scattering data at 1 atm. Our calculations are shown as solid lines. The reduction of the anomaly with pressure is further illustrated in the inset, comparing the evolution with density of the Grüneisen parameter for  $q \sim 0.65$  (maximum of the dispersion) and at the H point ( $q = 1$ ).

comparison of the pressure dependence of the H-point phonon energy in bcc-Fe. For similar volume compressions, we find a ~6% and ~22% increase in the zone boundary mode in Fe and Mo respectively [2]. A number of lines of evidence indicate that the explanation for this is a decrease in the magnitude of electron phonon coupling on compression. Our DFT calculations treat the p-like bands as part of the ion core, and yet, they accurately predict the pressure evolution of the H-point anomaly, thus ruling out a significant role for the p-like bands, as instead previously suggested. Furthermore, upon compression at room temperature, the thermal excitations are both minimal and decrease with increasing pressure. This, in light of the fact that the computational methods used here are within the quasi-harmonic approximation, indicates that intrinsic anharmonic contributions are unlikely to be responsible for the anomaly. Conversely, we suggest that the nested electronic bands 3 and 4 near the Fermi level at one atmosphere, give rise to the anomaly. Evidence for this comes from the sensitivity of the calculated H-point phonon energy to the Gaussian broadening of the electron density of states. Since the Fermi energy level increases with pressure, those nested bands will be lower relative to the Fermi level (effectively moving outside of  $k_B T$  of the Fermi level). Moreover, compression induces band broadening and consequent weakening of the electron-phonon coupling. This sensitivity is to be expected if electron-phonon coupling is an important effect in the anomaly.

In conclusion, we have shown how and why the peculiar lattice dynamics of molybdenum become more 'regular' upon compression, resulting in a much more 'normal' bcc metal at high pressures. This possibly explains the extraordinary stability (to pressures in excess of 400 GPa) of molybdenum in the bcc structure.

## References

- [1] D.L. Farber, D. Antonangeli, C. Aracne, J. Benterou, *High Pressure Research* **26**, 1 (2006).  
 [2] S. Klotz and M. Braden, *Physical Review Letters* **85**, 3209 (2000).

## Principle Publication and Authors

D. L. Farber (a), M. Krisch (b), D. Antonangeli (a), A. Beraud (b), J. Badro (a,c), F. Occelli (a) and D. Orlikowski (a), *Physical Review Letters* **96**, 115502 (2005).

(a) Lawrence Livermore National Laboratory, Livermore (USA)

(b) ESRF

(c) Institut de Minéralogie et de Physique des milieux condensés, Univ. Paris (France)

## Elasticity of hexagonal BN and graphite

Despite the interest of graphite and hexagonal BN (h-BN) as basic building block for intercalated compounds and nanostructured materials, there is no complete and reliable data set of their elastic properties. There are two reasons for this: Firstly, the lack of sufficiently large single crystals makes the application of classical experimental techniques such as ultrasound measurements impossible; secondly, the spread amongst computational results is large as there are two completely different types of interatomic bonding – exceptionally strong  $sp^2$  covalent intralayer bonding and weak van der Waals interlayer bonding.

Inelastic X-ray scattering (IXS) overcomes the intrinsic difficulties of inelastic neutron scattering (INS), namely sample size and energy transfer limitations, and it is not sensitive to the defect structure of the material, unlike ultrasonic methods. Indeed, the first experimental determination of the optical phonons in the entire in-plane Brillouin zone of graphite was performed by IXS [1]. Here we obtained complete sets of the five independent elastic moduli and found the upper limits for the on-axis Young's moduli of homogeneous nanotubes.

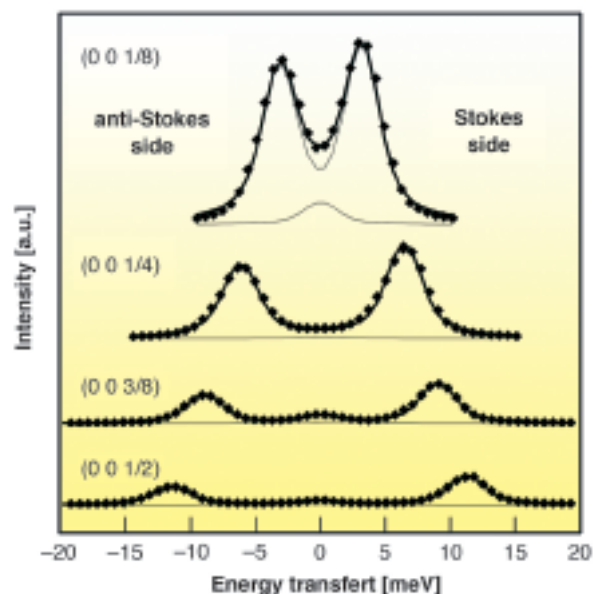


**Fig. 14:** Longitudinal acoustic phonons of graphite, measured close to the (004) Bragg spot, propagating along the  $c$  axis. Reduced momentum transfer values are given in reciprocal lattice units. The experimental data are shown together with the best fit results. The spectra are shifted in the vertical direction for clarity, conserving the same intensity scale. The counting time per point was 40 seconds.

	$C_{11}$ [GPa]	$C_{66}$ [GPa]	$C_{13}$ [GPa]	$C_{33}$ [GPa]	$C_{44}$ [GPa]	$B$ [GPa]
graphite	1109(16)	485(10)	0(3)	38.7(7)	5.0(3)	36.4(11)
h-BN	811(12)	321(8)	0(3)	27.0(5)	7.7(5)	25.6(8)

**Table 1:** Elastic moduli of hexagonal BN and graphite.

BN crystals were grown by high-pressure/high-temperature synthesis in a Ba-B-N catalyst system [2], while the graphite crystals were natural. In both cases the samples were platelets consisting of single crystalline domains. The size of a single grain was as large as 0.6-1.0 mm in the lateral direction and 50-120  $\mu\text{m}$  along the  $c$  axis. With the small beam dimensions, individual domains with angular spread of 0.025°-0.05° FWHM could be selected. The IXS experiment was performed on beamline **ID28**. The five independent elastic moduli were obtained *via* the sound velocities, as derived from the initial slope of the acoustic phonon branches along specific (mostly high-symmetry) directions, and the Christoffel's equation. The consequence of the high anisotropy of graphite and h-BN is the need to take into account the effect of the finite resolution in momentum transfer  $q$ , defined by the angular opening of the analysers. The instrument was operated utilising the silicon (9 9 9) setup, providing a total energy resolution of 3.0 meV. The momentum resolution was set to 0.2  $\text{nm}^{-1}$  and 0.7  $\text{nm}^{-1}$  in the horizontal and vertical plane, respectively. The acquisition time per point varied from 30 to 60 s. An example of the collected data is given in **Figure 14**.

The resulting elastic moduli (see **Table 1**) allow us to reconstruct the velocity of sound propagating in any direction as presented in **Figure 15**. While the overall topology of the sound velocity surface is similar for both systems, the difference in details is quite substantial. The elastic moduli are regularly higher for graphite, except for the  $C_{44}$  value.  $C_{44}$  is much larger in hexagonal BN due to the additional ionic interaction between layers, making them more rigid vs. shear deformation.

The values derived from the ultrasonic data are regularly lower than for INS and IXS. This fact is not surprising, as these measurements were performed on pyrolytic graphite and hBN, where the presence of defects greatly influences the macroscopic elastic properties. INS capabilities are limited by the sample size, which imposes again the utilisation of pyrolytic samples. INS measurements of phonon dispersion in graphite were the least reliable for the in-plane longitudinal acoustic branch due to the nature of the sample, while for lower-velocity branches the data are very close to our results.

The elasticity of layered substances is directly linked to the mechanical properties of derived nanotubes, of interest for applications such as high-strength fibres.

Our values of  $C_{11} = 1.1$  TPa for graphite and  $C_{11} = 0.8$  TPa for h-BN provide the upper estimate of the on-axis Young's modulus of homogeneous nanotubes. The majority of measurements performed on the nanotubes give overestimated values compared with our evaluations. We believe that our estimates provide a solid background for both theoretical modeling and analysis of experimental data.

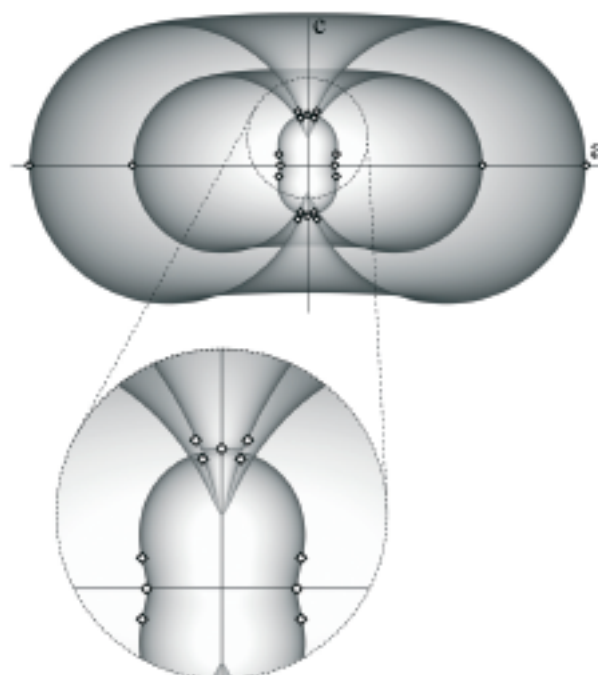


**Fig. 15:** 3D plot of the sound velocity data for the h-BN (half-space shown) and its  $a$ - $c$  plane section: experimental data are denoted by diamonds, the surface corresponds to the best fit. The low-velocity part is shown enlarged in the bottom panel.

## References

- [1] J. Maultzsch, S. Reich, C. Thomsen, H. Requardt, P. Ordejón, *Phys. Rev. Lett.* **92**, 075501 (2004).
- [2] K. Watanabe, T. Taniguchi, H. Kanda, *Nature Materials* **3**, 404 (2004).

## Principal Publication and Authors

- A. Bosak (a), J. Serrano (a), M. Krisch (a), K. Watanabe (b), T. Taniguchi (b), H. Kanda (b), *Phys. Rev. B* **73**, 041402 (2006); A. Bosak (a), M. Krisch (a), M. Mohr (c), J. Maultzsch (c), C. Thomsen (c), *submitted*.  
 (a) ESRF  
 (b) Advanced Materials Laboratory, National Institute for Materials Science, Tsukuba (Japan)  
 (c) Institut für Festkörperphysik, TU Berlin (Germany)



# Materials Science

## Introduction

Materials science and materials engineering involve the investigation of structure property relationships and the use of these findings to produce materials with predetermined properties. Studies of this type play a major role at the ESRF and span a wide range of applications. All aspects of materials science studies cannot be covered by this brief exposé. The trend in materials science research at the ESRF is that micro focussing; time-resolved studies in situ and the application of combinations of techniques are on the rise. Also, focussing down to the nanometre range and applications of extreme magnetic fields are emerging areas. In order to illustrate these trends we have chosen a few examples from the categories: extreme conditions; use of pair distributions; general applications of X-ray diffraction to problems in materials science; and new developments.

Enormous advantages in examining materials under non-ambient

conditions such as high pressure or high temperature have been made due to developments in diamond anvil cells, large volume presses and laser heating in combination with the third generation X-ray source at the ESRF. The use of pressure at ID09B shows for the first time a pressure-induced isomorphous volume collapse of the itinerant  $\text{YCo}_5$  magnet. High pressure at low temperature studies of magnetite prove that there is a clear correspondence between electronic and structural transitions (drop in conductance and cubic to cubic distortions) disproving the Verwey-Mott concept. High pressure studies of Fe above 2 Mbars at ID27 suggest that the Earth's inner core is lighter than a mixture of Fe and Ni at the same conditions implying a larger content of light elements.

High-resolution powder diffraction has proven to be a very useful tool in many materials science applications. Thanks to automatization, hundreds of diffraction patterns can now be

collected in a short time. A systematic investigation of the phase diagram of  $\text{LiNH}_2:\text{LiBH}_4$  at ID31 has revealed a new solid phase  $\text{Li}_4\text{BN}_3\text{H}_{10}$  with promising applications as hydrogen storage for fuel cells. ID31 has also been used to obtain detailed atomic models for icosahedral Mg-Zn-rare-earth quasicrystals from high-resolution powder diffraction via real space pair distribution functions indicating a procedure to obtain structural information from aperiodic crystals. Wide-angle X-ray scattering studies of the behaviour of nanolayered clay particles suspended in oil under a polarising electric field at BM01A suggest new ways to obtain self-assembled nanostructures. The high-energy beamline ID15 has been used to resolve the debated phase behaviour of the alloy Au-Ni by means of high-energy X rays (60 and 90 keV) by mapping the diffuse scattering of the system. It was concluded that this system exhibits a competition of ordering and phase

separation. Measuring of static structure factors of a new form of  $\text{CO}_2$  in combination with Raman measurements at ID27 proved that the new form  $\alpha\text{-CO}_2$  (carbonia) is a new single-bonded glass analogue to the known  $\text{SiO}_2/\text{GeO}_2$  polymorphs. The new amorphous material was synthesised above 40 GPa at temperatures as high 680 K in a diamond anvil cell.

New developments in the materials science sector include a detailed mapping of the photo-dissociation of  $\text{HgI}_2$  by pump (laser)-probe (single X-ray pulses) methods at ID09B. Probing the excited liquid with a time resolution of 100 ps showed a two-body dissociation channel ( $\text{HgI}_2$  to  $\text{HgI}+\text{I}$ ) to be the dominant channel. The sub-micrometre range is particularly interesting in materials science as it is the critical length scale for many intergranular interactions such as cracks and dislocations; these interactions give rise to the bulk properties of materials. To meet these challenges ID11 has been extended to a long beamline giving a transverse resolution of below 100 nm by using state-of-the art modular focussing optics. Pioneering work has also been performed employing high magnetic fields at beamline BM26B. Pulsed magnetic fields up to 30 Tesla were used to study the Jahn-Teller distortion of  $\text{TbVO}_4$ . It was shown that the high magnetic field modified the distortion and that these changes can be detected by X-ray powder diffraction.

Å. Kvick

## Magneto-elastic lattice collapse in $\text{YCo}_5$

Symmetry conserving collapses of crystalline lattices at elevated pressures are a particularly fascinating phenomena, well-known examples being samarium sulfide and cerium metal. Both transitions with about 15% volume reduction are ascribed to reorganisations of  $4f$ -electrons. In contrast, the lattice collapse of  $\text{YCo}_5$  is driven by magnetic interactions of itinerant  $3d$  electrons. In the present investigation, the associated magnetoelastic anomaly was studied by a combination of *ab initio* electronic structure calculations and high-pressure X-ray diffraction experiments.

Cobalt metal exhibits the most stable magnetic structure of all chemical elements and compounds. This is indicated by its very high magnetic ordering temperature  $T_C \approx 1400$  K. When cobalt is diluted with moderate amounts of non-magnetic metals, its tendency for strong magnetic coupling is essentially preserved. Co-rich intermetallic compounds like  $\text{Y}_2\text{Co}_{17}$  (90% Co,  $T_C \approx 1200$  K) or  $\text{YCo}_5$  (83% Co,  $T_C \approx 1000$  K) are strong ferromagnets with completely filled majority spin states in the Co- $3d$  subband, *i.e.* the Co spin moment is only slightly reduced by hybridisation. Compounds of such compositions ( $\text{SmCo}_5$  and  $\text{Sm}_2\text{Co}_{17}$ ) are frequently used in permanent magnet applications.  $\text{YCo}_5$  combines a high ordering temperature with a pronounced sensitivity to pressure.

We have studied the electronic structure of  $\text{YCo}_5$  by means of the full-potential local-orbital (FPLO) computational method [1] and found a transition to a low-spin state at a pressure within the experimentally available region. The computational results predict a reduction of the magnetic moment by one third which is coupled with a small, discontinuous contraction of the lattice. Although the transition is symmetry conserving with respect to both the lattice and the atomic positions, the abrupt change of the lattice parameters is calculated to be significantly anisotropic.

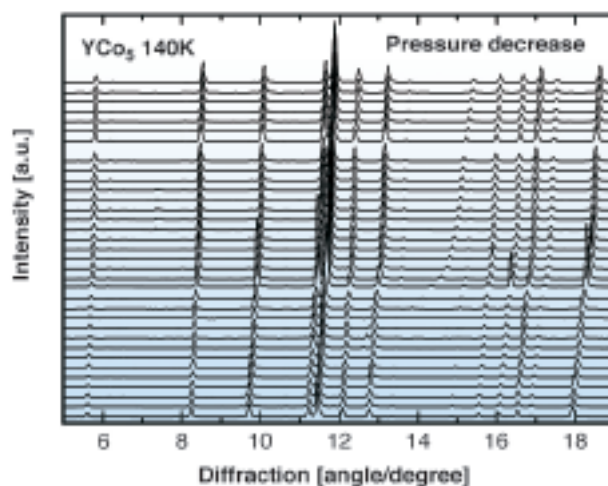
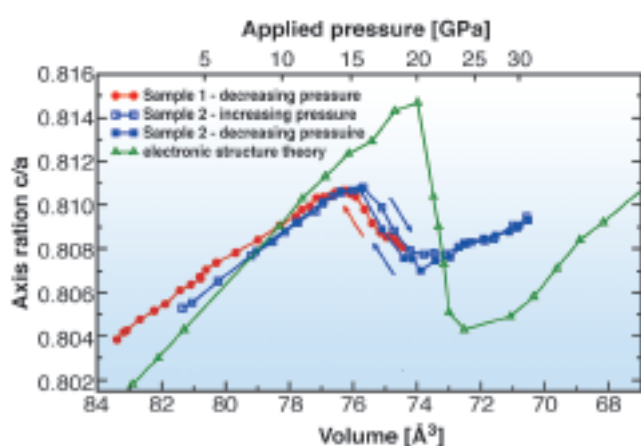


Fig. 16: X-ray diffraction diagrams at 140 K in the direction of decreasing pressure.

Angle-dispersive X-ray diffraction experiments at high pressures and low temperatures were performed at ESRF beamline ID09A to experimentally investigate the predicted anomaly. The measured X-ray diffraction patterns (Figure 16) exhibit the predicted anomalies of the lattice parameters but no indication of any symmetry change. Consequently, the transformation that  $\text{YCo}_5$  undergoes at 19 GPa is a symmetry-retaining phase transition. The experimental results (see Figure 17) are in perfect agreement with the theoretical volume dependence of the lattice parameter ratio,  $c/a$ . The comparison of theoretical and experimental data facilitates an assignment of the sudden change of  $c/a$  at 19 GPa to the predicted magneto-elastic transition. This is the first-ever observation of a pressure-induced isomorphic volume collapse of an itinerant magnet.



**Fig. 17:** Lattice collapse along the hexagonal  $c$ -axis in  $\text{YCo}_5$  at pressures up to 33 GPa. The blue and red curves show the measured  $c/a$  ratios for two different samples at 100 K and 140 K, respectively. The green curve is the result of the electronic structure calculations. Application of pressure reduces the volume of the crystal, continuously at first, then at 19 GPa a sudden drop of the  $c$ -axis parameter is observed.

The discontinuity at a cell volume of about  $74 \text{ \AA}^3$  indicates a metastable region. Such a thermodynamic instability which can be identified by calculating the free enthalpy of the system is characteristic for a first-order phase transition. Here, it is thermodynamically impossible to transfer one phase into the other by realising a continuous sequence of equilibrium states. Thus, the system cuts its own non-equilibrium path depending on the real structure of the specific sample, internal and external parameters and fluctuations. In general, different paths are taken for increasing and decreasing pressure. This phenomenon typically shows up in a hysteresis loop as the one observed in the present experiment (Figure 17).

At low pressures,  $\text{YCo}_5$  is a strong ferromagnet, *i.e.* the magnetism is not sensitive to moderate changes of thermodynamic variables. In particular, the magnetic

moment is rather stable since the majority-spin Co-3d band is completely filled. A characteristic feature of the majority band is a pronounced peak in the density of states (DOS) right below the Fermi level. The application of pressure reduces interatomic distances, the overlap of valence orbitals increases and the related bands broaden. Therefore, the majority Co-3d band edge moves towards the Fermi energy. When the related sharp DOS peak approaches the Fermi level, the system becomes electronically unstable, resulting in a sudden, partial depopulation of the majority-spin channel. The system transforms into a new stable state which is characterised by a smaller magnetic moment, a smaller volume and a reduced  $c/a$  ratio. Quantitatively, this scenario is described by a generalised Stoner criterion. Lifshitz predicted as early as 1960 that pressure-driven elastic anomalies can occur when the topology of the Fermi surface changes while the number of valence electrons is preserved [2].

## References

- [1] K. Koepernik, H. Eschrig, *Phys. Rev. B*, **59**, 1743-1757 (1999).
- [2] I.M. Lifshitz, *Sov. Phys. JETP* **11**, 1130-1135 (1960).

## Principal Publication and Authors

H. Rosner (a), D. Koudela (b), U. Schwarz (a), A. Handstein (b), M. Hanfland (c), I. Opahle (b), K. Koepernik (b), M. Kuz'min (b), K.-H. Müller (b), J. Mydosh (b), M. Richter (b), *Nature Physics* **2**, 470-473 (2006).  
 (a) Max-Planck-Institut für Chemische Physik fester Stoffe, Dresden (Germany)  
 (b) IFW Dresden (Germany)  
 (c) ESRF

## The origin of the Verwey transition in magnetite

Magnetite ( $\text{Fe}_3\text{O}_4$ ) is a fascinating natural mineral which is a metallic ferrimagnet at ambient conditions. It was used by early navigators to locate the magnetic North Pole and is synthesised naturally in living species such as fish and birds to be used as magneto-receptors in their navigation. Magnetite has become an important ingredient in the formation of metallic/magnetic nanocomposites.

In 1939 Verwey discovered [1] a remarkable phenomenon in magnetite, a discontinuous drop in the conductance on cooling the sample below 122 K. This temperature  $T_V$  has been nicknamed the *Verwey temperature* and was shown to be dependent on stoichiometry. Since then magnetite became the subject of numerous structural, electronic/magnetic and

thermodynamic studies. It is the only mixed-valence iron oxide and has an *inverse spinel* cubic structure,  $AB_2O_4$ , at ambient conditions. The octahedral six-coordinated *B*-site, twice as abundant as the *A*-site, is equally occupied by  $Fe^{3+}$  and  $Fe^{2+}$  whereas the tetrahedral four-coordinated *A*-site is occupied by  $Fe^{3+}$ . The presence of the mixed-valence in the *B* sites motivated Verwey and many others, including Mott, to hypothesise that electronic exchange  $[Fe^{2+}Fe^{3+}]_B \rightarrow [2Fe^{3+} + e^-]_B$  between the ferrous and ferric ions take place above  $T_V$  (*Verwey-Mott* theory). *Charge disorder* (CD) within the *B*-site, propagating throughout the crystal, would then explain the metallic nature of magnetite at  $T > T_V$ , whereas the onset of *charge ordering* (CO) within the *B*-site below  $T_V$  would explain the observed metal-insulator transition.

In recent years we have witnessed numerous studies searching for the elusive charge ordering taking place along the *B*-site, namely, for a transition from a CD-state (metallic) to a CO-state (insulator):



Several studies with spectroscopy sensitive to Fe valence have been applied to verify this theory but none could assert the onset of the CD  $\rightarrow$  CO below  $T_V$ . At  $T \leq T_V$  a first-order structure phase transition also takes place: a cubic to distorted-cubic spinel at  $T = T_{DIST}$ .

We carried out precise high-pressure (HP) X-ray diffraction (XRD) studies to determine the pressure

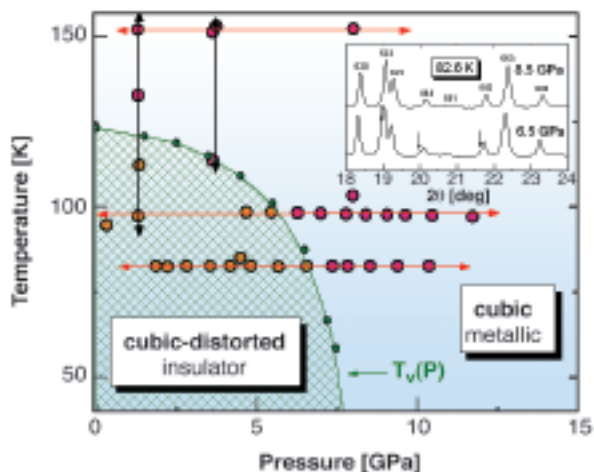


**Fig. 18:** The phase diagram of magnetite in the 0-150 K and 0-15 GPa (P,T) ranges. The shaded area is the insulating region encompassed by 0-120 K, 0-8 GPa and the  $T_V(P)$  curve, the latter obtained experimentally [2]. Isothermal and isobaric XRD measurements were carried out. The pink and orange circles correspond to the *cubic* and *cubic distorted* regimes as deduced from the XRD data and subsequent fitting. The inset shows a case of a PI-induced structural transition at 82.6 K. The 8.5 GPa spectrum corresponds to cubic phase and the 6.5 GPa to the distorted phase. Arrows indicate new peaks corresponding to the new phase.

dependence of  $T_{DIST}$  and look for a relationship with the well established  $T_V(P)$  [2]. Measurements were carried out at **ID09** using its diamond anvil cell in the  $75 < T < 160$  K and  $0.2 < P < 12$  GPa ranges. Hydrostatic pressure conditions were obtained by using He as a pressure medium.

The electronic and structural (P,T) phase diagram of magnetite in the above (P,T) ranges is shown in **Figure 18**. The green curve corresponds to the experimental (dots) electrical measurements of  $T_V(P)$  [2]. The double-headed paths, indicating reversibility of the process, clearly shows structural transformation, cubic  $\leftrightarrow$  cubic-distorted, once isothermal or isobaric changes take place throughout the border line of  $T_V(P)$ . This establishes the intimate *relationship between the electronic and structural transitions*. Thus, the cause of the Verwey transition originates from a gap opening once the cubic distorted regime is created, probably within the oxygen *p*-bands, contradicting the *Verwey-Mott* concept of CO within the *B*-sites.

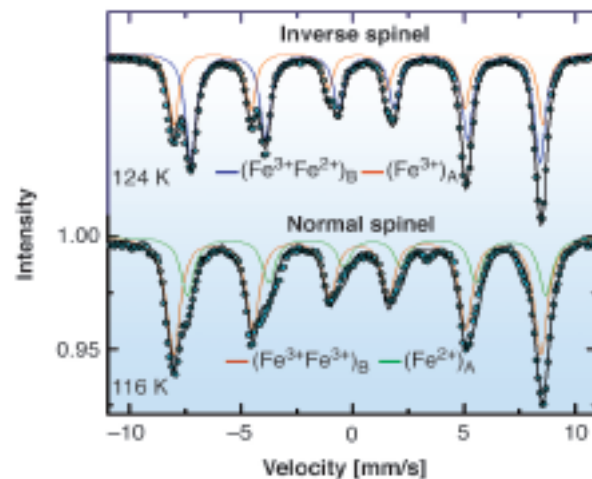
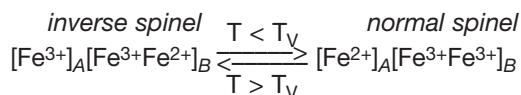


**Fig. 19:** The Mössbauer 124 K ( $T > T_V$ ) spectrum corresponds to the *inverse spinel* structure with two spectral hyperfine interaction components: two sixfold coordinated  $(Fe^{3+}Fe^{2+})_B$ , and one fourfold coordinated  $(Fe^{3+})_A$ . The 116 K ( $T < T_V$ ) spectrum corresponds to two sixfold coordinated  $(Fe^{3+}Fe^{3+})_B$ , and one fourfold coordinated  $(Fe^{2+})_A$ , consistent with a *normal spinel* structure.

A manifestation of this *contradiction* was encountered in our recent  $^{57}Fe$  Mössbauer Spectroscopy (MS) studies [3]. At ambient P (see **Figure 19**) the features of the spectra above and below  $T_V$  are clearly dissimilar. Both can be fitted with two spectral components, the first corresponding to an inverse- and the second to a normal-spinel.



Within the normal-spinel regime the CO concept becomes redundant, thus providing irrefutable proof that the Verwey-Mott concept is incorrect.

## References

- [1] E.J. Verwey, *Nature* (London) **144**, 327 (1939).  
 [2] N. Mori, S. Todo, N. Takeshita, T. Mori, Y. Akishige, *Physica B* **312-313**, 686 (2002).  
 [3] M. P. Pasternak, W. M. Xu, G. Kh. Rozenberg, R. D. Taylor, and R. Jeanloz, *J. Magn. Magn. Mater.*, **265**, L107 (2003).

## Principal Publication and Authors

G. Kh. Rozenberg (a), M.P. Pasternak (a), W.M. Xu (a), Y. Amiel (a), M. Hanfland (b), M. Amboage (b), R.D. Taylor (c), and R. Jeanloz (d), *Phys. Rev. Lett.* **96**, 045705 (2006).

(a) School of Physics and Astronomy, Tel Aviv University (Israel)

(b) ESRF

(c) MST-10, MS-K764, Los Alamos National Laboratory (USA)

(d) Department of Earth and Planetary Science, University of California, Berkeley (USA)

## Quasi-hydrostatic equation of state of iron above 2 Mbar

Iron is the major component of the Earth's core, alloyed with a few percent of nickel and lighter elements [1]. The thermodynamic conditions in this envelope are extreme: the pressure spans between 136 and 329 GPa in the liquid outer core and between 329 and 364 GPa ( $\sim 3.64 \times 10^6$  atm) in the solid inner core, and the temperature is estimated to lie between 5000 and 7000 K. The physical behaviour of iron under these conditions is essential knowledge for our understanding of the deep Earth. In particular, its Equation of State (EoS)  $P(V,T)$  ( $P$  pressure,  $V$  specific volume and  $T$  temperature) can be compared to seismological measurements to determine chemical and physical state of the core. Major geophysical issues thus rely directly on the accuracy of the EoS of iron.

The diamond anvil cell is the ideal tool to generate pressures in the range relevant to the Earth's interior. Combined with synchrotron X-ray diffraction, it has already allowed the measurement of the EoS of iron at 300 K up to 300 GPa, this was almost 20 years ago [2]. In the meantime, high pressure techniques and X-ray generation techniques have improved significantly. We thus decided to reexamine the EoS of iron using state-of-the-art diamond anvil cell techniques. The sample and the pressure gauge, tiny grains of iron and tungsten, were embedded in helium, which is used as a quasi-hydrostatic pressure transmitting medium (Figure 20), in

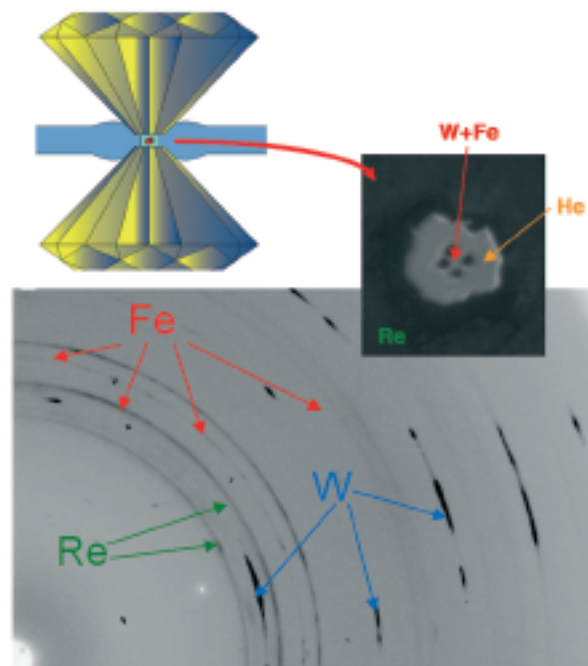


**Fig. 20:** Monochromatic diffraction pattern recorded at 190 GPa. Iron (sample), tungsten (pressure gauge), and rhenium (gasket) diffraction signal can be easily distinguished. The high-pressure chamber, filled with helium, containing the sample and the pressure gauge (photograph, the size of the chamber is  $\sim 20$  micrometres) is located between the two diamond anvils, in the hole of a rhenium gasket (top picture).

a diamond-anvil cell pressure chamber. The volume  $V$  of iron was then measured for increasing pressure steps by X-ray diffraction. The high flux and high focussing of the X-ray beam of the ID27 beamline allowed the collection of the monochromatic X-ray diffracted signal displayed in Figure 20 in less than one minute. The compression curve obtained by this method is plotted on Figure 21.

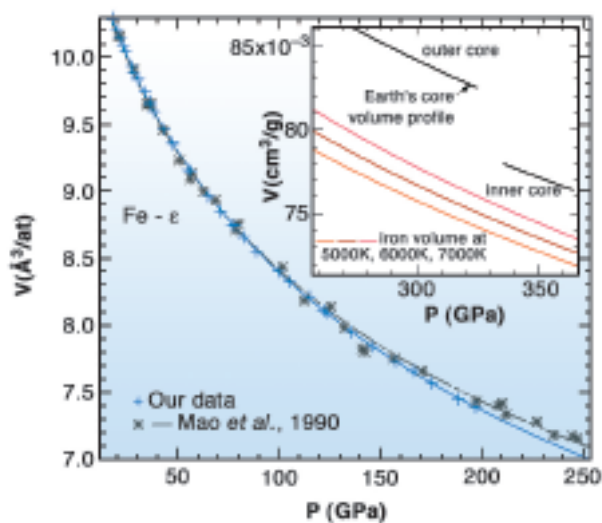


**Fig. 21:** Ambient temperature compression curve of iron measured on ID27 beamline, compared with the data obtained in 1990. The inset shows the volume of iron deduced from this compression curve in the possible temperature range of the Earth's core, compared with the volume profile measured by seismology.

We found that the compression of iron is significantly higher than previously measured [2]. This can be explained by non-hydrostatic pressurising conditions – no pressure transmitting medium was used – and a less accurate pressure metrology in the previous experiments [2].

Using these data, we built a P(V,T) EoS for iron, which suggests that the Earth's inner core is lighter than a mixture of Fe and Ni under the same conditions (Figure 21). This can be explained by the alloying of Fe and Ni with several percent of light elements (Si, S, O). These new data increases the estimated content of light elements in the Earth's core.

## References

- [1] J.-P. Poirier, *Phys. Earth Planet. Inter.*, **85**, 319-337 (1994).  
 [2] H.-K. Mao, Y. Wu, L.C. Chen and A.P. Jephcoat, *J. Geophys. Res.*, **95**, 21737-21742 (1990).

## Principal Publication and Authors

A. Dewaele (a), P. Loubeyre (a), F. Occelli (a), M. Mezouar (b), P.I. Dorogokupets (c) and M. Torrent (a), *Phys. Rev. Lett.* **97**, 215504-215507 (2006).  
 (a) CEA, Bruyères le Châtel (France)  
 (b) ESRF  
 (c) Institute of the Earth's Crust, Irkutsk (Russia)

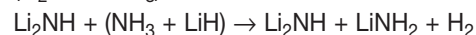
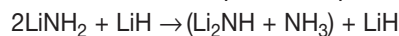
# Developing lightweight hydrogen storage materials

There is worldwide interest in the use of hydrogen as the basis for a future sustainable energy economy with low carbon emissions. Hydrogen production, storage and utilisation are the three key technological elements of a hydrogen economy and all face significant scientific and technological challenges. One of the key materials challenges is associated with hydrogen storage. Hydrogen contains more chemical energy on a weight for weight basis than any other material but, as the lightest element, it also has a very low energy density.

For hydrogen-fuel cell transportation use – widely regarded as *the* first major inroad into the hydrogen economy – a suitable material for on-board storage should be able to store a high weight-percent and high volume density of hydrogen and, equally importantly, rapidly discharge and charge this same amount of hydrogen at acceptable temperatures (typically around 50–100°C). This represents a particular challenging set of credentials for an ideal storage material and at present no known material meets these critical requirements.

In 2002, Chen *et al.* [1] discovered that the system  $\text{Li}_3\text{N-Li}_2\text{NH-LiNH}_2$  could reversibly cycle hydrogen with a

theoretical maximum of over 11wt%  $\text{H}_2$ . In practice, only cycling between lithium imide and amide is feasible at realistic pressures and temperatures. Close investigation of by-products of the decomposition of  $\text{LiNH}_2$ , however, showed that ammonia,  $\text{NH}_3$ , is formed as part of the  $\text{H}_2$  desorption process. This riddle was later resolved by careful measurements that showed that desorption occurred in two separate steps:



Although  $\text{NH}_3$  absorption by LiH is a rapid and efficient process. However, in practice it is difficult to reduce  $\text{NH}_3$  levels to below 200 ppm, a value that still is high enough to poison current fuel-cell operation.

In our search for new materials with similar properties to  $\text{LiNH}_2$  but with reduced  $\text{NH}_3$  production, we have investigated various solid solutions of  $\text{LiNH}_2$  with other materials. Our first study involved a detailed investigation of the  $\text{LiNH}_2\text{:LiBH}_4$  phase diagram. Using the ID31 diffractometer under robotic control, we were able to investigate stoichiometries in 1/12 steps across the phase diagram. We discovered a single stable phase with the composition  $\text{Li}_4\text{BN}_3\text{H}_{10}$ . Indexing of the pattern obtained on ID31 indicated a body-centred space group with a 10.6669(7) Å lattice constant and no apparent systematic absences – this is consistent with five possible cubic space groups leading to a significant crystallographic search for the correct structure.

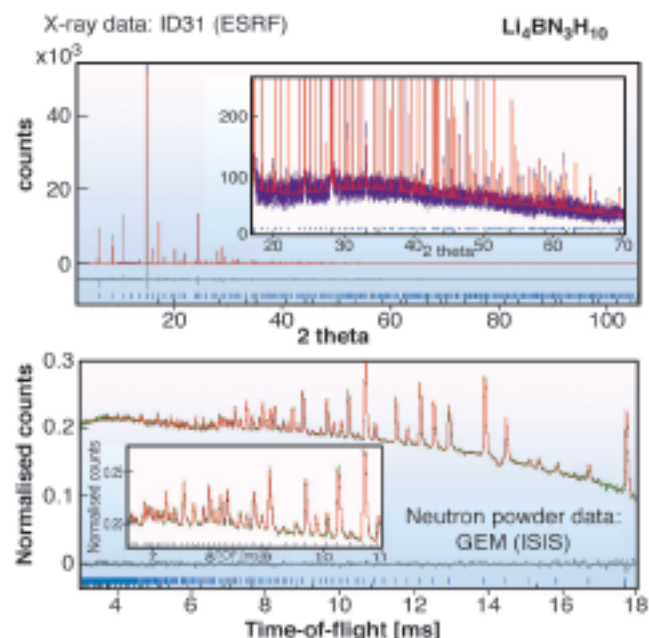


**Fig. 22:** X-ray and neutron powder diffraction patterns of  $\text{Li}_4\text{BN}_3\text{H}_{10}$ . Both datasets are fitted simultaneously to high precision providing strong validation of all aspects of the crystal structure including hydrogen positions.

Consideration of the likely density based on the stoichiometry  $3\text{LiNH}_2\text{:LiBH}_4$  led to the conclusion that space groups  $I23$  and  $I2_13$  were the most likely if the

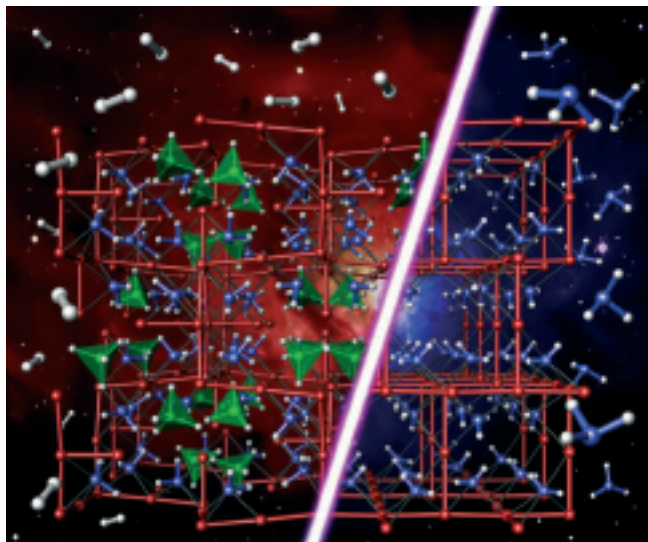


**Fig. 23:** Comparison of the crystal structures of  $\text{Li}_4\text{BN}_3\text{H}_{10}$  and  $\text{LiNH}_2$  highlighting the fact these two structurally similar materials principally desorb hydrogen and ammonia respectively.

crystal structure is ordered. Chemical considerations then led us to the hypothesis that both  $\text{NH}_2$  and  $\text{BH}_4$  groups were situated on an approximate face-centred cubic lattice. In common with  $\text{LiNH}_2$ , the Li atoms were presumed to occupy half of the available tetrahedral sites. Accordingly both  $I2_3$  and  $I2_13$  models were tested, with the condition that Li occupancies on all crystallographically independent sites were allowed to vary.  $I2_13$  was the marginally favoured space group over  $I2_3$ . The difference in goodness of fit is small as  $\text{NH}_2$  and  $\text{BH}_4$  are isoelectronic and thus have similar scattering cross sections. Neutron powder diffraction studies were performed on the GEM diffractometer at ISIS. Importantly, the high neutron flux on GEM enabled us to work with natural, unenriched  $\text{Li}_4\text{BN}_3\text{H}_{10}$ . The combination of X-ray and neutron diffraction studies (see **Figure 22**) led to a precise determination of the full crystal structure, which has been independently corroborated by computational studies [2] as the most precise determination of a number of recent studies. The structure itself is shown in **Figure 23** alongside the crystal structure of  $\text{LiNH}_2$ . The similarities between the structure are clearly evident. Remarkably,  $\text{Li}_4\text{BN}_3\text{H}_{10}$  produces predominantly hydrogen rather than ammonia on desorption with a theoretical  $\sim 11\text{wt}\%$   $\text{H}_2$ . Unfortunately having fulfilled the interim of reduced  $\text{NH}_3$  production, the reversibility of this system is significantly inferior to  $\text{LiNH}_2$ . Optimising all the desirable characteristics of an ideal hydrogen storage material proves to be a difficult task. However the continued study of these systems using ID31 will be a powerful tool in the search for the ideal hydrogen storage material.

#### References

- [1] P. Chen, Z. T. Xiong, J. Z. Luo, J.Y. Lin, K.L. Tan, *Nature* **420**, 302-304 (2002).  
 [2] D. J. Siegel, C. Wolverton, V. Ozolins, *Submitted* (2006)

#### Principal publication and authors

P.A. Chater (a), W.I.F. David (b), S.R. Johnson (c), P.P. Edwards (c), P.A. Anderson (a), *Chem. Comm.* **23**, 2439-2441, (2006).

(a) School of Chemistry, University of Birmingham (UK)

(b) Rutherford Appleton Laboratory (UK)

(c) Inorganic Chemistry Laboratory, Oxford University (UK)

## Atom location in quasicrystals from atomic pair distribution function refinement

Quasicrystals have been found in many intermetallic alloy systems in the last 20 years. Their unique feature is the non-crystallographic diffraction symmetry such as  $10/mmm$  or  $m-3-5$ . Due to the presence of discrete Bragg peaks they are classified as aperiodic crystals which can be described in higher dimensional ( $nD$ ,  $n > 3$ ) space. Their structure and electronic, magnetic, thermal, dynamic, mechanical and surface properties as well as their applications such as thin films have been of great interest in the last years [1]. Special interest has been paid to the Mg-Zn-rare-earth systems where the presence of  $4f$ -elements like holmium raises a question for quasiperiodic magnetic order. Icosahedral  $\text{Ho}_{11}\text{Mg}_{15}\text{Zn}_{74}$  (**Figure 24**) represents a promising candidate as it provides a primitive 6D space group  $Pm-3-5$  or  $P235$  allowing for such order. Its atomic structure determination is an essential prerequisite for any magnetic structure analysis.

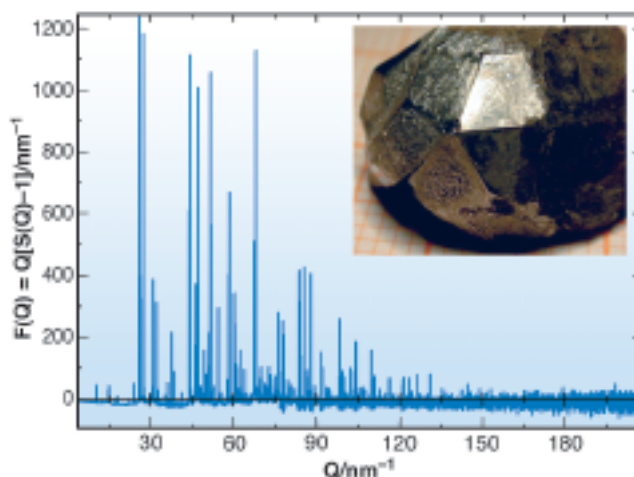


**Fig. 24:**  $P$ -type icosahedral  $\text{Ho}_{11}\text{Mg}_{15}\text{Zn}_{74}$ : 41 keV total scattering data  $F(Q)$  collected at ID31. The inset shows a cm-sized single crystal of triacontahedral morphology, point group  $m-3-5$ .

Since quasicrystals are not periodic in 3D space, their structure determination is not trivial. Complementary to the higher dimensional crystallography, we use the real space pair distribution function (PDF) from total

scattering powder data (local crystallography). This technique, well established for the structure analysis of glasses, has also been applied to the local structure determination of a number of crystalline but disordered systems [2].

The PDF  $G(r)$  is a direct Fourier transform of the scattering factor  $F(Q) = Q[S(Q)-1]$  where  $S(Q)$  is the corrected and normalised X-ray powder scattering intensity, dependent on the scattering vector length  $Q$ .  $G(r) = 4\pi r [\rho(r)-\rho_0]$  gives the probability of finding pairs of atoms separated by the distance  $r$  referenced with respect to the average electron density  $\rho_0$ . It is weighted by the respective  $Z$  of the involved atoms. The  $F(Q)$  of  $\text{Ho}_{11}\text{Mg}_{15}\text{Zn}_{74}$  from high-resolution data collected at ID31 is shown in Figure 24. The selected energy of 41 keV offers a  $Q_{\text{max}} = 300 \text{ nm}^{-1}$  which ensures a high resolution of the experimental PDF in real space. In turn, high resolution for  $Q$  at ID31 provides a minimal exponential decay of the PDF, consequently there are still sharp peaks at  $r > 10 \text{ nm}$  reflecting long-range quasiperiodic order. The corresponding PDF up to  $r < 2 \text{ nm}$  is displayed in Figure 25.

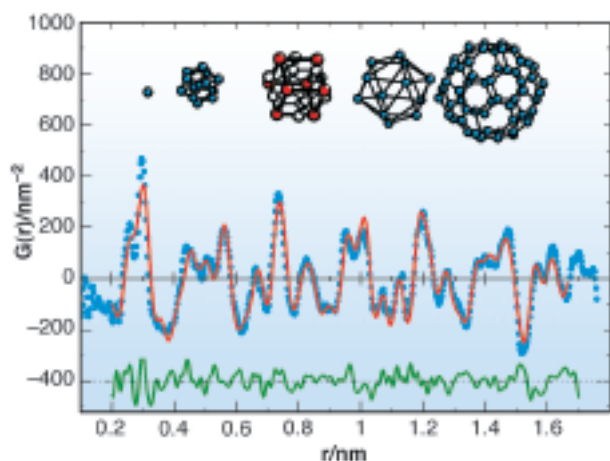


**Fig. 25:** Refined local structural model: Experimental (blue dots), model (red line) and difference (green line) PDF data. Inset: onion-like concentric shell model of the basic building block. Mg, Zn, Ho-atoms are marked in white, blue and red, respectively.

Structure solution is based on trial and error matching of PDFs of known related periodic alloy phases to the experimental data. In this case the PDF of cubic  $\text{Al}_{23}\text{Mg}_{40}\text{Zn}_{37}$  resembles well that of the quasicrystal. Our model for  $P$ -type  $\text{Ho}_{11}\text{Mg}_{15}\text{Zn}_{74}$  fits the experimental PDF nicely up to 2.5 nm after least-squares refinements have been performed using  $G(r)$  in the interval  $0.2 \text{ nm} < r < 1.8 \text{ nm}$ . Figure 25 contains the measured and calculated PDFs and their difference.

We find that the single atoms in the  $\text{Ho}_{11}\text{Mg}_{15}\text{Zn}_{74}$  quasicrystal are coordinated normally like in the Frank-Kasper phases, which are a well understood class. On a higher hierarchical level, the basic building block is a

“stuffed bucky ball” of diameter  $d \sim 1.5 \text{ nm}$ , this is sketched in Figure 25. It is composed like an onion by a concentric arrangement of icosahedra, a pentagon-dodecahedron with an inscribed cube and one central atom. In between neighbouring balls, which share atoms of the outer shell, so-called “glue atoms” can be located. The centres of the balls make up a 3D network defining the next hierarchy level ( $d \sim 5 \text{ nm}$ ) in the structure.

To conclude, detailed local atomic models for icosahedral Mg-Zn-rare-earth quasicrystals have been refined from ID31 high resolution powder diffraction data via PDF and yield real atoms, credibly coordinated at credible interatomic distances. Since the PDF simultaneously is a local ( $< 0.4 \text{ nm}$ ), medium (nm) and long-range ( $> 10 \text{ nm}$ ) probe, regardless of the samples degree of crystallinity, it serves as a versatile experimental function in real space to model atomic structures. Thus in this case the PDF tells us “where the atoms are” in any patch, of selectable size, in the quasicrystal structure.

#### References

- [1] H.R. Trebin (ed.); *Quasicrystals*, Wiley-VCH (2003).
- [2] T. Egami and S.J.L. Billinge; *Underneath the Bragg Peaks*, Pergamon (2003).

#### Principal Publication and Authors

- S. Brühne (a,b), E. Uhrig (a), K.-D. Luther (a), W. Assmus (a), M. Brunelli (c), A.S. Masadeh (d) and S.J.L. Billinge (d), *Z. Kristallogr.* **220**, 962-967 (2005).  
 (a) FB Physik, JWGU Frankfurt am Main (Germany)  
 (b) FB Chemie, JWGU Frankfurt am Main (Germany)  
 (c) ESRF  
 (d) Physics Department, MSU, East Lansing (USA)

## Electric polarisation and chain formation of nanolayered particles

When certain colloidal suspensions of electrically polarisable particles in insulating fluids are subjected to an external electric field, usually of the order of 1 kV/mm, the particles become polarised, and subsequent dipolar interactions are responsible for aggregating a series of interlinked particles that form chains and columns parallel to the applied field. This structuring occurs within seconds, and disappears almost instantly when the field is removed. The structuring coincides with a drastic change in rheological properties (viscosity, yield stress, shear modulus, etc.) of the suspensions, which is why such fluids are sometimes called electro-rheological fluids (ERs). The mechanical behaviour of such

suspensions is readily controllable by means of the external electric field, which has stimulated a great deal of scientific interest both in academic and industrial areas. Based on the ER effect, several possible industrial applications have been proposed, including “smart” devices such as clutches, brakes, damping devices, actuators, fuel injection valves, hydraulic valves, bearing dampers, seismic damping frame structures etc. Furthermore, it has been suggested that ER fluids could be used as and in photonic crystals, light shutters, mechanical polishers, displays, ink jet printers etc.

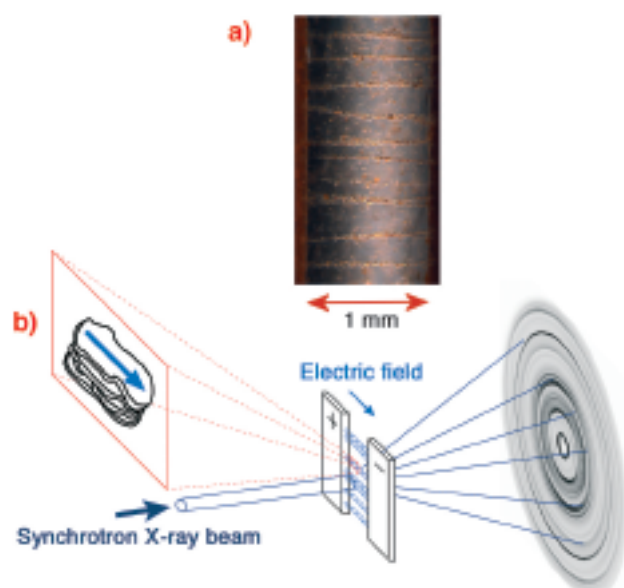


**Fig 26:** a) Optical microscope image of ER chain formation in a cell of 1 mm electrode gap with an electrical field applied in the horizontal direction. b) Sketch of the reported X-ray scattering experiments. The magnified area sketches a single nano-layered clay particle inside a dipolar chain and the attached arrow indicates the direction of the dipole moment induced by the external electric field. A corresponding diffractogram is shown in **Figure 27**.

Here we report structural studies of ER phenomena in systems consisting of nanolayered clay particles suspended in oil. Our optical microscopy observations show that suspensions in silicon oil of nanolayered smectite (swelling) clay particles, either synthetic or natural, undergo, when submitted to a strong external electric field, a fast and extended chain-like structuring characteristic of ER behaviour (**Figure 26**). This structuring results from interaction between induced electric dipoles of polarised clay particles.

The present synchrotron wide-angle X-ray scattering (WAXS) experiments were performed at the Swiss-Norwegian Beamline **BM01A** (SNBL), where diffractograms were recorded using a 2D Mar345 detector. These WAXS experiments provide information about the preferred direction of polarisation for individual clay particles, as well as information about the

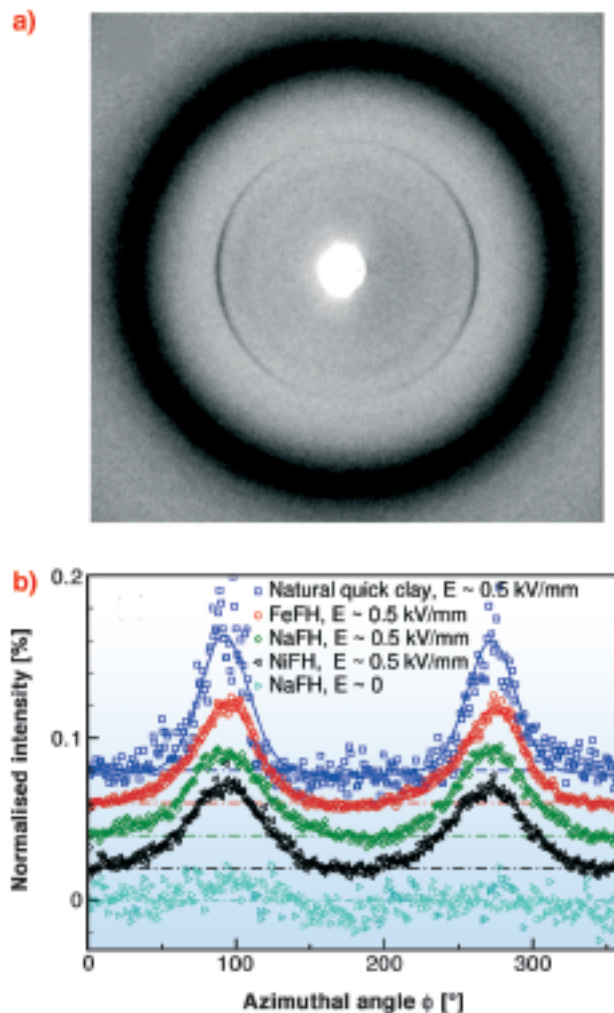


**Fig 27:** a) 2D Mar345 detector diffractogram from ER-oriented clay in silicon oil suspension. The broad dark ring is the scattering from the silicon oil. The narrow anisotropic (001) Bragg peak is the 1 nanometre layer stack scattering summed from the suspended clay particles when an external electric field is applied as sketched in **Figure 26**. b) Azimuthal representation of diffractograms of the type shown in the upper panel; scattering from ER structured chains formed in 4 different kinds of smectite clays are shown. Theoretical orientational fits are also included.

orientational distributions of polarised clay particles within the aggregated ER chain structures. Each individual clay particle is a stack of “nano-cards”, and thus a ring of Bragg powder scattering from randomly oriented clay particles in suspension is observed in zero applied electrical field, whereas anisotropic oriented powder scattering is observed above the ER triggering field of about 1 kV/mm (**Figure 27**). The reported experiments show that the clay particles polarise along their silica sheets, *i.e.* along the “easiest” direction for moving intercalated ions and water. A change in the platelet separation inside the clay nanolayered particles also indicates that intercalated ions and water molecules play a central role in their electrical polarisation. The resulting induced dipole is attached structurally to the clay particle, and this causes clay particles to reorient

and interact, resulting in the observed macroscopic structuring. Therefore, the macroscopic properties of the reported ER clay suspensions could, in principle, be tuned by controlling the nature and quantity of the intercalated species, at the nanoscale. This creates an opportunity for novel ways of producing guided self-assembled nanostructures for implementation into nanocomposite materials design, as well as for use in connection with nanostructured templates.

#### Principal Publication and Authors

J.O. Fossum (a), Y. Méheust (a), K.P.S. Parmar (a), K.D. Knudsen (b), K.J. Måløy (c) and D.M. Fonseca (a), *Europhysics Letters* **74**, 438-444 (2006).

(a) Norwegian University of Science and Technology, Trondheim (Norway)

(b) Institute for Energy Technology, Kjeller (Norway)

(c) University of Oslo, Oslo (Norway)

## Competition between order and phase separation in Au-Ni

Binary alloys are generally classified into two generic types of ordering or phase separating character. The phase behaviour of a binary A-B system is determined by a balance between the interactions  $V_{AA}$ ,  $V_{BB}$ , and  $V_{AB}$  which are typically of the order of 1 eV. The resulting effective pair interaction  $V = V_{AA} + V_{BB} - 2V_{AB}$ , on the other hand, is typically in the order of several ten meV, and, thus, competing with the thermal excitations in the system. In turn, only the accurate determination of these interactions by experiment and first-principle calculations allow a prediction of the alloy phase stability for a given system.

In many cases the phase behaviour of a given binary alloy system can be deduced from the short range order fluctuation spectrum in the high temperature disordered phase. Ordering systems show fluctuations with a dominant wave vector  $\mathbf{k} \neq 0$ , while fluctuations in phase separating systems are generally characterised by a dominant wave vector  $\mathbf{k} = 0$  [1]. The two cases can easily be distinguished via the diffuse scattering caused by the fluctuations in the system. However, there are many systems where such a simple picture fails. Some alloy system can indeed form a phase separated ground state while the high temperature fluctuations are of both, ordering and/or clustering type [2]. The alloy system Au-Ni, which has been regarded as a model system for phase separation, has developed into a particular conflicting case. Theoretical calculations indicated competing fluctuations of ordering- and clustering-type, while experimental studies did not provide a conclusive picture of the nature of the fluctuations in the Au-Ni alloy system.

High energy X-rays are an ideal tool to map the fluctuation spectrum of binary systems. The two main characteristics of high energy X-rays are a large penetration depth in conjunction with a large Ewald sphere. This allows one to map weak diffuse scattering intensity distributions on a timescale of a few seconds in entire planes in reciprocal space using a 2D detector. The measurements have been performed in transmission geometry at beamline **ID15A** at X-ray energies ranging from 60 keV to 90 keV. The  $\text{Au}_3\text{Ni}$  and  $\text{Au}_3\text{Ni}_2$  single crystals were mounted on a heating stage in a high vacuum environment. Scattering patterns were collected *in situ* at elevated temperatures and from samples quenched to room temperature.

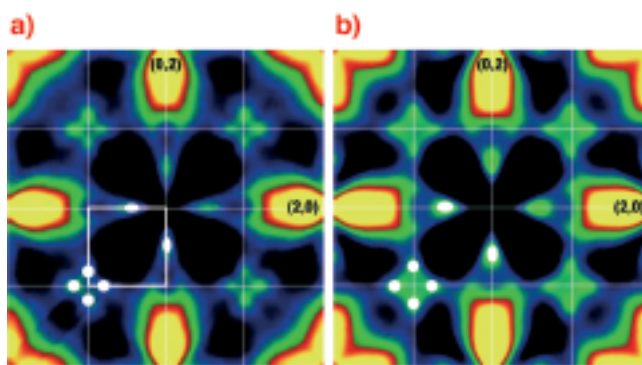


**Fig. 28:** Diffuse scattering in the (001) plane in  $\text{Au}_3\text{Ni}$  (a) and  $\text{Au}_3\text{Ni}_2$  (b). Both samples were quenched to room temperature. The positions of the diffuse scattering maxima are indicated in the lower left part.

**Figure 28** shows the diffuse scattering for both systems at room temperature. Several diffuse scattering maxima can be identified which demonstrate the presence of two different ordering fluctuations into the Z1 and L1<sub>2</sub> structure. The fluctuations into the phase separated state manifest themselves in the diffuse scattering intensity distribution close to the origin of reciprocal space. In **Figure 29** the central part of the diffuse

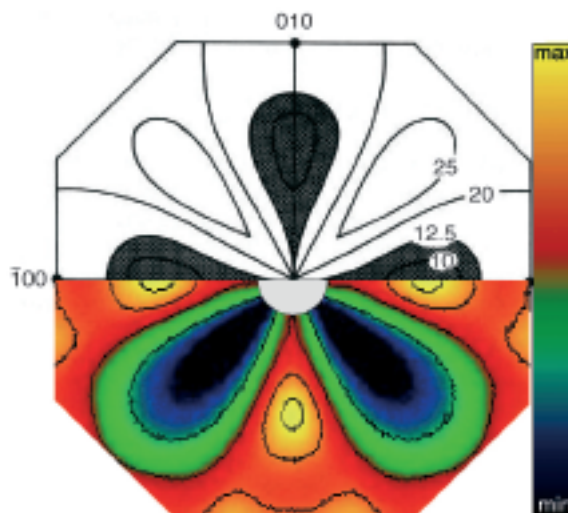


**Fig. 29:** Diffuse scattering in the (001) for  $\text{Au}_3\text{Ni}_2$  in the first Brillouin zone. The upper part displays model calculations, while lower part shows measured data from a quenched sample.

scattering pattern close to the origin of reciprocal space is shown together with model calculations, where both intensity distributions agree very well.

Our experiments provide clear-cut evidence that the system Au-Ni exhibits a competition between ordering and phase separation. Fluctuations characteristic for ordering and phase separation have been unambiguously identified via the location of their diffuse scattering maxima. We were able to reproduce the main features of the diffuse scattering intensity distribution by first-principles calculations, thus resolving a long-standing controversy on the nature of the fluctuations in the Au-Ni alloy system.

## References

[1] A.G. Khachatryan, *Theory of Structural Transformations in Solids*, Wiley (1983).

[2] C. Wolverton, V. Ozolins, A. Zunger, *J. Phys. Condens. Matter* **12**, 2749 (2000).

## Principal Publication and Authors

H. Reichert (a), A. Schöps (a), I.B. Ramsteiner (a), V.N. Bugaev (a), O. Shchyglo (a) A. Udyansky (a), H. Dosch (a), M. Asta (b), R. Drautz (c), V. Honkimäki (d), *Phys. Rev. Lett.* **95**, 235703 (2005).

(a) Max Planck Institute for Metals Research, Stuttgart (Germany)

(b) Northwestern University, Evanston (USA)

(c) Department of Materials, University of Oxford (UK)

(d) ESRF

# Carbonia: the amorphous silica-like carbon dioxide

Among the group IV elements only carbon forms stable double bonds with oxygen at ambient conditions and, at variance with SiO<sub>2</sub> and GeO<sub>2</sub>, the non molecular single-bonded crystalline form of CO<sub>2</sub>, phase V, only exists at high pressure [1]. Similarly, the amorphous phases of SiO<sub>2</sub> (a-silica) and GeO<sub>2</sub> (a-germania) are well known and stable at room conditions, but the amorphous, non molecular, form of CO<sub>2</sub> has been described so far only as a result of first-principle simulations [2]. We achieved the synthesis of an amorphous, silica-like form of carbon dioxide, a-CO<sub>2</sub> or “a-carbonia”, by compressing the molecular phase III of CO<sub>2</sub> above 40 GPa, at temperatures as high as 680 K, in a diamond anvil cell. State-of-the-art infrared absorption, Raman and synchrotron X-ray diffraction measurements were used to assess the amorphous character of the new material. Comparison with vibrational and diffraction data for amorphous silica and germania, as well as with the structure factor calculated on the a-CO<sub>2</sub> sample obtained by first-principle molecular dynamics [2],

shows that a-carbonia is structurally homologous to the other group-IV dioxide glasses.

In **Figure 30** we report vibrational spectra of temperature quenched a-CO<sub>2</sub>. The infrared spectrum shows broad absorption bands, whose large width is related to the disorder. By analogy to the infrared spectra a-SiO<sub>2</sub>, bands of a-carbonia have been assigned to different modes of the carbon–oxygen network made of single C–O bonds. The Raman spectrum also exhibits broad bands, compared to that of crystalline phase V, which in turn has much narrower lines. The Raman lines of CO<sub>2</sub>-V are close to the a-CO<sub>2</sub> band edges, therefore it was speculated that bands of a-CO<sub>2</sub> reflect vibrational density-of-state features of CO<sub>2</sub>-V. This also supported the notion that a-CO<sub>2</sub> is the glassy counterpart of phase V.

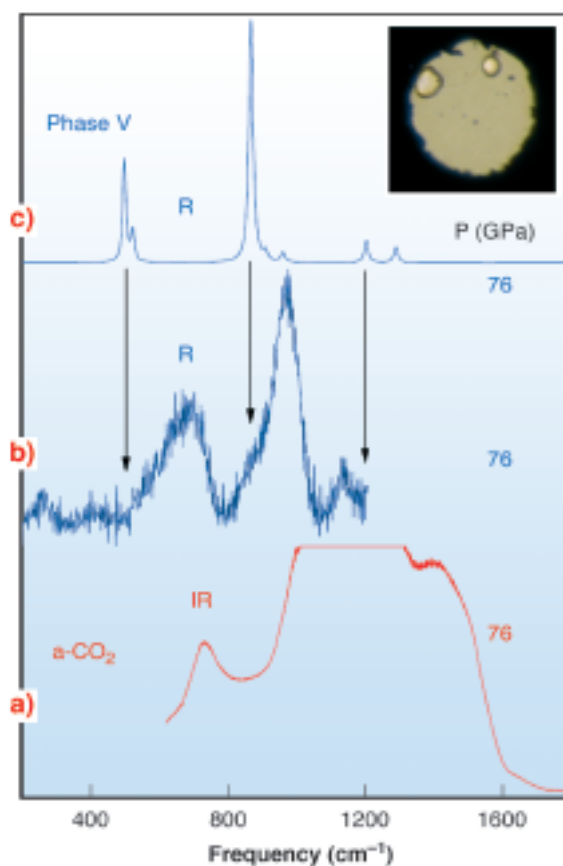


**Fig. 30:** Vibrational spectra of non-molecular CO<sub>2</sub>:  
**a)** Infrared spectrum of a-carbonia (the absorption of the strongest band is partially saturated);  
**b)** and **c)** Raman spectra of a-carbonia and phase V, respectively. Arrows indicate the correspondence of phase V Raman lines to band edges of a-carbonia.  
 Inset: typical temperature quenched a-CO<sub>2</sub> sample (P = 61 GPa, sample diameter about 80 μm; two ruby chips are close to the gasket).

As a crucial test of structural disorder in the new material, we measured its static structure factor S(Q) (**Figure 31**). The S(Q) is dominated by a broad peak (A), which lies in the Q region corresponding to the nearest neighbours atomic length scale, and a much broader

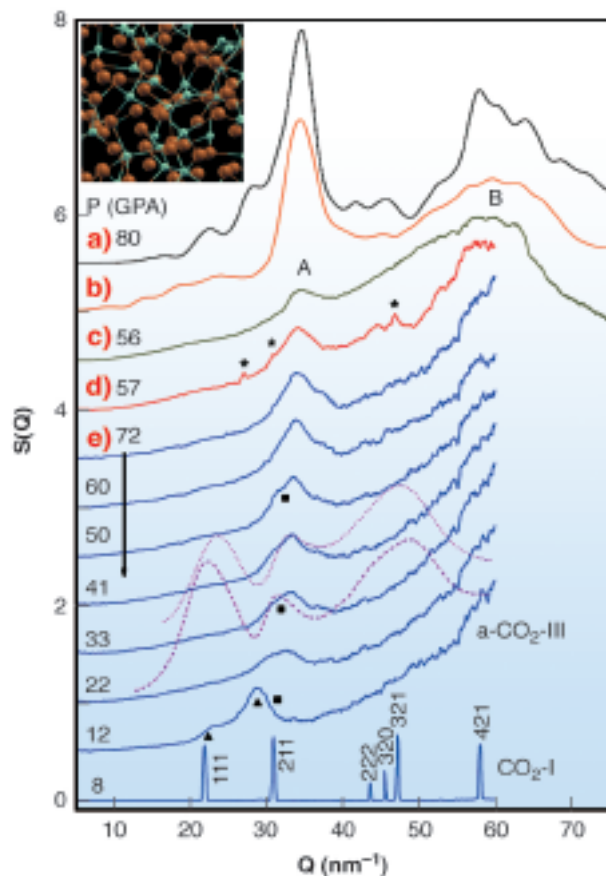


**Fig. 31:** Static structure factor  $S(Q)$  of  $a\text{-CO}_2$ . **a)** and **b)**: computer simulated  $S(Q)$  for  $\text{CO}_4$  (*ab initio* molecular dynamics) and higher (classical molecular dynamics), up to octahedral, carbon coordination, respectively; **c)**, **d)** and **e)**: temperature quenched samples. The structure factor of sample (e) has been measured by decreasing pressure. The experimental  $S(Q)$  of  $a\text{-SiO}_2$  is also reported at 42 GPa (dotted line) and 28 GPa (dashed line). Symbols indicate diffraction peaks of: (stars) rhenium gasket, (squares) phase V (the closest line to peak A of  $a\text{-CO}_2$ ), and (triangles) phase III. Inset: picture of *ab initio* simulated  $a\text{-carbonia}$ .

peak (B) positioned at higher  $Q$ . The theoretical  $S(Q)$ , calculated on a fully tetrahedral atomic structure obtained by first-principle molecular dynamics [2], reproduces both experimental peaks A and B. We also compare the  $S(Q)$  of  $a\text{-carbonia}$  to that of  $a\text{-SiO}_2$ : peaks A of the two materials are close to each other, while differences in the overall profile can mainly be ascribed to the different atomic form factors.

We notice that peak A is very close to the strongest Bragg peak of crystalline  $\text{CO}_2\text{-V}$ , whose intensity has been suggested to be enhanced by disorder, indicating once again that  $a\text{-CO}_2$  is the amorphous counterpart of phase V. Upon decreasing pressure below 16 GPa,  $a\text{-CO}_2$  transforms into a new amorphous material, whose diffraction features appear to be related to the strongest Bragg peaks of phase III, and which we suggest to be the amorphous molecular counterpart of

phase III. Below 10 GPa phase I (dry ice) is formed by recrystallisation of the amorphous material.

With the discovery of “ $a\text{-carbonia}$ ”, a new, extended analogy emerges between the structures of  $\text{CO}_2$  and those of the known  $\text{SiO}_2/\text{GeO}_2$  polymorphs. Our findings lead to the general conclusion that the class of archetypal network-forming disordered systems as  $a\text{-silica}$ ,  $a\text{-germania}$ ,  $a\text{-Si}$ ,  $a\text{-Ge}$ , and water, must be extended to include  $a\text{-CO}_2$ .

## References

- [1] M. Santoro, and F. A. Gorelli, *Chem. Soc. Rev.* **5**, 918 (2006).
- [2] S. Serra, C. Cavazzoni, G. L. Chiarotti, S. Scandolo, and E. Tosatti, *Science* **284**, 788 (1999).

## Principal Publication and Authors

M. Santoro (a,b), F.A. Gorelli (a,b), R. Bini (a,c), G. Ruocco (b,d), S. Scandolo (e) and W. Crichton (f), *Nature* **441**, 857 (2006).

(a) LENS, Sesto Fiorentino (Italy)

(b) CRS-SOFT-INFN-CNR, c/o Università di Roma “La Sapienza” (Italy)

(c) Dipartimento di Chimica dell’Università di Firenze, Sesto Fiorentino (Italy)

(d) Dipartimento di Fisica, Università di Roma “La Sapienza” (Italy)

(e) ICTP and CRS-DEMOCRITOS-INFN-CNR, Trieste (Italy)

(f) ESRF

## Spatiotemporal reaction kinetics probed by picosecond X-ray diffraction

Structural dynamics in the solution phase, the environment most relevant to biology and industrial chemistry, are quite complex due to the presence of solvent molecules near solute molecules. Typically solute molecules are dissolved in the ocean of solvent molecules and complex solvation cage structures are formed. Sometimes the photo-reacted atoms or molecules can be trapped inside the cage and recombine with each other (geminate recombination). In another case, the reacted species can escape from the cage and recombine with others from other cages (non-geminate recombination). Historically, time-resolved optical spectroscopy methods have provided ample information about such processes. However, more insight into the dynamics of molecular structure in solution can be obtained using time-resolved X-ray diffraction. It was recently demonstrated that the

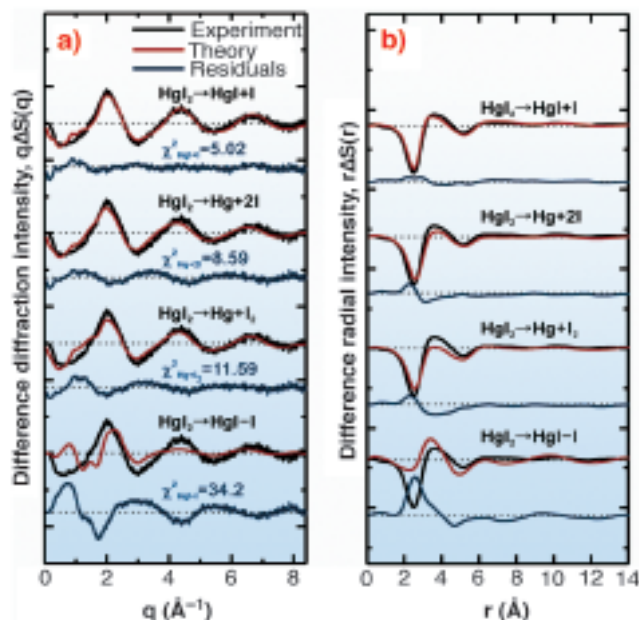


**Fig. 32:** Determination of primary photodissociation pathway of  $\text{HgI}_2$  in methanol solution. The experimental difference curves in  $q$  (a) and  $r$  space (b) at 100 ps are compared with theoretical curves using four possible putative primary pathways. The channel of two-body dissociation ( $\text{HgI}_2 \rightarrow \text{HgI} + \text{I}$ ) gives the best fit.

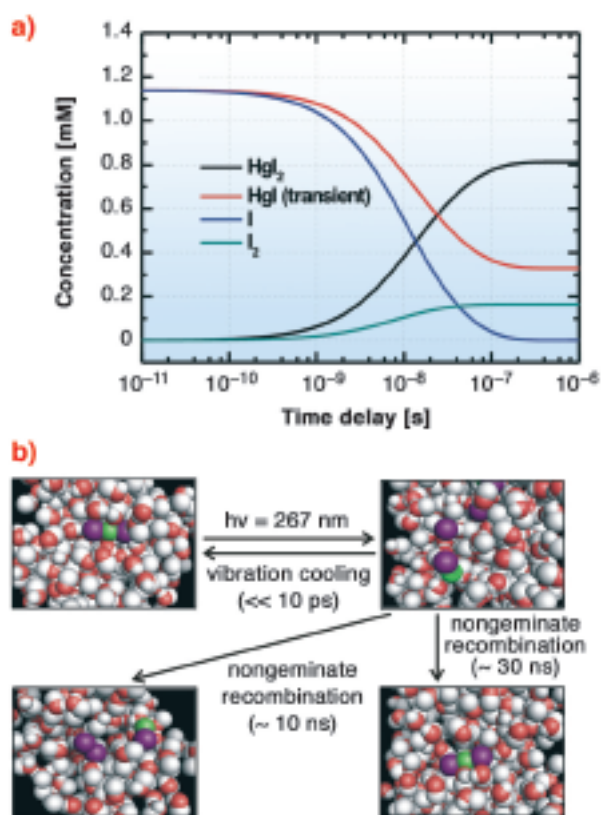


**Fig. 33:** Spatiotemporal reaction kinetics determined by time-resolved X-ray diffraction. a) The population changes of chemical species in the photodissociation of  $\text{HgI}_2$  in methanol solution. b) A schematic reaction mechanism of  $\text{HgI}_2$  photodissociation in methanol solution.

transient structure in solution can be determined by using time-resolved liquid X-ray diffraction [1].

In this work, 100 ps time-resolved liquid diffraction experiments on the photoreactions of diiodomercury ( $\text{HgI}_2$ ) dissolved in methanol (10 mM) were performed at beamline **ID09B**, using the optical pump and X-ray probe method. This molecular system has been investigated using the same technique as before, but the transient pathway and subsequent structural dynamics have not been elucidated due to the poor signal-to-noise ratio and limited data analysis method [2]. An optical pulse (267 nm, 2 ps, 986 Hz) triggers impulsive photodissociation of  $\text{HgI}_2$ , followed by subsequent reactions and then the X-ray pulse (100 ps, 0.067 nm, 986 Hz) interrogates the reacting sample by making the diffraction patterns on the CCD detector in a stroboscopic manner for the different time-delays spanning from 100 picosecond to 1 microsecond. The difference diffraction and corresponding radial intensities were extracted from the diffraction pattern and analysed using the so-called “*global-fitting method*” which considers time-dependent changes of solute and cage structures and changes of solvent structure, itself due to the time-dependent heat and density changes. Among four putative primary reaction channels (Figure 32), a two-body dissociation channel is the dominant dissociation pathway. After this primary bond fission, two parallel recombination processes proceed. Transient intermediate,  $\text{HgI}$ , associates with an iodine atom to form  $\text{HgI}_2$  nongeminately, and  $\text{I}_2$  is formed by nongeminate recombination of two iodine atoms (Figure 33) in several tens of nanoseconds. In the present work, we could clearly show two main conclusions. (1) The determination of transient species in solution is strongly correlated with solvent energetics, which depend on putative reaction channels due to the heat transfer to the solvent. Time-resolved X-ray diffraction can serve as an ultrafast calorimeter in addition to being a sensitive structural probe. (2) A manifold of structural channel can be resolved at the same time with high-precision measurement and global analysis.

Even if there are some limitations, time-resolved X-ray diffraction has matured sufficiently to provide the structure of the intermediates, correlation with solvent environment, and bulk properties of the solvent molecules in solution with unprecedented spatial and time resolution. The success of this work should stimulate future research using such outstanding capabilities for unravelling the structural dynamics of nanomaterials and proteins in the solution phase using time-resolved X-ray diffraction.

## References

- [1] H. Ihee, M. Lorenc, T.K. Kim, Q. Y. Kong, M. Cammarata, J.H. Lee, S. Bratos, and M. Wulff, *Science* **309**, 1223 (2005).

[2] A. Geis, M. Bouriau, A. Plech, F. Schotte, S. Techert, H.P. Trommsdorff, M. Wulff, and D. Block, *J. Luminescence* **94**, 493 (2001).

### Principal Publication and Authors

T.K. Kim (a), M. Lorenc (b), J.H. Lee (a), M. Lo Russo (b), J. Kim (a), M. Cammarata (b), Q.Y. Kong (b), S. Noel (b), A. Plech (c), M. Wulff (b), and H. Ihee (a), *Proc. Natl. Acad. Sci. USA* **103**, 9410 (2006).

(a) *Department of Chemistry and School of Molecular Science (BK21), Korea Advanced Institute of Science and Technology (KAIST) (Republic of Korea)*

(b) *ESRF*

(c) *Fachbereich Physik der Universität Konstanz (Germany)*

## New scientific opportunities at ID11

Most materials occurring in nature such as rocks, ice and soil appear as complex heterogeneous and hierarchical aggregates of crystallites, domains and dislocation structures. Man-made materials from synthetic products to engineering materials are also usually polycrystalline and inhomogeneous, as are drugs and trace particles relevant to environmental matters as well as objects of artistic or archaeological significance. Furthermore, it is a general principle that many species with high chemical activity and/or interesting mechanical properties tend to be small grained and highly defective. Examples are metal hydrides, catalysts, battery materials, and nano-grained metals.

As materials science is a field in which we try to “bring the experiment to the sample”, rather than the inverse, our goal is to obtain high quality crystallographic and micro-structural data on even these defective samples. Ultimately, we aim to perform *total simultaneous hierarchical characterisation* (Figure 34) of arbitrary samples. To this end, we have developed an array of new diffraction-based methods based on high-energy microfocussing called three-dimensional X-ray diffraction (3DXRD) microscopy, to characterise polycrystalline samples over several length scales, from the Ångström scale (crystal structure) to the grain

distribution over the entire sample (see [1] for a recent review).

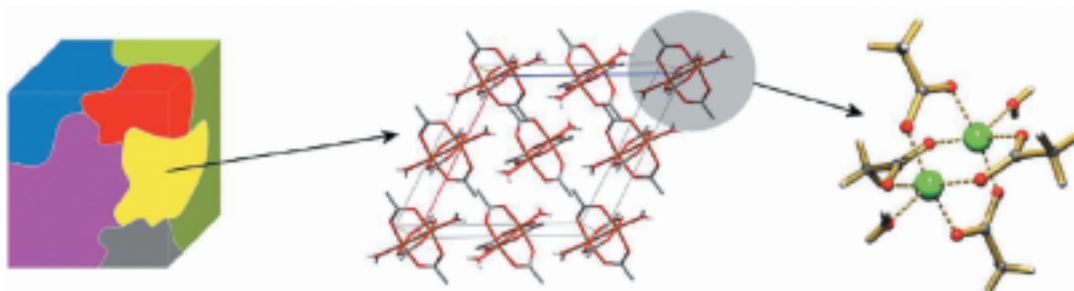
The sub-micrometre range is of particular interest in materials science as it is the critical length scale for many inter-granular interactions such as dislocations, cracks and interfaces; it is these interactions which ultimately give rise to the bulk properties of materials. The lack of a detailed knowledge of the distributional heterogeneity of properties on this scale has resulted in our inability to construct rigorous first-principles models of such basic materials properties as strength, fatigue resistance, and texture development. This length scale is also crucial in the microelectronics industry, where many features on modern chips are below 100 nm.

To study such features, bulk information may be collected by powder diffraction, but such data represents an ensemble average of the sample grains, and is uninformative on sample inhomogeneity, inter-granular interactions and the form of distributions of properties. Electron microscopy data has high spatial and angular resolution, but is limited to surfaces and static measurements. 3DXRD thus acts as the bulk equivalent of an electron microscope, acquiring spatial and structural data in the sub-micrometre scale in bulk samples in real time.

**ID11** was one of first beamlines to open at the ESRF, and has been continually upgraded over the last ten years to take advantage of emerging technology and follow trends in materials science research. The development of 3DXRD on ID11 led to the construction of a dedicated station for high-energy microfocussing in the late 1990s. Due to the growing interest in these techniques, a new station has been built in order to extend this effort into the domain of high-energy nano-focussing. At the beginning of 2007, this outstation will become the first of the second wave of long beamlines at the ESRF open for the user programme.

With the present 3DXRD microscope, the spatial resolution is  $\sim 5 \mu\text{m}$ , while grains of 150 nm can be observed. The extension project aims to allow us to obtain sub-micrometre mapping resolution, with transverse resolutions below 100 nm and sensitivity to the earliest stages of nano-crystallisation. In order to

**Fig. 34:** Characterisation of a sample on several length scales: from the distribution of grains (left) to the crystal and molecular structures via 3DXRD.



achieve this, it will be necessary not only to obtain high-energy sub-micrometre beams, but also for the entire experimental configuration to be controlled on that length scale. The strong and ongoing optics development programme within the ESRF assures that several methods to produce sub-micrometre beams are available. Beam and sample position monitoring, and the integration with a feedback system, are the target of in-house development projects uniting several groups.

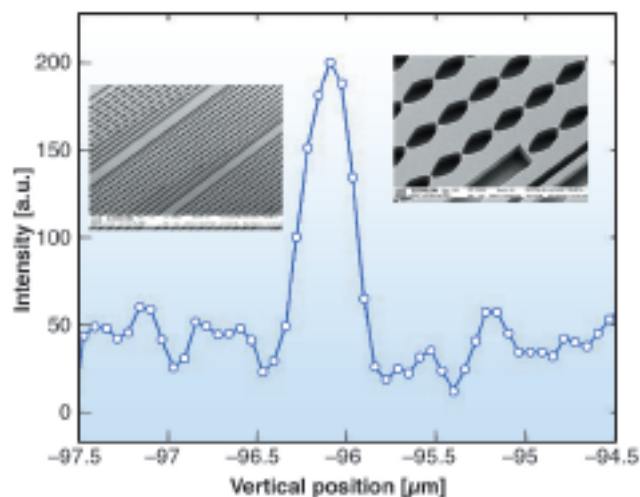


**Fig. 35:** 250 nm beam at 45 keV with nano-focussing silicon refractive lenses (inserts). Peak after deconvolution of knife-edge function.

In the initial phase, focussing optics will consist of bent Laue crystals, a K-B multilayer mirror system, and a compound refractive lens “transfocator”, which allows tunable focus between about 1  $\mu\text{m}$  and 1 mm by insertion of lenses in the beam. The smallest focus will be achieved by etched nano-lenses made with silicon wafer technology. During initial tests we have achieved 250 nm focus at 45 keV with this device (Figure 35) [2] and anticipate being able to achieve the design specifications of sub-100 nm focus at high (50 keV and greater) energy. Such high energy nano-focussed beams have never before been available, and should open up many exciting new experimental possibilities.

## References

- [1] D. Juul Jensen, E.M. Lauridsen, L. Margulies, H.F. Poulsen, S. Schmidt, H.O. Sørensen and G.B.M. Vaughan, *Materials Today* **9**, 8-25 (2006).  
 [2] A. Snigirev, I. Snigireva, V. Yunkin, M. Grigoriev, S. Kuznetsov, G.B.M. Vaughan, M. Di Michiel, *in preparation*.

## Authors

G.B.M. Vaughan (a), J.P. Wright (a), A. Bytchkov (a), C. Curfs (a), A. Snigirev (a), L. Margulies (a,b) and H.F. Poulsen (b).

(a) ESRF

(b) Risø National Lab. (Denmark)

# Synchrotron X-ray powder diffraction studies in pulsed magnetic fields

X-ray diffraction (XRD) is by far the dominant method for the determination of crystal structures. Until recently [1] there was no experimental tool for structure determinations under magnetic fields higher than 17 T, the highest magnetic field available at synchrotron or neutron facilities. Here we present the first XRD experiments up to 30 T. This technique can be extended to reach 60 T.

For our pilot studies we have chosen to combine synchrotron X-ray powder diffraction with pulsed magnetic fields. Our experiments were performed on the DUBBLE CRG-beamline (BM26B), using a pulsed field generator and high field magnet developed at the LNCMP, Toulouse (Figure 36). Magnetic fields up to 30 T were generated in the load magnet with the coil horizontally mounted into a cryostat. The beam axis was along the bore of the magnet (Faraday geometry).

Terbium ortho-vanadate,  $\text{TbVO}_4$  is a textbook example for a cooperative Jahn-Teller transition (JT) mediated by quadrupolar interactions between the  $4f$  moments [2]. At high temperatures  $\text{TbVO}_4$  crystallises in the tetragonal zircon structure. Upon lowering the temperature through  $T_{\text{JT}} = 33$  K it undergoes a cooperative JT transition: the crystal spontaneously distorts along the  $[110]$  direction to orthorhombic symmetry. Samples of  $\text{TbVO}_4$  were kindly provided by P.C. Canfield of Ames Laboratory (USA).

Powder X-ray diffraction diagrams were recorded on a MAR345 online image plate using an X-ray photon energy of 21 keV. Figure 37 shows the field dependence of the X-ray spectrum, as observed at  $T = 7.5$  K (left) and  $T = 39$  K (right) for different magnetic fields. We first consider the zero field measurements at 39 K and 7.5 K. In the high temperature phase we observe two Bragg reflections with Miller indices (using the high temperature tetragonal unit cell, subscript tet)  $(211)_{\text{tet}}$  near 11.8 deg and  $(112)_{\text{tet}}$  near 12.6 deg. The low temperature distortion due to the Jahn-Teller effect is clearly visible as a splitting of these peaks:  $(211)_{\text{tet}} \rightarrow (311)_{\text{ortho}} + (131)_{\text{ortho}}$  and  $(112)_{\text{tet}} \rightarrow (202)_{\text{ortho}} + (022)_{\text{ortho}}$ , where the subscript ortho signifies indexing with respect to the orthorhombic unit cell. Next, we investigate the evolution of the spectra as function of applied field at low temperature,  $T \approx 7.5$  K (Figure 37a). Immediately visible is a change in the relative amplitude of the high- and low-angle partners. We attribute this to the preferential population of domains, due to an in-plane ( $a_{\text{ortho}}$  vs.  $b_{\text{ortho}}$ ) magneto-crystalline anisotropy of  $\text{TbVO}_4$ . The splitting decreases with increasing field, indicating that the Jahn-Teller effect



**Fig. 36:** Photo showing, from left to right, the generator, X-ray detector and magnet/sample cryostat assembly (photo credit: D. Michon, Artechnique, Grenoble).

is suppressed. In the high temperature spectra (**Figure 37b**) we observed that upon applying the magnetic field a splitting ( $(202)/(022)_{\text{ortho}}$  pair) appears, and that a preferential domain population develops ( $(311)/(131)_{\text{ortho}}$  pair), *i.e.* the magnetic field *induces* the Jahn-Teller state. At  $B = 30$  T the magnitude of the distortion is similar for both temperatures. At all temperatures the peaks broaden as the field is applied. This is due to the strong dependence of the phase diagram on the angle between the magnetic field and the sample's *c*-axis.

Our experiment thus shows that the magnetic field pulse modified the Jahn-Teller distortion in  $\text{TbVO}_4$ , and that these changes can be detected using X-ray powder diffraction at a synchrotron source. An analysis of these data will be published.

### References

- [1] Y.H. Matsuda, Y. Ueda, H. Nojiri, T. Takahashi, T. Inami, K. Ohwada, Y. Murakami, T. Arima, *Physica B* **346–347** 519 (2004); Y. Narumi, K. Kindo, K. Katsumata, M. Kawauchi, C. Broennimann, U. Staub, H. Toyokawa, Y. Tanaka, A. Kikkawa, T. Yamamoto, M. Hagiwara, T. Ishikawa, H. Kitamura, *J. Syn. Rad.* **13**, 271 (2006).  
 [2] G. A. Gehring and K. A. Gehring, *Rep. Prog. Phys.* **38**, 1 (1975).

### Principal Publication and Authors

P. Frings (a), J. Vanacken (b), C. Detlefs (c), F. Duc (a), J.E. Lorenzo (d), M. Nardone (a), J. Billette (a), A. Zitouni (a), W. Bras (e) and G.L.J.A. Rikken (a), *Rev. Sci. Instr.* **77**, 063903 (2006).  
 (a) *Laboratoire National des Champs Magnétiques Pulsés, Toulouse (France)*

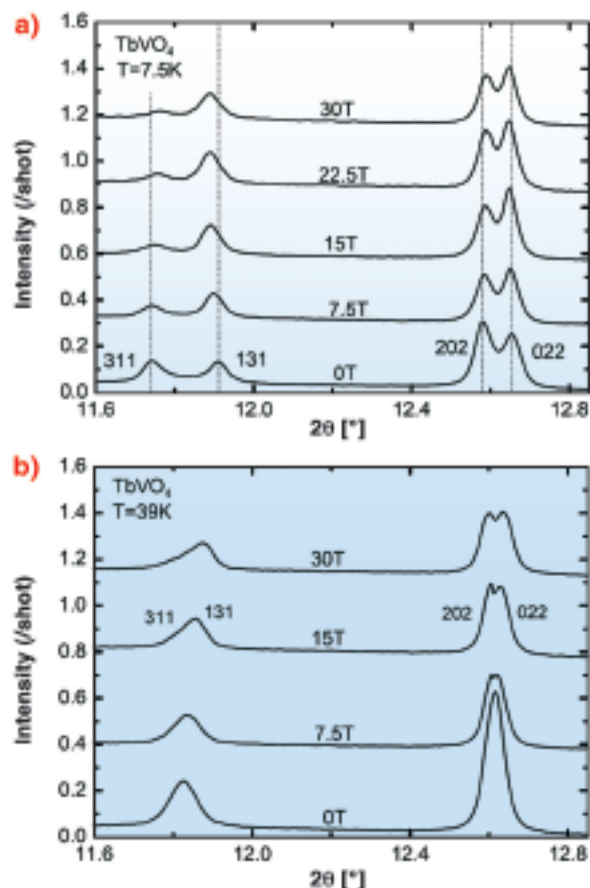


**Fig. 37:** Field dependence of the diffraction pattern at  $T = 7.5$  K and  $T = 39$  K. The graphs are shifted vertically for clarity.

(b) *Pulsveldegroep, Institute for Nanoscale Physics and Chemistry, Leuven (Belgium)*

(c) *ESRF*

(d) *Laboratoire de Cristallographie, CNRS, Grenoble (France)*

(e) *Dubble CRG, ESRF*



Highlights 2006

SCIENTIFIC HIGHLIGHTS

# Soft Condensed Matter

## Introduction

Over the past year, the soft condensed matter (SCM) beamlines have continued to be active across a wide variety of scientific areas, employing an equally diverse range of experimental techniques. These include studying phase transitions and the dynamics of colloidal systems (ID02: USAXS; ID10A: XPCS), probing the growth of organic layers (ID10B: GID & reflectivity) and investigating ancient silk fabrics (ID13: scanning diffraction). The highly interesting science performed at CRG beamlines is also exemplified here by a fundamental study on the inverse melting transition of a solution at BM29.

The trend towards biologically-related science has continued in 2006. This is demonstrated in the study of pressure-driven lyotropic liquid crystalline phases on ID02, an area which is of considerable interest for understanding the fusion of membranes. Also this year, high resolution structural data have been collected from micrometre-sized

A-amylose crystals on ID13. This suggests that a number of fibrous biopolymers could become amenable to single crystal techniques.

The increasing interest in micro- and nano-beams is emphasised by the participation of the SCM-group beamlines in the SAXIER FP6 project on "Small-angle scattering at high brilliance European synchrotrons for bio- and nano-technology" (Spokesman: D. Svergun, EMBL-Hamburg). The upgrade of the ID13 beamline by a nanofocus extension hutch is also a timely development (commissioning starting in Jan. 2007).

2006 became a particularly important year for the SCM group because of the development of an ESRF long term strategy. This has provided, through the various beamline upgrade programmes, a unique opportunity to shape the future of SCM at the ESRF. The overall aim is to maintain world-class instrumentation, whilst continuing to

provide the best possible support for the ESRF user community in the coming years. Among the different instrumental options proposed are: (i) extended pinhole optics for ID02 allowing accessing the USAXS range (ii) separation of ID10A and ID10B on a common sector by canted undulators and (iii) independently operating micro- and nano-branches by canted undulators for ID13. The SCM group is also proposing a new high-throughput bending magnet SAXS beamline with an emphasis on solution scattering and microfluidics. This would also be invaluable for studying proteins in solution, chemistry and materials. These proposals will be discussed with the relevant ESRF advisory committees and with the user community in particular. It will also be crucial to develop strategies for developing strategic long-range fields of research. These could involve several beamlines in collaboration with external user groups.

**C. Riekkel**

## Dynamics of structural transformations between the lamellar and inverse bicontinuous cubic lyotropic phases

Lyotropic liquid crystalline phases form when amphiphilic molecules are mixed with a polar solvent [1]. Such phases include the fluid lamellar ( $L_\alpha$ ; 1-D), hexagonal ( $H_I/H_{II}$ ; 2-D) and inverse bicontinuous cubic phases ( $Q_{II}^O/Q_{II}^P/Q_{II}^I$ ; 3-D). Whilst the complex phase behaviour and energetics of such structures have received a great deal of attention over the past half century, the study of their non-equilibrium behaviour is in its infancy with little understood about the mechanisms by which one phase transforms into another. The fluid lamellar to inverse bicontinuous cubic phase transition has particular biological relevance, being structurally

similar to the mechanism by which cell membranes fuse. Theoretical models for the process of membrane fusion between apposed lipid bilayers are summarised in [2]. All rely on the formation of transient lipid contacts known as stalks, which subsequently break through to form the beginnings of the tubular connections that are the fundamental connecting element in the inverse bicontinuous cubic phases. However, very few measurements have been made to test these models.

The liquid crystalline lamellar ( $L_\alpha$ ) to double-diamond inverse bicontinuous cubic ( $Q_{II}^P$ ) phase transition for the amphiphile monoelaidin in excess water was effected by means of a jump in pressure and monitored using small-angle X-ray scattering (SAXS) at the high brilliance beamline **ID02**. Pressure jumps of up to 4 kbar can be achieved in less than 7 ms using custom-built apparatus designed and built at the University of Dortmund. We observe a remarkable sequence of structural transformations, **Figure 38**. A weak and previously unreported signal from a highly swollen bicontinuous cubic phase,  $Q_{II}^P$ , of maximum spacing 232 Å, is consistently noted in coexistence with the fluid lamellar phase. Following the step change in thermodynamic conditions, the lamellar phase displays a marked decrease in lattice parameter. During this phase the highly-swollen bicontinuous cubic signal smears out, moves to higher scattering angle and merges with a broad, featureless ring of scatter (marked X in **Figure 38**). After a period of a few seconds the diffuse scatter resolves itself into a set of peaks from intermediate inverse bicontinuous cubic phases,  $Q_{II}^D$  and  $Q_{II}^P$ , which replace it. Initially these intermediate cubic phases are significantly more hydrated than expected from equilibrium results. They dehydrate over time while their phase composition increases simultaneously. Such phases may be used for transport of water; the small curvature elastic energy cost associated with increasing channel size in cubic phases means this can be an energetically favourable way of increasing water flux through the sample.

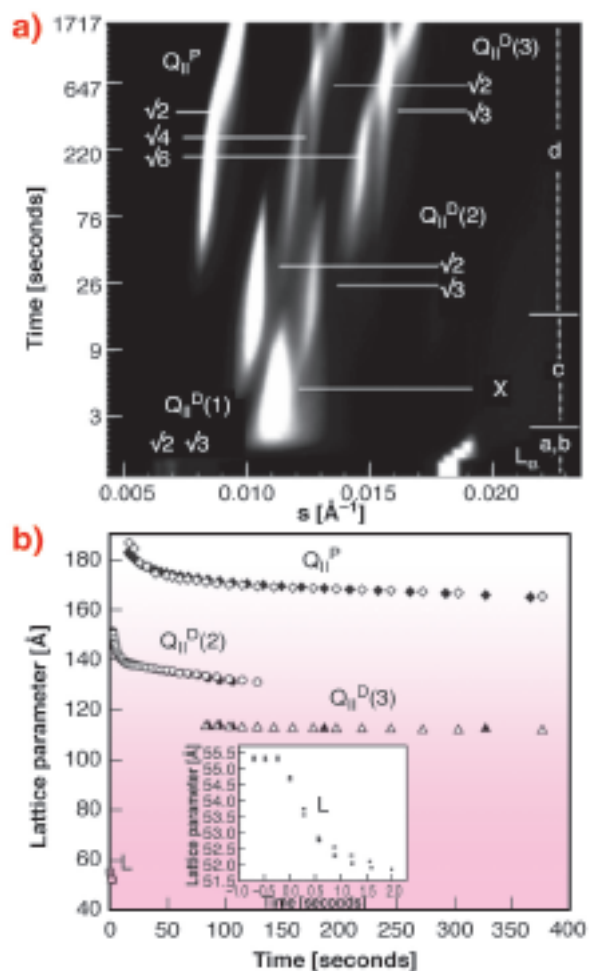


**Fig. 38:** The structural changes following a pressure-jump from 1100 to 260 bar,  $T = 46.7^\circ\text{C}$ . **a)** each 2D diffraction image is integrated to produce a 1D plot of intensity versus scattering vector  $s$  which is then stacked as a function of time. **b)** shows the change in lattice parameter of all phases with time following the same pressure jump.

**Figure 39** illustrates the structural transformations observed in our experiments by sketching the bilayer midplane. The figures are scaled relative to each other to reflect our experimental observations. Polarising microscopy results indicate that the lamellar phase forms multi-lamellar ‘onion’ vesicles of concentric spherical bilayers. The disappearance of the highly swollen cubic phase after a thermodynamic jump coincides with the appearance of diffuse scatter. This is strong evidence that it exists inside the onion vesicle, in coexistence with the lamellar phase. Furthermore, this suggests that its function is to act as a seed for the growth of the bicontinuous cubic phases out of an initial locally-ordered bicontinuous phase (the source of the diffuse scatter). We hypothesise that the swollen cubic phase is located in the centre of the onion vesicle

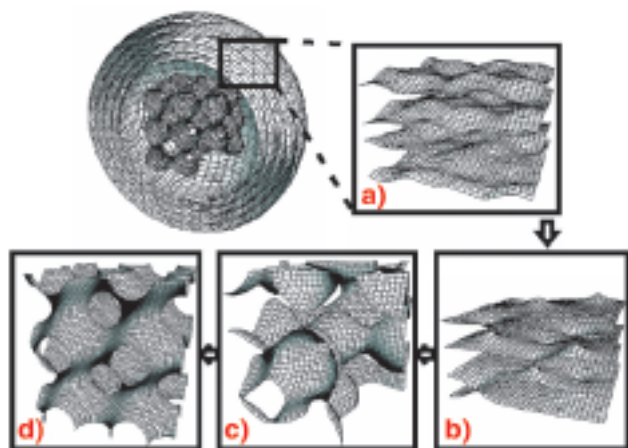


**Fig. 39:** The proposed structural transformations during the fluid lamellar to inverse bicontinuous cubic phase transition.

(**Figure 39**) removing the high energetic cost of filling the core with spherical bilayers of increasingly higher degrees of mechanically unfavourable curvature. Thermal undulations in the lamellar phase (a) disappear as interlamellar attachments (ILAs) are formed (b). This occurs because the bilayer's area and the volume it circumscribes are fixed in an onion vesicle and hence forming contacts exerts a lateral tension. When the tension reaches a critical value, ILAs rupture and form a disordered network of funnels (c) through which water flows from the centre of the vesicle. The disordered sponge structure soon resolves into ordered bicontinuous cubic structures such as the swollen  $P$  cubic (d). The cubic phases, which differ little in curvature elastic energy, may then interconvert easily.

#### References

- [1] J. M. Seddon, *Biochim. Biophys. Acta* **1031**, 1-69 (1990).  
 [2] L.V. Chernomordik, M.M. Kozlov, *Annu. Rev. Biochem.* **72**, 175-207 (2003).

#### Principal Publication and Authors

C.E. Conn (a), O. Ces (a), X. Mulet (a), S. Finet (b), R. Winter (c), J.M. Seddon (a) and R.H. Templer (a) *Phys. Rev. Lett.*, **96**, 108102 (2006).

(a) Department of Chemistry, Imperial College London (UK)

(b) ESRF

(c) Physical Chemistry I, University of Dortmund (Germany)

## Kinetic arrest and glass-glass transitions in short-ranged attractive colloids

Colloidal systems are ubiquitous in everyday life involved in many consumer and industrial products such as milk, cosmetics and paint. They also allow us to simulate many atomic-scale phenomena on a larger dimension. Model systems such as hard-sphere and sticky hard-sphere colloids have been extensively investigated over the past several decades. In recent years, short-ranged attractive colloids have received renewed interest in terms of their dynamical properties [1]. Mode coupling theory and computer simulations have predicted two different glass transitions in these systems. In hard-sphere like repulsive colloids, the glassy state is an alternative to crystalline order at high volume fractions. The ergodicity in the repulsive glass is lost due to blocking of particle diffusion by the dense surrounding cages formed by their nearest neighbours [1]. With the introduction of a short-ranged attraction of magnitude a few  $k_B T$  (where  $k_B$  is the Boltzmann constant) and range a few percent of the size of the particle, a different type of glassy state emerges that is called an attractive glass, where the particle motion is jammed by the strong stickiness. Attractive glass is a unifying term to describe the wide variety of dynamical arrest such as gelation, glassification, non-ergodicity transition, etc., induced by the stickiness.

Ultra small-angle X-ray scattering (USAXS) is a versatile technique for probing the subtle to dramatic changes in structure at different length scales in short-ranged interacting colloids [2]. A convenient model suspension for investigating the different facets of these systems is sterically stabilised silica colloids suspended in certain alkanes (e.g. n-dodecanol). In this case, a thermally reversible transition between repulsive and attractive colloids can be induced by lowering the temperature. Experiments were performed at beamline ID02. **Figure 40** shows the typical evolution of the scattered intensity  $I(q)$  as a function of the scattering wave vector ( $q$ ) at an intermediate volume fraction of 0.19.  $I(q)$  can be decomposed into the structure factor of interparticle interactions  $S(q)$  and the single particle scattering function which is dominant at high  $q$  values.  $S(q)$  can be modelled in terms of an interparticle potential  $V(r)$  involving a repulsive hard-sphere part, and an attractive square-well with depth,  $u$ , and width a few percent of the diameter of the particles within the Percus-Yevick approximation [2]. As the particles become attractive, they stick together to form clusters which is indicated by the excess scattering at small  $q$  ranges and in this case  $S(q)$  involves both the interparticle interaction and the morphology of these clusters. The quantitative scale and the wide  $q$  range provided by USAXS allow decomposition of the different contributions to  $I(q)$  and

an accurate deduction of the parameters of interparticle potential.

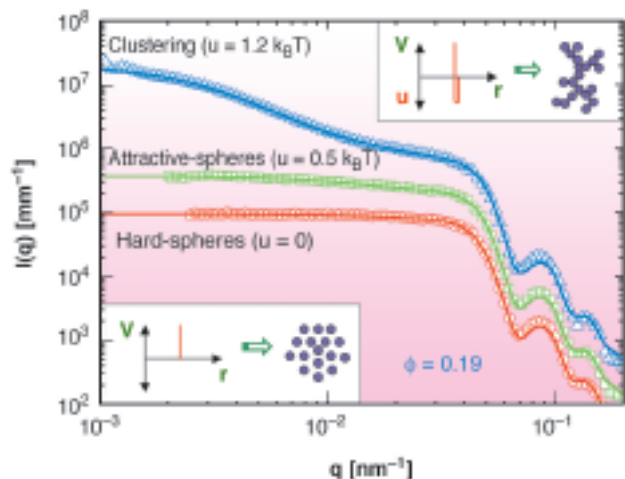


**Fig. 40:** Evolution of the microstructure of a colloidal system as a function of the strength of short-ranged attraction. Solid lines represent model for the corresponding interactions. The lower and the upper insets depict repulsive hard-sphere like suspension and clustering of particles when the depth of the attractive potential exceeds  $k_B T$ . For clarity the green and blue curves are displaced by a factor 3 and 10, respectively.

**Figure 41** presents the subtle variation of  $S(q)$  when the system transforms from hard-sphere repulsive to short-ranged attractive colloids at high volume fraction ( $\phi \approx 0.535$ ). With the onset of attraction, particles stick together but there is no signature of clustering. The inset shows the corresponding changes in the intermediate scattering function  $[f(q,t)]$  derived from dynamic light scattering (DLS) performed on the same sample. In the

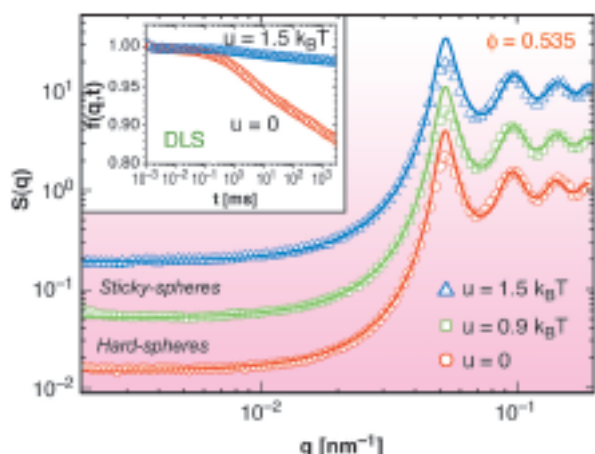


**Fig. 41:** Subtle changes in the static structure factor with the depth of attractive potential ( $u$ ) at high volume fraction ( $\approx 0.535$ ). The solid lines represent models for  $S(q)$ . The inset shows a more dramatic variation of the intermediate scattering function obtained from dynamic light scattering. For clarity the green and blue curves are displaced by a factor 3 and 10, respectively.

repulsive state ( $u = 0$ ),  $f(q,t)$  shows typical features of a repulsive colloidal glass. While in the attractive case ( $u \approx 1.5 k_B T$ ),  $f(q,t)$  remains close to 1 indicating that the particle dynamics are nearly frozen (jammed). This demonstrates a transition from repulsive to attractive glass as the depth of the attractive potential is systematically increased. Furthermore, the static  $S(q)$  shows only subtle changes while the dynamics and rheological properties vary dramatically [2] thereby establishing the kinetic nature of these glass transitions.

A combination of USAXS, DLS and bulk rheology provided complimentary information which allowed us to identify different dynamical transitions in short-ranged attractive colloids [2]. Observed features are broadly in agreement with recent theoretical predictions and computer simulations [1].

## References

- [1] F. Sciortino and P. Tartaglia, *Adv. Phys.*, **54**, 471 (2005), and references therein.
- [2] T. Narayanan, M. Sztucki, G. Belina, and F. Pignon, *Phys. Rev. Lett.*, **96**, 258301 (2006).

## Principal Publication and Authors

M. Sztucki (a), T. Narayanan (a), G. Belina (a), A. Moussaïd (a), F. Pignon (b) and H. Hoekstra (c), *Phys. Rev. E*, **74**, 051504 (2006).

(a) ESRF

(b) Laboratoire de Rhéologie, CNRS, Grenoble (France)

(c) Katholieke Universiteit, Leuven (Belgium)

## Structure and function of self-assembled liposome-DNA-metal complexes for gene transfer

Gene therapy is an innovative technique for correcting the defective genes responsible for disease development. The goal is to achieve the transfer of extracellular genetic material into somatic cells and thereby provide therapeutic effects. Realisation of the full potential of gene therapy will depend in a major way on future developments of safe and efficient *nonviral* gene delivery (NGD) agents. Cationic lipid-DNA complexes [1] are presently the most diffuse DNA carriers in NGD applications and are extensively used in clinical trials. This is due to their ability to mimic natural viruses as chemical carriers of extracellular DNA across outer-cell and nuclear membranes (transfection). However, their transfection efficiency is still relatively low compared to that of viral vectors and they are also unstable in the presence of serum, which creates problems for *in vivo*

applications. Furthermore, cationic liposomes are frequently toxic for the cells. These drawbacks are stimulating scientists to look for new *synthetic* gene vectors with a focus on understanding the structure-function relationships, where the ultimate goal is to enable a design-based approach to gene delivery.

We have recently started to study new ternary complexes formed by the self-assembled association of neutral liposomes, DNA and bivalent metal cations in water solution. Complexes composed of neutral lipids offer a promising alternative to cationic liposomes as they exhibit lower inherent cytotoxicity and longer circulation lifetimes. The supramolecular packing of these Liposome-DNA-Metal<sup>2+</sup> complexes forms lyotropic liquid crystals that display rich phase and structural behaviour [2,3]. Recent measurements at ID02 have demonstrated the self-assembled formation of the lamellar  $L_{\alpha}$  phase in dioleoylphosphatidylcholine (DOPC)-DNA(plasmid)-Metal<sup>2+</sup> complexes (Figure 42). This is a novel liquid crystal phase consisting of the multilamellar aggregation of stacked alternating lipid bilayers and DNA monolayers, which are mutually bound by the metal cations (inset of Figure 42). The process of self-aggregation is driven by the release of counter-ion entropy upon neutralisation of the DNA phosphate groups by the metal cations. The use of plasmid DNA instead of the more usual *linear* DNA is preferred because the native supercoiled conformation of the

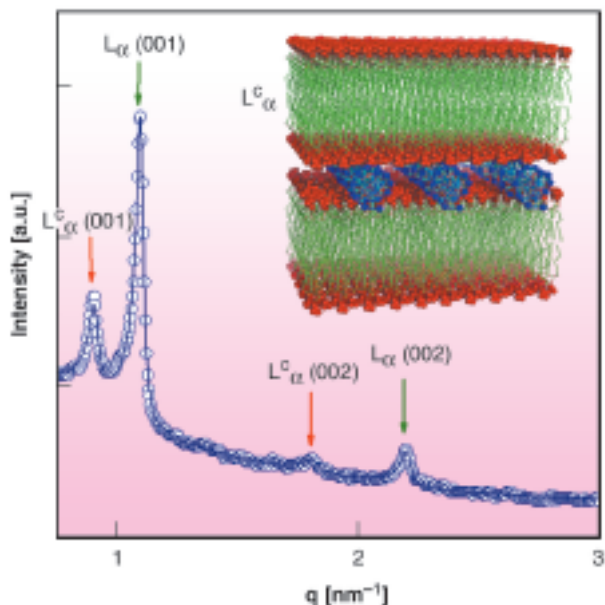


**Fig. 42:** The SAXS pattern of the DOPC-DNA-Mn<sup>2+</sup> (4:3:12) solution mixture.  $L_{\alpha}^c$  and  $L_{\alpha}$  refer to the lamellar structure of the ternary complex and of the coexisting unbound liposome, respectively. The structure of the  $L_{\alpha}^c$  phase consists of smectic-like arrays of stacked lipid bilayers with monolayers of DNA molecules intercalated within the water gaps; the metal cations bind the polar headgroups of DOPC with the negatively charged phosphate groups of DNA. The lamellar repeat distance is  $d \approx 7$  nm. Similar results were obtained for DOPC-DNA-Ca<sup>2+</sup>.

former is physiologically-active and hence the most promising for future therapeutic applications.

Preliminary tests were carried out to probe the transfection capacity of these systems. We have attempted *in vitro* transfections on mouse fibroblast cell lines (NIH 3T3), using DOPC-DNA(pGreenLantern1 plasmid)-Metal<sup>2+</sup> as DNA vectors. The expression of the green fluorescent protein (GFP) that is codified by the plasmid once it is at the cell nucleus was analysed by means of fluorescence microscopy. Figure 43 shows the results obtained for DOPC-DNA-Ca<sup>2+</sup> where the expression of the GFP is clearly apparent. Similar results were obtained for DOPC-DNA-Mn<sup>2+</sup>. These findings unquestionably demonstrate the capability of these complexes to transfect DNA.

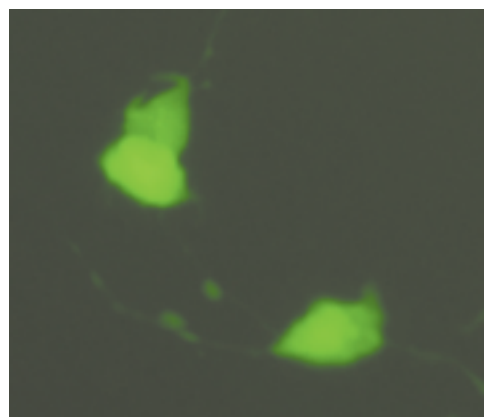


**Fig. 43:** Fluorescence micrograph of mouse fibroblast NIH 3T3 cell lines transfected with pGreenLantern1 DNA. The DNA was complexed to liposome of DOPC in presence of Ca<sup>2+</sup>. The photo was obtained using a standard FITC filter (excitation wavelength 488 nm with the objective at 10X).

Encapsulation of the DNA in these ternary complexes combined with effective targeting and endosome-release technologies may represent an important alternative to current systemic gene approaches. Our results represent a first but nonetheless fundamental step towards the development of the materials and refinement of the procedures to achieve efficient and tissue-specific transfection for future gene therapy applications.

## References

- [1] J. O. Rädler, I. Koltover, T. Salditt, C. R. Safinya, *Science* **275**, 810 (1997).
- [2] O. Francescangeli, V. Staniç, L. Gobbi, P. Bruni, M. Iacussi, G. Tosi, S. Bernstorff, *Phys. Rev. E* **67**, 011904 (2003).
- [3] O. Francescangeli, M. Pisani, V. Staniç, P. Bruni, T. Weiss, *Europhys. Lett.* **67**, 669 (2004).

## Principal Publication and Authors

P. Bruni (a), M. Pisani (a), A. Amici (b), C. Marchini (b),

M. Montani (b), and O. Francescangeli (c), *Appl. Phys. Lett.* **88**, 073901 (2006).

(a) *Dipartimento di Scienze dei Materiali e della Terra, Università Politecnica delle Marche, Ancona (Italy)*

(b) *Dipartimento di Biologia Molecolare, Cellulare e Animale, Università di Camerino (Italy)*

(c) *Dipartimento di Fisica e Ingegneria dei Materiali e del Territorio, Università Politecnica delle Marche, Ancona (Italy)*

## Diffusion and hydrodynamic interactions in charge-stabilised colloidal suspensions

Charge-stabilised suspensions are ubiquitously found in chemical and waste-treatment industries, and in medical and biological products. These systems are composed of meso-scaled colloidal particles dispersed in a low-molecular polar solvent like water. Examples include proteins and viruses, paint and clay particles, and well-characterised model systems consisting of spherical latex spheres. Diffusion properties of charge-stabilised colloids are determined by a subtle interplay of electrostatic and hydrodynamic inter-particle forces. Hydrodynamic interactions (HI) are transmitted by a complicated solvent flow pattern created by the moving particles. The inherent many-body character of the long-range HI causes challenging problems in theoretical and computer simulation studies of particle diffusion.

A salient measure of the strength of HI with regard to diffusion is given by the hydrodynamic function  $H(q)$ . It can be determined by a combination of static and dynamic small-angle X-ray scattering experiments. Without HI,  $H(q)$  is equal to one. Any variation in its dependence on the wavenumber  $q$  is a hallmark of HI. At large  $q$ ,  $H(q)$  becomes proportional to the short-time self-diffusion coefficient  $D_S$ . In earlier work [1], it was concluded that HI between charged colloidal particles are screened in the important case of a low-salt suspension. This conclusion was based on the observation of experimentally extracted values of  $H(q)$  and  $D_S$  that are smaller than for a suspension of neutral hard colloidal spheres at the same concentration. The interpretation of the strong hydrodynamic hindrance in terms of hydrodynamic screening caused a controversy since, according to theory, HI screening should not occur for liquid-state suspensions of mobile particles.

In a recent article [2], we show that, in fact, there is no hydrodynamic screening present in low-salinity systems. This important result has been obtained from combining

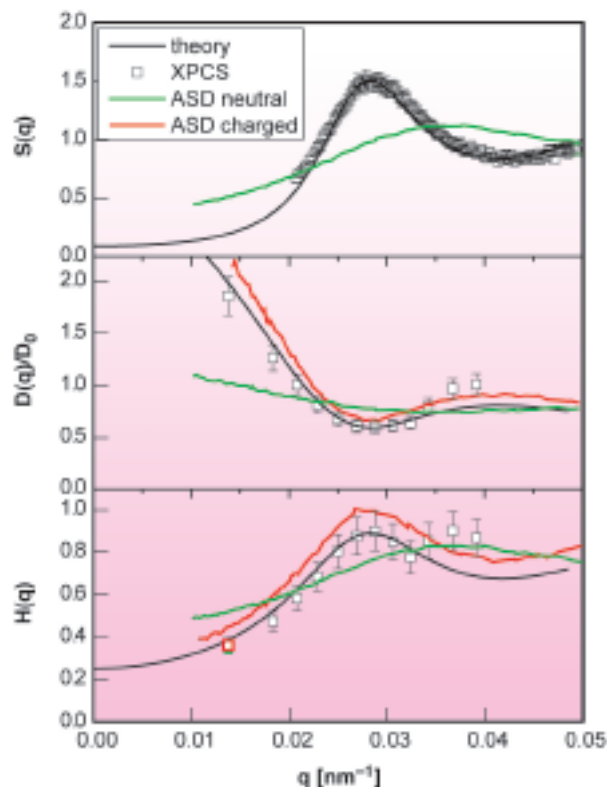


**Fig. 44:** Diffusion functions  $H(q)$  and  $D(q)$ , and structure factor  $S(q)$ , of a low-salt suspension. Experimental results (open squares) vs. ASD simulation (red lines) and theory (black lines) are shown. Green lines: simulation data for neutral hard spheres at same concentration.

SAXS and XPCS measurements of  $H(q)$ , and of the static structure factor  $S(q)$ , for aqueous suspensions of fluorinated latex spheres, with dynamic computer simulations and predictions of a modified hydrodynamic many-body theory. The XPCS experiments on aqueous suspensions of fluorinated latex spheres of radius  $a = 82.5$  nm, with well-defined amounts of NaCl added, have been done at the ESRF's Troika beamline, **ID10A**. The simulations were performed using a novel accelerated Stokesian Dynamics (ASD) method. Our simulation results for  $H(q)$  are the only ones available so far for charge-stabilised suspensions with significant many-body HI. All our experimental data on  $H(q)$ , and on the collective diffusion function  $D(q) = D_0 H(q)/S(q)$ , where  $D_0$  is the diffusion coefficient of an isolated sphere, can be quantitatively described by the simulations, and by the modified hydrodynamic theory. In particular, the behaviour of  $H(q)$  for deionised dense suspensions can be explained by many-body HI effects, without the need to conjecture hydrodynamic screening. In addition, boundaries are provided in our study for the maximum of  $H(q)$ , and for  $D_S$ , over the entire range of salt concentrations. Experimental, theoretical and computer simulation results for the  $H(q)$ ,  $D(q)$  and static structure factor  $S(q)$  of a low-salt system are included in **Figure 44**. These data are compared to the simulation prediction for a suspension of neutral hard spheres of the same size

and volume fraction. **Figure 45** displays upper and lower boundaries for the principal peak height,  $H(q_m)$ , of  $H(q)$ . These boundaries are approached at very small and large amounts of added salt, respectively.

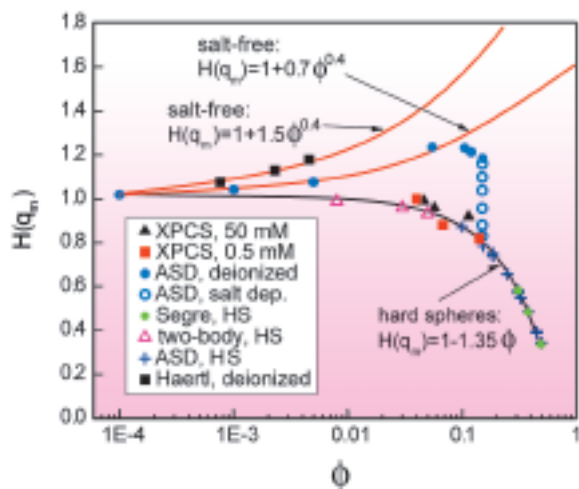


**Fig. 45:** Simulation and theoretical predictions for  $H(q_m)$  versus volume fraction  $\phi$ . Red lines: prediction for charged spheres at zero salinity, with near-field HI disregarded; black line: hard spheres. The filled black triangles and red squares are our XPCS/SAXS data. Earlier experimental data [3] are included for comparison.

In conclusion, by a concerted experimental-theoretical effort, we could explain and quantify the influence of many-body HI on diffusion properties of charge-stabilised colloidal spheres. A consistent understanding of the micro-hydrodynamics of charge-stabilised spheres is important to gain improved insight into transport properties of more complex colloidal particles of interest for industry and biology.

## References

- [1] D.O. Riese, G.H. Wegdam, W.L. Vos, R. Sprik, D. Fenistein, J.H.H. Bongaerts and G. Grübel, *Phys. Rev. Lett.*, **85**, 5460 (2000).  
 [2] A.J. Banchio, J. Gapinski, A. Patkowski, W. Häußler, A. Fluerasu, S. Sacanna, P. Holmqvist, G. Meier, M.P. Lettinga and G. Nägele, *Phys. Rev. Lett.*, **96**, 138303 (2006).  
 [3] Härtl *et al.*, *J. Chem. Phys.* **110**, 7070 (1999) and Segre *et al.*, *Phys. Rev. E* **52**, 5070 (1995).

## Principal Publication and Authors

A.J. Banchio (a), J. Gapinski (b), A. Patkowski (b), W. Häußler (c), A. Fluerasu (d), S. Sacanna (e), P. Holmqvist (f), G. Meier (f), M.P. Lettinga (f) and G. Nägele (f), *Phys. Rev. Lett.*, **96**, 138303 (2006).

(a) *Facultad de Matematica, Astronomia y Fisica, Universidad Nacional de Cordoba (Argentina)*

(b) *Institute of Physics, A. Mickiewicz University, Poznan (Poland)*

(c) *FRM-II, Technische Universität München (Germany)*

(d) *ESRF*

(e) *Van't Hoff Laboratory, University of Utrecht (The Netherlands)*

(f) *Institut für Festkörperforschung, Forschungszentrum Jülich (Germany)*

## Dynamics of a lamellar phase studied by XPCS and dynamic light scattering

X-ray photon correlation spectroscopy (XPCS) is a relatively new technique, successfully used to study the dynamics of soft-matter systems. Conceptually, it is rather similar to the traditional dynamic light scattering (DLS) technique, but its main advantages with respect to DLS are the potential for reaching much higher scattering wave vectors and the fact that it is less affected by multiple scattering.

Smectic phases are amenable for study by XPCS, since their high degree of order confines the scattered signal in the vicinity of the Bragg peaks. In the present work we used XPCS to measure the dispersion relation of fluctuations in bulk samples of a lamellar lyotropic phase (exhibiting smectic symmetry) and compared the results with DLS measurements.

XPCS had never been applied to lamellar lyotropic phases. Although the symmetry is the same for thermotropic smectics, there are notable differences due to the two-component character of the lyotropic phase (leading to additional hydrodynamic modes), to its lower elastic moduli, which influence both the relaxation rates and the 'spread' of the diffuse scattering around the Bragg position (thus limiting the accessible wave vector range). The relaxation rate of the fluctuations is described by the elasticity of the phase and the associated dissipation coefficients (viscosities). We should therefore be able to determine these material constants, compare them with the values obtained by other methods and (as a next step) test the validity of the elasticity theory at high wave vectors.

The samples were prepared in flat glass capillaries and oriented by thermal cycling between the lamellar and the isotropic phases, resulting in very good homeotropic anchoring. The experiments were performed at **ID10A** using an X-ray energy of 13 keV, in the uniform filling mode of the storage ring. The scattered signal was detected by a fast avalanche photodiode (APD) and the output signal was processed online by a FLEX autocorrelator.

It is well known that bulk lamellar phases exhibit the Landau-Peierls instability, leading to a characteristic

power-law variation of the scattered signal close to the Bragg peak (Figure 46), related to the product of the compression modulus of the lamellar phase B and the bending modulus of the bilayer,  $\kappa$ .

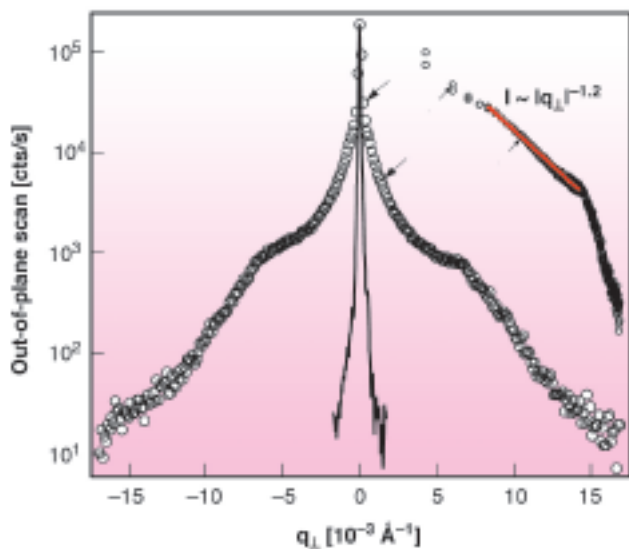


**Fig. 46:** Out-of-plane scan of the first Bragg peak (open symbols) shown in log-lin and log-log (inset) representation. The scan of the primary beam is presented for comparison (solid line) scaled by a factor  $10^{-4}$ . In both graphs, the arrows indicate the range of the XPCS measurements. In the log-log graph, the straight line is the power-law fit to the intensity (see text).

We recorded the time correlation function  $g(t)$  of the diffuse scattered signal, and analysed it to obtain the relaxation rate  $\Omega$ . The dispersion relation  $\Omega(q)$  for fluctuations in the lamellar phase is described taking into account the finite size of the capillary. The fit quality is excellent (Figure 47) and, putting together the static and dynamic data, we determined the elastic moduli B and  $\kappa$  as well as the sliding viscosity of the phase  $\eta_3$ ; the results are in very good agreement with previously available data. We also checked our results against light scattering experiments: the relaxation rate measured in DLS agrees very well with the XPCS values (Figure 47).

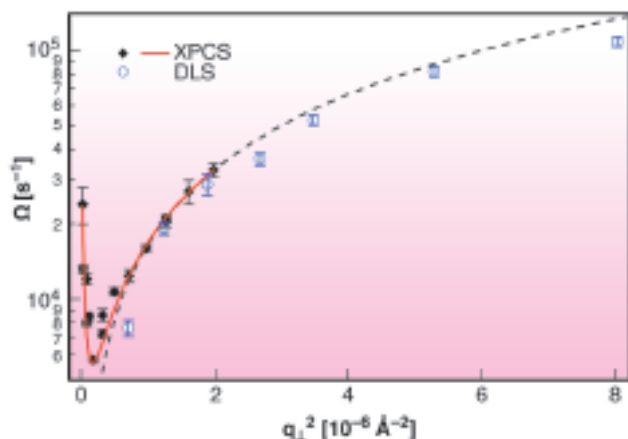


**Fig. 47:** Comparison between the XPCS and DLS results. Diamonds and solid line: XPCS data and fit. Dotted line: fit extrapolation at high  $q$ . Open dots: DLS results.

We have successfully demonstrated that the XPCS technique can be applied to the study of lamellar lyotropic phases. We measured the dispersion relation of the undulation mode in a lyotropic lamellar phase up to a wave vector  $q_{\max} = 1.4 \cdot 10^{-3} \text{ \AA}^{-1}$ . Our results are in very good agreement with DLS measurements and comparable in terms of accessible range and accuracy. Combining XPCS and static data measured on the same sample using the same setup we obtained precise results for the material parameters of the lamellar phase. XPCS, therefore, complements and extends the range of DLS experiments.

#### Principal Publication and Authors

D. Constantin (a), G. Brotons (b), T. Salditt (c), É. Freyssingeas (d) and A. Madsen (e) *Physical Review E* **74**, 031706 (2006).

(a) *Laboratoire de Physique des Solides, Orsay (France)*

(b) *Laboratoire de Physique de l'État Condensé, Le Mans (France)*

(c) *Institut für Röntgenphysik, Göttingen (Germany)*

(d) *Laboratoire de Physique ENS-Lyon, Lyon (France)*

(e) *ESRF*

## Watching organic crystalline films grow

Organic semiconductors have attracted much attention in recent years as they offer potential for low cost, large area, and flexible (opto-) electronics. Organic materials are also interesting from the perspective of growth physics, as organic molecules have vibrational, conformational, and orientational degrees of freedom which influence their growth behaviour. Therefore, in a recent experiment at beamline **ID10B**, *in situ* and real-time measurements were performed during evaporation of the organic semiconductor diindenoperylene ( $C_{32}H_{16}$ , a red dye). These X-ray experiments yield insight into the evolution of surface roughness and the evolution of competing crystal structures. Importantly, real-time measurements give information which would be missed in post-growth experiments, such as information on post-growth de-wetting of the film or transient structures existing only for a short moment during growth.

The X-ray reflectivity and diffraction experiments were performed at beamline **ID10B**, using a portable ultra high vacuum growth chamber which allows *in situ* measurements during organic molecular beam deposition of the organic semiconductor diindenoperylene.

In one set of experiments we used time-resolved grazing incidence diffraction to follow Bragg reflections of two different crystalline structures with molecules that are

i) standing upright or ii) lying down. The data show that on silicon oxide substrates the molecules already stand upright in the very early stages of growth. Interestingly though the first monolayer exhibits a transient structure which disappears when more molecules are heaped upon the first monolayer (transient strain).

When the substrate temperature is lowered ( $< 30$  C) or a substrate with stronger van-der-Waals interactions (*i.e.* a 'stickier' surface such as gold) is used, the molecules start to lie down more and more on the substrate.

In a second set of experiments we acquired the specular reflectivity (see schematic of scattering geometry in **Figure 48**) to measure growth oscillations, which give information on the filling of individual crystal layers during growth. Commonly growth oscillations are measured at the anti-Bragg point ( $q = 1/2 \cdot q_{\text{Bragg}} = 1/2 \cdot 0.37 \text{ \AA}^{-1}$ ) where consecutive crystalline layers interfere destructively resulting in an oscillating reflected intensity.

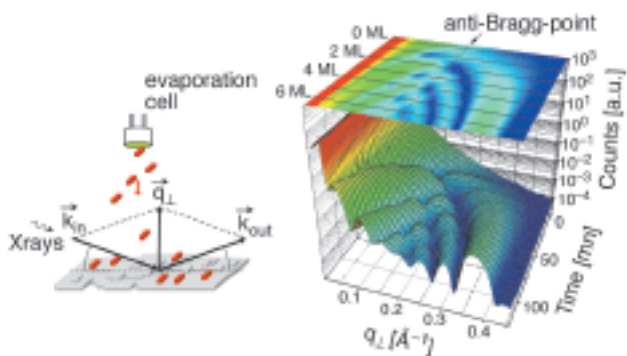


**Fig. 48:** Organic molecular beam deposition is used to grow thin films of the organic semiconductor diindenoperylene. During growth the specular X-ray reflectivity is acquired in real-time not only at the anti-Bragg point, but in a wide  $q$ -range.

To get a better understanding of the complex growth behaviour of organics, in this work we have developed a method to acquire and analyse real-time growth oscillations not only at the anti-Bragg point, but in a wide

$q$ -range, *i.e.* a large number of Fourier components are sampled simultaneously (**Figure 48**). Following the time evolution of the reflectivity at fixed  $q$ -values such as  $q = 2/3 \cdot q_{\text{Bragg}}$ ,  $q = 3/4 \cdot q_{\text{Bragg}}$ , ... growth oscillations with a longer period are visible (**Figure 49a**). Importantly the damping of growth oscillations at these  $q$ -values is lower than the damping at the anti-Bragg point, so that it is possible to follow the crystalline growth up to larger film thickness. From a combined fit of these growth oscillations at different  $q$ -values the evolution of layer coverages and the film roughness can be extracted as shown in **Figure 49b**; the data show that a pronounced transition from layer-by-layer growth to rapid roughening occurs after  $\sim 7$  monolayers of diindenoperylene have been deposited. While the driving force for this transition is not clear, the model results indicate a significant drop in interlayer transport. Several factors may contribute to this decreased transport such as faster nucleation, a decreased diffusion, and an increased Schwoebel barrier for thicker films.

In conclusion we have used *in situ* and *real-time* X-ray scattering to follow the development of different crystal structures and the consecutive filling of crystal planes during the growth of organic thin films. We have identified a roughening transition in diindenoperylene growth after deposition of about 7 monolayers. As growth is a dynamic phenomenon, real-time measurements in a wide  $q$ -range are required for a comprehensive picture of the growth kinetics. In our experiments, changes in growth mode and transient structures were revealed, which would be missed in post-growth experiments.

#### Principal publication and authors

S. Kowarik (a, b), A. Gerlach (a, b), S. Sellner (b), F. Schreiber (a, b), L. Cavalcanti (c) and O. Kononov (c), *Physical Review Letters* **96**, 125504 (2006).

(a) *Physical and Theoretical Chemistry Laboratory, University of Oxford (UK)*

(b) *Institut für Angewandte Physik, Universität Tübingen (Germany)*

(c) *ESRF*

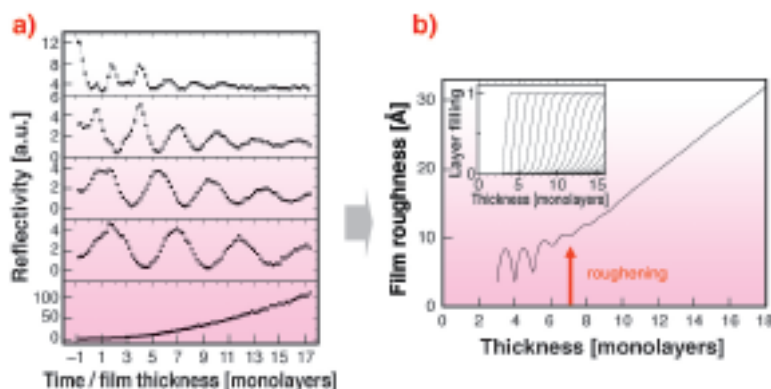


**Fig. 49:** a) Time evolution of the reflectivity at fixed  $q$ -values: the anti-Bragg, 2/3-, 3/4-, 4/5- growth oscillations and the Bragg intensity are shown. b) The evolution of crystalline layer coverages and the film roughness, deduced from (a). The growth shows a pronounced transition from layer-by-layer growth to rapid roughening after 7 monolayers.

## Effect of OH group position on the 2D crystalline structure of Langmuir monolayers of hydroxystearic acids

The family of hydroxystearic acids (HSA) is involved in many fundamental processes and applications: from a proposed role in biological cell apoptosis to waxes and cosmetics. In all applications, the role of the chain hydroxyl substituent is deemed essential, albeit not understood. This is due to the complexity of competing interactions in the most common morphological situations of interest (membranes, films, interfaces). In particular, HSA molecules at the air-water interface present an interesting bi-competitive adsorption between primary and secondary hydrophilic groups on either end of an alkyl chain, which –depending on the

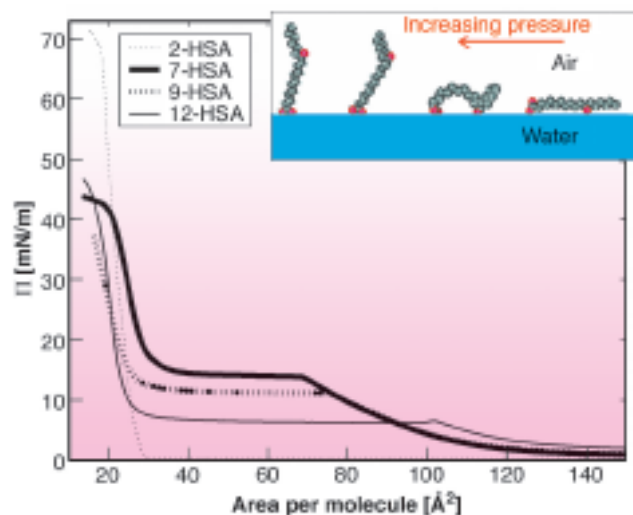


**Fig. 50:** Langmuir compression isotherms for different HSAs, indicated in the legend, at room temperature. **Inset:** a sketch of the molecular conformation at the air-water interface as a function of the surface pressure.

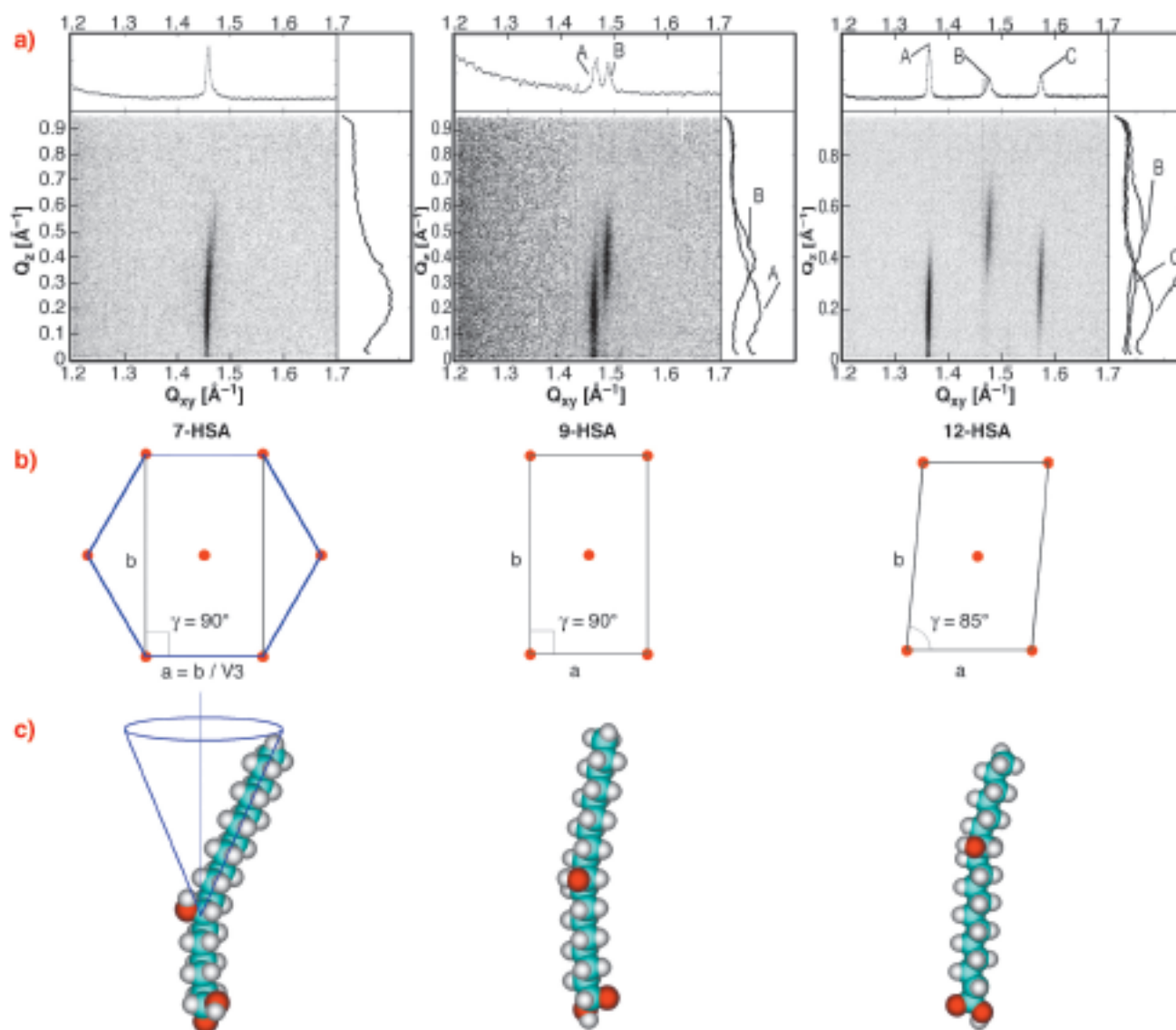


**Fig. 51:** a) GID diffraction patterns for the HSA molecules. For each HSA, the GID pattern was measured at a pressure immediately above the plateau in the  $\Pi$ -A isotherm of that particular compound. b) direct space crystallographic structures obtained from GID data. c) representation of the HSA molecules showing the assumed molecular conformation, in particular, for the 7-HSA, the proposed rotor phase is indicated.

position of the second hydrophilic group— may lead to a sharp transition from an expanded phase to a crystalline condensed morphology as surface pressure is increased. In **Figure 50** we show the Langmuir compression isotherms for different HSAs, and a sketch of the molecular conformations at the air-water interface.

In this highlight we report quantitative results on the microscopic structure of 2D crystalline phases of several HSAs, which, particularly for the case of the important 12HSA, may give important indications on its structural and morphological role in biological systems. The measurements were performed at beamline **ID10B** on a series of hydroxystearic acids in which the position of the secondary competing hydrophilic group was varied along the whole extent of the alkyl chain from the position 2- (*i.e.* close to the primary hydrophilic group) to the positions 7- 9- and 12-, the latter being the compounds most frequently studied in the literature. We obtained direct microscopic evidence, by synchrotron radiation reflectometry and grazing-incidence diffraction, that the position of the secondary hydrophilic group not only strongly influences the phase diagram as determined by compression isotherms and ellipsometry, but also induces different crystallisation patterns in the 2D system of the Langmuir monolayer. In particular we report for the first time the existence of a turning point in the effects of the hydroxyl position on the monolayers structure at 7-HSA.

In **Figure 51a**, we show the GID diffraction patterns for the different HSA molecules indicated in **Figure 51c**, as measured on the **ID10B** beamline. For each HSA, the GID pattern was measured at a pressure immediately above the plateau in the  $\Pi$ -A isotherm of that particular compound. In **Figure 51b** the direct space crystallographic structures obtained from GID data are shown, while **Figure 51c** shows the assumed molecular conformation, in particular, for the 7-HSA, the proposed rotor phase is indicated.

In summary, our results show that as the position of the second OH group is moved further away from the carboxylic polar head, the crystalline symmetry is decreased: 2-HSA does not seem to form true crystalline layers and shows a pseudo-hexagonal arrangement of molecular units; 7-HSA was found to have true hexagonal symmetry, which most likely is in a free rotor phase; 9-HSA was found to have rectangular symmetry; and a true oblique cell was found for 12-HSA. Also, the average molecular tilt with respect to the normal to the water surface increases as symmetry is lowered.

Finally, by X-ray reflectivity from monolayers at high surface pressure we could confirm the structures identified by GID and we have been able to locate the layer formed by the second hydrophilic group, which was shown to form a 2D network of hydrogen bonds,

which in 12-HSA is located 0.9 nm out of the water surface.

#### Principal Publication and Authors

L. Cristofolini(a), M.P. Fontana(a), C. Boga (b), O. Konovalov (c), *Langmuir* **21**, 11213 (2005).  
 (a) CRS-SOFT & Physics Dept. Uni Parma (Italy)  
 (b) Chemistry Dept. Uni Bologna (Italy)  
 (c) ESRF

## Simultaneous micro-Raman spectroscopy and microfocus X-ray diffraction

Raman spectroscopy and X-ray scattering are complementary techniques. Whilst one provides information relating to molecular bond energies and orientations, the other probes the sample's crystallographic structure and morphology. Not only do they provide differing information, but this relates to quite different length scales within a material's hierarchical structure. However, the two techniques also share several similarities. For example, they are non-contact and non-destructive for many materials, and neither requires modified or coated samples. Consequently both are used extensively for *in situ* studies such as investigating the effects of deformation, temperature or pressure.

During recent years, Raman spectroscopy and X-ray scattering have independently evolved microfocus capabilities. With smaller laser and X-ray beams, smaller structural heterogeneities can be resolved from within a single sample. Microfocussing also allows confined sample volumes to be studied, and reduces averaging when performing *in situ* experiments (such as chemical modification). The combination of  $\mu$ Raman and  $\mu$ XRD on the **ID13** beamline provides a completely new tool for the characterisation of materials [1]. Whilst the techniques' similarities make their combination practical, their differences make it scientifically important. A combinatorial approach also ensures a common sampling location on the specimen, consistency during dynamic studies, reduces experimental time, and is beneficial for rare and valuable samples (which may be only available in small volumes).

The ID13 beamline's  $\mu$ Raman apparatus was designed in collaboration with Renishaw. It comprises an Invia spectrometer and 785 nm near-IR laser, coupled via a single-mode fibre optic to a remote probe located within the sample environment. The spectrometer has a 1200 lines/mm grating whilst the probe head incorporates an integrated camera and white-light

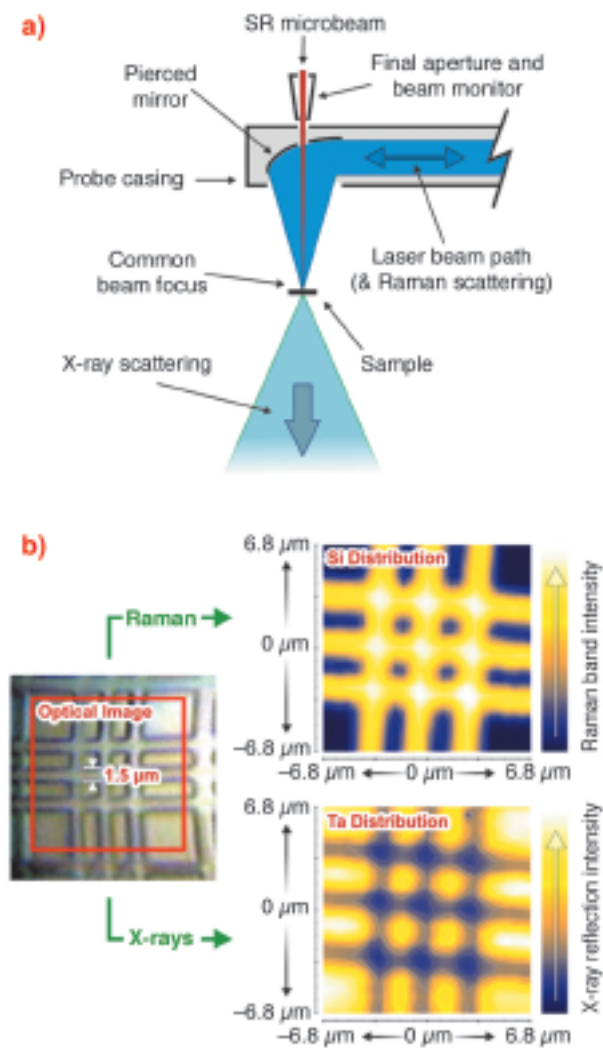


**Fig. 52:** a) Schematic showing on-axis beam delivery within the probe head and b) a Si/Ta structured sample from which simultaneous Raman and X-ray scattering reveals the spatial distribution of Si and Ta independently.

illumination for sample (and beam) visualisation. The system is designed in an on-axis configuration with the laser beam delivered to the same point on the sample as the X-ray beam, simultaneously. This is made possible by a pierced mirror within the probe head which focuses the laser beam onto the sample whilst allowing the X-ray beam to pass through (Figure 52a). The laser beam spot size at the focal position is approximately 1  $\mu\text{m}$ . This is comparable to the X-ray beam size from a number of different ID13 optics [2]. Both techniques can therefore resolve microstructural variations, such as 1.5  $\mu\text{m}$  Si/Ta structures on laboratory-produced samples (Figure 52b).

In a recent demonstration of the system's capabilities, a single poly(*p*-phenylene terephthalamide), PPTA or Kevlar fibre was deformed *in situ*. Raman spectra and diffraction patterns were recorded at regular intervals using simultaneous exposures of 5 seconds. The Raman spectra of PPTA is characterised by a strong band at 1610  $\text{cm}^{-1}$ . This is assigned to a vibrational mode of the *p*-phenylene ring and shifts to a lower wavenumber under tension. This band shift corresponds to deformation of the fibres molecular "backbone". The diffraction pattern of PPTA has several meridional layer lines corresponding to the axial crystal lattice spacing (*c*-spacing). Changes in layer line position under tension reflect direct distortion of the crystal lattice (crystal strain). During deformation, both the 1610  $\text{cm}^{-1}$  Raman band and crystal strain change linearly with macroscopic stress (Figure 53). This indicates stress transfer between crystalline domains and individual molecular bonds. The resulting Raman band shift rate and crystal modulus are -3.3  $\text{cm}^{-1}/\text{GPa}$  and 214 GPa respectively. Deformation also causes a stress-induced increase in the degree of crystalline domain orientation consistent with the non-reversible rotation of chains.

Whilst the PPTA diffraction pattern provides information exclusive to the crystalline phase, its Raman spectra contains both a crystalline and amorphous contribution. Combining this information allows individual contributions to be isolated. For example, broadening of the 1610  $\text{cm}^{-1}$  Raman band during deformation suggests an increasing stress heterogeneity between the crystalline and amorphous fractions. This can be explained in terms of low- and high-stress uniform-strain mechanical models. At low stresses, linear Raman band broadening can be attributed to a phase-related difference in mechanical properties. At high stresses, an increasing degree of crystalline domain orientation causes heterogeneous stiffening within the PPTA fibre's structure. Consequently, the amorphous fraction remains "under-stressed" during subsequent deformation.

Combining  $\mu\text{Raman}$  and  $\mu\text{XRD}$  has provided a new insight into deformation micromechanics within single PPTA fibres. It reveals how molecular- and crystallographic-scale contributions influence a material's mechanical properties and how heterogeneous stiffening can occur within a material's microstructure.

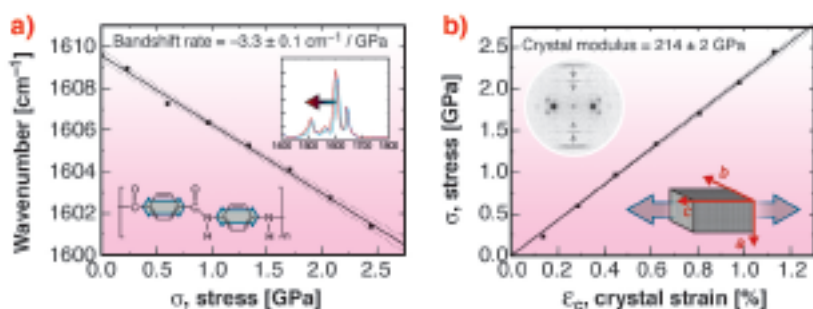


**Fig. 53:** a) Variation of the 1610  $\text{cm}^{-1}$  Raman band and b) crystal strain with applied stress (determined simultaneously). Inset graphics reflect how the Raman band and layer line shifts correspond to *p*-phenylene ring stretching and axial lattice distortion respectively.

## References

- [1] R.J. Davies, M. Burghammer, C. Riekkel, *Applied Physics Letters*, **87**(26), 264105 (2005).  
 [2] C. Riekkel, R.J. Davies, *Current Opinion in Colloid & Interface Science*, **9**, 396–403 (2005).  
 ESRF

## Principal Publication and Authors

R.J. Davies, M. Burghammer, C. Riekkel, *Macromolecules* **39**, 4834–4840 (2006).  
 ESRF

## Microdiffraction on A-amylose single crystals

The difficulty in obtaining sufficiently large single crystals usually limits polymer and biopolymer studies to X-ray powder and fibre diffraction methods. Until recently, this was also the case for the polysaccharide amylose. Amylose is a linear molecule of (1-4)-linked  $\alpha$ -D-glucopyranosyl units and is found in native

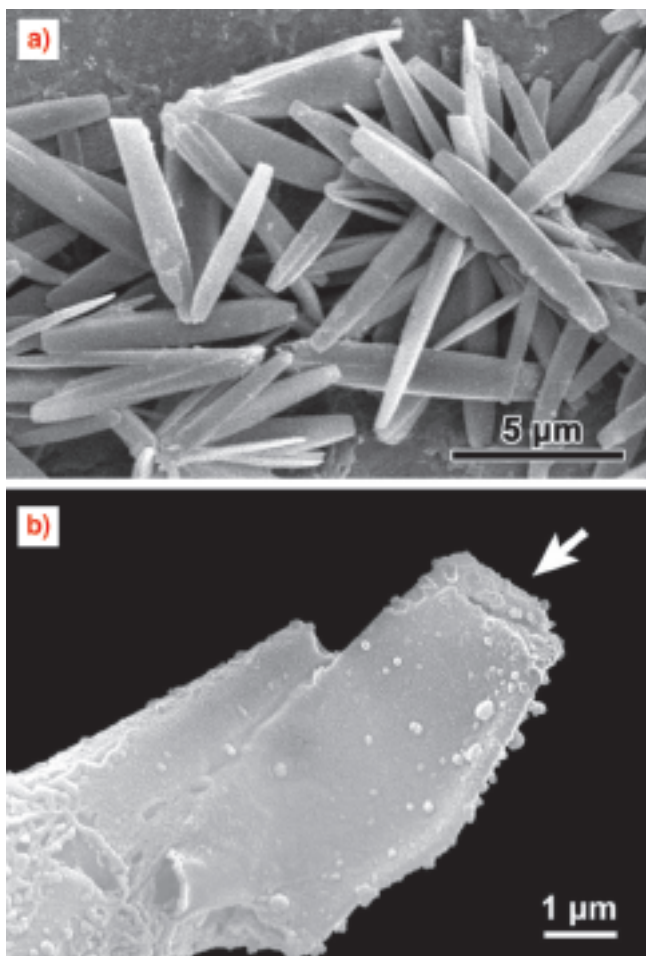


**Fig. 54:** a) SEM image of A-type amylose crystal aggregate; b) SEM image of an air-dried amylose single crystal glued to a borosilicate glass capillary tip. The small ripples on the glass capillary are due to glue.

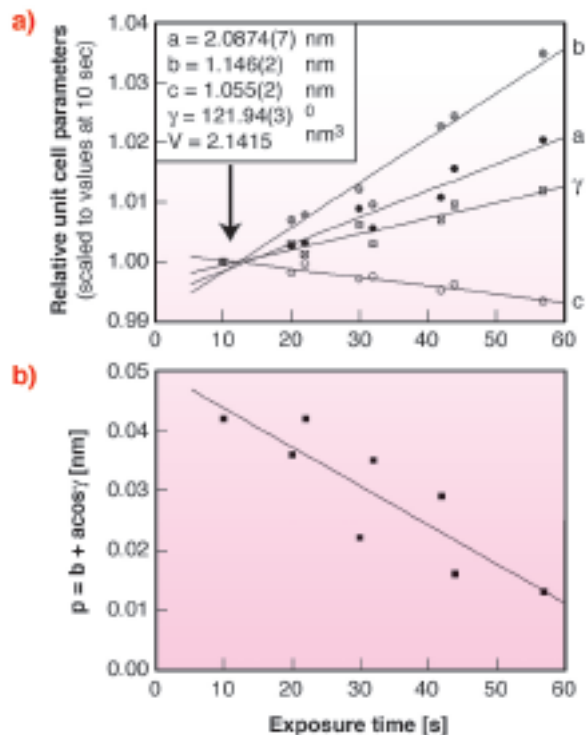


**Fig. 55:** a) variation of relative unit cell parameters with exposure time. Data were scaled to the unit cell parameters refined at the shortest exposure time (10 sec); b) variation of the parameter  $p = b + a \cos \gamma$  with exposure time ( $a/b$  and  $\gamma$  are the refined monoclinic cell parameters). The  $p$ -value becomes zero for an orthorhombic lattice with monoclinic setting. The straight lines in A, B correspond to linear least-squares fits.

starch granules. Progress in synchrotron radiation microdiffraction and crystal growth techniques has now allowed the study of micrometre-sized A-amylose crystals by single crystal diffraction methods.

A typical aggregate of needle-shaped A-amylose microcrystals is shown in **Figure 54a** [1]. Micromanipulation techniques developed at the **ID13** beamline allowed the selection and mounting of individual crystals from such an aggregate. A SEM image of a typical crystal glued to a glass capillary is shown in **Figure 54b**. The two crystals studied were rotated in steps of  $20^\circ$  and  $40^\circ$  with 1 and 2 second exposure time per step, respectively. The highest resolution obtained was 1.51 Å.

In previous structural analysis by an electron diffraction method and from packing considerations [2], a clear-cut difference between orthorhombic and monoclinic symmetries could not be firmly established for A-amylose. The present X-ray microdiffraction data allows the analysis of a large set of symmetry equivalent and statistically significant reflections. This allowed testing for the best space group by using the XDS program package, which clearly established the monoclinic symmetry for A-amylose. The space group B2 was

chosen as equally possible space groups Bm and B2/m can be excluded on the basis of optical activity of A-amylose.

A systematic change of unit cell parameters was observed with increasing X-ray exposure at 100 K (Figure 55a). It is also interesting to note that the monoclinic unit cell gets closer to a pseudo-orthorhombic cell with increasing dose (Figure 55b). This phenomenon can be described using the parameter  $p = b + a \cos \gamma$ , which becomes 0 for a pseudo-orthorhombic lattice. Here  $a/b$  and  $\gamma$  are the refined monoclinic unit cell parameters.

Progress in data collection and structural analysis has recently allowed us to solve the A-amylose structure using a molecular replacement technique and its refinement for data, achieving a highest resolution of 1.2 Å [3].

### References

- [1] G. Potocki-Veronese *et al.*, *Biomacromolecules* **6**(2), 1000-1011 (2005).  
 [2] A. Imberty, H. Chanzy, S. Pérez, A. Buléon, & Tran, *J. Mol. Biol.* **201**, 365-378 (1988).  
 [3] D. Popov *et al.*, to be published.

### Principal Publication and Authors

D. Popov, (a), M. Burghammer, (a), A. Buléon (b); N. Montesanti (c); J. L. Puteaux (c); C. Riekel (a), *Macromolecules* **16**, 3704-3706 (2006).

(a) ESRF

(b) INRA, Nantes (France)

(c) CERMAV, Grenoble (France)

## Characterising the decay of ancient silk fabrics by microbeam synchrotron radiation diffraction

Understanding and quantifying the decay process of silks is of prime importance for the restoration and conservation of ancient silk fabrics. We have been using synchrotron radiation microdiffraction at beamline ID13 to characterise the fibre microstructure and the overall state of the fabric coming from the *Famen* temple, China. The temple is situated 120 km west of the ancient Chinese capital Xi'an and is one of China's most important buddhistic sanctuaries. The silk fabrics were part of a treasure once laid down by the T'ang dynasty (618-907 AD) emperors as a gift to the temple [1]. Three plain-weave silk fabrics were selected according to their loss of structural integrity, which was assumed to reflect different states of degradation.

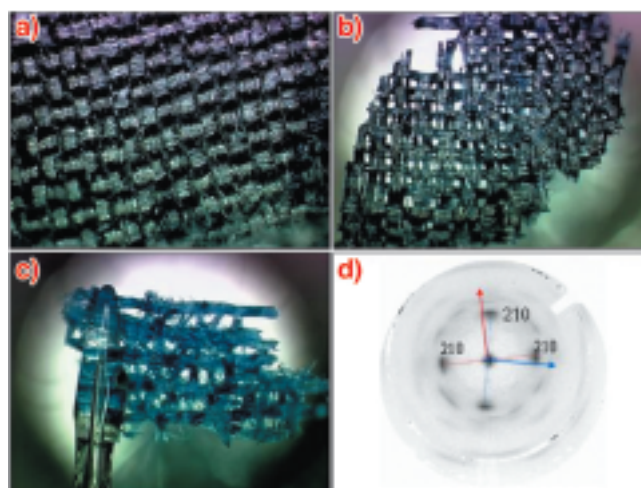


**Fig. 56:** a) current plain-weave silk fabric; b) and c) ancient silk fabrics showing different degrees of decay; d) diffraction pattern from fabric showing 210 reflections of two nearly orthogonal fibres hit by the beam.

The decay of a silk fabric is a complex process starting at the level of the fibres and propagating through the fabric until the destruction of its morphology. Decay of the amorphous protein chain fraction in a fibre will reduce the network of amorphous chains connecting the crystalline domains and consequently broadens their axial orientation distribution. The azimuthal width of the 210  $\beta$ -sheet reflection (Figure 56d) allows quantification of this orientation distribution and is therefore a sensitive indicator for the state of decay. We have mapped extended areas of a current silk fabric and ancient fabrics at different levels of decay (Figure 56 a-c) using a beam of about 1 micrometre in size and recorded a diffraction pattern at every position. For comparison, a single *Bombyx mori* thread (2 fibres) was mapped in the same way. The extracted 210 reflections allow the creation of a composite image as shown in Figure 57 for

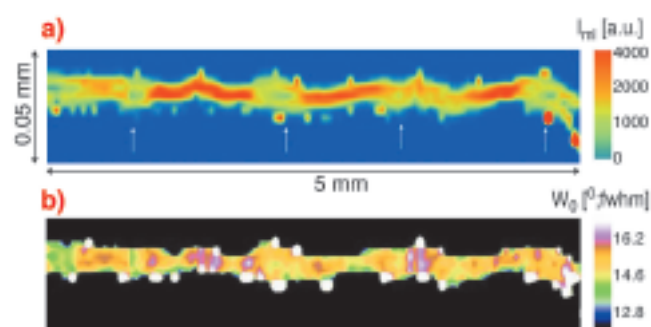


**Fig. 57:** a) composite plot of the 210-reflection intensity across a *Bombyx mori* thread. Size of individual pixels: 2.5 x 50  $\mu\text{m}^2$ . The thread was cylindrically twisted so that the two individual fibres can only be seen at the positions marked by white arrows; b) composite plot of the azimuthal width ( $W_0$ ) of the 210 reflection across the thread. The white spots correspond to fwhm values outside of the colour scale, which are due to low counting statistics.

the *Bombyx mori* thread. The integrated intensity is proportional to the crystalline fraction (**Figure 57a**) and the plot of the azimuthal width reflects variation in orientation distribution across the thread (**Figure 57b**).

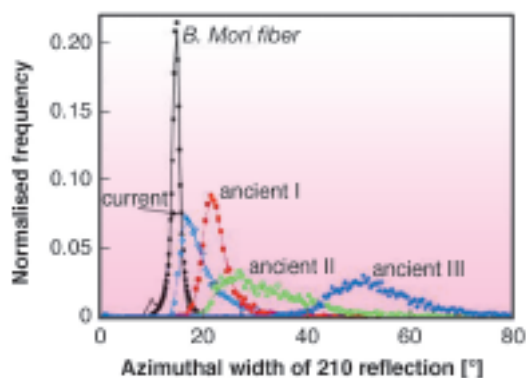


**Fig. 58:** Experimental data (symbols) and fitted functions (solid lines) of histograms of 210-width distribution. The frequencies of each sample-series have been normalised to the sum of frequencies.

A more quantitative analysis of the state of decay can be based on the histogram of azimuthal width distribution for the different samples (**Figure 58**). The histogram peak was found to be symmetric for the silk thread and asymmetric for the fabrics. The asymmetry suggests a convolution of a symmetric microscopic term due to the orientation distribution of the fibres and a macroscopic term introducing tails due to the angular spread of fibres sampled along the beam path. An increasing decay broadens the symmetric term peak and shifts the peak centre to larger values, presumably due to a loss of the connecting amorphous network. The break up of the fibre network due to decay processes can explain the tails of the histograms.

The current results suggest that the microscopic decay process in the fibres starts by a loss of amorphous protein chains. At a subsequent stage of ageing, cleavage proceeds into the fibrils and the silk fibres break up into even smaller fragments. Restorative action requires probably that the nanofibrillar morphology remains largely intact and can be embedded in an artificial random polymer chain matrix.

### Reference

[1] S. Greiff, H. Kutzke, S. Lahlil, C. Riekkel, P. Wyeth, in *AHRC Research Centre for Textile Conservation and Textile Studies First Annual Conference (2004)*. Winchester: Archetype Publications Ltd, London, UK.

### Principal Publication and Authors

A.C. Hermes (a), R.J. Davies (a), S. Greiff (b), H. Kutzke (c), S. Lahlil (d), P. Wyeth (d), C. Riekkel (a), *Biomacromolecules* **7**(3), 777-783 (2006).

(a) ESRF

(b) Römisch Germanisches Zentralmuseum, Mainz

(Germany)

(c) University of Applied Science Cologne, Köln

(Germany)

(d) Textile Conservation Centre, University of Southampton Winchester Campus, Winchester (UK)

## Phase diagram of a solution undergoing inverse melting

The phenomenon of inverse melting happens when a liquid heated at constant pressure undergoes a reversible liquid-to-crystal transition [1,2]. Such a transition of endothermic nature implies the passage from a low-temperature liquid (LTL) to a high-temperature crystal (HTC) with absorption of heat. This behaviour, which is the opposite to what is expected for common liquids, indicates the presence of a crystal with entropy higher than its liquid counterpart. On further heating, the HTC may eventually melt into a high temperature liquid (HTL).

Using differential scanning calorimetry (DSC) and X-ray diffraction methods we have investigated the phase diagram of a system belonging to this class of materials, a solution of  $\alpha$ -cyclodextrin ( $\alpha$ CD) ( $C_{36}H_{60}O_{30}$ ), water and 4-methylpyridine (4MP) ( $C_6H_7N$ ) [3]. DSC measurements were performed to determine and characterise the inverse phase transitions from an energetic point of view. The measurements of heat absorption as a function of the temperature show peaks of endothermic nature. In **Figure 59** the temperature of the peak ( $T_{peak}$ ) and of the onset ( $T_{onset}$ ) are reported as full circles and squares respectively.

In the concentration region 150-350 mg/ml of  $\alpha$ CD-in 4MP three endothermic transitions are observed on increasing the temperature: the first corresponds to the LTL-HTC, the second has been associated to a solid-solid transition, the third corresponds to the HTC-HTL transition. At decreasing  $\alpha$ CD concentration, in the region 50-150 mg/ml, the solid region becomes thinner until it disappears and single endothermic transition peak is observed. This experimental observation is compatible with a direct LTL-HTL transition.

In order to give a microscopic interpretation of the behaviour of the liquid and to investigate its local structure in the low concentration region, an X-ray diffraction experiment was performed as a function of the temperature along the LTL-HTL transition on the beamline **BM29**. Three different concentrations of  $\alpha$ CD in 4MP have been investigated. An example of the integrated scattered intensity  $I(Q)$  at the concentration 108 mg/ml and in the temperature range 295 to 413K is reported in **Figure 60**. It confirms the existence of a

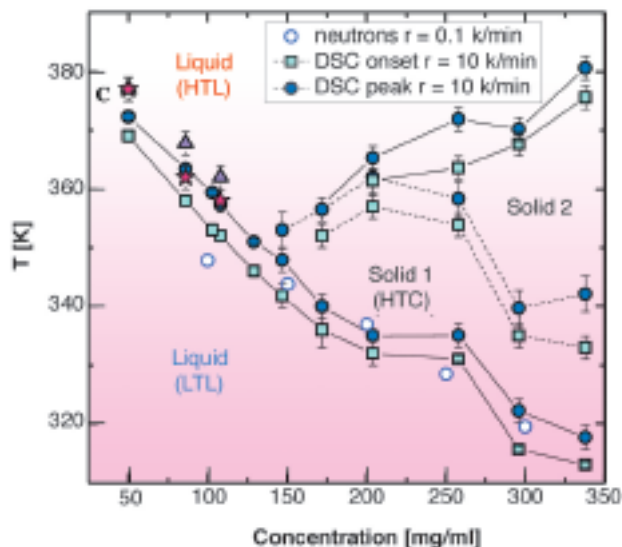


**Fig. 59:** Phase diagram of  $\alpha$ CD-water-4MP solutions. The transition temperatures obtained with the DSC measurements at a heating rate  $r = 10$  K/min are reported as a function of the concentration. The full squares and the full circles represent the onset and the peak transition temperature respectively. The open circles are obtained from neutron scattering measurements of ref. [3] performed at a heating rate  $r = 6$  K/hour. The stars and triangles represent the transition temperatures obtained by the X-ray static structure factors of Figure 60. They are associated to the jump of the  $Q$  position of the first maximum and first minimum respectively of the integrated scattered intensity  $I(Q)$  of Figure 60.

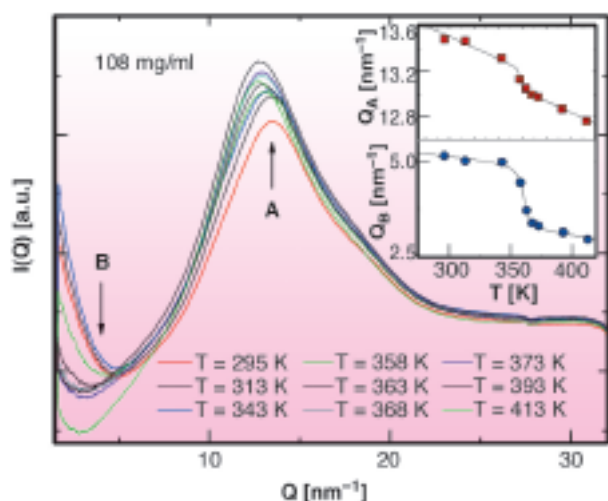


**Fig. 60:** Integrated scattered intensity from a solution of  $\alpha$ CD-in 4MP at the concentration 108 mg/ml of  $\alpha$ CD-in 4MP in the temperature range 295K-413K. The insets show the  $Q$  position of the maxima  $Q_A$  (top panel) and the minima  $Q_B$  (bottom panel) of the integrated scattered intensity reported as a function of the temperature at the indicated concentration.

disordered structure both below and above the transition temperature detected by DSC. The temperature evolution of the structure of the liquid has been followed looking at the  $Q$  position of the first maximum (around  $Q = 13 \text{ nm}^{-1}$ ) and minimum (around  $Q = 4 \text{ nm}^{-1}$ ) of the  $I(Q)$  respectively identified as positions  $Q_A$  and  $Q_B$ . The  $Q$  values of these two points reported as a function of temperature in the insets of Figure 60 show a jump at the temperatures corresponding to the LTL-HTL transition, as derived by the DSC measurements. The three transition temperatures for the maxima (full triangle) and the minima (full stars) of  $I(Q)$  reported on the phase diagram of Figure 59 show a good agreement.

The combination of DSC and X-ray diffraction allowed us to draw the phase diagram of a solution undergoing inverse melting and to characterise the microscopic local different structure of the two disordered liquid phases, the LTL and the HTL, observed in the low concentration region.

### References

- [1] A. Lindsay Greer, *Nature* **404**, 134 (2000).
- [2] A. Crisanti and L. Leuzzi, *Phys. Rev. Lett.* **95**, 087201 (2005) and references within.
- [3] M. Plazanet, C. Floare, M.R. Johnson, R. Schweins, and H.P. Trommsdorff, *J. Chem. Phys.* **121**, 5031 (2004).

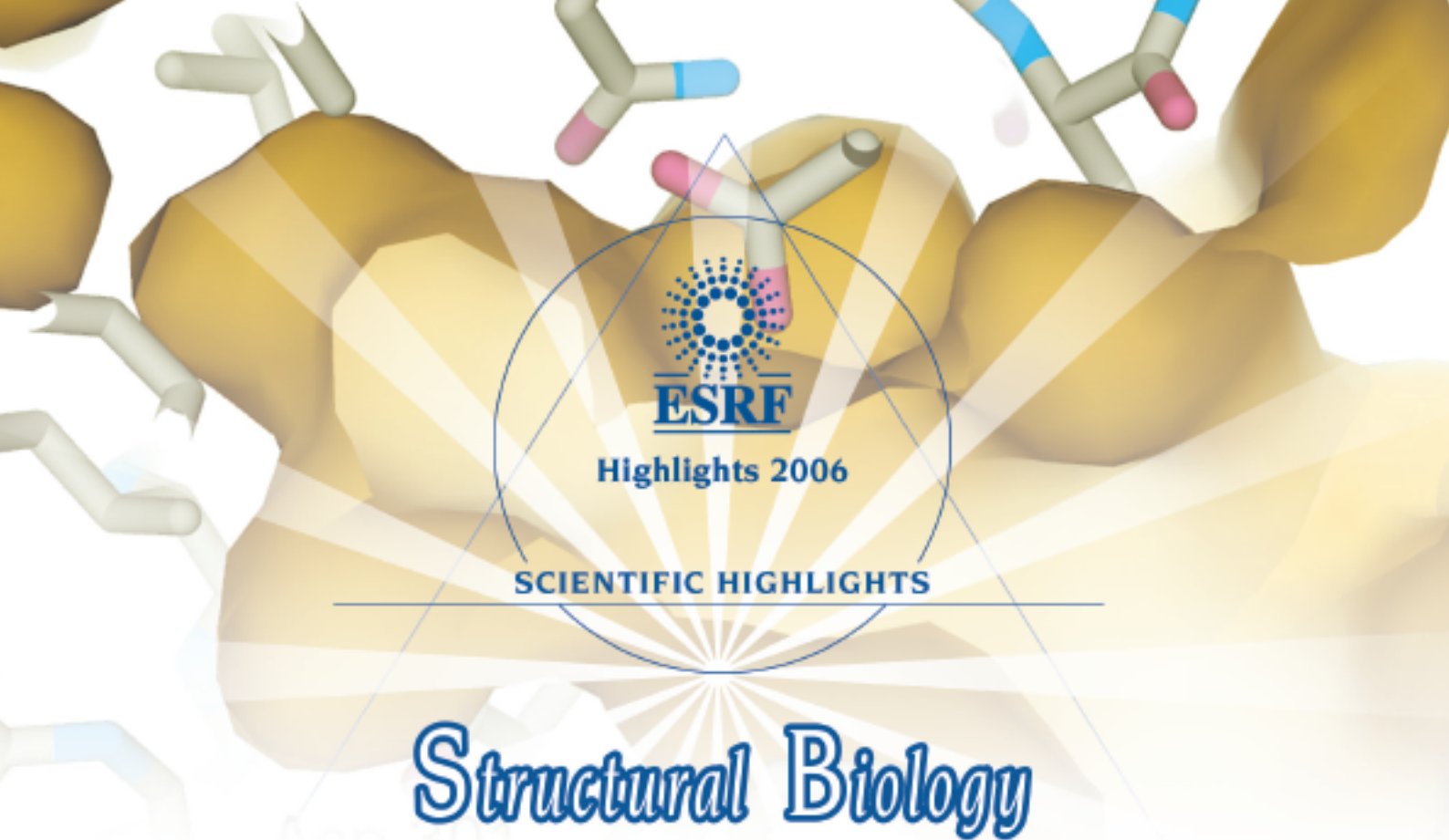
### Principal Publication and Authors

R. Angelini (a), G. Ruocco (a,b), S. De Panfilis (c), F. Sette (c), *submitted*.

(a) CRS SOFT- INFM-CNR, Università "La Sapienza", Roma (Italy)

(b) Dipartimento di Fisica, Università "La Sapienza", Roma (Italy)

(c) ESRF



## Introduction

We had hoped that 2006 would be a calm year for the MX Group, used for consolidation of the work performed during 2005. Of course this has not proven to be the case! During 2006, the MX beamlines welcomed over 2000 visitors carrying out more than 660 separate experimental sessions. Moreover, and as predicted, the availability of sample changing robots has fundamentally altered the way in which the beamlines are used: in the period 1<sup>st</sup> April to 16<sup>th</sup> December 2006, the sample changers were used to mount around 13,000 crystals. The availability of sample changers means that users can either screen large numbers of samples before collecting data from the best possible crystal or, in the case of pre-screened samples, collect many datasets very rapidly indeed. Such an intensive use of the beamlines means they must be highly reliable. That they continue to remain so is a tribute to the work of all the members of the MX Group (particularly our technical staff) and the support groups with whom we collaborate. We should not forget

that, as well as maintaining the beamlines in an excellent operational state, the MX Group also continues to develop the facilities available - a prototype of an automatic data collection pipeline is in an advanced state and we are taking our first, tentative, steps towards making remote access to the beamlines routine for academic users.

The commissioning of the microfocus beamline ID23-2 allowed us to open the beamline to the MX community in November 2006. Use of this latter facility has required a steep learning curve on the part of beamline staff and external users and highlighted the need for improvements in optical components and beamline usage. Nevertheless, the availability of a microfocus beamline on a routine basis for MX has provided an extremely valuable, currently unique, additional tool for structural biology allowing structure determination from crystals that were previously considered too small to be useful (see the report of Flot and colleagues, page 58).

We are also increasing the availability of techniques complementary to X-ray diffraction. In addition to an on-line microspectrophotometer working in the UV-visible range, Raman spectroscopy is now available on the beamlines and allows the on-line monitoring of radiation damage to crystals of biological macromolecules (see McGeehan *et al.*, page 59). This facility will be extended when the move of the “cryo-bench” lab is completed. The relocation will install the laser and spectroscopic tools of the lab into custom facilities situated on ID23. The intention is to provide the community with online access to these tools from both of the endstations of ID23. A workshop will be arranged in early 2007 to further explore the scientific exploitation of these spectroscopic techniques.

Increasingly, structural biologists study systems implicated in research areas such as cancer and drug resistance. This trend is reflected in several of the highlights found in this chapter. Hsp90 (heat shock protein 90) is essential for cell viability

in all eukaryotes. The involvement of many Hsp90 client proteins in the development and progression of cancer means that Hsp90 is an exciting potential target for new anti-cancer drugs. The crystal structure analysis of an Hsp90-nucleotide-p23/Sba1 closed chaperone complex (Pearl *et al.*, page 50) provides detailed insight into the conformational biochemistry of the macromolecular systems in which Hsp90 is involved, information which may ultimately help the development of drugs to combat cancer. The ability of bacteria to recombine gene cassettes using integron integrases is an important factor governing their adaptability to changing environmental conditions. The elucidation of the structure of the integron integrase VchInt1a from *Vibrio cholerae* in complex with a target *attC* site (MacDonald *et al.*, page 51) provides information on how, at a molecular level, one might try to limit acquired genetic traits such as antibiotic resistance. *Escherichia coli* strains that have acquired multiple-antibiotic resistance overproduce two proteins: the periplasmic fusion component AcrA and the resistance-nodulation-cell division (RND) type efflux pump AcrB. These interact with the outer membrane protein TolC to transport drugs out of cells. Seeger and colleagues (page 52) have determined the structure of AcrB as an asymmetric trimer and propose a novel mechanism for the transport of antibiotics. This knowledge may help to understand how to overcome the problem of multiple-antibiotic resistance in bacteria.

The fourth highlight in this chapter (Selmer *et al.*, page 54), is an example of another increasing and encouraging trend that we observe. As well as providing crucial information on how ribosomes interact with release factors at the end of the translation process, the work illustrates how European synchrotron sources can work together to provide the best opportunities for the elucidation of scientifically important macromolecular crystal structures. For the structure

described, initially data could only be collected to a resolution of 4.6 Å at the ESRF. However, taking advantage of the sample changers installed at the ESRF, subsequent screening of hundreds of crystals showed that a refinement in crystallisation conditions had produced crystals diffracting to a much higher resolution limit ( $d_{\min} = 2.8$  Å). These crystals were taken to the SLS, where beam time was available, and a full data set collected.

The in-house research highlights concentrate on the role of metal ions in biology. Cuypers *et al.* (page 55) describe the crystal structures of two Dps (DNA protecting protein under starved conditions) proteins: Dps1 and Dps2 from *Deinococcus radiodurans*. The iron storage and DNA binding functions of Dps proteins provide protection for cells during stress, possibly by the inhibition of Fenton chemistry and the suppression of free-radical chemistry. The crystal structures reveal channels in the surface of the proteins that facilitate the transit of iron from solvent to the ferroxidase centres of Dps. In the second example of in-house research, the structure of the nickel regulator, NikR from *Helicobacter pylori* is presented. This bacterium colonises the human stomach and its presence can lead to severe gastric diseases including stomach cancer. The bacterium's ability to survive the low pH found in the human stomach is centred on the Ni-dependent enzyme urease. However as nickel can also be toxic at high concentrations, *H. pylori* has developed a mechanism enabling tight regulation of nickel content, usage and storage that depends on NikR. The structural studies by Dian *et al.*, (page 56), combined with their biochemical analysis, provide a structural basis for nickel regulation by NikRs.

As well as providing facilities for use by academic researchers, the MX Group beamlines are used for proprietary research, mainly by pharmaceutical companies. Rowland

and colleagues (page 60), provide an example of the type of research carried out. They describe the crystal structure of the 2D6 isoform of human Cytochrome P450. This structure shows a well-defined cavity above the haem group, explains why three residues, Asp301, Glu216 and Phe120 are important for substrate binding, accounts for published site-directed mutagenesis data and has provided insight into the metabolism of several compounds, including the antihypertension drug debrisoquine.

The final article in this year's chapter describes progress in obtaining molecular envelopes from macromolecular powder diffraction data (Wright *et al.*, page 61). Despite the advances made in the field of structural biology and the advent of microfocus beamlines dedicated to the technique, some macromolecules may never provide single crystals from which useful diffraction data can be obtained. Although currently a low resolution technique, this article shows that phases produced from powder diffraction experiments can produce accurate molecular masks. Improvements in the technique should lead to higher resolution information being obtainable.

**G. Leonard and S. McSweeney**

## Crystal structure of an Hsp90-nucleotide-p23/Sba1 closed chaperone complex

Hsp90 (heat shock protein 90) is essential for cell viability in all eukaryotes and plays a central role in the maturation and activation of signalling proteins including steroid hormone receptors and protein kinases. The involvement of many Hsp90 client proteins in the development and progression of cancer has led to Hsp90 emerging as an exciting and key target for the development of new anti-tumour therapeutics. Activation of client proteins by the dimeric Hsp90 chaperone involves a range of co-chaperone proteins that complex with Hsp90 at different stages of the chaperone cycle and regulate and facilitate client protein activation [1]. One of the best-characterised client protein activation processes is that of steroid hormone receptors. During this process the steroid hormone receptor is bound to Hsp90 in a complex that is stabilised by the binding of the co-chaperone p23/Sba1 in an ATP dependent manner and allows the receptor to attain the activated conformation in which it can bind steroid hormone.

Despite initial uncertainty Hsp90 was identified as an ATPase. However the structural mechanism of this activity, and its role in Hsp90 chaperone function have been poorly understood and often contentious. From structural studies of individual domains of Hsp90, combined with biochemical and mutagenesis studies, we developed a mechanistic model in which binding and hydrolysis of ATP is coupled to a conformational cycle involving transient dimerisation of the N-terminal domains, which facilitates ATP turnover [2]. Biochemical evidence suggested that the p23/Sba1 co-chaperone functioned by binding selectively to this N-terminally dimerised conformation of Hsp90 and extended the lifetime of the closed ATP-bound state required for activation of a bound client protein.

With the recent determination of the crystal structure of full-length Hsp90 in the closed state, in a ternary complex with a non-hydrolysable ATP analogue (AMP-PNP) and the p23/Sba1 co-chaperone, we have now been able to confirm this model and reveal the plethora of interconnected conformational changes that accompany ATP-binding (Figures 61 and 62). Central to the process is the movement of a segment in the N-terminal domain of Hsp90, the 'lid' region, which undergoes a

very substantial restructuring on ATP-binding, folding over the mouth of the nucleotide binding pocket to interact with the  $\gamma$ -phosphate of the nucleotide. Lid closure exposes a hydrophobic patch on the N-terminal domains which forms a dimer interface. Accompanying this is a strand exchange between the two N-terminal domains which is also seen in other dimeric members of the GHKL ATPase superfamily including DNA gyrase B and MutL. The conformational changes in the N-domains also allow the docking of the middle segments of the chaperone and the formation of the active site at the interface of the N-domain and middle segments.

The p23/Sba1 co-chaperone binds across the dimerised N-terminal domains of Hsp90, interacting with the middle segment of the chaperone and with the lid segment in its closed conformation. Intriguingly, the binding site of p23/Sba1 on the middle segment overlaps the binding site for another co-chaperone, Aha1 which greatly activates ATP turnover. Both co-chaperones cause restructuring of a catalytic loop in the middle segment of the chaperone allowing a key catalytic arginine residue to interact with the  $\gamma$ -phosphate of ATP and promote hydrolysis. However, because of its additional interaction with the closed conformation of the lid segment, p23/Sba1 slows turnover and release of the products, extending the lifetime of the closed state.

The structure of the full Hsp90-ATP-p23/Sba1 complex, along with previous crystal structures of Hsp90 domains and their complexes with other co-chaperone is providing an unparalleled level of insight into the detailed conformational biochemistry of this complex macromolecular system. The main challenge for the

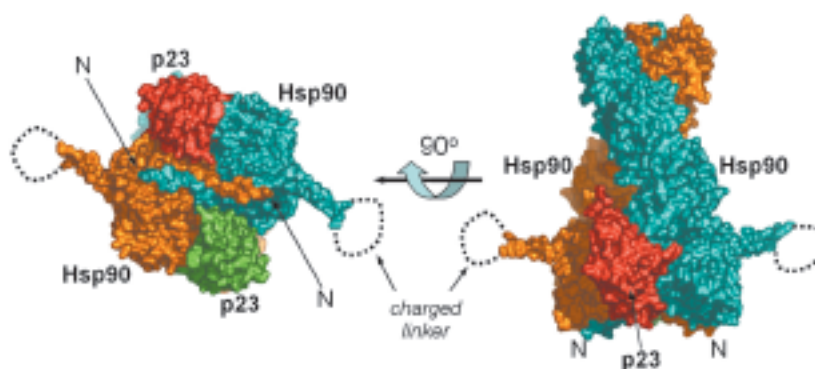


**Fig. 61:** Full-length hsp90-nucleotide-p23/sba1 shown as a molecular surface representation. The left handed twist of Hsp90 (blue and orange) can be seen (right), with the two p23/Sba1 (red and green) molecules symmetrically disposed on each side, contacting the N-terminal and middle domains. When the view is rotated 90° along the horizontal axis (left) the strand exchange between the two monomers is evident. The charged linker is disordered in the crystal. The crystal structure was refined to 3.1 Å resolution and data were collected at beamline ID29. The high intensity and stability of the beam was crucial for data acquisition.

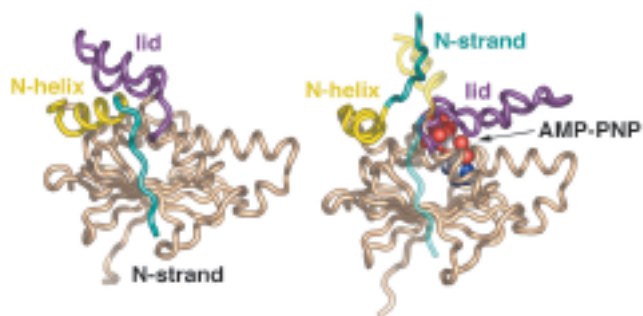


**Fig. 62:** Secondary structure diagram comparing the isolated N domain (left) and the AMP-PNP-bound state (right). Upon nucleotide binding the lid region closes over the active site, with considerable movement of the N-terminal helix and complete detachment of the N-terminal strand, which swaps into the other N domain of the dimer.

future lies in determining structures for Hsp90 complexes with client proteins so that the coupling of the Hsp90 ATPase cycle to client protein activation can finally be understood.

#### References

- [1] L.H. Pearl and C. Prodromou, *Annu Rev Biochem* **75**, 271-294 (2006).  
 [2] C. Prodromou *et al.*, *EMBO J.* **19**, 4383-4392 (2000).

#### Principal Publication

M.M. Ali, S.M. Roe, C.K. Vaughan, P. Meyer, B. Panaretou, P.W. Piper, C. Prodromou and L.H. Pearl, *Nature* **440**, 1013-1017 (2006).

*Section of Structural Biology, Institute of Cancer Research, London (UK)*

## Site specific recombination by the integrase: Broad DNA specificity

Integron integrases catalyse recombination reactions between gene cassettes in bacteria, leading to the acquisition or dispersion of genetic traits. Enzymes in this group belong to the category of site specific recombinases from the tyrosine recombinase family. They possess a conserved set of active site residues (R-K-H-R-H/W-Y) which are involved in DNA cleavage, stabilisation of the phospho-tyrosine transition state intermediate and Holliday junction [1], and protonation of the leaving hydroxyl group. The catalysed reaction is isoenergetic with no ATP molecule required due to a concerted transfer of the high energy phospho-tyrosine bond to the phospho-diester DNA linkage. Site specific

integrases use short stretches of double-stranded DNA which contain palindromic regions and a central asymmetric sequence as substrates. The integrons are mobile elements that carry an integrase enzyme, an insertion site (*attI*) and several gene cassettes composed of an open reading frame and an *attC* site. The *attI* site is around 40 base-pairs (bp) in length, whilst the *attC* site can vary from 40 bp to 160 bp, with a GTTRRRY (R:purine, Y:pyrimidine) consensus region. Integron integrases catalyse the integration of cassettes by recombining the *attC* sites with the *attI*, whilst they disperse cassettes by recombining *attC* sites. They have been shown to preferentially recombine the bottom strand of the recombination site.

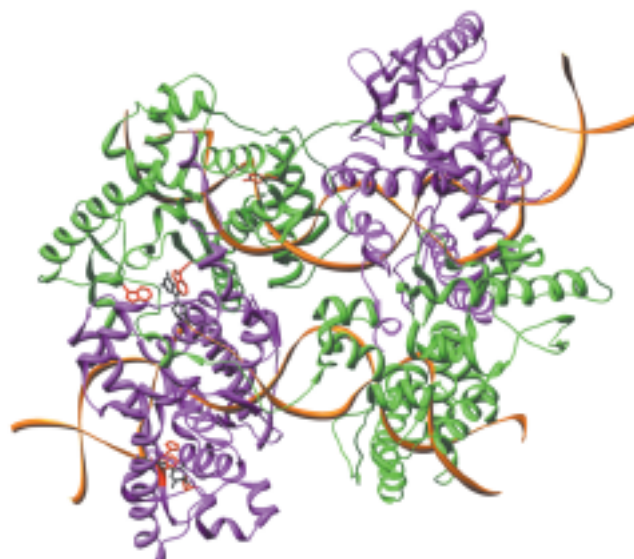


**Fig. 63:** X-ray structure of the VchIntIa-VCRbs integrase-DNA complex. The synaptic complex is composed of a tetramer of enzyme molecules bound to two DNA hairpin stems. Specific recognition of extruded bases (G20' and T12', black) by conserved residues (W157, W219 and H240-241, P232 respectively, red) orients the active site tyrosine Y302 (red), into attacking (green) and non-attacking (magenta) sub-units. Image copyright D. Gopaul/Institut Pasteur.

Structural information exists for the canonical enzymes namely Cre recombinase [2]. However, the structural basis of integrase use of varying sequences and single stranded DNA was still a conundrum. In order to address the mechanism of this reaction we proceeded with the determination of the three-dimensional structure of the integrase VchIntIa from *Vibrio cholerae* in complex with a target *attC* site reconstituted from a folded bottom strand (VCR<sub>bs</sub>), by X-ray crystallography. The structure was solved from a seleno-methionine derivatised protein-DNA crystal, using the single wavelength anomalous dispersion technique, with data recorded at beamline ID14-4. The crystal structure revealed a tetrameric arrangement of enzyme monomers on DNA, with two protein molecules bound to each DNA site. The VCR<sub>bs</sub> DNA includes key base-pair mismatches which were found to orient the enzyme on its substrate

through specific recognition of the G20" base by a sandwich of conserved tryptophans (W157, W219), and of the T12" base by a stacking of histidines (H240, H241) and a proline (P232). The structure also explained the mechanism of regulation in the cleavage step whereby only a single cut is orchestrated in the complex due to the scaffolding of the  $\beta_{4,5}$  hairpin in *trans* across the synapse thus upsetting the positioning of the tyrosine in the non-attacking subunit (Figure 63). This data and other recent findings are providing information on the role of enzymes that use base recognition without performing chemistry on the base itself. Site directed mutagenesis of the protein as well as the DNA bases of the VCR<sub>bs</sub> followed by biochemical electromobility shift assays or *in vivo* recombination frequency measurements agree with the structural information. We are now in the process of approaching the *attI* x *attC* complex by similar methods.

The ability of bacteria to recombine incoming gene cassettes based on structural recognition elements instead of sequence information *per se* greatly enhances their ability to adapt to changing environmental conditions. This study opens the field to finding more efficient ways of limiting antibiotic resistance acquisition and spread, as well as new molecular tools for manipulating DNA.

### References

- [1] D.N. Gopaul, F. Guo, and G.D. Van Duyne, *Embo J*, **17**(14), 4175-87 (1998).  
 [2] F. Guo, D.N. Gopaul, and G.D. van Duyne, *Nature*, **389**(6646), 40-6 (1997).

### Principal Publication and Authors

D. MacDonald, G. Demarre, M. Bouvier, D. Mazel and D.N. Gopaul, *Nature* **440**, 1157-62 (2006).  
*Institut Pasteur, Paris (France)*

## A proton motive force driven peristaltic antibiotic pump

Multidrug resistance is a serious threat in the fight against cancer and microbial infections. This resistance is often associated with the overproduction of membrane transport proteins that are capable of extruding chemotherapeutics, antibiotics, detergents, dyes and organic solvents from the cell. Multiple-antibiotic resistant *Escherichia coli* strains have been shown to overproduce two proteins: the periplasmic fusion component AcrA and the resistance-nodulation-cell division (RND) type efflux pump AcrB. In conjunction with the outer membrane channel TolC, the tripartite AcrAB-TolC system transports drugs directly into the medium, bypassing the periplasmic space and outer membrane. We solved the crystal structure of the inner-membrane component AcrB as an asymmetric trimer and postulate a novel peristaltic pump mechanism for transport of antibiotics via a tunnel with alternating access.

Crystals grown in a trigonal space group, assigned as R32, yielded a symmetric structure of an AcrB trimer at 3.5 Å resolution [1,2]. However, we observed merohedral twinning of the crystals in this space group, which led us to pursue the structure from different crystal forms. Eventually we solved structures of trimeric AcrB determined at 2.9 and 3.0 Å resolution in space groups (C2, P1), which do not entail three-fold symmetry of the trimer. In contrast to the symmetric structure, this asymmetric structure reveals three different monomer conformations representing consecutive states in a

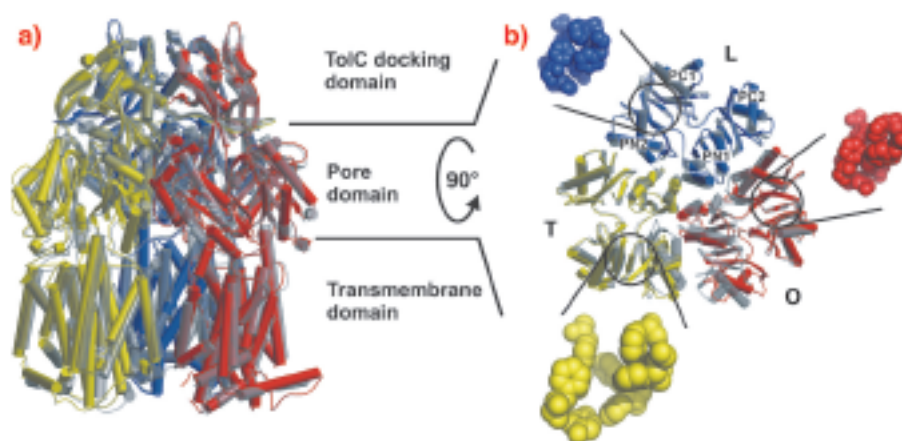


**Fig. 64:** Main structural differences of the AcrB monomers. The three AcrB monomers, shown in cylinder representation in blue (loose, L), yellow (tight, T) and red (open, O), are superimposed onto the symmetric AcrB trimer model [1,2], which is depicted in transparent grey. **a)** A side view superimposition of the entire AcrB asymmetric trimer (coloured) and symmetric AcrB (transparent grey). **b)** A top view superimposition of the pore domain of the asymmetric and symmetric AcrB trimer structure. The structural changes in the T monomer create a hydrophobic pocket (emphasised with yellow space-filled model) in the PN2/PC1 subdomain interface, which is closed in the L (blue) and O (red) monomers.

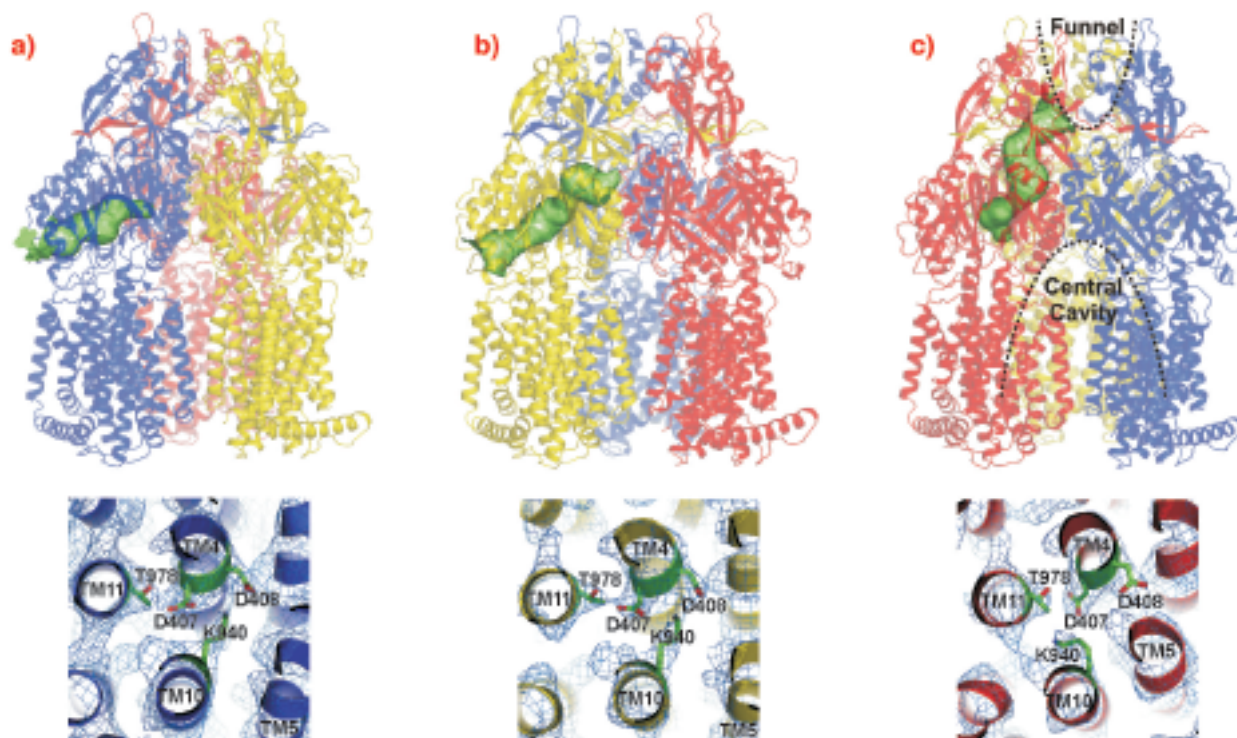


**Fig. 65:** Upper panel: Visualisation of the tunnels in the pore domain of the trimeric AcrB peristaltic drug efflux pump. The AcrB monomers are presented in **a)** blue (loose, L), **b)** yellow (tight, T) and **c)** red (open, O). The tunnels are highlighted as green surfaces in a ribbon model of the AcrB trimer. Lower panel: the putative proton translocation site with conserved residues D407, D408 (TM4) and K940 (TM10) in the three monomers is depicted as viewed from the cytoplasm with 2Fo-Fc electron density map contoured at 0.5  $\sigma$  (**a**) or 1  $\sigma$  (**b**, **c**) superimposed. In the L (**a**) and T monomers (**b**) the same conformation is observed, whereas in the O monomer (**c**) K940 forms a salt bridge with D407. This interaction seems to be stabilised by hydrogen bonding of T978 (TM11).

transport cycle, loose (L), tight (T) and open (O) (**Figure 64**). The structural changes in the T monomer create a hydrophobic pocket, which is not present in the other monomers. We assume that this pocket is a substrate binding pocket inside the pore domain.

The AcrB monomers show tunnels with occlusions at different sites leading from the lateral side through the pore domains towards the funnel of the trimer and TolC (**Figure 65**, upper panel). From these structures, we postulate a possible peristaltic pump transport mechanism based on a functional rotation of the trimer.

The large conformational changes observed in the periplasmic part of this protein coincide with more subtle changes in the transmembrane domain. In this domain of AcrB, TM4 and TM10 are surrounded by the other transmembrane helices of the monomer and harbour the residues K940 (TM10), D407 and D408 (TM4). As AcrB is energised by the proton-motive force, transient protonation of titratable groups within the transmembrane domain of the protein is probably the mechanism which delivers the energy required for the conformational changes described above. Indeed, we observe a prominent K940 (TM10) side chain reorientation away from D408 and towards D407 (both on TM4) in the O conformation (**Figure 65**, lower panel), and a bulging of

TM5 towards TM4 and TM10, strengthening the hypothesis that this part of the transmembrane domain is central to proton binding and release.

In conclusion, our model merges Jardetzky's alternate access pump mechanism with the rotating site catalysis of  $F_1F_0$ -ATPase and suggests a working hypothesis for the transport mechanism of RND transporters.

## References

- [1] S. Murakami, R. Nakashima, E. Yamashita and A. Yamaguchi, *Nature* **419**, 587-593 (2002).
- [2] K.M. Pos, A. Schiefner, M.A. Seeger and K. Diederichs *FEBS Lett.* **564**, 333-339 (2004).

## Principal Publication and Authors

M.A. Seeger (a,c), A. Schiefner (b), T. Eicher (a), F. Verrey (a), K. Diederichs (b) and K.M. Pos (a) *Science* **313**, 1295-1298 (2006).

(a) *Institute of Physiology and Zurich Centre for Integrative Human Physiology (ZIHP), University of Zurich (Switzerland)*

(b) *Department of Biology, University of Konstanz (Germany)*

(c) *Institute of Microbiology, Swiss Federal Institute of Technology (ETH), Zürich (Switzerland)*

## Crystal structures of the ribosome in complex with RNAs and release factors

The ribosome is the large (2.5 Megadalton) protein-RNA complex in the cell that makes proteins according to the sequence of codons (groups of 3 bases) present on the genetic template in the form of mRNA [1]. The process is extremely complicated and involves large tRNA substrates that bring in the amino acids to be added to the protein chain. Ribosomes consist of two subunits, the small (30S) which binds the mRNA template and the large (50S), which contains the active site for peptide bond formation between the incoming amino acid and the growing protein chain. These subunits undergo major conformational changes during translation and the tRNAs and mRNA move precisely through the ribosome in a remarkably precise and rapid process [2].

Following the solution of the atomic structures of both ribosomal subunits in 2000, the focus has shifted to crystallography of the ribosome in complex with its substrates in various states, in an effort to understand the detailed mechanism of translation. This process is difficult because it is hard to purify homogeneous complexes of a defined state that are stable enough to crystallise. Moreover, with such large complexes, most crystals do not diffract well. We have overcome this problem using a variety of techniques.

Release factors RF1 and RF2 recognise when the ribosome has reached a stop codon. In response to this

they trigger the release of the finished protein chain from the ribosome. However, it is not currently known how release factors can distinguish between the various stop codons or between them and other codons that code for amino acids. We “tagged” the release factors RF1 and RF2 and used the tag to separate fully assembled ribosomal complexes from defective ones. These complexes were crystallised and data collected at ID14-4 [3]. The structure (Figure 66) shows how a “GGQ” motif present on RF1 and RF2, that is thought to be required for cleavage of the peptide chain, is ordered in the catalytic centre of the 50S subunit. A loop thought to contain the motif that recognises stop codons is close to the position of the codon in the 30S subunit. These structures, at about 6 Å resolution, allowed accurate placement of the domains. We are currently trying to improve the resolution of the crystals so that we can see atomic details of these interactions.

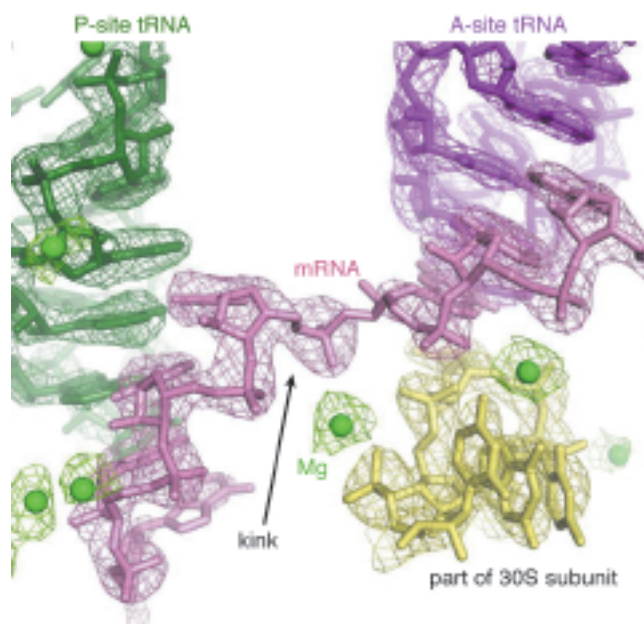


**Fig. 67:** Detail of a high-resolution structure of the ribosome complexed with mRNA and tRNA, showing electron density for a kink in the mRNA as well as metal ions (green spheres), one of which stabilises the kink.

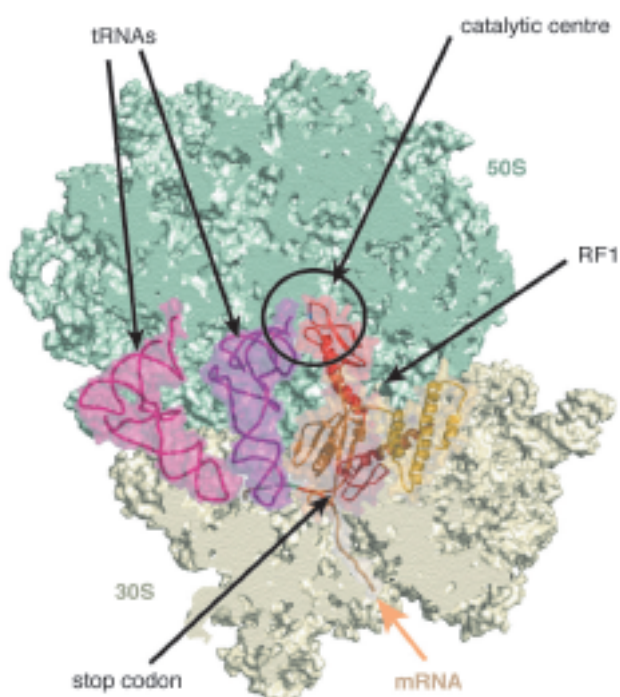


**Fig. 66:** A view of the structure of the ribosome with mRNA, tRNAs and release factor RF1.

Structures of functional complexes of ribosomes have remained at about 5-6 Å resolution for the past few years. At this resolution, it is possible to fit known structures or domains into electron density maps, but it is impossible to interpret unknown regions or reveal details of the chemical interactions in the molecule. We made a concerted effort to obtain improved crystals of the 70S ribosome in complex with mRNA and tRNA. This effort involved screening hundreds of crystals, both at Daresbury Laboratory and at the ID14 beamlines at ESRF, where the automatic crystal mounting robotics greatly facilitated the process. Eventually, we were able to identify an improved crystal form that allowed us initially to collect a 4.6 Å data set at ID14-4 and, after further improvement in crystallisation, a 2.8 Å data set at beamline X10SA at the SLS. This structure (Figure 67)

reveals atomic details of how the ribosome interacts with its mRNA and tRNA ligands, and also how metal ions play an important structural and functional role in the ribosome [4]. For example, metal ions are not only important to hold the structure together, they also form crucial elements of the “bridges” between the two subunits. Interestingly, a metal ion also stabilises a kink in the mRNA that helps to demarcate the difference between the sites for the tRNA that holds the growing protein chain (“P site”) and that which brings in the new amino acid (“A site”). We hope that this new crystal form will be useful for studying how various ligands and antibiotics bind to the entire ribosome in a defined state.

### References

- [1] V. Ramakrishnan, *Cell* **108**, 557-572 (2002).  
 [2] A movie that outlines this process can be seen at <http://alf1.mrc-lmb.cam.ac.uk/~ribo/movies/>  
 [3] S. Petry *et al.*, *Cell* **123**, 1255-66 (2005).  
 [4] M. Selmer *et al.*, *Science* **313**, 1935-42 (2006).

### Authors

M. Selmer, C.M. Dunham, F.V. Murphy IV, A. Weixlbaumer, S. Petry, A.C. Kelley, J. Weir and V. Ramakrishnan.  
 MRC Laboratory of Molecular Biology, Cambridge (UK)

## The crystal structures of the Dps1 and Dps2 from *Deinococcus radiodurans* reveal new metal binding sites

*Deinococcus radiodurans* (*Dr*) is an aerobic non-pathogenic bacterium able to withstand up to 10 kGy of ionising radiation whereas other organisms cannot survive a small fraction of this dose [1]. The *Dr* genome codes for two Dps (DNA protecting protein under starved conditions): *DrDps1* and *DrDps2* [1,2]. Their cellular functions are unknown but both proteins may function as iron storage proteins and have also been shown to bind DNA [2]. The combination of non-specific DNA binding with iron entrapment and detoxification is a strong

beneficial combination of properties that the Dps proteins provide for the protection of cells. The determination of the *DrDps* structures, in the presence and absence of iron, sheds light on how these proteins function.

Like other members of the Dps family, *DrDps1* and *DrDps2* assemble as hollow spherical dodecamers of symmetry P23 with an outer shell diameter of around 90 Å and an interior diameter of 40 Å. Ferroxidase sites, formed between monomers confer fast iron oxidation capability to Dps, which in turn prevent the formation of highly cytotoxic reactive oxygen species (ROS) from the reaction of free Fe(II) with hydrogen peroxide or dioxygen [3,4]. In the *DrDps2*-Fe structure, a distinct iron site is observed 6.1 Å from the ferroxidase centre, probably representing a bio-mineralisation intermediate.

*DrDps1* has a unique extended N-terminus where an unsuspected novel zinc binding site was identified (Figure 68). The N-terminal sequence also contains a number of positively charged residues and although the function of this sequence remains unclear, it is possible it functions as a metal sensor, or indeed interacts with DNA.

Two types of 3-fold related channels are thought to play a role in the transit of iron from the solvent to the ferroxidase centres. Clusters of negative electrostatic potential at the 3-fold N-terminal and C-terminal channels of *DrDps1* guide cations to the target sites.

*DrDps1* harbours a metal coordination site at the N-terminal side of the protein whereas in *DrDps2* the equivalent metal binding site is found in a pocket located near to the external edge of the C-terminus (Figure 69). The latter is a non-specific metal site suspected to play a regulative role in iron uptake or release from the protein. In fact, the 3-fold C-terminal channel of *DrDps2* can be thought of as an ion path able to control the flow of cations. The pathway is directed away from the centre of the 3-fold axis but passing through the metal site (Fe3, Figure 69). Under iron uptake conditions, iron can be captured at the external metallic site, followed by migration to the 3-fold axis channel and thereafter the centre of the protein. This is followed by iron capture by the ferroxidase centre and nucleation of the iron core.

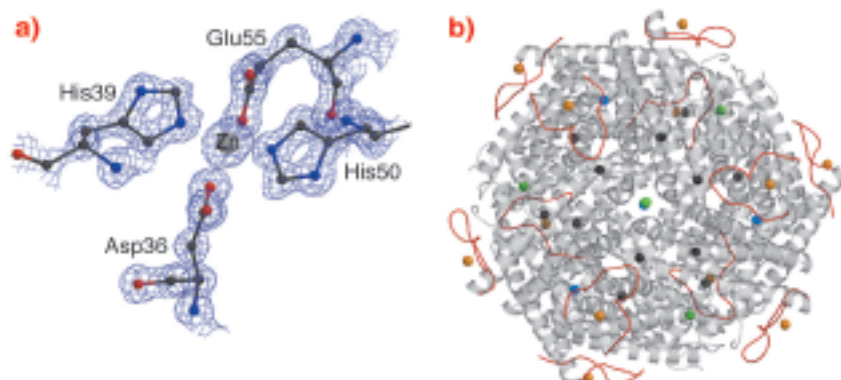


**Fig. 68:** a) The *DrDps1* Zn site at the external N-terminal extension of the protein dodecamer. The electron density map is contoured at 1.5σ. b) Spherical assembly of *DrDps1* showing the metal sites: the zinc atom on the N-terminal finger is in yellow, the other coloured spheres are iron.

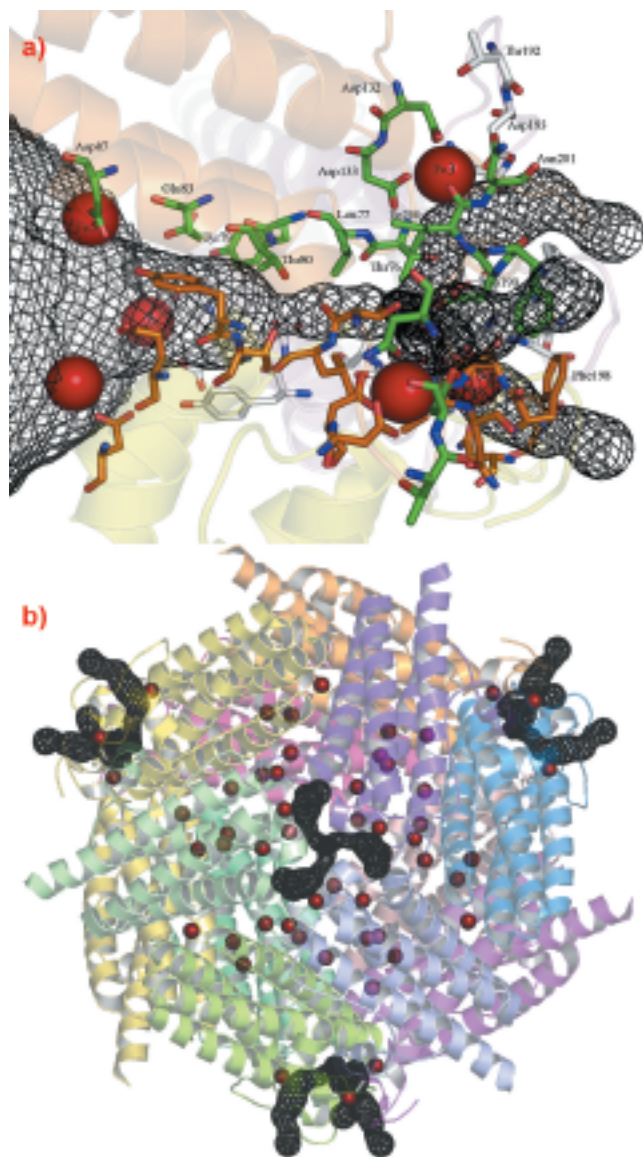


**Fig. 69:** a) The C-terminal pathway of *DrDps2* with annotated residues forming the channel. The red spheres on the right are in the lateral channel pathway. b) The spherical assembly of *DrDps2* showing iron locations. Each subunit is drawn in a different colour. The channel pathway in black isomesh is drawn with the plugin Caver for Pymol ([www.pymol.com](http://www.pymol.com)).

Ongoing work focuses on the implications of metal binding to the non-specific site on the outer part of *DrDps2* C-terminal channel, on the structural analysis of iron uptake and DNA interactions using small angle X-ray scattering and UV-visible spectroscopy.

#### References

- [1] O. White, J.A. Eisen *et al.*, *Science* **286**(5444), 1571-7 (1999).
- [2] A. Grove, and S.P. Wilkinson, *J. Mol. Biol.* **347**(3), 495-508 (2005).
- [3] K. Zeth, *et al.*, *Proc. Natl. Acad. Sci. U.S.A.* **101**(38), 13780-5 (2004).
- [4] P. Wardman, and L.P. Candeias, *Radiat. Res.* **145**(5), 523-31 (1996).

#### Principal Publications and Authors:

M.G. Cuypers (a), E. Mitchell (a), S. McSweeney (a) *et al.*, *J. Mol. Biol.* (in press); C. V. Romão (b) *et al.*, *J. Bio. Inorg. Chem.* **11**: 891-902 (2006).

(a) ESRF

(b) ITQB, Oeiras (Portugal)

## Sensing nickel to survive the acid bath

*Helicobacter pylori* is a resilient bacterium that colonises the human stomach. While most organisms would be killed instantly by the acidic pH (~1), the bacterium thrives and can settle down for years. Its presence can ultimately lead to the most severe gastric diseases, including gastric ulcers, chronic gastritis and stomach cancer. Central to the bacterium's ability to sustain such a low pH is the urease enzyme that rapidly detoxifies the environment of the bacterium by producing ammonia. The ammonia buffers the high proton content and enables *H. pylori* to enter the mucus layer. However, the urease enzyme requires huge amounts of nickel ions as a co-factor. This is a real dilemma for the bacterium since nickel can also be toxic at high concentrations. *H. pylori* has therefore developed a fine sensing mechanism that enables precise regulation of its nickel content, usage and storage.

The key element in this mechanism is the HpNikR protein (*H. pylori* Nickel Regulator), a transcription factor that binds specifically to DNA promoter sequences when nickel is present [1]. Although NikR proteins are present in most bacteria, their role is limited to the repression of nickel import when concentrations have reached dangerous thresholds. In *H. pylori*, HpNikR has multiple functions as it can repress expression of storage or import proteins as well as activating urease transcription depending on nickel concentration and/or pH value.

In collaboration with the Institut Pasteur, we have solved the structures of HpNikR in its apo form and in two different nickel-bound states (Ni1-HpNikR and Ni2-HpNikR) using data collected on ID14-1 and ID29. The structure of apo-HpNikR reveals that the protein has a fold similar to that of its *E. coli* homologue EcNikR [2] but adopts an unusual closed-*trans* conformation (Figure 70).

We compared the structure of apo-HpNikR with the Ni1-HpNikR and Ni2-HpNikR structures, obtained from crystals soaked in solutions containing Ni<sup>2+</sup> and identified the route of nickel uptake within the protein (Figure 71a). Mutagenesis and *in vivo* complementation studies confirmed that the amino acid residues identified by crystallography play an important role in HpNikR function. These studies therefore provide firm support for the nickel-sensing mechanism that enables

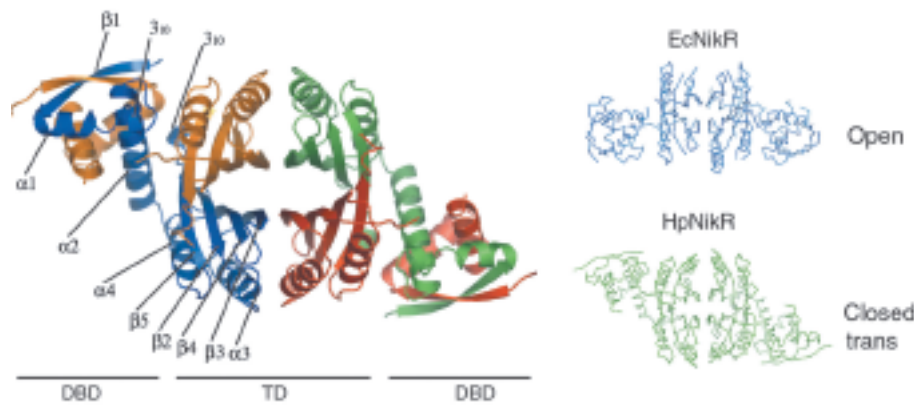


**Fig. 70:** Crystal structure of apo-HpNikR and comparison with its *E. coli* homologue, EcNikR .

the nickel response in *H. pylori* (Figure 71b). A close examination of the structures showed that Ni<sup>2+</sup> entering HpNikR leads to an opening of the tetramerisation interface. The resulting movement is echoed via stacking interactions between the  $\alpha 3$  and  $\alpha 4$  helices and the  $\alpha 1\alpha 2$  loops (Figure 71c). This affects other secondary structure elements involved in the DBD/TD interface. Moreover, when nickel is fully transported, the involved  $\alpha 3$  helices close down the interface (Ni1-HpNikR) and modify the position of the DBDs.

Together with previous studies, our findings provide insight into the structural basis of the nickel response in NikRs. We hypothesise that nickel transport in HpNikR involves three separate binding steps moving the Ni<sup>2+</sup> from an external site via an intermediate site to its final high affinity site using coordinated movements of the side chains of crucial amino acids. The passage of four Ni<sup>2+</sup> ions (one per monomer) via this route affects the dynamics of the DBDs of HpNikR which results in an active (DNA binding) form of the tetramer. Slight differences in primary sequence between HpNikR and

EcNikR result in subtle changes in structure that could explain how the two proteins have different functions. For instance, occupation of a low affinity Ni<sup>2+</sup> site present in EcNikR may not be necessary for the activation of urease transcription by HpNikR. This study firmly establishes that HpNikR is a modified, evolution driven shaped nickel sensor protein, structurally adapted to provide flexible sensor mechanisms.

**References**

[1] N.S Dosanjh, and S.L. Michel, *Curr Opin Chem Biol* **10**, 123-130 (2006).  
 [2] E.R. Schreiter, M.D. Sintchak, Y.Guo, P.T. Chivers, R.T. Sauer, and C.L Drennan, *Nat. Struct. Biol.* **10**, 794-799 (2003).

**Principal Publication and Authors**

C. Dian (a), K. Schauer (b), U. Kapp (a), S. McSweeney (a), A. Labigne, (b), and L. Terradot, (a), *J. Mol. Biol.* **361**, 715-730 (2006).  
 (a) *ESRF*  
 (b) *Institut Pasteur (Paris)*

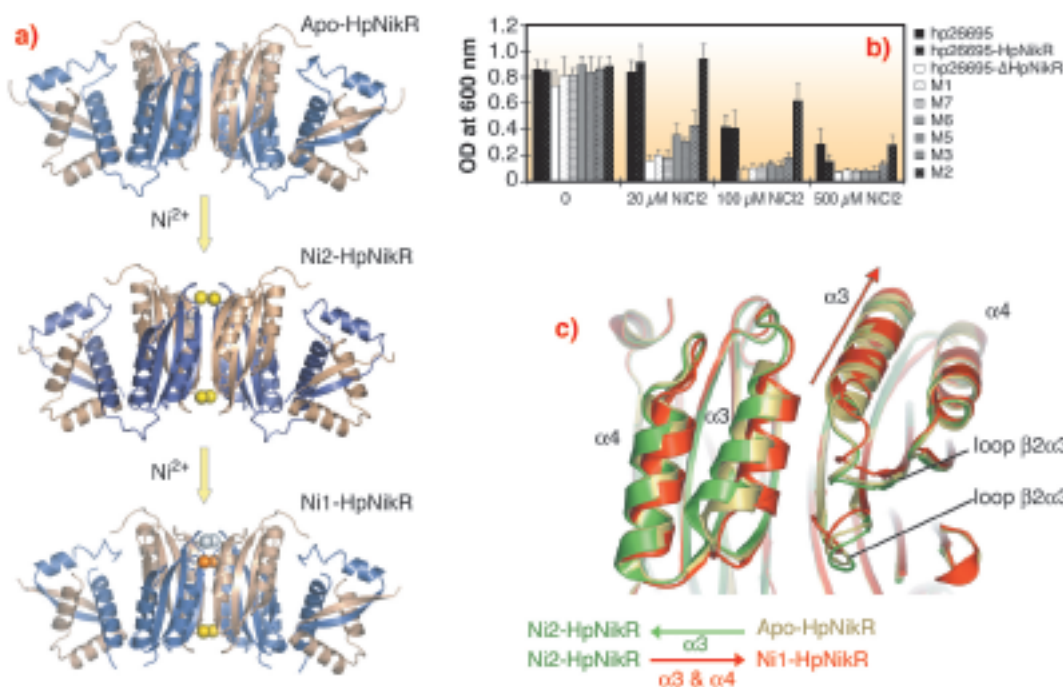


**Fig. 71:** a) Ribbon representations of the crystal structures of HpNikR, in apo and nickel bound states obtained with different nickel concentrations. b) Mutational analysis of HpNikR during the acidic response. Structure based mutants were generated and cell viability was monitored upon increasing amount of nickel in the media. Clearly, mutation of residues involved in the nickel entrance in the crystal structure significantly reduce the survival of *H. pylori* cells. c) Ribbon representation of the movements generated by nickel incorporation in HpNikR.

## The ID23-2 Microfocus Beamline

Users of Macromolecular Crystallography (MX) beamlines regularly analyse crystals that are smaller than 50  $\mu\text{m}$  and the tendency is towards even smaller, micro-sized samples. Quite often there is a need to analyse multiple rather than single crystals. One of the reasons for this is that increasingly challenging projects may only give tiny crystals. Additionally, increasing competition among structural biology groups demands a reduction in the time from project inception to structure publication and adequate time to optimise the production of crystals is not always available. To enable the MX user community to collect good quality data from such samples, synchrotron sources around the world are opening beamlines with so-called microfocus X-ray beams. These beamlines, of which ID13 at the ESRF was one of the pioneers, allow the collection of diffraction data with the X-ray beam matched to micro-sized crystals and also allow the ‘searching’ of poor quality crystals to find a portion suitable for the collection of good quality diffraction data.

In July 2001, the ESRF took the decision to build ID23. This beamline has two end-stations that operate as independently from each other as is reasonably possible. ID23-1 is a fully tunable MAD beamline. ID23-2 is the first microfocus beamline fully dedicated to MX and builds on the experience gained at ID13. The central challenge for ID23-2 was to provide the MX user community with a beamsize smaller than 10  $\mu\text{m}$  in diameter whilst keeping the same “easy-to-use” environment and reliability as the other ESRF MX beamlines (ID14, ID23-1, ID29).

The X-ray source for ID23 is a canted undulator system comprising two undulators with a radial separation of 1.5 mrad. A canted undulator design was chosen to enable the installation of two end-stations on a single straight section, whilst retaining a maximal independence of beamline operation. For microbeam work to be routine, the beamline must be highly stable. To help achieve this, the optical setup of ID23-2 is as simple as possible and is composed only of high power primary slits, a ‘single bounce’ silicon monochromator, a set of secondary slits and the Kirkpatrick-Baez (KB) focussing element. The KB architecture is an easy-to-use system providing fine focussing. The ID23-2 device, housed in a steel container under helium gas, is composed of two 300 mm long Pt coated Si mirrors positioned 2 m from the sample. This results in a beam size of 7.5 by 5.5  $\mu\text{m}^2$  (FWHM). The user environment is that of a standard MX beamline comprising a single-axis minidiffractometer and sample changer in the ID23-2 experimental hutch, together with the ancillary cryostream, attenuators, shutter, etc.

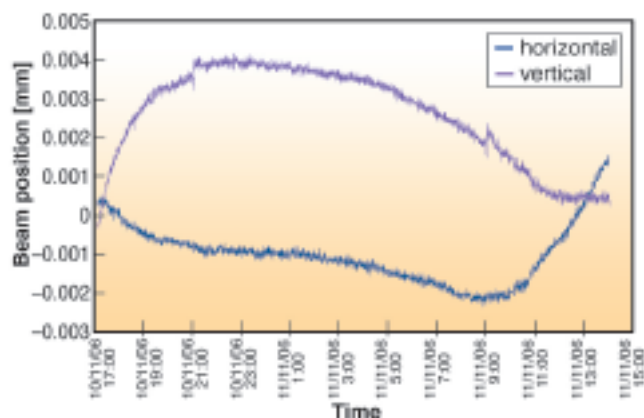


**Fig. 72:** The variation in vertical (magenta) and horizontal (blue) beam position on ID23-2 as a function of time. The slow drift observed is easily corrected before each data collection.

Maintaining a beam focus of less than 10  $\mu\text{m}$ , whilst keeping the beam centred precisely on the same section of a sample is challenging. At this scale, beam movements result from even small changes in ambient temperature. Indeed during initial beamline commissioning, beam drifts in the range of 15  $\mu\text{m}$  over 12 hours were measured. Monitoring of the beam position and hutch temperature as a function of time showed that vertical beam drifts were correlated with a variation in the hutch temperature while horizontal drifts correlated with both hutch and monochromator motor temperature. Consequently, the KB chamber has been surrounded by a perspex box to improve its insulation from temperature changes. Beam drifts have been reduced to less than 5  $\mu\text{m}$  over a 20 hour period (Figure 72) and we are working to reduce this further. To be 100% sure of the beam alignment, a pop-up fluorescent screen is available at the sample position allowing users to check the beam position before data collection starts. Beamline ID23-2 has been in standard operation for more than a year and has proved that microbeam X-ray diffraction can be made routine.

Many projects have benefited from the availability of a microfocus beam. In one case, after many attempts, only long needle-shaped crystals of IREM 1 [1] could be obtained from crystallisation screening carried out at the High Throughput Crystallisation Laboratory (HTX Lab) of the EMBL Grenoble Outstation. Therefore, the scientists turned to ID23-2 to collect X-ray data from this single long needle crystal, which was 300 by 10 micrometres in size (Figure 73). Due to the high intensity of the ID23-2 X-ray beam, radiation damage was evident after only a few degrees of data had been collected, hence successive partial datasets were collected from four different sections of the same crystal and subsequently merged. This made it possible to obtain the crystal structure of the IREM-1 extracellular domain to 2.6 Å resolution [2].

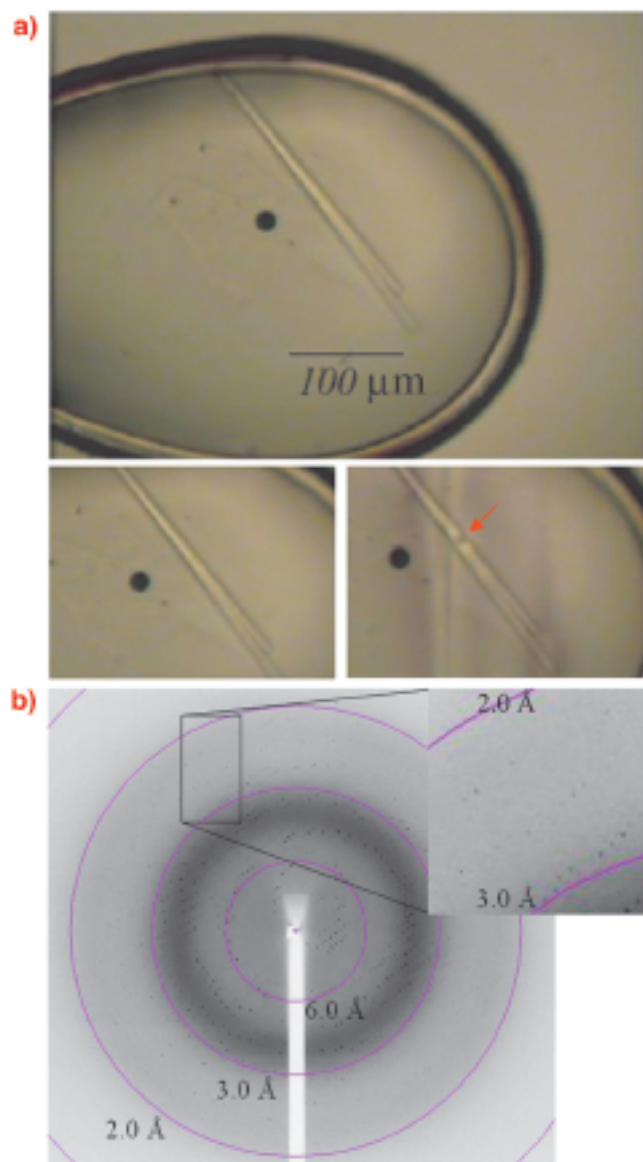


**Fig. 73:** The IREM -1 crystal (top) used for collecting the dataset described in the text. The diffraction pattern (bottom) was collected by exposing the portion of the crystal shown in the middle, right plate of this figure.

#### References

- [1] The inhibitory receptors expressed on myeloid cells (IREM) are type I transmembrane proteins encoded on human chromosome 17 (17q25.1), whose function is believed to be important in controlling inflammation. IREM-1 functions as inhibitory receptor, whereas IREM-2 and IREM-3 serve an activating function.
- [2] Dimasi *et al.*, *Acta F*, submitted.

#### Authors

D. Flot (a), T. Mairs (b), T. Giraud (b), M. Guijarro (b), V. Rey (b), D. van Brussel (b), P. Fajardo (b), O. Hignette (b), J. Chavanne (b), J.-C. Biasci (b), S. McSweeney (b), E. Mitchell (b).

(a) EMBL Grenoble Outstation (France)

(b) ESRF

## X-ray radiation-induced damage in DNA monitored by online Raman spectroscopy

The interaction of biological tissue with ionising radiation such as X-rays, electrons and  $\gamma$ -rays causes damage initiated by free radicals. Much effort has been invested in trying to understand the mechanisms involved, in particular for DNA, but these are still not well understood. It would therefore be of great interest if we could obtain new insights into the detailed structural consequences of early events of radiation damage to DNA.

Raman spectroscopy is a powerful technique capable of providing detailed information about the chemical nature of individual bonds. Due to the intricate molecular makeup of proteins and nucleic acids, the resulting Raman spectra are correspondingly complex. However, when the technique is adapted to crystals of biological macromolecules it offers distinct advantages compared to solution studies [1]: such crystals contain a 10 to 100 fold higher concentration of the macromolecule and have a relatively low solvent content. This improves the Raman signal-to-noise ratio substantially. Crystal packing forces, which reduce high-order movements, result in an increased resolution of Raman bands.

Recent technical advances in Raman spectroscopy include the advent of CCD detectors sensitive in the red-light region, thus avoiding luminescence at lower excitation wavelengths, and precision holographic notch filters to remove elastically-scattered photons. It is now possible to measure detailed backbone orientations, ring torsions and individual bond chemistry in nucleic acids. Here we employ Raman spectroscopy as a means to probe detailed chemical events during MX data collection.

A Raman spectrometer was adapted for use on a goniometer either at the cryobench laboratory [2] or on MX beamlines at the ESRF. Raman spectra of high-quality could be reproducibly collected from single DNA crystals kept at 100 K in a flow of cold nitrogen gas. Collection of non-resonant Raman spectra from native, single- and dibrominated DNA crystals allowed the unambiguous identification of the non-symmetric bending vibration for C-Br bonds in 8-bromo-2'-deoxyguanosine at  $293\text{ cm}^{-1}$ . Following these studies, Raman spectra were collected using the online setup at **ID14-2** on a single dibrominated crystal before and after X-ray exposure. Debromination was clearly visible with the loss of the  $293\text{ cm}^{-1}$  band corresponding to what

was observed with MX at a similar dose (Figure 74). Comparison of spectra before and after exposure demonstrates multiple vibrational changes corresponding to specific X-ray induced damage sites in the DNA.

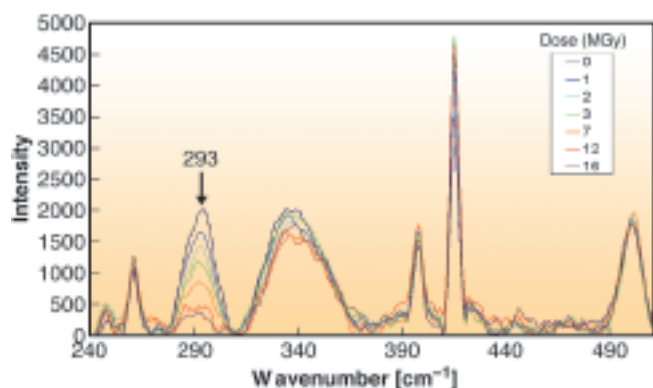


**Fig. 74:** Real-time Raman online monitoring of a dibrominated DNA crystal during continuous X-ray exposure at beamline ID14-2. Debromination can be followed using the decay of the 293  $\text{cm}^{-1}$  band as a function of dose.

A series of Raman spectra were collected whilst a stationary dibrominated DNA crystal was exposed to the X-ray beam. X-ray induced debromination was monitored in real-time as a function of dose. A decay constant of 7.1 MGy was obtained fitting the curve with a single exponential. Transient chemical changes could also be measured. A series of X-ray diffraction datasets were collected on a similar dibrominated DNA crystal on **ID14-4**. The decay of the electron density for the bromine atoms as a function of dose was analysed with the program SHARP. This allowed dose-dependant occupancy refinement which could also be fitted to a single exponential, correlating with the Raman studies.

Our initial online Raman studies have provided an independent observation of the susceptibility to radiation damage of halogenated nucleotides. We are now in the process of analysing the wealth of information available in the Raman spectra to further investigate the very fine details of the chemistry that takes place when X-rays ravage important (native) biomolecules.

#### Reference

- [1] P.R. Carey, *Annual Review of Physical Chemistry* **57**, 527-554 (2006).  
 [2] <http://www.esrf.fr/UsersAndScience/Experiments/MX/Cryobench/Instruments/raman>

#### Principle Publication and Authors

J.E. McGeehan (a), P. Carpentier (b), A. Royant (b), D. Bourgeois (b), and R.B.G. Ravelli (a), *Journal of Synchrotron Radiation* **14**, 99-108 (2007).  
 (a) EMBL, Grenoble Outstation (France)  
 (b) Institut de Biologie Structurale, CNRS/CEA/UJF, Grenoble and ESRF (France)

## Crystal structure of human cytochrome P450 2D6

Cytochrome P450 2D6 is a haem-containing enzyme which catalyses the metabolism of at least 20% of known drugs. It exhibits considerable genetic polymorphism, affecting the rates of metabolism of some important drug molecules. Substrate metabolism is achieved by activation of molecular oxygen by the haem group in a process involving the delivery of two electrons to the P450 system followed by cleavage of the dioxygen bond to give an activated iron-oxygen species. This can then react with substrates. 2D6 typically recognises substrates containing a basic nitrogen and an aromatic ring - features which are especially found in a large number of central nervous system and cardiovascular drugs.

We determined the crystal structure of 2D6 to a resolution of 3.0 Å using data collected on ESRF beamline **ID23-1**. Crystallisation was carried out using a novel free interface diffusion technique, leading to rectangular plates with maximum dimensions of about 80 x 20 x 10  $\mu\text{m}$ . The crystals suffered from considerable radiation damage during data collection and it was necessary to build up a complete dataset using data from multiple crystals. The structure was solved by molecular replacement, with the crystal asymmetric unit containing four 2D6 molecules, related by 222 symmetry.

The 2D6 molecule has the characteristic P450 family fold (Figure 75), with the lengths and orientations of the individual secondary structural elements being very



**Fig. 75:** A ribbon diagram of the 2D6 structure.  $\alpha$ -helices are shown in blue,  $\beta$ -strands in mauve. The haem group is shown in ball and stick representation.

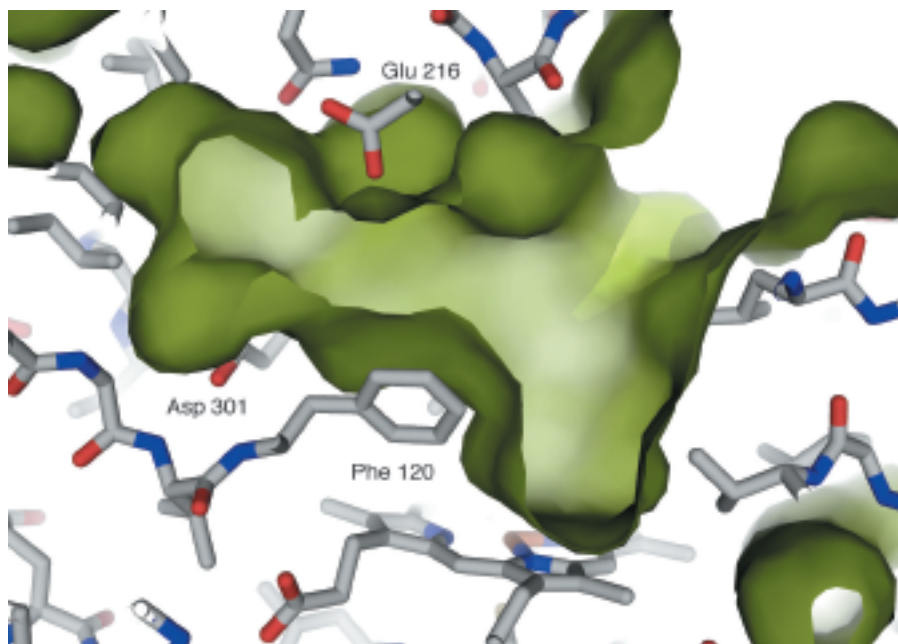


**Fig. 76:** The active site cavity above the haem group. Some key residues are labelled.

similar to those of the related 2C9 isozyme. There are, however, six main areas where large differences exist, several of which are directly involved in defining the shape and character of the 2D6 active site. There is a well-defined cavity above the haem group (**Figure 76**), bordered by many important residues previously implicated in substrate recognition and binding. The structure helps to explain how two of these residues, Asp301 and Glu216, can act as substrate binding residues and suggests that the role of Phe120 is to control the orientation of the substrate's aromatic ring above the haem. The structure has also allowed an explanation of much of the published site-directed mutagenesis data and has helped in understanding the metabolism of several compounds, including the antihypertensive drug debrisoquine. Future structures of 2D6 with bound substrates and inhibitors will clarify the details of ligand recognition, and provide a structural basis for studying the effects of different 2D6 polymorphs on substrate metabolism.

#### Principal Publication and Authors

P. Rowland, F.E. Blaney, M.G. Smyth, J.J. Jones, V.R. Leydon, A.K. Oxbrow, C.J. Lewis, M.G. Tennant, S. Modi, D.S. Eggleston, R.J. Chenery and A.M. Bridges, *J. Biol. Chem.* **281**, 7614-7622 (2006).

*Molecular Discovery Research Department, GlaxoSmithKline (UK)*

## Molecular envelopes from protein powder diffraction data

Deriving the crystal structure of protein molecules has been one of the key advances in understanding biology on the atomic length scale. The complexity of these molecules is so great that often several datasets must be used in combination to solve the crystallographic phase problem. In these cases, by carefully measuring the differences in diffracted intensities between different crystals, some containing additional heavy atoms, a sub-structure consisting of the positions of the added heavy atoms can often be found. Approximate values of the crystallographic phases can be computed from the heavy atom positions and observed intensities, leading to an electron density map.

Until recently, protein structures seemed to be too large to tackle using powder diffraction methods. Nevertheless, it is very appealing to be able to determine protein structures without having to produce large single crystals! Since the possibility of refining protein structures from powder data has already been shown [1], and that powder data can be used to solve simple molecular replacement problems [2], we wondered whether powder data would also be good enough for the *de novo* phasing of macromolecular structures.

Powdered samples of heavy atom derivatives for two model systems were prepared: uranium-derivatised porcine pancreatic elastase and chicken egg white lysozyme derivatised with a gadolinium complex (Gd-

Hp-Do3A). High resolution powder diffraction data were collected at the beamlines ID31 and BM01. Comparison of these data with those collected from native samples shows small shifts in lattice parameters and changes in peak intensities indicative of the binding of the heavy atoms. Integrated peak intensities were extracted from the powder profiles and supplied for processing with software originally developed for single crystal data. In order to combat the peak overlap problem, multiple datasets were combined to exploit anisotropic lattice changes which lead to peak shifts between different diffraction patterns. For elastase these peak shifts were caused by radiation damage and for lysozyme they were induced by using samples prepared at different pH values.

In the case of elastase, the position of the uranium atom could be found from a difference Patterson map (Figure 77). The gadolinium positions in the lysozyme sample were found using the SHELXD software. In both cases the heavy atom positions found from powder data are fully consistent with earlier single crystal studies.

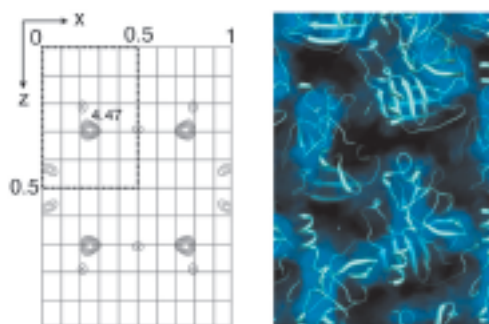


**Fig. 77:** Difference Patterson map (left) and solvent mask (right) for the porcine pancreatic elastase [3].

Once the heavy atom positions had been determined, they were refined and phase calculations carried out using the SHARP software. Since there was only a single heavy atom derivative in each case, there is still an ambiguity in the determination of the phase. SHARP employs statistical methods and density modification techniques to resolve this.

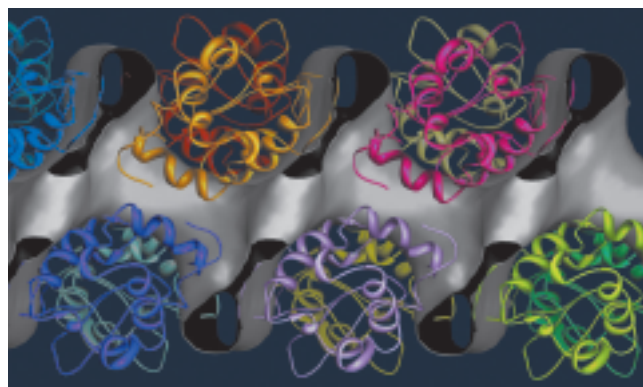


**Fig. 78:** Solvent channel in lysozyme superimposed with the molecular structure.

Electron density maps are produced at the end of the phasing procedure, as well as a solvent mask which delineates the regions of the unit cell occupied by protein and solvent respectively. Inspection of these maps indicates that the phasing procedure has been successful with a clear identification of the correct solvent boundaries within the unit cell (Figure 77 and Figure 78). Quantitatively, the derived phases show a good correlation with the true values up to a resolution of around 6 Å, indicating that using powder data in this way is still a relatively low resolution technique. Improvements in this area are anticipated with the development of phasing methods which take into account peak overlap in the powder data.

#### References

- [1] R.B. Von Dreele, *J. Appl. Cryst.* 32, 1084-1089 (1999).
- [2] I. Margiolaki, J.P. Wright, A.N. Fitch, G.C. Fox and R.B. Von Dreele, *Acta Cryst.*, D61, 423-432 (2005).
- [3] C. Besnard, F. Camus, M. Fleurant, A. Dahlström, J. P. Wright, I. Margiolaki, P. Pattison M. Schiltz. *Z. Krist Submitted.*

#### Principle publication and authors

J.P. Wright (a), C. Besnard (b), I. Margiolaki (a), S. Basso (a), F. Camus (b), A.N. Fitch (a), G. Fox (a), P. Pattison (a,b) and M. Schiltz (b), *To be submitted.*

(a) ESRF

(b) Laboratoire de Cristallographie, École Polytechnique Fédérale de Lausanne (EPFL) (Switzerland)



Highlights 2006

SCIENTIFIC HIGHLIGHTS

# Surface and Interface Science

## Introduction

The year 2006 has been both eventful and productive for surface and interface science (SIS) at the ESRF. Beamline ID03 came back on line after roughly one year of rigorous refurbishment and rebuilding. For twelve years ID03 has been a benchmark beamline for surface X-ray diffraction (SXR). To continue serving the European surface X-ray diffraction community with the same level of excellence, an upgrade of the beamline was necessary. Now, two large hutches are available for experimental equipment. The first (EH1) houses a vertical axis 2 + 2 diffractometer, dedicated to surface characterisation during heterogeneous catalytic reactions. A batch reactor with a gas handling system is also available to users. The second hutch (EH2)

houses a horizontal axis diffractometer coupled with a (refurbished) UHV chamber for *in situ* surface preparation and growth. There is also a surface magneto-optic Kerr effect setup for the characterisation of magnetic thin films.

The beamline is windowless up to the experiment and served by three 11 mm gap undulators. The first optical element is a highly stable, cryogenically cooled, monolithic Si(111) double-crystal monochromator, optimised for 5 to 24 keV. Horizontal focussing is performed by a cylindrical mirror with variable bending radius. A second flat mirror keeps the beam horizontal. Both mirrors in the first optics hutch are palladium coated, delivering a flux exceeding  $10^{13}$  ph/sec (at 200 mA) to a spot size of  $45 \times 35 \mu\text{m}^2$  (H x V),

which corresponds to a three-fold increase of the flux at the sample in both experimental stations. A short focal length Kirkpatrick-Baez (KB) focussing system allows spot sizes in the  $\mu\text{m}$  range on the samples.

The “resurfaced” ID03 beamline (Figure 79) is now not only suited to surface crystallography but also allows *in situ* GISAXS studies, coherent surface diffraction, and anomalous scattering experiments owing to the non-dispersive focussing elements, thus providing new opportunities in surface science. Increased flux as well as increased speed of the diffractometers and data acquisition should allow users to study time-dependent phenomena, e.g. during heterogeneous catalysis under real conditions.



**Fig. 79:** The refurbished ID03 beamline: **a)** Vertical axis diffractometer in EH1 to accommodate small sample environments. The KB system in the foreground focuses down to the micrometre range. **b)** Horizontal axis diffractometer with UHV chamber for *in situ* preparation and growth in EH2.

The other beamlines of the SIS group, ID01 and ID32 have not been idle either. The beamline review panel acknowledged the success and productivity of ID01. This beamline is now continuing its path under full steam towards new applications using microfocussing and coherent scattering. The staff of ID32 has commissioned a new primary monochromator, which improves flux, versatility, reliability, and beam quality for the two stations (SXR and XSW/XPS) at the beamline.

The three insertion device beamlines ID01, ID03, and ID32 of the SIS group, with about 50% (ID01) and 90% (ID02 and ID32) of their beamtime scheduled for SIS experiments represent the SIS specialists together with the French CRG beamline BM32 (70% SIS). However, more than 80 SIS proposals are typically received each proposal round and roughly 50% of all beamlines end up on the list of the SIS beamtime allocation panel. Thus, besides reports originating from the usual culprits, these SIS highlights also feature contributions from the French-CRG beamline BM02 (typically 40% SIS) and the UK-CRG beamline BM28 (typically 20% SIS).

Continuing the trend of the last years, the SIS highlights are dominated by non-classical SIS.

While experimental work in the area of classical SIS such as surface crystallography is certainly continuing, it has become routine and the study of some new surface structure is no longer guaranteed to create much excitement, unless there is some interesting twist. "Runts", no wimpy dwarfs, but nicely "rolled-up-nanotubes", are in fact twisted enough. In the first contribution, the detailed analysis of these nifty structures at ID01 is reported. This is followed by another ID01 experiment: the diffraction analysis of nanodot pattern produced by ion sputtering. The third contribution is also about nanoscience and in this case the analysis of the influence of capping layers on the structure of quantum GaN dots was investigated by anomalous diffraction at BM02.

The next section contains two contributions about the investigation of thin films:  $\text{Pr}_2\text{O}_3$  on Si(001) was grown in the surface characterisation laboratory of ID32.  $\text{Pr}_2\text{O}_3$  is a possible candidate to replace  $\text{SiO}_2$  in the CMOS devices and the structure of the Si(001)/ $\text{Pr}_2\text{O}_3$  interface has been scrutinised at ID32 using a wide range of surface science techniques. Shallow implanted As layers in Si, likewise important for future devices, were investigated at ID01 by diffuse scattering, and a report is given in the second contribution.

Three contributions belong to the field of surface chemistry: The *in situ* X-ray analysis of the homoepitaxial growth of gold from electrolyte was performed at ID32. The structure and reactivity of a PtRh alloy catalyst under real catalytic conditions was investigated at ID03. The surface chemical aspects of cultural heritage artefacts were investigated at BM28 with the aim of finding ways of protecting such priceless items from decay.

Finally, the last contribution reports about a seemingly impossible investigation of the magnetic semiconductor GaMnAs, *i.e.*, identifying the detailed lattice site distribution of Mn at very low concentration of 4% in a just 4 nm thick GaAs film. The XSW imaging technique allows one to "see" the majority of Mn on Ga substitutional sites and data refinement gives the exact quantity (< 10%, depending on post-growth treatments) of Mn on the (magnetically inactive) As interstitial site.

We think that these contributions provide an impressive account of the range of investigations in surface and interface science today and we hope that you will enjoy the reading.

**J. Zegenhagen**

# Small is beautiful: nanostructures

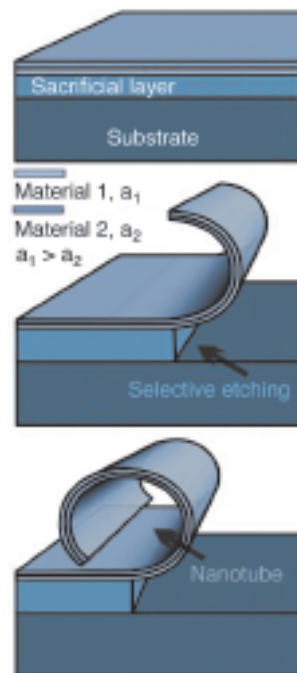
## Local structure of a rolled-up single crystal nanotube

Crystals with cylindrical symmetry, which do not exist in nature, are mimicked by the roll-up of single crystalline and highly pseudomorphically strained GaAs/InGaAs semiconductor bilayers. The resulting objects, the rolled-up nanotubes (RUNTs) [1], are depicted in **Figure 80**.

We established a method to find and measure individual single nanotubes coherently connected with the substrate. Their structure was probed and quantified non-destructively by X-ray microbeam diffraction. Varying the composition and thicknesses of the layers allows tailoring of the tube formation and properties. As an example, results for three different layer thicknesses (thus yielding different tube diameter) are shown in **Figure 81** (left).

For all samples measured, the crystalline bilayer is still present in the RUNTs as proved by the observation of two well-separated Bragg peaks: one peak close to the bulk GaAs position (marked as C in **Figure 81 (a-c)**); and another between the strained InGaAs position A, found in the as-grown film perpendicular to the substrate, and the completely relaxed position B, *i.e.* the InGaAs lattice parameter expected from Vegard's law. This

**Fig. 80:** Formation principle of the rolled-up nanotubes.



intermediate position of the InGaAs peak shows that the individual layers only partially relax since both of them exert strain on each other.

With increasing GaAs layer thickness, the intensity ratio between the GaAs and the InGaAs peak increases. The shape of the peaks is determined by the interference of the X-rays scattered by both layers. From the comparison to simulations based on the minimisation of the elastic energy, we determined in a non-destructive way the layer thicknesses, the lattice parameter distribution (both along the tangential direction,  $a_t$  and along the radial direction,  $a_r$ ) and strain within the rolled-up single crystalline bilayer. The continuum elasticity theory proved to be applicable even for layers as thin as 10 nm and allows us to understand their formation in full agreement with the experimental data (for more details see the publication).

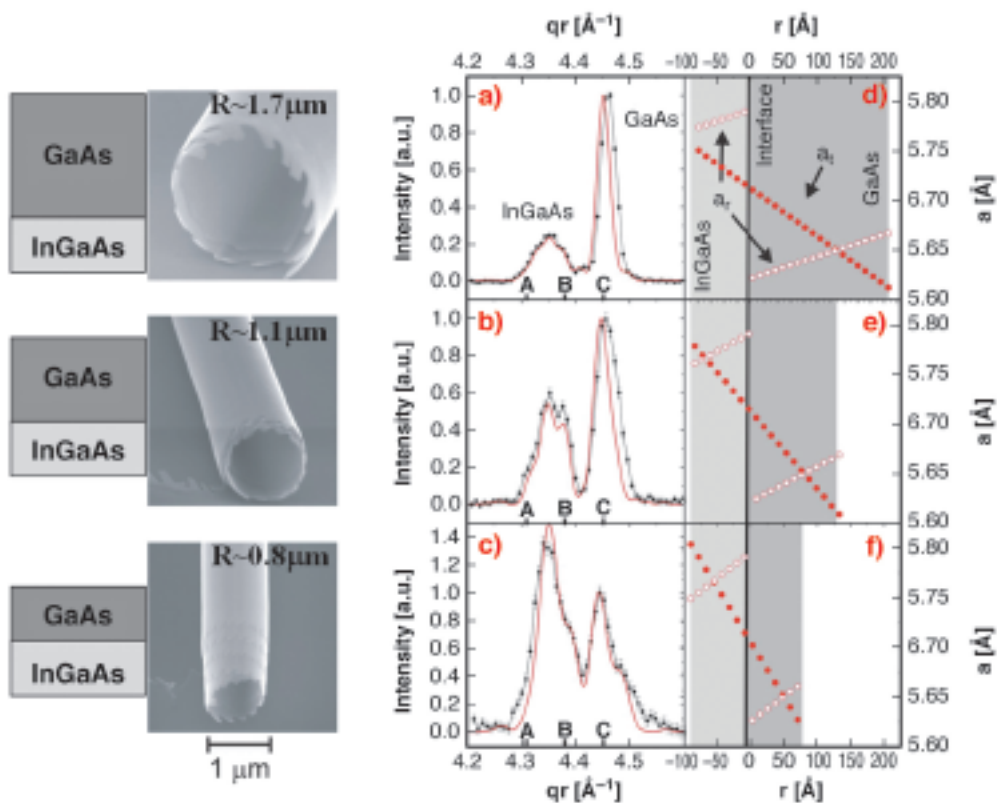


**Fig. 81:** (left) Schematic view of the bilayer and SEM images of the resulting nanotubes ( $R$  is the tube diameter); (a-c) Intensity distribution, normalised to the GaAs (004) reflection. The experimental data are shown as black dots, the simulations as red lines. (d-f) simulation results of the data before: lattice parameter distribution in tangential direction ( $a_t$ , filled symbols) and in radial direction ( $a_r$ , open symbols) as function of the distance  $r$  from the interface ( $r = 0$ ) between the GaAs and InGaAs layers in the bilayer.

Such objects show a great potential as integrative components, including 2D confined channels for fluid filling and transport, coils, transformers, capacitors, or (optical) wave guides [2].

### References

- [1] V.Y. Prinz *et al.*, *Physica (Amsterdam)* 6E, 828 (2000); O.G. Schmidt, K. Eberl, *Nature (London)* 410, 168 (2001).  
 [2] C. Deneke, O.G. Schmidt, *Appl. Phys. Lett.* 85, 2914 (2004); O.G. Schmidt *et al.*, *IEEE J. Sel. Top. Quantum Electron.* 8, 1025 (2002); S. Mendach *et al.*, *Appl. Phys. Lett.* 88, 111120 (2006).

### Principal Publication and Authors:

B. Krause (a,\*), C. Mocuta (a), T.H. Metzger (a), Ch. Deneke (b) and O.G. Schmidt (b), *Phys. Rev. Lett.* 96, 165502 (2006).

(a) ESRF

(b) Max-Planck-Institut fuer Festkoerperforschung, Stuttgart (Germany)

(\*) now at Carl Zeiss GmbH (Germany)

## Temperature influence on silicon nanodot pattern formation by ion-beam sputtering

The production of semiconductor nanostructures has awakened great interest due to their application in opto- and microelectronic devices. This has motivated intense research on new nanofabrication routes to further reduce feature size, which is of special importance for silicon due to its use in current semiconductor technology.

On the way to further miniaturisation, self-organisation methods are emerging as a promising approach, where nanoscale units are building-blocks that auto-assemble in meso- and macro-structures. Among these methods, ion beam sputtering (IBS), *i.e.* removal of atoms from the surface by ion impingement, has proven to be a competitive option for surface nanostructuring [1]. In a fast and convenient way, large areas of either metals, semiconductors or insulators, can be patterned in well-defined ways by choosing the proper IBS parameters. Typically, ripple or nanodot patterns are induced on semiconductor surfaces at off-normal and normal ion incidence, respectively. Theoretically, the formation of such patterns by IBS can be described from the balance between surface smoothing processes and an instability induced by the dependence of the sputtering yield on the local surface curvature.

Among the relevant IBS parameters, temperature can play a significant role in the nanostructuring process by governing diffusion processes. In contrast with other variables, temperature has not been extensively studied experimentally in the case of IBS nanodot patterns. This

has motivated our study of pattern formation on Si(001) surfaces. The patterns were produced by 1 keV Ar<sup>+</sup> at normal incidence (for more details, see Ref. [2]) in the 300-625 K range and the resulting surface topography was imaged by atomic force microscopy (AFM) (Figure 82a). The nanodot pattern appears after some seconds (60-120s) of IBS for T < 525 K, and reaches a saturation state after a few minutes. The autocorrelation of the AFM images (Figure 82b) reveals short-range hexagonal ordering. As a result of the ion bombardment, a ~ 2 nm amorphous surface layer is induced [2].

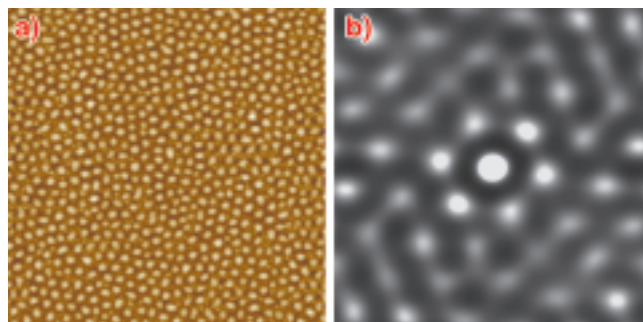
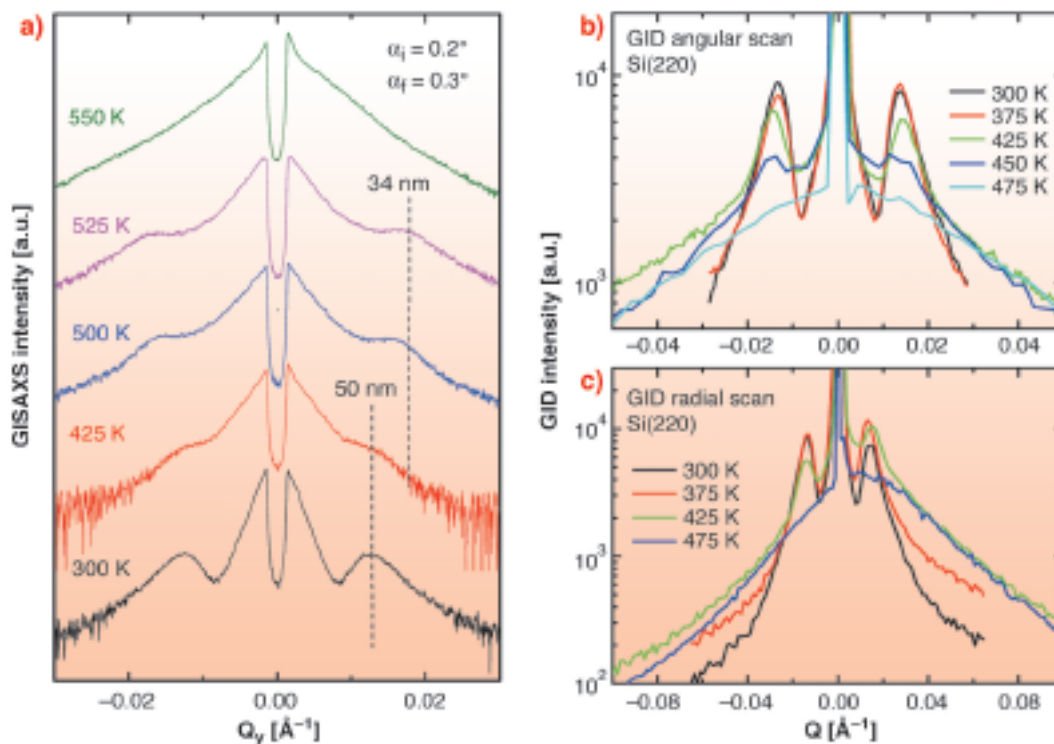


Fig. 82: a) AFM image (1x1  $\mu\text{m}^2$ ) of a nanodot (height 6-7 nm) pattern produced by IBS on Si(001) surfaces after 10 min sputtering at 375 K; b) Autocorrelation image showing the hexagonal arrangement.

The patterns were further analysed with synchrotron light at the ESRF. The experiments were performed at the Anomalous Scattering Beamline (ID01) by using grazing incidence diffraction (GID) and small-angle X-ray scattering (GISAXS). These methods provide complementary information about the characteristic wavelength (interdot distance) and correlation length (ordered domain size), with additional hints about the relative contribution of the amorphous and crystalline volumes of the surface nanostructures. Radial GID scans are also sensitive to the presence of strain in the near surface region.

GISAXS and GID results from IBS patterns produced at different temperatures are displayed in Figure 83. The correlation peaks on both sides of the reflected and diffraction signal, respectively, are related to the pattern formation. The direct comparison of GID and GISAXS spectra shows that the nanodots are mostly crystalline at low temperatures (< 400 K). The correlation peak position gives the average inter-dot distance and the peak width is related to the degree of ordering. In contrast to theory, which predicts an increase of the pattern wavelength with temperature if thermal-diffusion dominates the smoothing mechanisms [3], AFM and X-ray methods reveal a decrease of the interdot distance (higher dot density). Also, the loss of correlation within the crystalline cores at 475 K indicates an increase of the amorphous volume with temperature which, in light of AFM data, can be understood by a progressive decrease of the dot height. Finally, there is an emerging strain near the surface (Figure 83c), which may affect diffusion processes. The former could explain the disagreement that has been found with theory.



**Fig. 83:** GISAXS (a) and GID (b-c) scans. GID spectra were taken around the (220) in-plane Bragg peak in angular (b) and radial (c) directions.

In conclusion, the synchrotron analysis has provided a deeper understanding of the pattern formation on Si(001) surfaces by IBS. Also, X-ray methods have given complementary information to local imaging techniques with better sampling statistics.

### References

- [1] U. Valbusa *et al.*, *J. Phys. Condens. Matter. C* **14**, 8153 (2002).
- [2] R. Gago *et al.* *Appl. Phys. Lett.* **78**, 3316 (2001).
- [3] B. Kahng, H. Jeong, A.L. Barabasi, *Appl. Phys. Lett.* **78**, 805 (2001).

### Principal Publication and Authors

R. Gago (a), L. Vázquez (b), O. Plantevin (c,d), J.A. Sánchez-García (b), M. Varela (e), M.C. Ballesteros (e), J.M. Albella (b), and T.H. Metzger (d), *Phys. Rev. B* **73**, 155414 (2006).

(a) *Universidad Autónoma de Madrid (Spain)*

(b) *ICMM, CSIC, Madrid (Spain)*

(c) *CSNSM, Orsay (France)*

(d) *ESRF, Grenoble (France)*

(e) *Universidad Carlos III de Madrid (Spain)*

## Step-by-step capping of GaN/AlN quantum dots, studied by grazing-incidence anomalous diffraction

We report on the investigation of strain and composition of GaN nanostructures (dots) grown on an AlN(0001) epilayer as a function of the thickness of the AlN capping layer, with which the GaN dots were covered after growth. The capping strongly modifies the strain state in the quantum dots (QDs)

and therefore plays a decisive role in the modification of the optical properties. Strain is closely related to the composition, shape and aspect ratio of the nanostructures, and on the mutual stress which nanostructures, substrate and the matrix exert on each other.

A model-independent approach can be used to recover the strain and composition by exploiting the chemical sensitivity of resonant elastic X-ray scattering. Two complementary methods, based on resonant X-ray scattering are now available. Multiwavelength anomalous diffraction (MAD) allows an extraction of the scattering amplitude of the resonant atoms (chemical mapping in the reciprocal space) and the diffraction anomalous fine structure (DAFS) spectroscopy that allows a determination of the local environment of atoms located in an iso-strain volume selected by diffraction.

GaN QDs were grown on thin films of AlN on sapphire and on SiC substrates, according to a modified Stranski-Krastanov growth mode. The thickness of the subsequently grown AlN capping layer was in the range of 0-20 monolayers. The average height (diameter) of the free standing nanostructures were found to be 3nm (15 nm) for QDs on AlN/sapphire and 4 nm (30 nm) for QDs on AlN/SiC, respectively. Grazing-incidence MAD (GIMAD) and Grazing-incidence DAFS (GIDAFS) were performed at the Ga K-edge at beamline BM02. Enhanced sensitivity to out-of-plane strain was gained with the sample surface perpendicular to the X-ray beam polarisation vector. We recovered the GaN QDs in-plane strain as a function of AlN cap thickness, by applying the GIMAD method. For this purpose, we measured a set of h-scans (radial scan), close to the in-plane (30-30) Bragg reflection of the AlN substrate with grazing incidence and exit, at 12 different energies. This enabled us

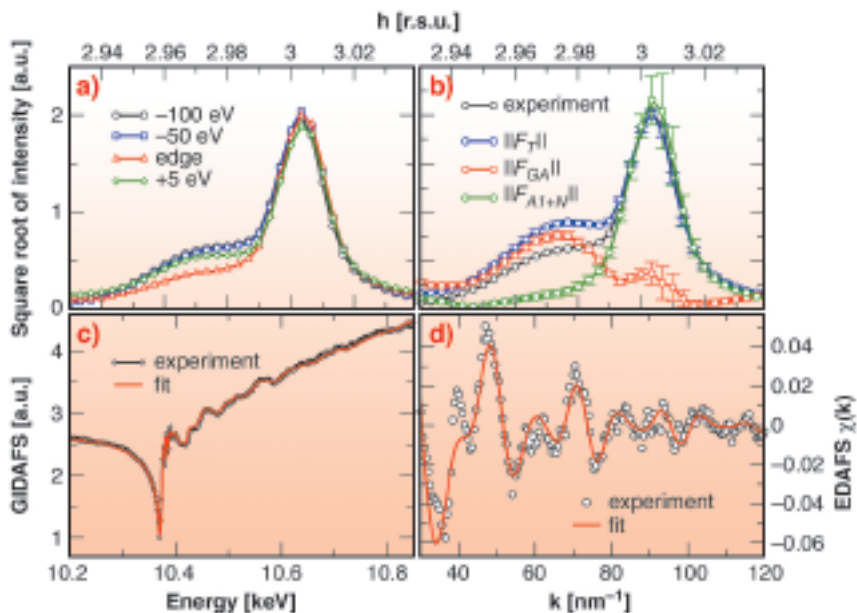


**Fig. 84:** Data corresponding to the 10 monolayers AlN coverage. **a)** experimental intensities measured below (-100 and -50 eV), at the edge, and above (+5 eV) the Ga K-edge; **b)** experimental intensities measured at 10.317 keV (50 eV below the Ga K-edge),  $F_{\text{Ga}}$  and  $F_{\text{Al+N}}$ ; **c)** GIDAFS spectra measured at the maximum of  $F_{\text{Ga}}$  ( $h = 2.973$ ) together with the best fit obtained with experimental anomalous scattering factors  $f'_{\text{Ga}}$  and  $f''_{\text{Ga}}$  of Ga in a GaN thin film. **d)** experimental EDAFS compared with the best fit.

to extract the Ga atoms partial structure factor ( $F_{\text{Ga}}$ , **Figure 84b**) and to determine the average in-plane strain and size of the GaN nanostructures. Out-of-plane strain and the QDs composition were obtained by recording the Extended DAFS oscillations, above the Ga K-edge at the maximum of  $F_{\text{Ga}}$ , in order to probe the QDs core (**Figures 84 c,d**). The EDAFS oscillations analysis was performed with the IFEFFIT code by fixing the QDs in-plane unit cell parameter ( $a$ ) to the values found by GIMAD, letting the  $c$  parameter vary according to the hexagonal symmetry. For all samples, the Al content was not significant.

followed by a noticeable change in the capping process that corresponds to the filling of the lateral space in between the dots.

By combining MAD and DAFS, we have systematically determined the in- and out-of-plane strains, as well as the atomic intermixing in the GaN/AlN(0001) nanostructures, as a function of the AlN cap thickness, with a sensitivity to the AlN coverage as small as 2 ML.

#### Principal Publications and Authors

J. Coraux (a,b), M.G. Proietti (c), V. Favre-Nicolin (a,b), B. Daudin (a), H. Renevier (a,b,\*), *Phys. Rev. B* **73**, 205343 (2006); *Appl. Phys. Lett.* **88**, 153215 (2006).

(a) Commissariat à l'Energie Atomique, Département de Recherche Fondamentale sur la Matière Condensée, SP2M, Grenoble (France)

(b) Université Joseph Fourier, Grenoble (France)

(c) Departamento de Física de la Materia Condensada, Instituto de Ciencia de Materiales de Aragon, CSIC-Universidad de Zaragoza (Spain)

\* Present address : Ecole Nationale Supérieure de Physique de Grenoble, INP Grenoble, MINATEC (France).

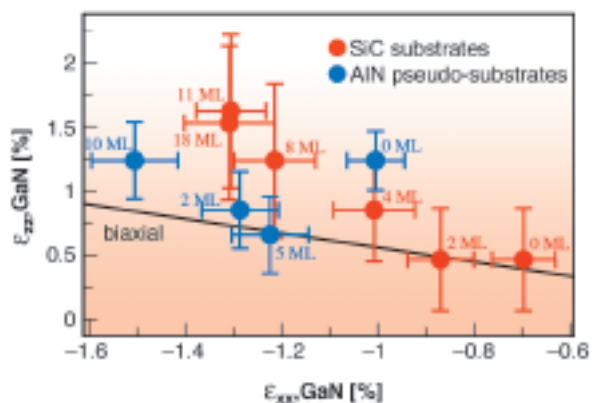


**Fig. 85:** GaN QDs strain  $\epsilon_{zz}$  vs  $\epsilon_{xx}$  values for all the samples studied compared with elastic biaxial strain of a pseudomorphic GaN thin film.

**Figure 85** shows the in-plane strain ( $\epsilon_{xx}$ ) versus the out-of-plane strain ( $\epsilon_{zz}$ ) for the QD for two kinds of substrates and as a function of the capping layer thickness. The differences between the two series of samples demonstrate the influence of the QDs aspect ratio and the densities of threading edge and misfit dislocations at the AlN/GaN interface on the strain relief mechanism. Finally, the Al fraction as a function of the capping layer thickness, which was obtained by analysing the GIDAFS lineshape (**Figure 84c**), indicates a wetting of the QDs,

## Low dimensions with high impact: interfaces and epilayers

### Characterisation of the interface of high-K praseodymium oxide thin films on silicon surfaces

Further scaling down of microelectronic devices requires a thickness of the  $\text{SiO}_2$  gate oxide (**Figure 86a**) of 1 nm,

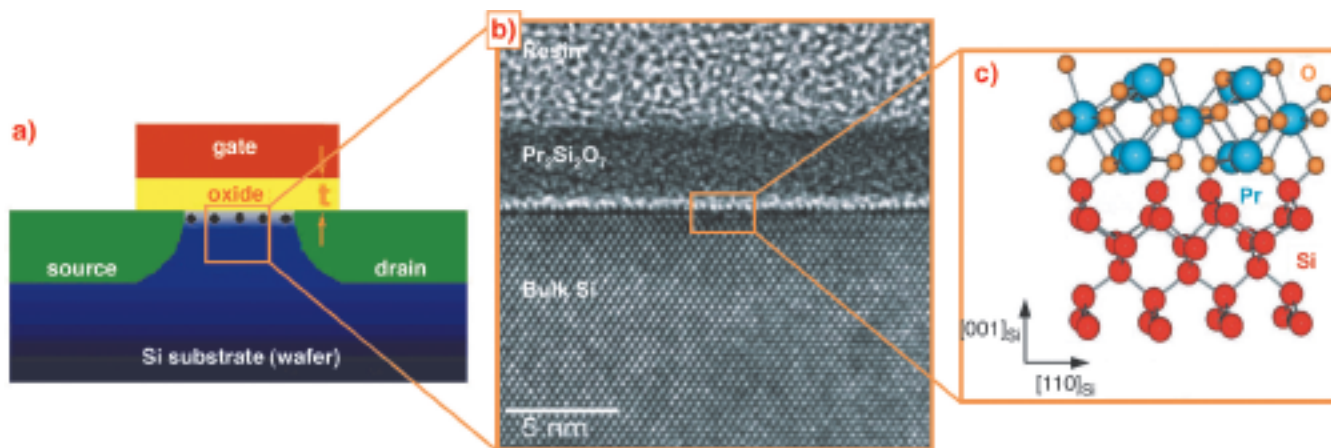


**Fig. 86:** High-K oxide / Si(001) interface studied at the atomic scale. **a)** Schematic cross-section of a CMOS transistor. The square indicates the region of interest in our study. **b)** Cross sectional TEM picture of a 3 nm thick Pr-oxide film on Si(001), which indicates the presence of an interfacial layer. **c)** Refined atomic structure based on GIXRD data.

which leads to a large leakage current. Thus, a severe challenge facing semiconductor technology is to replace the  $\text{SiO}_2$  gate dielectric in CMOS transistors. Candidates must have a high dielectric permittivity  $K$ , a large band gap, and exhibit high thermal stability and low interface state density in contact with silicon [1]. Rare-earth oxides, particularly praseodymium oxide  $\text{Pr}_2\text{O}_3$ , which show several properties that meet these requirements, are therefore considered as promising candidates.

With feature sizes reaching the nanoscale, surfaces and interfaces begin to dominate the silicon device performance, due to the increasing surface to volume ratio. Owing to the complexity of these structures and the difficulties in characterising such low dimensional systems, the Pr-oxide/Si(001) interface is not well understood despite its importance. Therefore, in this work, we have investigated the growth of Pr-oxide on Si(001) at the atomic scale and from the very early stages. We used grazing-incidence X-ray diffraction (GIXRD) and photoelectron spectroscopy (XPS) *in situ*, with the sample kept in ultra high vacuum (UHV), complemented by other techniques such as scanning tunnelling microscopy (STM) and transmission electron microscopy (TEM).

Pr-oxide thin films with thicknesses up to 4 nm were prepared by molecular beam epitaxy on atomically clean Si(001) surfaces. **Figure 86b** shows a TEM cross section of one of our 3 nm thick Pr-oxide films. An interfacial layer is observed but cannot be identified with TEM. The atomic structure (cf. **Figure 86c**) was determined by GIXRD based on 20 non-equivalent Si crystal truncation rods (CTRs). Four of them are presented in **Figure 87a**. The result of the structural refinement reveals a 0.5 nm interfacial epitaxial layer of cubic  $\text{Pr}_2\text{O}_3$ , which exhibits a  $3 \times 1$  superstructure, on top of which a disordered layer forms.

The high resolution STM topograph presented in **Figure 87b** displays the surface morphology of the Si

surface after the deposition of 0.1 nm of Pr-oxide. Dimer rows of the  $2 \times 1$  reconstruction of the Si(001) surface are visible between the oxide clusters, which appear bright in the topograph. A line profile is presented in the bottom inset of **Figure 87b**. The height difference between the areas marked by the first and second arrows from the left corresponds to a Si atomic step ( $\approx 0.14$  nm). The presence of small domains containing dimer rows aligned in two perpendicular directions indicates the formation of small patches of holes separated by atomic steps. Such surface morphology suggests a reaction of Si with the Pr-oxide, leading to the removal of some of the Si atoms in the topmost layer.

**Figure 87c** exhibits the core level XPS spectra of the Pr4d and Si2p states collected at different emission angles  $\alpha$ , *i.e.* the angles between the sample surface and the outgoing photoelectrons, from a 1 nm thick Pr-oxide film using a photon energy of 2.5 keV. The spectra are background subtracted and normalised to the Pr4d integrated peak intensities. The Si2p component appearing at  $\approx 102.7$  eV corresponds to Si-Si bonds in a silicate (Si-O-Pr) [2]. The  $I(\text{Si2p-silicate})/I(\text{Pr4d})$  ratio measured at  $\alpha = 4^\circ$  suggests the  $\text{Pr}_2\text{Si}_2\text{O}_7$  stoichiometry. The fact that this intensity ratio decreases as  $\alpha$  increases, *i.e.*, when the measurement is more bulk sensitive, supports the existence of a thin Si-free Pr-oxide layer at the interface identified by GIXRD.

With the help of GIXRD and XPS we identified a crystalline Pr-oxide layer at the high-k-oxide/Si interface, hidden underneath a  $\text{Pr}_2\text{Si}_2\text{O}_7$  silicate structure (on top of which cubic  $\text{Pr}_2\text{O}_3$  eventually grows upon further deposition [3]). These findings may be relevant for the growth of other dielectrics such as  $\text{Gd}_2\text{O}_3$ ,  $\text{Nd}_2\text{O}_3$ ,  $\text{Y}_2\text{O}_3$ , and even  $\text{HfO}_2$  on silicon.

## References

[1] International Technology Roadmap for Semiconductors,

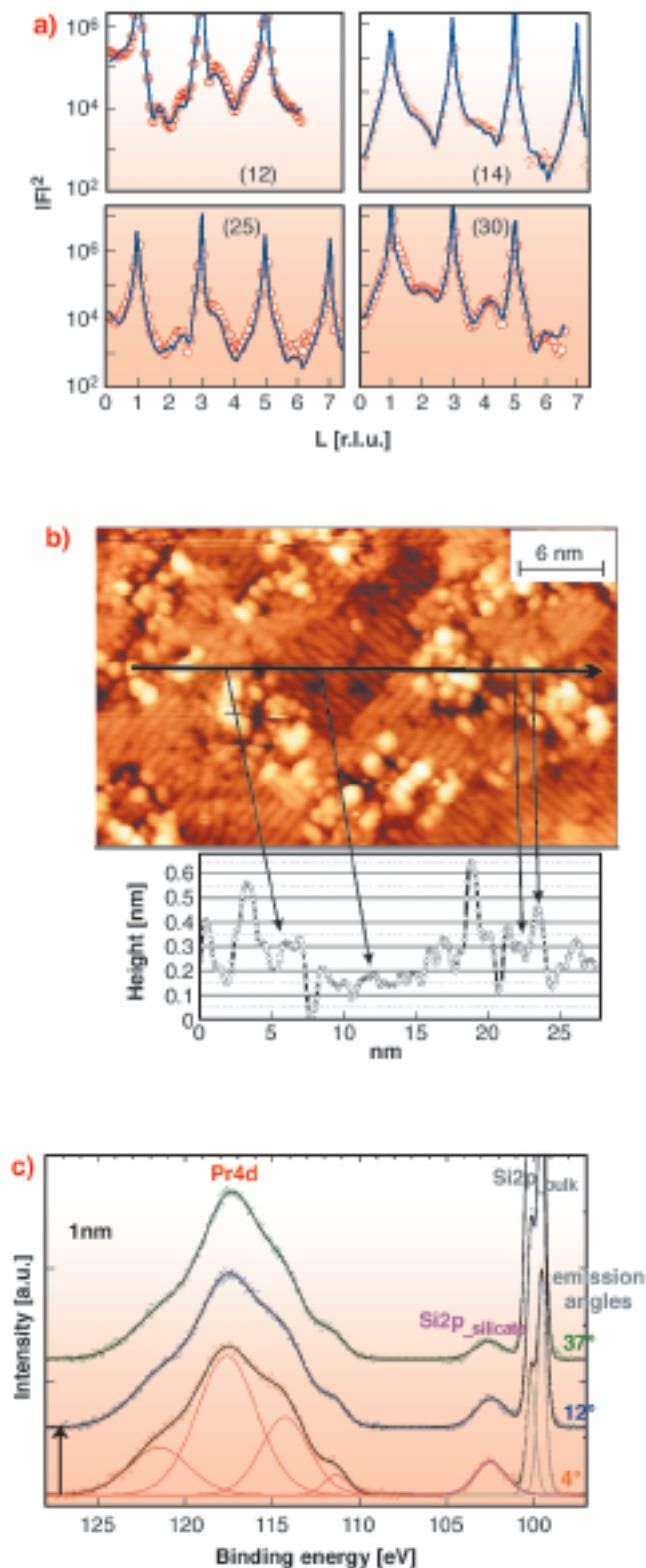


**Fig. 87:** a) Four CTRs measured in the case of a 1 nm thick Pr-oxide film. Each rod is labelled by its (HK) values. The red symbols correspond to the integrated intensities extracted from the experimental data and the blue curves correspond to the best fit from the structural refinement analysis. b) STM topography of a 0.1 nm thick film.  $30 \times 20 \text{ nm}^2$ ,  $U_s = 2 \text{ V}$ ,  $I_t = 0.50 \text{ nA}$ . c) Core-level XPS spectra of Pr4d and Si2p states, collected at different  $\alpha$ , from a 1 nm thick Pr-oxide film. Experimental data points and simulated curves are plotted together to show the evolution of the ratio  $I(\text{Si2p-silicate})/I(\text{Pr4d})$  versus  $\alpha$ .

2005 ed., <http://public.itrs.net>.

[2] D. Schmeisser, H.-J. Müssig, J. Dabrowski, *Appl. Phys. Lett.* **85**, 88 (2004).

[3] T. Schroeder *et al.*, *Appl. Phys. Lett.* **85**, 1229 (2004).

#### Authors

L. Libralesso (a), T.-L. Lee (a), C. Dubourdieu (b), J. Zegenhagen (a).

(a) ESRF

(b) LMGP / CNRS – INPG (France)

### Implantation-induced crystalline defects in silicon studied by grazing incidence diffuse X-ray scattering

In the fabrication of CMOS devices, successive ion implantation and thermal annealing processing is employed. Increasing device performance is achieved by continuous shrinking of feature sizes. Therefore, front-end processors require an extremely accurate tailoring of the dopant profile especially close to the channel region, where ultra-shallow junctions are located with a junction depth lower than 50 nm. Industrially, ultra-shallow junctions are created by ultra-low energy (< 5 keV) implantation. Pre-amorphised Si substrates are often used to improve control of the dopant profile by avoiding ion-channelling. Understanding the mechanisms of dopant interaction with unavoidable implantation-induced defects has become a crucial issue.

The effects of pre-amorphisation on residual defects, especially end-of-range defects consisting of excess Si-interstitials [1], were investigated by focussing on two substrate series: pre-amorphised Si wafers ( $\alpha$ -Si series) and untreated Si wafers (c-Si series). The  $\alpha$ -Si substrates had been amorphised with Xe ions at 130 keV. Subsequently, As<sup>+</sup> ions were implanted at 3 keV in all wafers to generate the ultra-shallow dopant profile. The As-implantation was followed by a treatment at 600°C for 20 minutes or by spike annealing at 1130°C, close to the processing conditions for industrial devices.

X-ray scattering experiments were carried out using an 8 keV beam at the beamline ID01. A combination of X-ray scattering methods optimised to characterise Si wafers implanted at ultra-low energy [2] was used. Grazing incidence diffuse X-ray scattering (GI-DXS) proved to be well suited to the investigation of defects confined within thin crystalline layers. The 220 surface Bragg reflection was selected and the X-ray grazing incident angle  $\alpha_i$  was tuned to reach the depth where the defects are located. Reciprocal space maps in the ( $1\bar{1}0$ ) plane (*i.e.*  $q_r$  vs.  $q_z$ ) were recorded using a linear position sensitive detector.

The analysis of the decay of the defect-induced DXS along  $q$  reveals information on the nature of the

predominant defect. As expected for point defects and small defect clusters, a  $q^{-2}$  decay of the scattered intensity and a linear dependence from the defect concentration are found. For the c-Si samples, the intensity of the DXS progressively diminishes with increased annealing time, thus indicating the gradual annihilation of the defects. For spike-annealed  $\alpha$ -Si, the transformation of point defects into faulted dislocation loops was observed. These extended defects were identified from the DXS intensity streaks along the  $\langle 111 \rangle$  directions, which are their characteristic “footprint” (Figure 88). All residual interstitials are condensed into loops with a diameter of  $\sim 50$  nm measured from the width of the corresponding DXS streak.

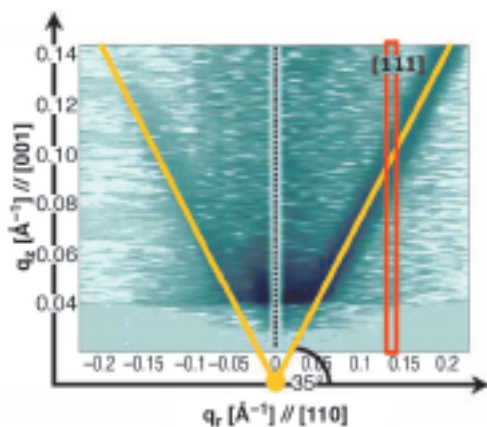


**Fig. 88:** Reciprocal space map of DXS in the  $q_r$ - $q_z$  plane close to the 220 Bragg reflection for spike-annealed  $\alpha$ -Si sample. The intensity streak points in the  $[111]$  direction with an angle of  $35^\circ$  with respect to the radial direction  $[110]$ . The rectangle indicates the position of the measurement along the position sensitive detector in Figure 89.

For small defects (*i.e.*  $q^{-2}$  decay of the DXS), it is possible to extract the depth profile of the defects by simulating the corresponding  $q_z$ -resolved measurements. Figure 89 shows the quality of the fit performed using the program developed in [2]. The main information obtained is the value of the mean depth of the defects  $z_{\max}$

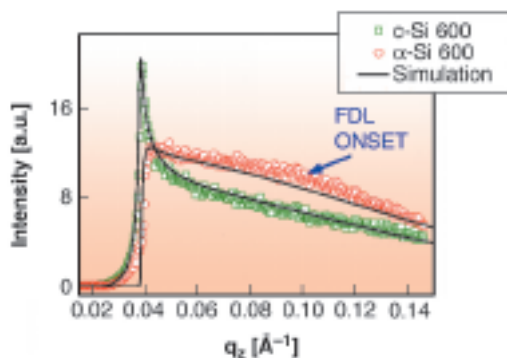


**Fig. 89:** Defect-induced diffuse intensity along  $q_z$  at  $q_r = 0.14 \text{ \AA}^{-1}$  for  $\alpha$ -Si and c-Si samples annealed at  $600^\circ\text{C}$  together with the simulations (full line). FDL = Faulted dislocation loops.

where  $z_{\max} = 12.5 \pm 1$  nm, for c-Si 600, and  $z_{\max} = 100 \pm 20$  nm, for  $\alpha$ -Si 600, in agreement with the outcome of TEM and MEIS and TRIM calculations.

The results obtained differ significantly between the two sample series and are compatible with the ‘excess interstitial’ model [1]. The distance of the defects from the sample surface is one of the key parameters which determine their evolution. In the  $\alpha$ -Si series, the end-of-range defects are deeply buried after Xe implantation. Therefore, they evolve from point-like into extended defects during annealing without losing Si interstitials. Due to the shallow location of the end-of-range damage, for c-Si implants, defect annihilation occurs by migration of Si interstitials towards the surface.

These X-ray techniques offer a non-destructive tool for defect characterisation with high statistical accuracy, depth resolution and without the need for sample preparation.

### References

- [1] A. Claverie, B. Colombeau, B. De Maudit, C. Bonafos, X. Hebras, G. Ben Assayag, F. Cristiano, *Appl. Phys. A* **75**, 1025 (2003).
- [2] L. Capello, T.H. Metzger, V. Holý, M. Servidori, A. Malachias, *J. Appl. Cryst.* **39**, 517 (2006).

### Principal Publication and Authors

- L. Capello (a), T.H. Metzger (a), M. Werner, J. van den Berg (b), M. Servidori (c), L. Ottaviano, C. Bongiorno, G. Mannino (d), T. Feudel, M. Herden (e), V. Holý (f), *J. Appl. Phys.* **100**, 103533 (2006).
- (a) ESRF  
 (b) University of Salford, (UK)  
 (c) CNR-IMM, Bologna, (Italy)  
 (d) CNR-IMM, Catania (Italy)  
 (e) AMD Saxony, Dresden (Germany)  
 (f) Charles University, Praha (Czech Republic)

## Chemistry counts: Coatings, catalysis, and electrochemistry

### Microscopic growth kinetics of gold electroplating

Galvanic metal plating is a widely used industrial method for the formation of metal structures with sub-micrometre dimensions. Its applications include dual-damascene plated ULSI microchips, magnetic storage devices, and micromechanical devices (LIGA process). The continuing need for smaller feature sizes demands even better control of these electrochemical deposition processes and hence an improved fundamental

understanding of the underlying elementary steps. A central challenge is to clarify the relationship between the atomic-scale structure of the solid-liquid interface, the growth behaviour and the resulting surface morphology, which requires direct structure-sensitive investigations during the growth process.

To provide a deeper insight into this complex interplay, metal electroplating from aqueous electrolyte solutions was investigated *in situ* by surface X-ray diffraction, using Au(001) homoepitaxial growth in 0.1 M HCl as an example. The results demonstrate that studies of the kinetic growth behaviour at a solid-liquid interface are possible by this technique and reveal a pronounced influence of the applied electrode potential on the growth process.

Experiments were performed at beamline ID32 ( $E_{\text{ph}} = 18\text{--}20$  keV) using a “hanging meniscus” transmission electrochemical cell with minimised electrical cell resistance and nearly unrestricted mass transport, which allows the combination of *in situ* surface X-ray diffraction studies of rapid structural changes with high quality electrochemical measurements [1]. The electrodeposition process was initiated by exchanging the Au-free solution via a remote controlled pump system by electrolytes containing 0.1 to 0.5 mM  $\text{HAuCl}_4$ , resulting in diffusion-limited (*i.e.*, potential-independent) deposition rates up to four monolayers (ML) per minute.

To study the growth behaviour, the sample potential was first kept at  $0.6 V_{\text{Ag}/\text{AgCl}}$ , where the very high surface mobility results in a rapid smoothing even of rough surfaces, and then stepped to a more negative value while the intensity ( $I$ ) of the scattered X-rays was monitored as a function of time at selected reciprocal

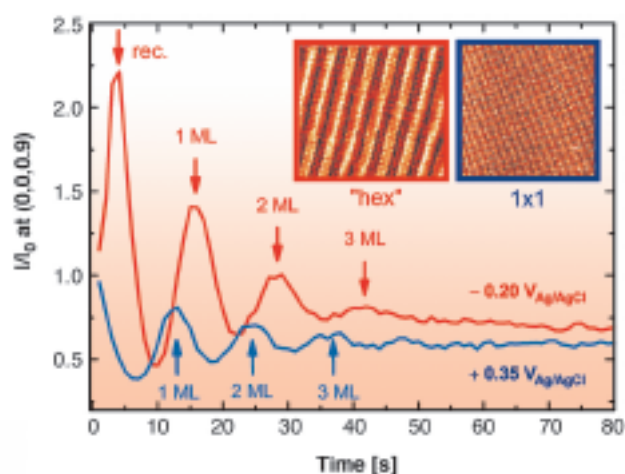


**Fig 90:** Growth oscillations indicating layer-by-layer growth for Au electrodeposition on Au(001) in 0.1 M HCl + 0.5 mM  $\text{HAuCl}_4$ , after potential steps into the regime of the unreconstructed (1x1) (blue line) as well as the “hex” reconstructed (red line) Au surface. The insets show high-resolution STM images of both surface structures.

space positions along specular and nonspecular crystal truncation rods (CTR). In an analogous way, as in MBE growth studies under UHV conditions, different kinetic growth modes become manifest in characteristic  $I(t)$  curves. Specifically, in a wide potential regime intensity oscillations (Figure 90) indicating layer-by-layer growth were observed (typically only 3-4 oscillations due to imperfect 2D growth). The oscillation period is in very good agreement with the deposition time per Au monolayer obtained from parallel electrochemical measurements, supporting the interpretation of these data as growth oscillations.

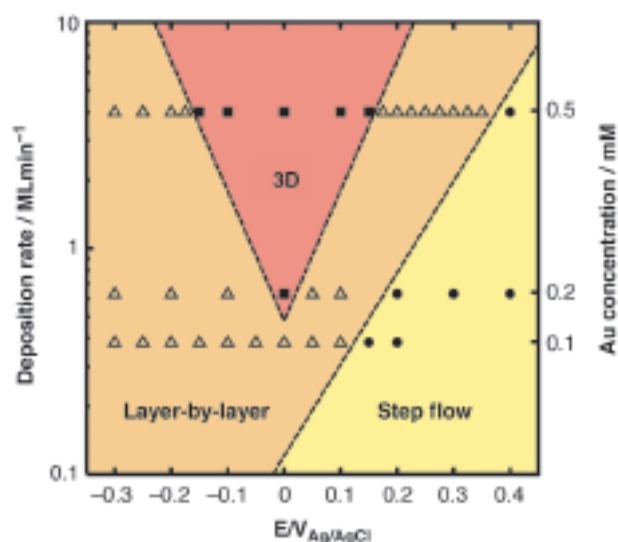


**Fig. 91:** Kinetic growth mode diagram for Au electrodeposition on Au(001) in 0.1 M HCl, showing the dependence of the kinetic growth mode on potential and deposition rate.

As illustrated by the kinetic growth mode diagram in Figure 91, the growth mode depends strongly on the potential as well as on the Au deposition rate. With decreasing potential, regimes of step-flow growth, layer-by-layer growth, multilayer growth, and a “reentrant” layer-by-layer growth are observed. This behaviour can be rationalised within the framework of kinetic growth theory by the pronounced influence of the potential on the interface structure and consequently the surface transport processes. The potential-dependent growth behaviour in the positive potential regime, where the Au(001) surface is unreconstructed, is in accordance with the known substantial increase in Au adatom diffusion with increasing potential, caused by the change in the electric field at the interface and the influence of coadsorbed anions [2]. The crossover from 3D to 2D growth at negative potentials can be attributed to the formation of the “hex” reconstruction on the Au(001) surface, which results in an enhanced Au surface mobility. The formation of the “hex” reconstruction directly after the potential step also leads to an initial increase in the scattered intensity, resulting in the noticeable “phase shift” of the curve with respect to that observed on the unreconstructed surface at  $0.35 V_{\text{Ag}/\text{AgCl}}$ .

In summary, these experiments demonstrate that by surface X-ray scattering in transmission geometry direct *in situ* studies of the kinetic growth mode are possible not only for MBE, but also for solid-liquid interfaces. The results obtained for homoepitaxial deposition on Au(100) revealed that the surface mobility and consequently the growth behaviour is strongly affected by the complex solid-liquid interface structure, *i.e.* the presence of the surface reconstruction, the electric field at the interface, as well as the coadsorbed species on the solution side of the interface. Since this method affords studies at deposition rates that approach those used in practical applications, it is a promising new tool for future fundamental and applied studies of galvanic deposition processes.

## References

- [1] A.H. Ayyad, J. Stettner, O.M. Magnussen, *Phys. Rev. Lett.* **94**, 066106 (2005).  
 [2] M. Giesen, *et al.*, *Surf. Sci.* **595**, 127 (2005).

## Principal Publications and Authors

K. Krug, J. Stettner, O.M. Magnussen, *Phys. Rev. Lett.*, **96**, 246101 (2006).  
*Institut für Experimentelle und Angewandte Physik, Universität Kiel (Germany)*

## Structure and reactivity of a model catalyst alloy under realistic conditions

Whereas most traditional electron or ion based surface science techniques are limited to vacuum environment, surface X-ray diffraction (SXR) is able to determine structural parameters of surfaces under a pressure of several bars because of the negligible attenuation of hard X-rays by the reactant gas. The development of an *in situ* high pressure chamber for catalytic research at ID03 [1] has opened the door to an area in surface science, which has previously been impossible because of the so-called pressure gap between the conditions in an UHV experiment and those surrounding an operating industrial catalyst.

PtRh alloys can be used as “three-way” automotive exhaust gas catalysts. They have the ability to simultaneously remove unwanted, toxic exhaust gases such as CO, NO<sub>x</sub> and hydrocarbons. Gas interactions had been studied on PtRh surfaces under ultra high vacuum (UHV) conditions, but under realistic pressures, the behaviour of the alloy is in principle unexplored, in particular concerning the relationship between structure and reactivity.

Previous measurements under UHV conditions from the Pt<sub>25</sub>Rh<sub>75</sub>(100) had clearly indicated the formation of a well ordered ultra-thin RhO<sub>2</sub> film at O<sub>2</sub> pressures around

$5 \times 10^{-3}$  mbar using a sample temperature of 700 K. The resulting  $c(8 \times 2)$  surface structure could be explained by an hexagonal RhO<sub>2</sub> overlayer, or a so-called surface oxide [2]. The experimental observations were confirmed by DFT calculations and the resulting structure can be seen in Figure 92.

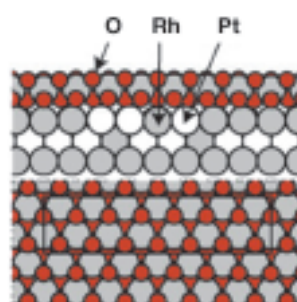


**Fig. 92:** The atomic arrangement of the  $c(8 \times 2)$  surface oxide tri-layer structure as found by UHV experiments and DFT calculations. Similar structures has been found on Rh(111), Rh(110) and Rh(100) [2].

Because of electron based techniques being limited to UHV conditions, we turn to SXR in order to study the surface phase under almost atmospheric gas pressures. The aim of these experiments was to approach conditions under which a real catalyst operates. A sketch of the in-plane reciprocal space in the presence of oxygen is shown in Figure 93a. Here the Pt<sub>25</sub>Rh<sub>75</sub>(100), the  $c(8 \times 2)$  and the corundum Rh<sub>2</sub>O<sub>3</sub>(0001) bulk oxide reflections and their unit-cells are indicated.

By performing a scan in H and K as indicated in Figure 93a, we may detect the surface oxide as well as the bulk Rh<sub>2</sub>O<sub>3</sub> corundum reflections at higher O<sub>2</sub> pressures. Repetitive HK-scans as a function of time are shown in Figure 93b. In this way, we are able to connect our UHV observations with the SXR studies at realistic conditions.

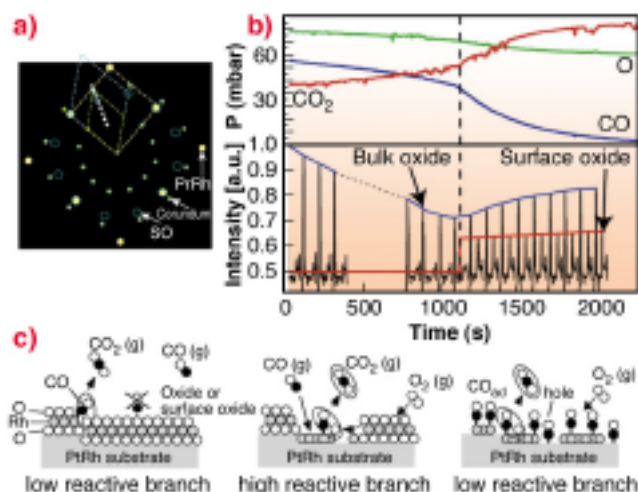


**Fig. 93:** a) In-plane reciprocal space illustrating the unit cells of the Pt<sub>25</sub>Rh<sub>75</sub>(100) (yellow), the surface oxide (blue) and the Rh<sub>2</sub>O<sub>3</sub> bulk oxide (green). b) Repetitive HK-scans according to the white dashed line in (a) for  $L = 0.5$  during reaction conditions (bottom part) with simultaneous mass-spectroscopy measurements of the gas content (top part). c) Models of the surface phases and the CO-oxidation reaction process.

To investigate the connection between surface structure and CO-oxidation reactivity, we simultaneously monitor the surface phases by SXRD and the gas composition by mass spectrometry, as shown in **Figure 93b**. As the CO is consumed by the oxidation into CO<sub>2</sub>, the partial CO/O pressure ratio is continuously reduced. When the CO pressure is sufficiently low, the non-bulk oxide covered surface reoxidises, which can be seen by the reappearance of the diffraction signal from the surface oxide. Concomitantly, the CO oxidation rate increases, as deduced from the measured partial pressures. Our observations lead us to conclude that under these conditions, the surface oxide film formed on the Pt<sub>25</sub>Rh<sub>75</sub>(100) surface is more active in the CO-oxidation than the corundum Rh<sub>2</sub>O<sub>3</sub> bulk oxide and the metal surface on the Pt<sub>25</sub>Rh<sub>75</sub>(100) surface.

Although CO cannot adsorb on the surface oxide according to our DFT calculations (see **Figure 93c**), the oxygen stored in the film provides an additional source of oxygen expelled onto the metal surface, where it reacts with CO forming CO<sub>2</sub>. Under steady state conditions, the consumed surface oxide film is continuously regenerated by oxygen in the gas phase and consumed by the CO. The results provide confirmation *in situ* at the atomic scale and under realistic conditions of a general mechanism originally proposed by Turner in 1981 [3], and are likely to explain experimental observations on other late transition metal surfaces as well as on their corresponding nanoparticles.

## References

- [1] M.D. Ackermann, *et al.*, *Phys. Rev. Lett.* **95**, 255505 (2005); P. Bernard, *et al.*, *Rev. Sci. Instrum.* **70**, 1478 (1999).  
 [2] E. Lundgren, *et al.*, *J. Phys. Cond. Matter* **18**, 481 (2006).  
 [3] J. E. Turner, B. C. Sales, M. B. Maple, *Surf. Sci.* **103**, 54 (1981).

## Principal Publication and Authors

E. Lundgren (a), J. Wang (b), M. Ackermann (c), R. Westerström (a), J. Gustafson (a), A. Resta (a), J. N. Andersen (a), A. Mikkelsen (a), O. Balmes (d), X. Torrelles (e), J. W. M. Frenken (c), B. Hammer (b), *to be published*.

(a) Department of Synchrotron Radiation Research, Lund University, (Sweden)

(b) Interdisciplinary Nanoscience Center (iNANO) and Department of Physics and Astronomy, University of Aarhus (Denmark)

(c) Kamerlingh Onnes Laboratory, Leiden University (The Netherlands)

(d) ESRF

(e) Institut de Ciencia de Materials de Barcelona (Spain).

## ***In situ electrochemical and SR-XRD time-resolved study of lead carboxylate coating for the protection of cultural heritage artefacts***

European lead heritage ranges from simple ornaments to vast artistic and engineering masterpieces such as pipe organs (**Figure 94**) - all in danger of decay and loss through corrosion. Indeed, lead organ pipes are amongst the most seriously jeopardised artefacts: their sound is critically dependent on the material, as well as their shape, size, and condition. Corrosion usually starts at the foot of the pipe and proceeds invisibly from the inside towards its mouth, resulting in changes to the tonal quality due to distortion of the mouth geometry. Cracks and holes then develop, at which point the pipe becomes mute and requires repair or replacement [1]. Lead is seriously affected by the presence of organic acids (formic, acetic...) in the environment, and both original and restored wood (e.g. in the wind chest) are a source of these.

Coating lead artefacts to protect them is fraught with difficulty since badly researched coatings and treatments can lead to irreversible changes in appearance and function, and even more rapid degradation. Only after meticulous investigation can a coating be applied with relative confidence. An attractive feature of the carboxylate coating process is simplicity. The lead is soaked in a non-toxic solution of sodium decanoate [2]. The result is a dark coating, similar to aged lead in appearance. In this initial study, we set out to measure the growth characteristics of such layers using time resolved X-ray diffraction (XRD), electrochemical impedance spectroscopy (EIS), scanning electron microscopy (SEM) and mass gain measurements, as a prelude to testing its performance in a corrosive environment.

On BM28 (XMaS) we made simultaneous EIS and X-ray diffraction (XRD) measurements in a novel electrochemical cell (the eCell), developed especially for the characterisation of rough heterogeneous metal surfaces



**Fig. 94:** The Stellwagen organ in St Jakobi church in Lübeck. The prospect pipes dating from 1467 have suffered heavy corrosion on the inside (Photo courtesy C.J. Bergsten).

and the characterisation of conservation methods using synchrotron-based techniques. A particular objective is to obtain correlated, time-resolved spectroelectrochemical data. eCell [3] is an adaptive kit consisting of the cell itself, a range of mounting options, a custom miniature potentiostat, and a data system running on a notebook PC.

An especially important feature of XRD is the use of a fast 2D detector such as the Mar CCD 165 to collect the data. The sample cannot easily be rotated to randomise the diffraction pattern because it is the working electrode in an electrochemical cell whose operation would be disturbed by the motion. However, the samples are polycrystalline and may contain large crystals or some preferred orientation so that a 1D detector can give misleading and apparently irreproducible spectra. An image can be integrated to provide more random spectra. Intensity variations in the rings can indicate differences or similarities in grain size and orientation of the metal substrate and its coating. The geometry of the experiments dictates that the camera axis is aligned between 20 and 50 degrees to the incoming beam, so that the intersections between the diffraction cones and the camera plane are elliptical. Usually the diffraction centre is well below the camera plane and the rings are incomplete. Therefore, we have developed a package, esaProject, which centres the images and then transforms them into a space where the rings are linear (Figure 95). Thus, spectra corrected for the arc length from all or part of the image can then be extracted and processed further.

Figure 95a shows a time sequence of images and their reprojection from a growing lead carboxylate coating. In detail, the lead rings are spotty whereas the carboxylate

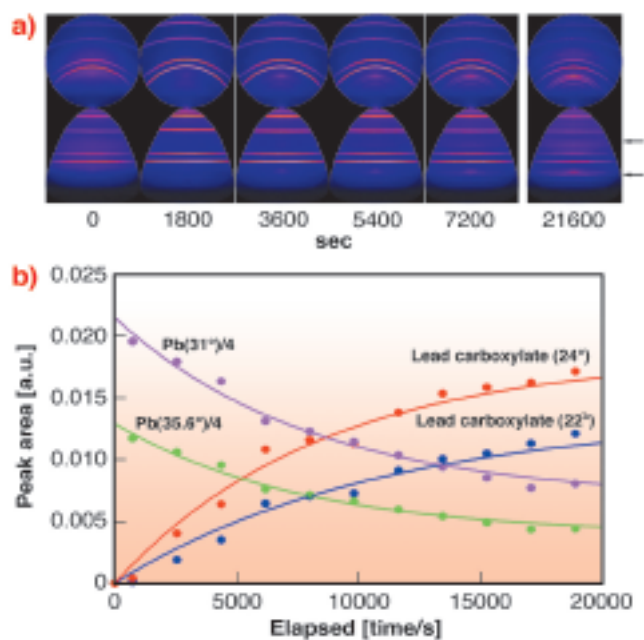


Fig. 95: a) XRD images (upper row) measured *in situ* and esaProject transforms (lower row) from the developing coating. The lead carboxylate regions are arrowed, other rings are due to lead. b) Areas of the X-ray peaks from the images as a function of time.

rings are smooth, which is indicative of a dense interlocking microcrystalline structure, ideal in a potential protective coating. Figure 95b shows the change in peak area extracted from a sequence of CCD images. That the lead is covered over is clearly evident and the data correlate well with the mass gain measurements. The simultaneous EIS measurements are indicative of the development of a high integrity layer free from pinholes.

The combination of XRD and EIS shows that the carboxylate coating is promising and has the basic characteristics required for a protective coating on lead. Future work will establish its durability.

## References

- [1] For more information see the website of the FP5 project COLLAPSE at [www.goart.gu.se/collapse/](http://www.goart.gu.se/collapse/).
- [2] E. Rocca, C. Rapin and F. Mirambet, *Corrosion Science* **46**, 653-665 (2004).
- [3] M. G. Dowsett and A. Adriaens, *Analytical Chemistry* **78**, 3360-3365 (2006).

## Principal publication and authors

M.G. Dowsett (a), A. Adriaens (b), B. Schotte (b), G.K.C. Jones (a) and L. Bouchenoire (c), *manuscript in preparation*.

(a) *Departments of Physics, University of Warwick, Coventry (UK)*

(b) *Department of Analytical Chemistry, Ghent University (Belgium)*

(c) *ESRF*

## What you see is what you get: Imaging on the atomic scale

### X-ray standing wave imaging of Mn in GaAs

The discovery of ferromagnetism in binary compound semiconductors doped with small amounts of magnetic elements has attracted great attention due to their potential applications in spintronic devices. GaMnAs is one of the prototype materials of such dilute magnetic semiconductors. It has achieved a Curie temperature ( $T_c$ ) of 170 K at a Mn concentration of 5% [1]. Theoretical calculations [2] show that when substituting the Ga, the Mn acts as an acceptor with a local spin moment of 5/2 and ferromagnetic ordering can be mediated by the itinerant holes. However, depending on the growth conditions and post-growth treatments, small fractions of Mn may occupy the interstitial sites (Figure 96a), where it acts as a donor, compensating the hole doping, and thus decreasing  $T_c$ . Determining the site distribution of the Mn is therefore important in order to achieve an

optimal  $T_c$ . However, as of now this had not been possible because of lack of reliable methods for characterising the structure of very dilute systems.

In the present study carried out at ID32, X-ray standing waves (XSW) generated by substrate (hkl) Bragg reflections at a photon energy of 10 keV were used to locate the Mn in the GaAs lattice. For each reflection, the amplitude as well as the phase of the (hkl) Fourier component of the Mn distribution were determined by recording the Mn  $K\alpha$  fluorescence during angular scans of the sample traversing the Bragg peak. Using a sufficiently large number of the reflections, a real-space image of Mn within the GaAs unit cell can be reconstructed via direct Fourier expansion.

Four nm thick epitaxial layers of GaMnAs with 4% of Mn were prepared by low-temperature molecular beam epitaxy on GaAs(001). Three samples with different post-growth treatments (as-grown, hydrogenated, and low-temperature annealed) were used for the XSW experiment. **Figure 96b** shows the 3-dimensional image of Mn reconstructed from 22 reflections for the as-grown film. Compared to the bulk GaAs structure shown in **Figure 96a**, the measured image gives direct evidence that the majority of the Mn substitutes the Ga. The images also reveal a vertical lattice expansion of the film, which increases after hydrogenation. **Figure 96c** and **Figure 96d** present simulations using the same 22 reflections assuming that 100% and 90%, respectively, of the Mn substitutes the Ga. In **Figure 96d** the remaining 10% of the Mn is placed at the Ga interstitial sites. Comparison of **Figure 96b** with **Figure 96c** and **Figure 96d** leads to the further conclusion that no Mn substitutes the As or occupies the Ga interstitial sites, based on the observation that the intensities of the eight weaker spots

inside the unit cell in **Figure 96b** appear identical. **Figure 96c** shows that these eight weaker spots arise mainly from the finite number of the Fourier components used in the expansion. Note that XSW imaging is limited to Fourier components given by the substrate (hkl) reflections. Due to the zinc blend symmetry, Mn atoms at the As interstitial sites are “invisible” as long as the majority substitutes the Ga.

To quantify the Mn site distribution, a structural model considering the Ga sites and As interstitial sites was introduced and refined. **Figure 96e** shows that this model, deduced from the images created by the Fourier expansion, is able to well reproduce the measured amplitudes and phases of the Fourier components of the Mn distribution for all three samples. The result of the refinement is summarised in **Figure 96f**, which provides the exact Mn site distributions for the different post-growth treatments and allows direct correlations between the structures and magnetic properties for dilute magnetic semiconductors.

#### Reference

- [1] A.H. MacDonald, P. Schiffer and N. Samarth, *Nature Materials* **4**, 195 (2005).
- [2] T. Dietl, H. Ohno and F. Matsukura, *Phys. Rev. B* **63**, 195205 (2001).

#### Principal Publication and Authors

T.-L. Lee (a), I. Joumard (a), J. Zegenhagen (a), W. Schoch (b), and M. Brandt (c)

(a) ESRF

(b) Abteilung Halbleiterphysik, Universität Ulm, Ulm (Germany)(c) Walter Schottky Institut, Technische Universität München, Garching (Germany)

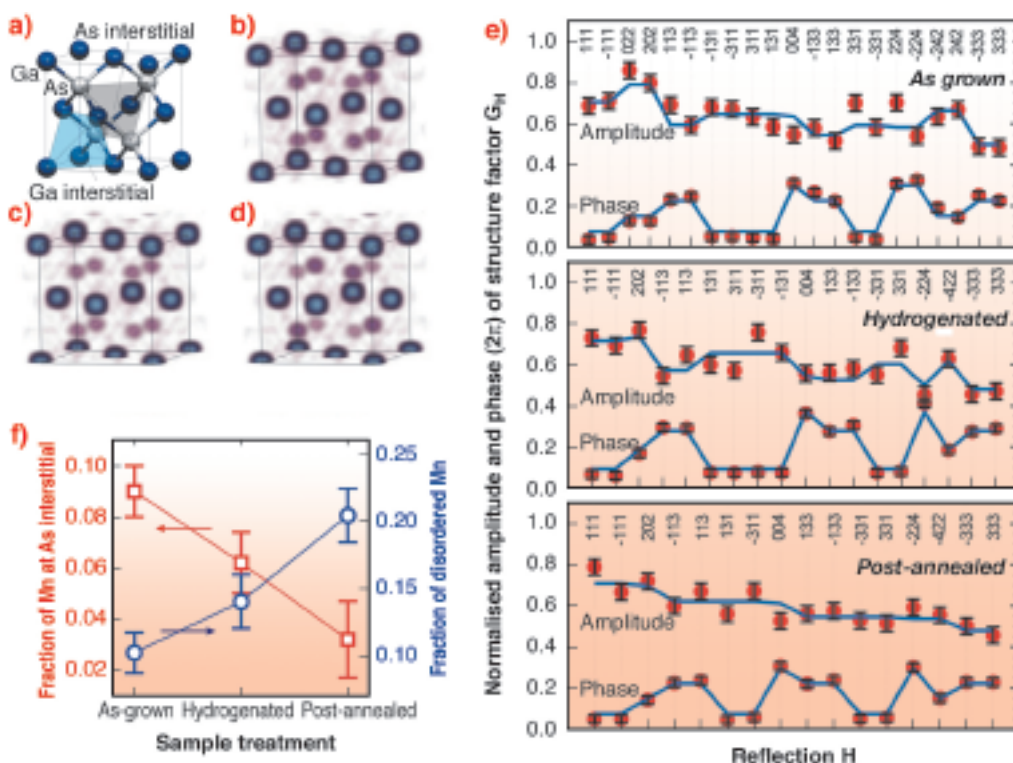


**Fig. 96:** a) Bulk structure of GaAs. The interstitial sites are located at the centres of the tetrahedrons. b) Direct image of Mn in the GaAs unit cell reconstructed from XSW measurements. c) and d) Simulated images of Mn assuming 100% and 90%, respectively, substitution of the Ga. In (d) the remaining 10% of the Mn is placed at the Ga interstitial sites. e) Measured (red dots) and refined (blue curves) amplitudes and phases of the Mn structure factors for the three samples. f) Site distribution and disorder of the Mn deduced from the structural refinement for the three post-growth treatments. It shows that up to 10% of the Mn occupies the As interstitial sites.



Highlights 2006

SCIENTIFIC HIGHLIGHTS

# X-ray Absorption and Magnetic Scattering

## Introduction

The Highlights in our selection this year are extremely diverse in their subject matter. This demonstrates the great versatility of the techniques used and the scientific interest in many fields of research. There are materials problems (ferroelectrics [Laulhé *et al.* p80] and negative thermal expansion [Sanson *et al.* p82]), catalysis [Newton *et al.* p78], geology [Muñoz *et al.* p79], studies at interfaces [Luches *et al.* p86], impurity problems [Sarigiannidou *et al.* p87] and dynamical studies [Goulon *et al.* p90], to name a few.

As in the past few years there are also many X-ray absorption studies which combine techniques, whether it be with diffraction (X-ray or neutron) or other spectroscopic methods. These combinations allow unique information to be obtained that would otherwise not be possible; see for example the catalysis study combining *in situ* time-resolved infrared and X-ray absorption spectroscopy [Newton *et al.* p78].

Studies with an emphasis on basic research also have a prominent place. For example, Kondo phenomena

[Venturini *et al.* p94], spin states [Haverkort *et al.* p88], dynamics [Goulon *et al.* p90] and multipolar ordering [Mazzoli *et al.* p91 and McEwen *et al.* p92]. This is extremely important, showing the health of the entire scientific field where both basic and applied problems can be addressed and where the limits are only the imagination of the scientists.

Clearly, there are many other examples of outstanding research which could not be included for space reasons. There are contributions to our understanding of the physics of magnetism at interfaces (ferromagnetic/antiferromagnetic [1] and ferromagnetic/superconducting [2]), magnetic impurities [3] and magnetism in nanoparticles [4]. Important work on metal-insulator transitions [5] and undercooling phenomena in nanoparticles [6] has also been carried out. In addition, synchronised time-resolved UV-Vis/XAS studies of catalysts [7] has added to the suite of *in situ* studies in chemistry. Nevertheless, these studies only represent a small part of the important research work being undertaken in this general research area. This large body of work gives us confidence

in the scientific future for the research fields addressed by X-ray absorption and magnetic scattering.

With the strong growth of synchrotron research in Europe and around the World there will be many possibilities for making important gains in our scientific understanding and consequently, it is important to look beyond what we have today and will have tomorrow and look towards the scientific challenges of the future. This will give us the "Highlights" of the coming decades.

**N. Brookes**

## References

- [1] J. Camareo *et al.*, *Appl. Phys. Lett.* **89**, 232507 (2006).
- [2] J. Chakhalian *et al.*, *Nature Physics* **2**, 244 (2006).
- [3] K. W. Edmonds *et al.*, *Phys. Rev. Lett.* **96**, 117207 (2006).
- [4] F. Luis *et al.*, *Europhys. Lett.* **76**, 142 (2006).
- [5] T. C. Koethe *et al.*, *Phys. Rev. Lett.* **97**, 116402 (2006).
- [6] G. B. Parravicini *et al.*, *Appl. Phys. Lett.* **89**, 033123 (2006).
- [7] G. Guilera *et al.*, *Chem. Commun.* **41**, 4306 (2006).

## Synchronising subsecond infrared and X-ray absorption spectroscopies to see inside a reactive process

Catalytic reactions mediated by heterogeneous catalysts are the hub of many important processes; the abatement of toxic emissions from car exhausts is a prime example. To this day, catalysts based upon a Rh component supported on an  $\text{Al}_2\text{O}_3$  dispersant can be found in practically any petrol driven car. Rh is present as it has a unique capacity for so called “de NOx” chemistry, wherein toxic species such as NO and  $\text{N}_2\text{O}$  are removed from the exhaust and replaced by  $\text{N}_2$ .

The details of how this conversion is mediated by Rh are, however, far from complete. Part of the reason for this is that such systems have never been studied in a manner that addresses their structural, functional, and reactive character at the same time, and with sufficient speed to see inside rapid processes. To this end a new experiment has been developed and implemented on **ID24**. This fuses a reactivity probe (mass spectrometry), a probe of surface functionality (diffuse reflectance infrared spectroscopy (DRIFTS)), and a time resolving probe of local structure (energy-dispersive extended X-ray absorption fine structure), to produce a methodology that can probe a reactive system in a more holistic manner.

**Figure 97** shows data typical of the DRIFTS (a) and dispersive EXAFS (b) components of the experiment. DRIFTS indexes the presence of a range of molecular NO species adsorbed on the surface of the catalyst, e.g.: linear ( $\text{NO}^+$ ),  $1911\text{ cm}^{-1}$ ; bent ( $\text{NO}^-$ ),  $1745\text{ cm}^{-1}$ ; geminal ( $\text{Rh}(\text{NO})_2$ ),  $1830$  and  $1745\text{ cm}^{-1}$ ; and NO associated with metallic Rh surfaces ( $1680\text{ cm}^{-1}$ ).

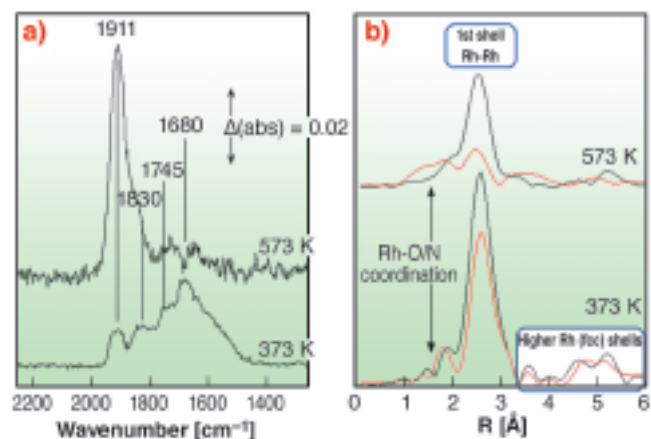


**Fig. 97:** a) DRIFTS spectra, acquired in 64 milliseconds, recorded after 50 seconds exposure of a 5wt%Rh/ $\text{Al}_2\text{O}_3$  catalyst to 5%NO/He at the temperatures indicated. b) Fourier Transform representation of dispersive EXAFS data, acquired in 62 milliseconds, before reaction (black) and after (red) NO exposure.

Dispersive EXAFS reveals how the local Rh structure changes in response to NO adsorption. At 373 K the Rh remains face centred (*fcc*), as indicated by the persistence of higher Rh shells that follow the expected radial progression for this structure. The average particle size (from the first shell Rh-Rh intensity) appears diminished as a result of molecular NO adsorption. At 573 K the interaction with NO changes the phase of the Rh. At this temperature NO dissociation predominates and the formation of an oxidic form of Rh results.

In between these points, a variety of structural-reactive chemistry has occurred. Some specific aspects of this “hidden” detail are shown in **Figure 98**. In this figure, for several temperatures, and for three of the observed NO species, the DRIFTS intensity (in absorbance units) is plotted as a function of Rh oxidation (from EXAFS). Additionally, the far right panel shows how the net selectivity of the interaction of NO varies with Rh oxidation.

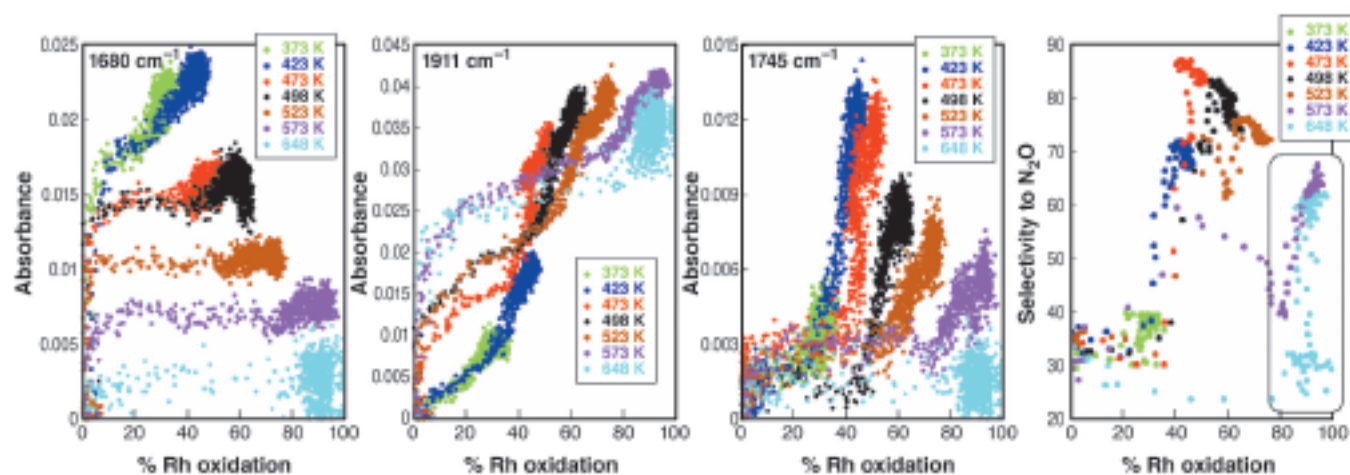


**Fig. 98:** Correlation plots relating Rh oxidation to surface nitrosyls and selectivity. 100% Rh oxidation is assumed as the attainment of an  $\text{Rh}_2\text{O}_3$  stoichiometry.

A clear correlation emerges between the bent nitrosyl species ( $1745\text{ cm}^{-1}$ ) and the selectivity, suggesting that it is this form of NO that plays a predominant role in the production of  $\text{N}_2\text{O}$ . Moreover, this species is only supported by the Rh in significant amounts over a relatively narrow range of Rh oxidation. Other forms of NO, associable with either very reduced ( $1680\text{ cm}^{-1}$ ) or very oxidised ( $1911\text{ cm}^{-1}$ ) Rh sites appear not, by and large, to have any great relation to the most active route for the production of  $\text{N}_2\text{O}$  from NO.

That said, the experiment also shows that a second route to  $\text{N}_2\text{O}$  can exist, but only at high T and high levels of Rh oxidation. The increase in selectivity for  $\text{N}_2\text{O}$  (circled in black) observed in these cases links this second mechanism to the persistence of the linear nitrosyl ( $1911\text{ cm}^{-1}$ ) on an oxidic Rh phase. Addition of an  $\text{NO}_{(g)}$  molecule, to this nitrosyl species can form  $\text{N}_2\text{O}$  directly, whilst simultaneously adding an O atom to, and removing a defect site from, the growing oxidic phase.

In summary, by combining time resolved EXAFS with infrared spectroscopy and mass spectrometry we have been able to see inside a fundamental gas-solid interaction and begun to reveal the parameterisation that determines how a catalyst mediates the conversion of a given substrate molecule to one or other possible end result.

This research was funded by the EPSRC UK (Grant Number GR/60744/01) and carried out under a Long Term Proposal award from the ESRF.

#### Principal Publications and Authors

M.A. Newton (a), A.J. Dent (b), S.G. Fiddy (c), B. Jyoti (d), J Evans (d), *Catal. Today*, doi: 10.1016/j.cattod.2006.09.034., *Phys. Chem. Chem. Phys.* **9**, 246-249 (2007); *J. Mater Chem.*, (2006) in press.

(a) ESRF

(b) Diamond Light Source (UK)

(c) SRS Daresbury laboratory (UK)

(d) School of Chemistry, University of Southampton, and Diamond Light Source (UK)

## Redox and speciation dispersive-XANES micro- mapping: application to a natural sample

We have recently developed a new way to investigate heterogeneous samples that lets us derive quantitative information relating to the oxidation state and/or the speciation of a given element as well as its concentration. The technique takes advantage of the key

features of a “dispersive-XAFS” beamline such as **ID24** at the ESRF, namely (1) simultaneous collection of a complete spectrum, (2) extremely fast data collection, and (3) high stability of the X-ray beam during data acquisition thanks to the “motionless optics”. Moreover, recent improvements of the optics allow a focal spot of around 5 by 5  $\mu\text{m}$  at the iron *K*-edge [1].

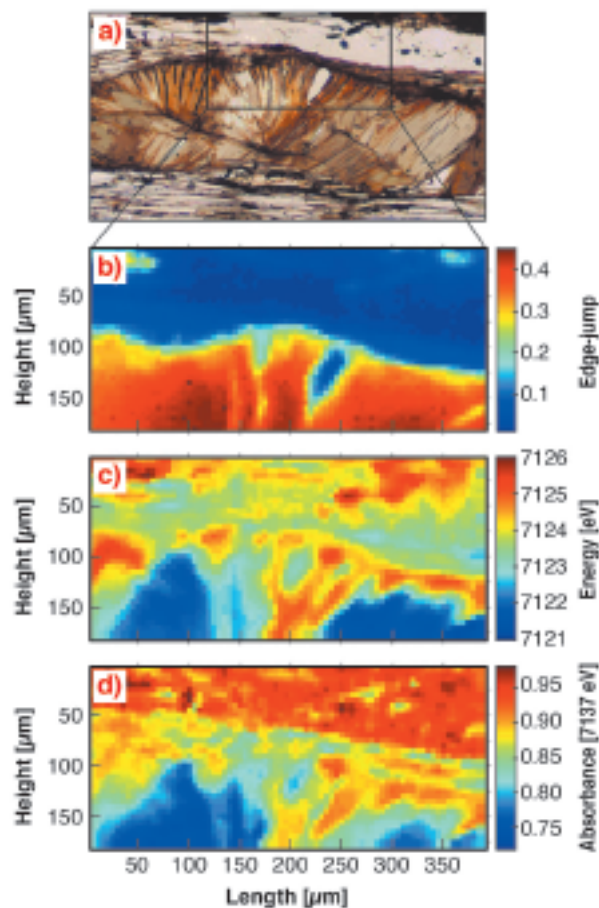


**Fig. 99:** a) Optical image showing chlorite (middle), quartz (top), and phengite (between chlorite and quartz and at the bottom); b) iron contents (edge-jump); c) iron redox (edge-position); d) iron speciation.

The first XANES measurements were made at the iron *K*-edge on a thin section of a metamorphic rock from the Sambagawa high-pressure belt (Shikoku Island). The sample was 30  $\mu\text{m}$  in thickness and was positioned on a 1 mm glass holder so that fluorescence detection was possible using the so-called “Turbo-XAFS” setup. The mapped region (390 by 180  $\mu\text{m}$ ) included minerals that are highly differentiated in terms of iron contents, examples being chlorite (~ 30 wt.%), phengite (~ 4 wt.%) and quartz (hundreds of ppm). The sampling was performed every 5  $\mu\text{m}$  so that around 3000 XANES spectra were collected in around 100 minutes. At this stage, it was possible to generate maps from the raw data at different energies, which are comparable to the “standard” XANES mapping technique (*i.e.* a collection of maps at different energies). However, dispersive-mapping provides “full-XANES spectra” collected in a single scan of the sample.

Such a “good quality” data set has potential for processing to extract quantitative information. Thus, the most significant part of this work consisted of developing tools to automate a reliable normalisation, and to provide access to information relating to the complete set of data. The program has been developed with Matlab®. Results revealed less than 0.5% of the spectra with aberrant normalisation, exclusively for extremely low iron content regions of the sample. **Figure 99** presents qualitative maps obtained after normalisation of the XANES spectra. In particular, edge-jump information was used to visualise the distribution of iron in the sample, and edge-position was used to visualise qualitatively the oxidation state of iron. Another map displays the normalised-absorbance at 7137 eV for the speciation of iron. Results show that iron is mainly located in chlorite (red region), while phengite and quartz are much less concentrated (**Figure 99b**, blue and dark blue regions, respectively). Also, the oxidation state of iron in chlorite appears highly contrasted. The dark blue corresponds to the more reduced regions whereas the red corresponds to the more oxidised ones (**Figure 99c**). Moreover, the “speciation” map shows a clear contrast for quartz, and a relatively good correlation with the “redox” distribution in chlorite (**Figure 99d**).

In order to derive quantitative information, we defined masks corresponding to each region highlighted from the different maps. **Figure 100** presents the different masks as well as the corresponding XANES (*i.e.* average of the spectra corresponding to the pixels of the masks). The signal-to-noise ratio is then high enough to analyse pre-edge peaks (see graph inset). Results obtained for

the redox contrast in chlorite are in excellent agreement with thermodynamic calculations [2].

This new approach of micro-XANES mapping opens new ways for the characterisation of heterogeneous materials in Earth Sciences, including *in situ* high-pressure and high-temperature “diamond-anvil cell” experiments. Other domains such as Physics, Chemistry or Life Sciences may also find some useful applications.

## References

- [1] S. Pascarelli, O. Mathon, M. Muñoz, T. Mairs, J. Susini, *J. Synchrotron Rad.*, **13**, 351-358 (2006).  
 [2] O. Vidal, V. De Andrade, E. Lewin, M. Muñoz, T. Parra, S. Pascarelli, *J. Metamorphic Geol.*, **24**, 669-683 (2006).

## Principal Publication and Authors

M. Muñoz (a, b), V. De Andrade (a), O. Vidal (a), E. Lewin (a), S. Pascarelli (b), J. Susini (b), *Geochem. Geophys. Geosyst.*, **7**, Q11020 (2006).  
 (a) *Laboratoire de Géodynamique des Chaînes Alpines, OSUG, Grenoble (France)*  
 (b) *ESRF*

## Study of size-effects on local polarisation in lead-free relaxor ferroelectrics $\text{BaTi}_{1-x}\text{Zr}_x\text{O}_3$

First discovered in 1959, the relaxor behaviour has become a major topic in materials science since the discovery of giant electromechanical responses in relaxor-based solid solutions [1]. The best properties are currently obtained with lead-containing relaxors (e.g.  $\text{PbMg}_{1/3}\text{Nb}_{2/3}\text{O}_3$ ). However, their toxicity raises environmental concerns, and a significant research effort is also concentrated on lead-free relaxors [2], such as  $\text{BaTi}_{1-x}\text{Zr}_x\text{O}_3$ .

Below the critical temperature  $T_c$ , classical ferroelectrics present a macroscopic polarisation. In the ferroelectric perovskite  $\text{BaTiO}_3$ , this polarisation is due to displacements of  $\text{Ba}^{2+}$  and  $\text{Ti}^{4+}$  cations with respect to the  $\text{O}^{2-}$  anions, which all occur in the same direction. Such displacements result in distortions with respect to the ideal cubic perovskite structure presented in **Figure 101a**. With increasing temperature, a sharp and frequency-independent divergence of the dielectric permittivity is observed at  $T_c$ , which corresponds to a structural phase transition: the ideal cubic perovskite structure is recovered. On the other hand, relaxors are characterised by a broad and frequency-dependent maximum of the dielectric permittivity as a function of

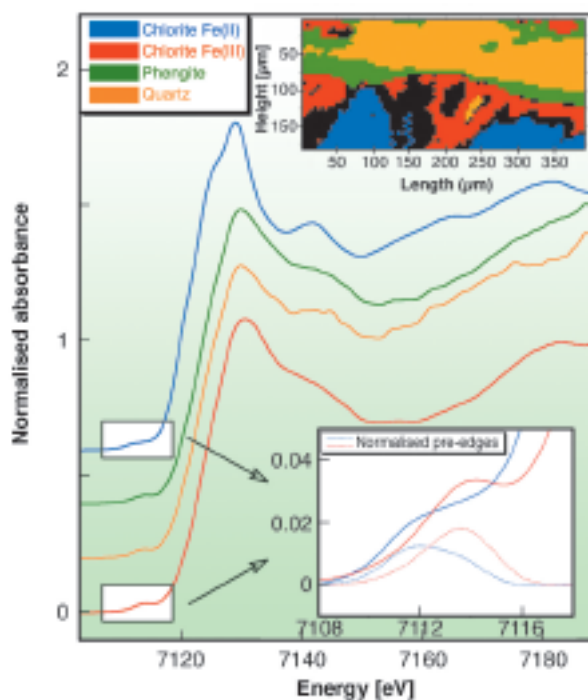


**Fig. 100:** Averaged XANES spectra corresponding to the different masks defined from the maps, and an enlargement of pre-edge peaks and their normalisation (dashed lines) for chlorite-Fe(II) and chlorite-Fe(III).

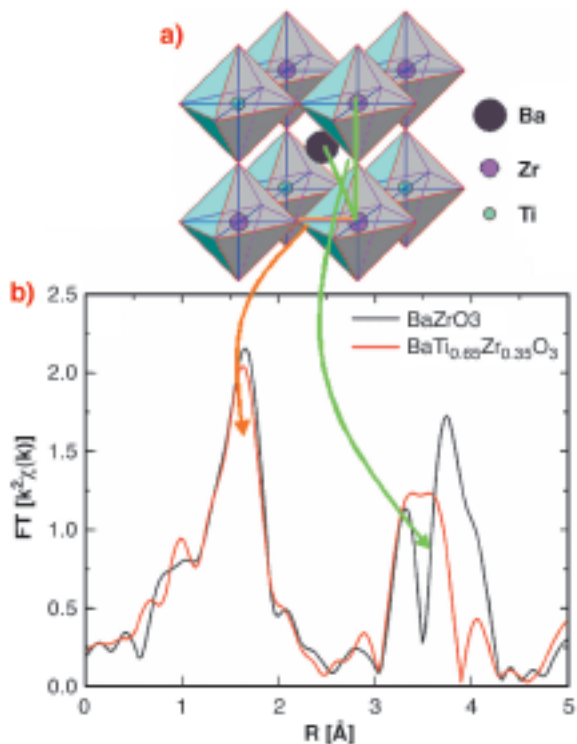


**Fig. 101:** a) The ideal perovskite structure, consisting of corner-linked oxygen octahedra. b) Modulus of the Fourier Transform of the  $k^2$ -weighted EXAFS signal for  $\text{BaZrO}_3$  and  $\text{BaTi}_{0.65}\text{Zr}_{0.35}\text{O}_3$  at the Zr  $K$ -edge.

temperature, which is not linked to a structural phase transition. In relaxor ferroelectrics, the polarisation is not macroscopic but local [3], due to cation displacements which are correlated on a nanometre scale only. Note that diffraction studies, which are sensitive to the average structure, suggest an apparently undistorted ideal perovskite structure in  $\text{BaTi}_{1-x}\text{Zr}_x\text{O}_3$  relaxors at any temperature, because all local cation displacements are averaged to zero.

The mechanism that leads to the formation of polar nanoregions in relaxors is still unclear. In most studied relaxors, an aliovalent cationic disorder (e.g.  $\text{Mg}^{2+}$  and  $\text{Nb}^{5+}$  in  $\text{PbMg}_{1/3}\text{Nb}_{2/3}\text{O}_3$ ) is related to a random fluctuation of charges and thus to random local electric fields, which in turn break long-range ferroelectric correlations. Contrary to this, the relaxor  $\text{BaTi}_{1-x}\text{Zr}_x\text{O}_3$  ( $0.25 \leq x \leq 0.5$ ) presents a homovalent  $\text{Zr}^{4+}/\text{Ti}^{4+}$  substitution on the octahedral sites, which cannot directly induce random electric fields. However, the difference in size of  $\text{Zr}^{4+}$  and  $\text{Ti}^{4+}$  cations ( $r_{\text{Zr}^{4+}}/r_{\text{Ti}^{4+}} = 1.18$ ) induces random elastic deformations, which could affect the displacement of the ferroelectrically active  $\text{Ti}^{4+}$  ions in their oxygen octahedra.

To investigate the local deformations induced by the Zr atoms in  $\text{BaTi}_{1-x}\text{Zr}_x\text{O}_3$ , X-ray absorption fine structure (EXAFS) experiments were carried out at the Zr  $K$ -edge in  $\text{BaTi}_{1-x}\text{Zr}_x\text{O}_3$  samples ( $x = 0.25, 0.30, 0.35$ , and 1), on the BM30B-FAME beamline. The Fourier Transforms of the EXAFS signals of the  $\text{BaTi}_{0.65}\text{Zr}_{0.35}\text{O}_3$  relaxor and the

end-member compound  $\text{BaZrO}_3$  are compared in **Figure 101b**. In the distance-range 1.2 – 2.3 Å, the analysis shows that the Zr-O distance measured by EXAFS is independent of  $x$  and equal to that measured in  $\text{BaZrO}_3$ . On the other hand, the X-ray cubic cell parameter increases linearly with  $x$  (**Figure 102a**). The  $\text{ZrO}_6$  octahedra thus form rigid units, which do not fit to the average structure volume. In the distance-range 2.5 – 4.5 Å, a careful analysis of the multiple scattering contributions reveals a buckling of the Zr-O-Zr bonds, which is not present in a perfect cubic structure (**Figure 102 c,d**). Although a partial accommodation to the average structure is probably obtained through the latter deformation, the Zr-Zr distance is still approximately 2% larger than the average (Zr/Ti)-(Zr/Ti) distance deduced from X-ray diffraction (**Figure 102b**). Moreover, the chemical sensitivity of EXAFS allows us to evidence a tendency of Zr atoms to segregate in Zr-rich regions.

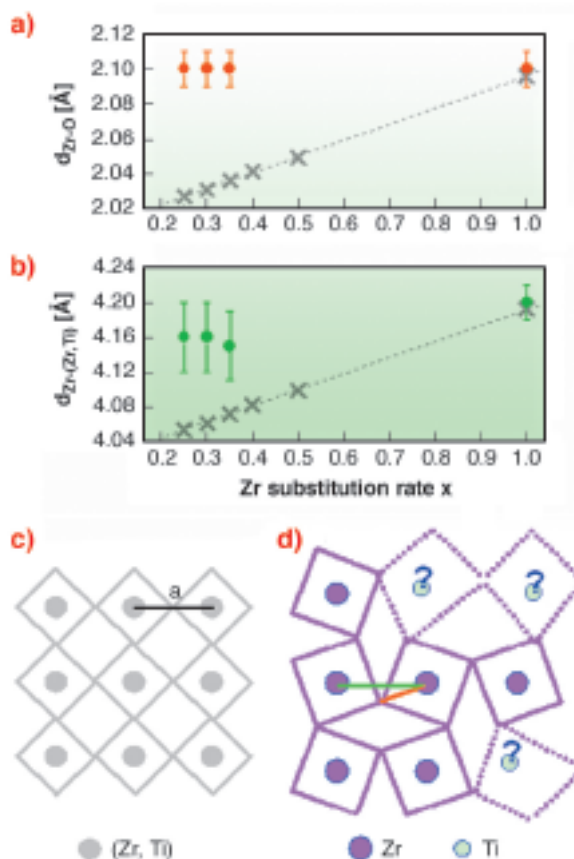


**Fig. 102:** Evolution of a) Zr-O and b) Zr-Zr distances with  $x$ : EXAFS results (circles), compared to  $a/2$  and  $a$  deduced from X-ray diffraction (crosses). Schematic top views of the structure of  $\text{BaTi}_{1-x}\text{Zr}_x\text{O}_3$  relaxors, according to either c) X-ray diffraction or d) EXAFS (the buckling angle is exaggerated for clarity).

From our results, one can conclude that the  $\text{ZrO}_6$  octahedra likely exert a significant tensile stress on the  $\text{TiO}_6$  octahedra at the interface of the Zr-rich regions. This tensile stress may generate particular  $\text{Ti}^{4+}$  local displacements (and thus local polarity). In this scenario, fluctuating local structural stress could then influence the formation of polar nanoregions in  $\text{BaTi}_{1-x}\text{Zr}_x\text{O}_3$  relaxors, similarly to fluctuating charges in common relaxors.

## References

- [1] S.E. Park and T.R. Shroud, *J. Appl. Phys.* **82**, 1804 (1997).  
 [2] L.E. Cross, *Nature* **432**, 24 (2004); Y. Saito *et al.*, *Nature* **432**, 84 (2004).  
 [3] L.E. Cross, *Ferroelectrics* **76**, 241-267 (1987); *Ferroelectrics* **151**, 305-320 (1994).

## Principal Publication and Authors

C. Laulhé (a), F. Hippert (a), J. Kreisel (a), M. Maglione (b), A. Simon (b), J.-L. Hazemann (c), V. Nassif (d), *Phys. Rev. B* **74**, 014106 (2006)

(a) *Laboratoire Matériaux et Génie Physique, CNRS-INP Grenoble (France)*

(b) *Institut de Chimie de la Matière Condensée de Bordeaux, CNRS Bordeaux (France)*

(c) *Laboratoire de Cristallographie, CNRS Grenoble (France)*

(d) *DRFMC/SP2M/NRS, CEA Grenoble (France)*

## Negative thermal expansion and local dynamics in $\text{Cu}_2\text{O}$ and $\text{Ag}_2\text{O}$

While most crystals expand when temperature is increased, some framework structures, composed by networks of corner-sharing polyhedral structural units, exhibit negative thermal expansion (NTE) extending over temperature intervals of several hundreds of Kelvin; the most popular example is  $\text{ZrW}_2\text{O}_8$ , where NTE extends up to 1050 K. The macroscopic thermal expansion is generally considered the result of competition between a positive contribution due to bond stretching and a negative contribution of geometrical origin, like bond bending, which in framework structures is often connected to low-frequency rigid unit modes (RUMs) which cause rigid rotations of the basic polyhedral units. While it is generally accepted that thermal vibrations perpendicular to inter-atomic bonds play a key role in NTE, a satisfactory quantitative understanding of the local mechanisms is still lacking [1].

New information on the origin of NTE can be gained by combining Bragg diffraction and EXAFS, and exploiting the different sensitivity of the two techniques to atomic vibrations and thermal expansion. Bragg diffraction measures the distances between average atomic positions and the atomic thermal factors of individual atoms (MSDs), EXAFS is sensitive to the average bond distances and measures the variance of the bond-length distribution (parallel MSRD). The thermal expansions measured by EXAFS and diffraction are different, and their comparison allows one to evaluate the MSRD perpendicular to the bond length [2].

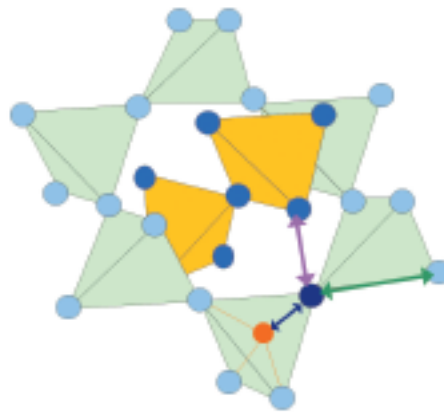


**Fig. 103:** The cuprite structure is made by two interpenetrating networks of corner sharing  $\text{M}_4\text{O}$  tetrahedra ( $\text{M}=\text{Cu}, \text{Ag}$ ).

Copper(I) and Silver(I) oxides,  $\text{Cu}_2\text{O}$  and  $\text{Ag}_2\text{O}$ , are particularly well suited to study the NTE mechanism. Both compounds share the same simple cuprite structure, made by two interpenetrating lattices, one fcc of metal atoms, one bcc of oxygen atoms, which can alternatively be considered as formed by two interpenetrating networks of corner-sharing  $\text{M}_4\text{O}$  tetrahedra ( $\text{M}=\text{Cu}, \text{Ag}$ ); each M atom is linearly coordinated to two O atoms, and each O atom is tetrahedrally coordinated to four M atoms (Figure 103).

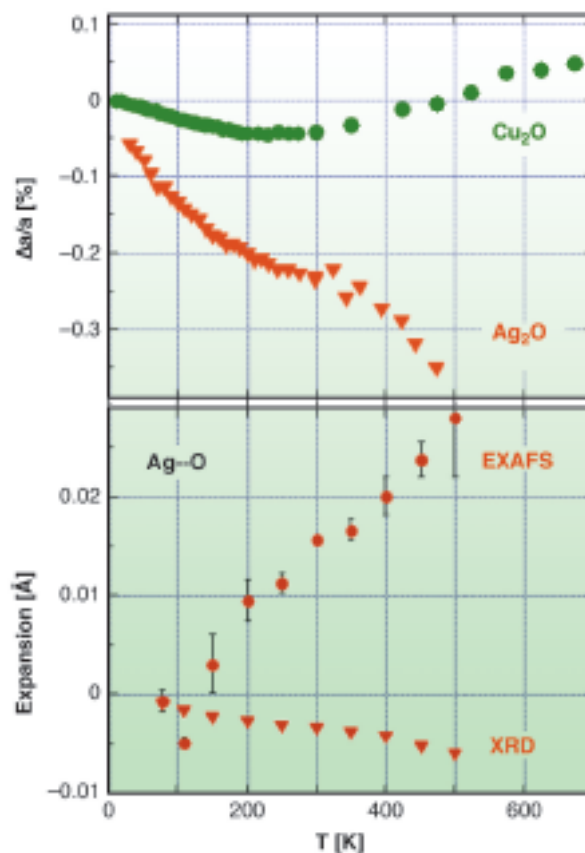


**Fig. 104:** Relative lattice expansions of  $\text{Cu}_2\text{O}$  and  $\text{Ag}_2\text{O}$  measured by Bragg diffraction (top panel) and comparison between Ag-O distance expansion measured by Bragg diffraction and EXAFS (triangles and circles, respectively, in bottom panel).

Both compounds are characterised by NTE extending over large temperature intervals, although with different extents and temperature dependencies (**Figure 104**).

$\text{Cu}_2\text{O}$  and  $\text{Ag}_2\text{O}$  have been studied at the ESRF by diffraction (beamlines BM16 and ID31) and EXAFS (BM08 and BM29). According to diffraction, thermal expansion in  $\text{Cu}_2\text{O}$  is negative below 240 K, and becomes positive above 300 K, while in  $\text{Ag}_2\text{O}$  it is negative up to at least 470 K, and much stronger than in  $\text{Cu}_2\text{O}$ . The thermal factors of M atoms are anisotropic, characterised by a large vibrational amplitude perpendicular to the O-M-O linear link.

EXAFS shows that the nearest neighbour M-O distance (dark blue arrow in **Figure 103**, and bottom panel in **Figure 104**) undergoes *positive* expansion in both compounds. Moreover, the stronger the lattice negative expansion ( $\text{Ag}_2\text{O}$  versus  $\text{Cu}_2\text{O}$ ), the larger the positive M-O expansion and the perpendicular MSRD. Further information was gained by comparing the EXAFS MSRDs with the diffraction MSDs. The correlation of atomic motion in the parallel direction is near its maximum possible value, while a weaker correlation affects the perpendicular motion, indicating that the M-O bond is much stiffer towards stretching than towards bending, and that the perpendicular to parallel anisotropy of relative thermal motion (EXAFS) is stronger than the anisotropy of the absolute motion of Cu and Ag atoms (diffraction).

A refined second-shell analysis led us to distinguish the different behaviour of the two kinds of M--M pairs, having the same crystallographic bond-lengths but belonging to the same or to different networks of  $\text{M}_4\text{O}$  tetrahedra (green and pink arrows in **Figure 103**, respectively): negative and positive expansion is observed for the intra-network and inter-network pairs, respectively, the former undergoing a weaker parallel relative motion than the latter.

These results reveal a complex local behaviour in a relatively simple structure, the correlation of vibrational motion playing a key role. The intense relative motion of second-shell M--M atomic pairs indicates a strong deformation of the  $\text{M}_4\text{O}$  tetrahedra, ruling out the possibility of explaining NTE in cuprite structures by a simple RUM model. The stiffness of the M-O bonds suggests that an alternative model for NTE in cuprites could be based on the more flexible idea of rigid M-O rods.

## References

- [1] G.D. Barrera, J.A. Bruno, T.H.K. Barron and N.L. Allan, *J. Phys.: Condens. Matter* **17**, R217 (2005).  
 [2] P. Fornasini, S. a Beccara, G. Dalba, R. Grisenti, A. Sanson, M. Vaccari and F. Rocca, *Phys. Rev B* **70**, 1 (2004).

## Principal publication and authors

A. Sanson (a), F. Rocca (a), G. Dalba (b), P. Fornasini (b), R. Grisenti (b), M. Dapiaggi (c) and G. Artioli (c), *Phys.*

*Rev B* **73**, 214305 (2006).

(a) IFN-CNR, Trento (Italy)

(b) INFM & Dip. Fisica, Univ. Trento (Italy)

(c) Dip. Scienze della Terra, Univ. Milano (Italy)

## Bacterial S-layers as template for the formation of Pd nanoclusters

Nanocatalysts made from palladium and other noble metals promise to accelerate chemical reactions even at low temperatures. Critical for the efficiency of these catalysts is a perfect control of their cluster-size. By using the surface protein layer (so-called S-layer) of a bacterium, particles with a uniform size distribution of 50 to 80 Pd atoms can be generated. For the first time, the bonding sites between the metal and the S-layer protein have been characterised. Hereby, the prerequisite is given to manipulate this protein by genetic engineering enabling the design of materials with new optic, magnetic and catalytic properties.

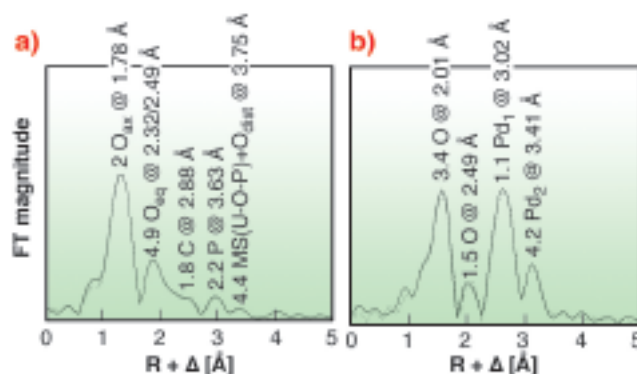


**Fig. 105:** a) U  $L_{III}$ -edge EXAFS of U(VI) complexes, and b) Pd K-edge EXAFS of Pd(II) complexes, formed by S-layers of *B. sphaericus*.

To produce nanoparticles of the noble metal palladium, a team of biologists from the Forschungszentrum Dresden-Rossendorf (FZD)/Germany use the S-layer of *Bacillus sphaericus* strain JG-A12. The biologists discovered this bacterium in 1997 from a uranium mining waste pile and have since then cultivated it in the laboratory. The bacterium survives in the extreme environment because it is able to tolerate high amounts of heavy metals including uranium [1,2]. One part of its survival strategy seems to be the formation of a protective outer layer, the S-layer, which exhibits a high metal-binding capacity, thereby preventing the cellular uptake of heavy metals. The S-layer protein of this bacterium is regularly structured with pores of identical size on the nanometre scale. The uranium uptake mechanism was investigated by EXAFS performed at the Rossendorf Beamline (BM20). The measurements

revealed that the purified S-layer proteins of this bacterium coordinate uranium through phosphate groups of phosphorylated serine and threonine in a monodentate mode as well as through carboxyl groups of aspartic and glutamic acids in a bidentate mode (**Figure 105a**) [2].

The heavy metal binding capacity of the S-layer led to the idea to use it as template for the formation of Pd nanoclusters. Within the pores of the S-layer, isolated from vegetative bacteria, Pd(II) solutions are reduced to metallic palladium by the use of hydrogen. This procedure forms nanoclusters of metallic palladium, with a uniform particle size of 50 to 80 Pd atoms, which are regularly arranged on the surface layer (**Figure 106**).

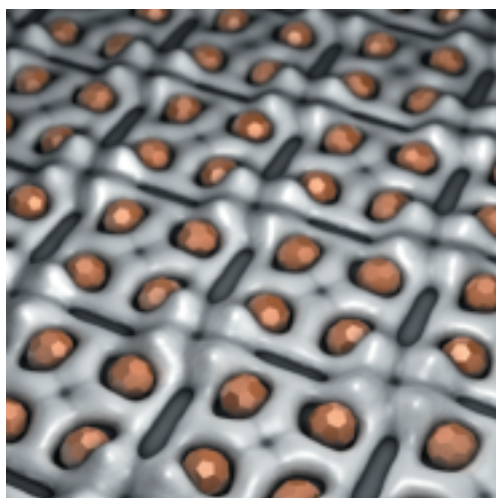


**Fig. 106:** Schematic view of Pd nanoclusters located at the S-layer protein.

In order to investigate the metal-protein interactions and their impact on the secondary structure, a solution of Pd(II) ions has been adsorbed on the S-layer matrix. The combination of Fourier transform infrared spectroscopy and EXAFS spectroscopy revealed that the surface Pd(II) is predominantly coordinated by aspartic and glutamic residues through four nitrogen and oxygen atoms at a distance of 2.01 Å (**Figure 105b**). In contrast to U(VI), that binds to carboxyl and phosphate groups, Pd(II) binds exclusively to the carboxyl groups of the S-layer. The topology of nitrogen- and carboxyl-bearing side chains appears to mediate the binding of heavy metals to aspartic and glutamic acids. These side chains are thus targets for the design of engineered S-layer based nanoclusters.

Because the metal stabilises the protein and vice versa, the S-layer stays intact at higher temperatures or even in an acidic environment. By modifying the distribution of functional groups and the ternary structure of the proteins, the Pd cluster size can be modified and a uniform size distribution can be achieved. A few laboratories are already producing and testing this new technology.

## References

- [1] C. Hennig, P.J. Panak, T. Reich, A. Rossberg, J. Raff, S. Selenska-Pobell, W. Matz, J.J. Bucher, G. Bernhard, H. Nitsche, *Radiochim. Acta* **89**, 625-631 (2001).  
 [2] M.L. Merroun, J. Raff, A. Rossberg, C. Hennig, T. Reich, S. Selenska-Pobell, *Appl. Environ. Microbiol.* **71**, 5532-5543 (2005).

## Principal publication and authors

K. Fahmy (a), M. Merroun (b), K. Pollmann (b), J. Raff (b), O. Savchuk (a), C. Hennig (b,c), S. Selenska-Pobell (b), *Biophysical J.* **91**, 996-1007 (2006).

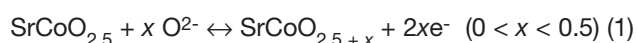
(a) *Institute of Nuclear and Hadron Physics, Division of Biophysics, Forschungszentrum Dresden-Rossendorf (Germany)*

(b) *Institute of Radiochemistry, Forschungszentrum Dresden-Rossendorf (Germany)*

(c) *Rossendorf Beamline, ESRF (France)*

## Time resolved *in situ* studies of oxygen intercalation into SrCoO<sub>2.5</sub> performed by X-ray absorption spectroscopy and neutron diffraction

Fuel cells based on solid oxides allow the transformation of chemical to electrical energy using a large variety of different molecules. They represent a key technology in a modern and more environmentally friendly society. In recent years, great effort has been made in the optimisation of membranes characterised by good oxygen mobility. Unfortunately, good oxygen mobility is usually reached at high temperatures. For fuel cells, the operating temperatures are usually about 1000°C. Under such extreme conditions the mechanical and thermal stability of electrodes are significantly limited. One of the very few exceptions is the SrCoO<sub>2.5</sub> system, which can be electrochemically oxidised via a reversible topotactic redox reaction, in an aqueous alkaline electrolyte at room temperature, yielding SrCoO<sub>3.0</sub> as the final reaction product [1]. The reaction can formally be described by:



The electrochemical oxidation of the antiferromagnetically ordered SrCoO<sub>2.5</sub>, with brownmillerite type structure, to the cubic ferromagnet SrCoO<sub>3</sub>, with perovskite structure, has been investigated *in situ* by neutron powder diffraction (NPD) as well as by XAFS spectroscopy, in specially designed electrochemical cells as a function of the charge transfer.

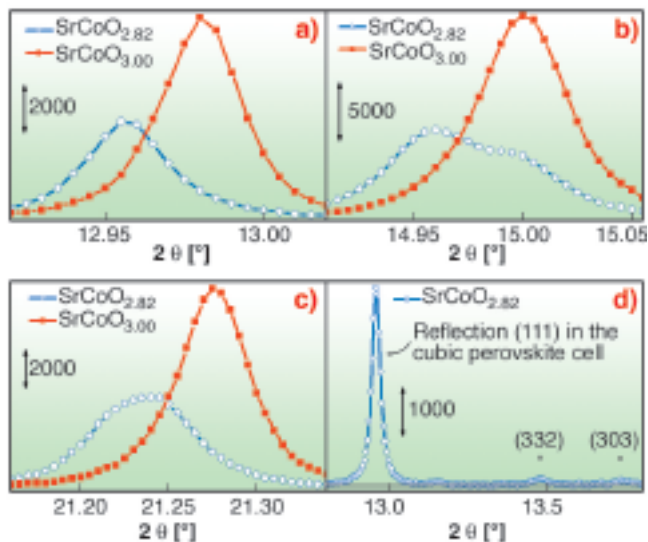


**Fig. 107:** High resolution XRPD collected at BM01B of cubic SrCoO<sub>3.00</sub> (red) and SrCoO<sub>2.82</sub> (blue) phases for the reflection profiles a) (111); b) (200); c) (220). d) the weak superstructure reflections ( $d = 2.48$  and  $2.08$  Å), marked by the stars, are indexed in the  $I4/mmm$  space group.

From the NPD experiments, two intermediate phases, SrCoO<sub>2.75</sub> and SrCoO<sub>2.82±0.07</sub>, have been characterised. Superstructure reflections have been observed for the SrCoO<sub>2.82</sub> phase only. To investigate the true symmetry of the intermediate phase, an electrochemically prepared sample of SrCoO<sub>2.82</sub> has been measured *ex situ* on the high-resolution powder diffractometer at beamline **BM01B**. It was found that reflections, indexed in the averaged cubic perovskite cell as (h00) or (hh0), are clearly separated into two distinct diffraction peaks, whereas (hhh) reflections were unique, see **Figure 107a-c**, where the profiles of (111), (200), (220) reflections are reported and compared with that of the cubic SrCoO<sub>3</sub> perovskite. This combined NPD and XRPD study represents the first observation of 3D oxygen ordering during an oxygen intercalation reaction. The SrCoO<sub>2.82</sub> phase can be described as being in a tetragonal unit cell, related to the perovskite cell by  $a = b = 2a\sqrt{2}$  and  $c = 2a$ . The structure of this intermediate phase confirms the strongly topotactic character of the oxygen intercalation reaction. Moreover, the observation of the reflections with XRPD, **Figure 107d**, at the same  $d$ -values found with NPD ( $2.48$  Å and  $2.08$  Å) proves their non-magnetic origin.

The SrCoO<sub>2.5</sub> → SrCoO<sub>3.0</sub> oxidation has also been followed by *in situ* XAFS spectroscopy at the Co K-edge at BM29. **Figures 108a** and **108b** report the evolution of the XANES, of the extended region of the absorption spectra, and of their  $k^3$ -weighted FT. **Figure 108d** summarises the XAFS data, where all XANES (squares) and EXAFS (circles) spectra along the reaction have been simulated as a linear combination of the two reference spectra of the starting (SrCoO<sub>2.5</sub>) and final (SrCoO<sub>3.0</sub>) phases [2], without imposing the sum of the fraction to be equal to unity, see **Figure 108e**. From

**Figure 108d** it emerges that the evolution of the Co valence state from formally +3 to +4 (XANES and edge shift) as well as the average Co local environment does not proceed continuously but gives the first evidence for the formation of O<sup>-</sup> species during an oxygen intercalation reaction, and more specifically for stoichiometries corresponding to SrCoO<sub>2.82±0.07</sub>.

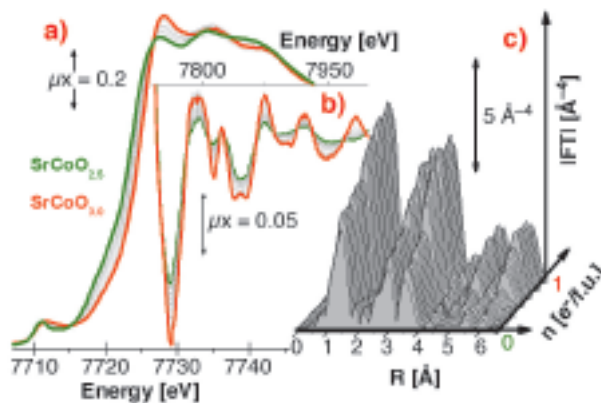


**Fig. 108:** a) Evolution of the XANES; b) of the extended region of the absorption spectra; c) of their  $k^3$ -weighted FT along the *in situ* SrCoO<sub>2.5</sub> → SrCoO<sub>3.0</sub> oxidation. The spectra of the starting phase and final phase are green and red respectively. d) reports the fractions of the reduced,  $x^{\text{red}}$ , and oxidised,  $y^{\text{ox}}$ , estimated by reproducing the generic spectrum (both XANES and EXAFS) along the reaction as a linear combination of the two reference spectra of the starting (SrCoO<sub>2.5</sub>) and final (SrCoO<sub>3.0</sub>) phases; e) without imposing the sum of the fraction to be equal to unity.

## References

- [1] J.C. Grenier, A. Wattiaux, J.-P. Doumerc, L. Fournes, J.-P. Cheminade, M. Pouchard, *J. Solid State Chem.* **96**, 20-30 (1992).
- [2] C. Lamberti, S. Bordiga, F. Bonino, C. Prestipino, G. Berlier, L. Capello, F. D'Acapito, F. X. Llabrés i Xamena and A. Zecchina, *Phys. Chem. Chem. Phys.*, **5**, 4502-4509 (2003).

**Principal publication and Authors**

R. Le Toquin (a,b), W. Paulus (a), A. Cousson (b), C. Prestipino (c,d), S. De Panfilis (d) C. Lamberti (c), *J. Am. Chem. Soc.*, **128**, 13161-13174 (2006).

(a) *Sciences Chimiques de Rennes, Université de Rennes 1 (France)*

(b) *Laboratoire Léon Brillouin, CEA-CNRS, Gif sur Yvette, (France)*

(c) *NIS centre of excellence University of Turin, and INSTM (Italy)*

(d) *ESRF (France)*

## Structure of the Fe/NiO(001) interface measured by polarisation dependent XAFS

Interfaces between ferromagnetic (FM) and antiferromagnetic (AFM) materials constitute one of the active elements of new magneto-electronic devices, which exploit the electron's spin rather than its charge for information processing and transfer. The exchange interactions at the interface formed between the FM and the AFM layers result in an unidirectional magnetic anisotropy, the so called exchange bias, of which a quantitative explanation is presently lacking [1]. Exchange bias leads to a shift of the magnetic hysteresis curve. In many cases, real FM/AFM interfaces are not ideal in their structure and chemistry and their atomic configuration is expected to have a very strong influence on the magnetic couplings between the two materials.

We investigated the case of an epitaxial system, Fe/NiO(001), taken as a model for a FM metal/AFM oxide interface, and obtained a combined experimental and theoretical description for it, which provides new insight in the understanding of magnetic couplings in such systems.

The sample used for this study was a UHV grown 2 ML Fe/10 ML NiO/Ag(001) multilayer, capped by a 10 nm thick Au layer to prevent sample contamination by the atmosphere. Fe K-edge X-ray absorption fine structure (XAFS) measurements were performed at the BM08 "GILDA" beamline. We exploited the polarisation dependence of the XAFS cross section in order to separately probe the in-plane and out-of-plane structure [2].

The background subtracted XAFS spectra in the two geometries are shown in **Figure 109a** and the corresponding magnitude of the Fourier transforms and the results of structural fits are shown in **Figure 109b**. The data demonstrate the formation of a planar FeO-like layer at the Fe/NiO interface and fitting allowed to

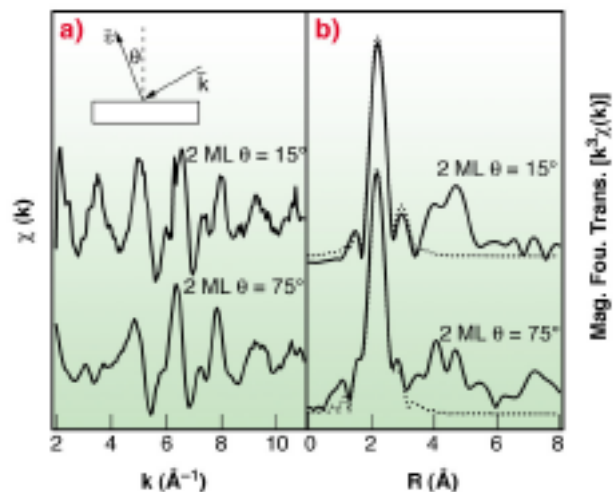
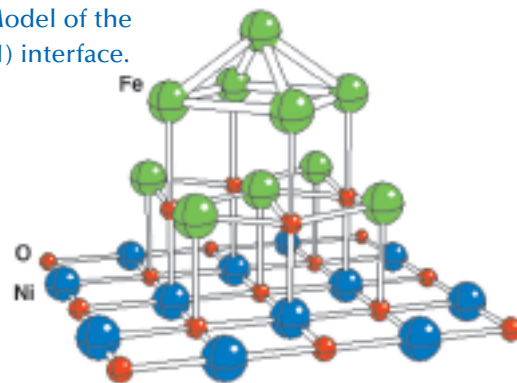


**Fig. 109:** a) Background subtracted Fe K-edge XAFS spectra for the 2 ML Fe film in the two geometries. b) Corresponding  $k^3$  weighted magnitude of the Fourier transforms (solid line) and fit (dashed line).

determine the interface geometry (see **Figure 110**). The FeO-like layer exhibits a buckling, with O and Fe atoms respectively shifted towards and away from the underlying NiO substrate. Moreover, the distance between the last NiO plane and the average position of the FeO plane is 7% larger than the interplanar distance of bulk NiO. A body-centered-tetragonal (bct) Fe-Ni phase is present on top of the interfacial FeO layer.

**Fig. 110:** Model of the Fe/NiO(001) interface.



We have compared the structural parameters obtained by the XAFS analysis to the results of density functional theory calculations performed by means of the all-electron linearised augmented plane wave method + local orbital in the generalised gradient approximation. The atomic configurations of the structurally relaxed system compare very well with the experimental ones. In particular, the numerical agreement between the values for the buckling of the FeO layer (experiment:  $0.29 \pm 0.07$  Å; theory: 0.34 Å) and for the expanded distance between the FeO layer and the underlying NiO (exp.  $2.24 \pm 0.08$  Å; th. 2.25 Å) is notable. Our calculations also allowed us to evaluate the spin magnetic moment of the Fe atoms at the interface, providing an original insight into the relation between structure and magnetic properties. We compared the

values obtained assuming the presence of a pure, pseudomorphic, Fe layer and the formation of an oxidised FeO layer. A significant increase of approximately  $0.6 \mu_B$  (from  $2.6 \mu_B$  to  $3.2 \mu_B$ ) in the presence of the distorted FeO layer was found. The origin of this change lies in a depopulation of minority spin  $d$  orbitals involved in the Fe-O bonds. The Fe atoms of the interfacial FeO layer assumed in our model are in fact more coordinated with oxygen atoms than Fe atoms situated in the first layer of the ideal Fe/NiO interface, therefore a higher spin polarisation is achieved. Uncompensated moments coming from the interfacial FeO layer, which may couple ferromagnetically with the Fe layer, are expected to dramatically influence the exchange interaction at the Fe/NiO interface, with significant consequences also for the exchange bias mechanism.

In summary, we give evidence for the presence of a structurally distorted FeO layer at the Fe/NiO(001) interface, in which the spin magnetic moment of Fe atoms is increased compared to the abrupt interface. This work provides the atomic level characterisation necessary in order to provide a structural basis for a physical understanding of exchange bias in FM/AFM interfaces.

## References

- [1] J. Nogués and I.K. Schuller, *J. Magn. Magn. Mater.* **192** 203 (1999).  
 [2] E. Groppo *et al.*, *J. Phys. Chem. B* **107** 4597 (2003).

## Principal publication and authors

P. Luches (a), V. Bellini (a), S. Colonna (b), L. Di Giustino (a), F. Manghi (a,c), S. Valeri (a,c), F. Boscherini (d), *Physical Review Letters* **96**, 106106 (2006).  
 (a) S3, CNR-INFN, Modena (Italy)  
 (b) ISM-CNR, Roma (Italy)  
 (c) Department of Physics, University of Modena and Reggio Emilia, Modena (Italy)  
 (d) Department of Physics and CNISM, University of Bologna (Italy)

# Hard X-ray dichroism in a ferromagnetic GaMnN wurtzite film

The idea of achieving room-temperature ferromagnetism in diluted magnetic semiconductors (DMS) attracts a lot of interest due to DMS importance for developing future “spintronic” devices. One of the most promising systems is GaN diluted with Mn. A ferromagnetic ordering of (Ga,Mn)N at room temperature has been observed by several groups, while others have reported on its paramagnetic behaviour. State-of-the-art characterisation techniques and single-phase (Ga,Mn)N layers are required

to clarify the electronic and magnetic properties of Mn atoms, and consequently to reveal the microscopic origin of magnetism that occurs in this DMS.

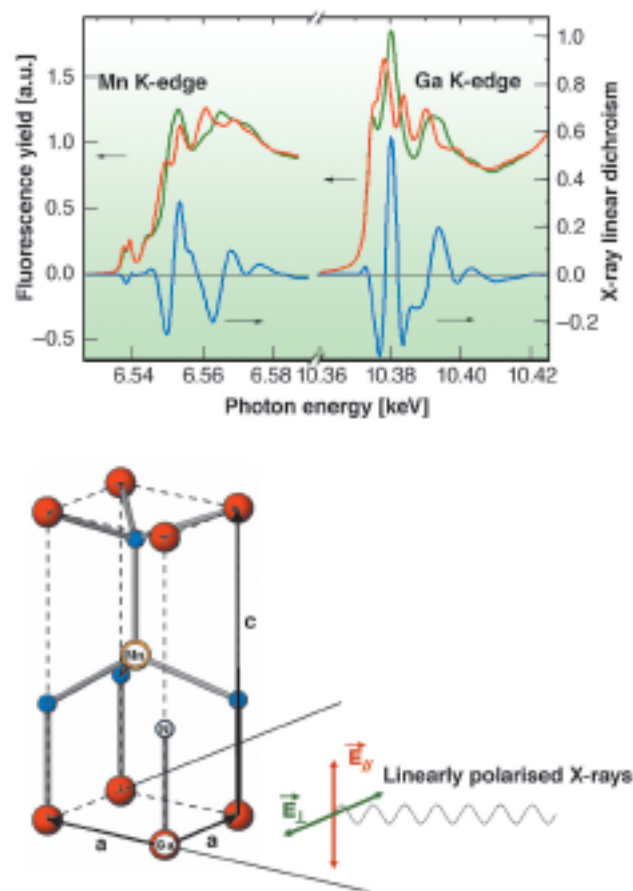


**Fig. 111:** Experimental configuration for XLD measurements. Normalised experimental XANES spectra (left scale) for linearly polarised X-ray light oriented parallel (red line) and perpendicular (green line) to the  $c$  axis and XLD (blue line, right scale) signal recorded at the Mn and Ga  $K$  edges for a (Ga,Mn)N epilayer with 6.3% Mn.

X-ray linear dichroism (XLD) and X-ray magnetic circular dichroism (XMCD) spectroscopies have been used to study the structural, electronic, and magnetic properties of DMS thin films. Since these techniques are element specific, they are the most appropriate tools for directly probing the electronic structure and magnetism of the diluted transition metal. Wurtzite (Ga,Mn)N with 6.3% Mn epilayer film was grown using plasma-assisted molecular beam epitaxy, with standard effusion cells for Ga and Mn, and a radio-frequency plasma cell to supply active nitrogen. XLD and XMCD experiments were performed at beamline ID12. XLD were recorded at both the Mn and the Ga  $K$ -edge using a diamond quarter wave plate to convert circularly polarised X-rays into linearly polarised ones. Using the geometry of the experiment shown on **Figure 111**, the XLD measures the anisotropy of the unoccupied density of states of the  $4p$  shell of the Ga and Mn atoms in the  $(a,c)$  plane of the wurtzite structure. The Mn  $K$ -edge XLD spectral shape (**Figure 111**) is very similar to the one observed at the Ga

K edge (identical to the Ga K-edge XLD of GaN single crystal), but its amplitude is 1.8 times smaller. This is precisely what one would observe for the Mn atoms in substitution with Ga atoms, whereas for other possible Mn sites occupation, e.g. N-substituted or interstitial sites, the spectral shape and amplitude of XLD signal should be drastically different [1]. Within the detection limit of the method, the presence of any secondary phases or metallic clusters have not been revealed. The XANES spectrum at the Mn K edge in contrast with XLD spectra are quite different from those at the Ga K edge. Two additional peaks at the low-energy side of the absorption edge are observed. These two peaks originate from both quadrupolar ( $1s \rightarrow 3d$ ) and dipolar ( $1s \rightarrow 4p$ ) transitions reflecting hybridisation of the Mn impurity  $4p$  band with the  $3d$  band located in the GaN gap. The presence of these two peaks in the XANES spectra indicates that the valence state of Mn is mainly  $3+$  ( $d^4$ ) rather than  $2+$  ( $d^5$ ), where only one peak is usually observed. To elucidate the microscopic origin of the magnetic behaviour of (Ga,Mn)N, we have performed XMCD measurements at the Mn K edge (Figure 112). A very intense XMCD signal (1.6% with respect to the edge jump) is observed mainly at the first peak of the XANES spectrum. Given the fact that only the orbital magnetisation of the absorbing atom gives rise to the K-edge XMCD signal, our result provides another strong argument in favour of the  $Mn^{3+}$  valence state in wurtzite (Ga,Mn)N. Indeed, in the case of  $Mn^{2+}$  where the  $3d$  and  $4p$  orbital moments are vanishingly small, the XMCD signal is at least one order of magnitude smaller. Moreover, the negative sign of the XMCD signal suggests that the Mn orbital magnetic moment is antiparallel to the applied field and, therefore, to the sample magnetisation. The inset of Figure 112 shows the magnetisation curve recorded by monitoring the Mn K-edge XMCD signal as a function of applied field at 7 K. This magnetisation curve

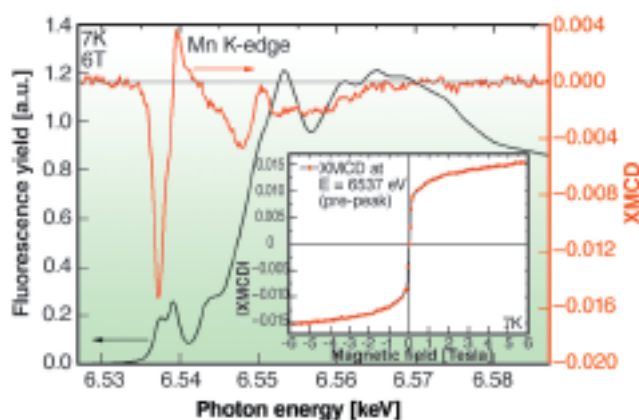


**Fig. 112:** Isotropic XANES spectrum (black line, left scale) and corresponding XMCD signal (red line, right scale) recorded at the Mn K edge measured under 6 Tesla in-plane field and at 7 K for a (Ga, Mn)N film with 6.3% Mn. Inset: magnetisation curve measured at 7 K by monitoring the amplitude of the Mn K-edge XMCD signal.

is a typical signature of a ferromagnetic system in the vicinity of a transition temperature. In conclusion, thanks to the element specificity of XLD and XMCD, we have demonstrated that wurtzite (Ga,Mn)N with 6.3% Mn is an intrinsic ferromagnetic DMS with a rather low Curie temperature of only 8K.

## References

[1] F. Wilhelm, E. Sarigiannidou, E. Monroy, A. Rogalev, N. Jaouen, H. Mariette and J. Goulon, *AIP Conference Proceedings* 879, 1675 (2007).

## Principal Publication and Authors

E. Sarigiannidou (a,d), F. Wilhelm (b), E. Monroy (a), R.M. Galera (c), E. Bellet-Amalric (a), A. Rogalev (b), J. Goulon (b), J. Cibert (c), and H. Mariette (a), *Phys. Rev. B* 74, 041306(R) (2006).

(a) CEA-CNRS-UJF group "Nanophysique et Semiconducteurs", CEA-Grenoble (France)

(b) ESRF

(c) Institut Néel, Grenoble (France)

(d) INPG, Grenoble (France)

## Spin state transition in $LaCoO_3$ studied using soft X-ray absorption spectroscopy and magnetic circular dichroism

$LaCoO_3$  shows a gradual non-magnetic to magnetic transition with temperature, the nature of which has been highly debated over the last few decades. Starting from a low-spin (LS,  $t_{2g}^6e_g^0$ ,  $S=0$ ) ground state for the  $Co^{3+}$  ion at low temperatures, either a high-spin (HS,  $t_{2g}^4e_g^2$ ,  $S=2$ ) or an intermediate-spin (IS,  $t_{2g}^5e_g^1$ ,  $S=1$ ) first excited state becomes populated at elevated temperatures. In the recent past, local density approximation + Hubbard U (LDA+U) band structure calculations predict the IS state to be lower in energy than the HS [1]. Nowadays, this forms the basis of most explanations for the fascinating properties of the recently synthesised layered cobaltate materials, which show giant magnetoresistance and metal-insulator/magnetic transitions with various forms of charge, orbital, and spin ordering. In this work carried out at the ID08 beamline, we examined the validity of this prediction and have arrived at an unexpected conclusion.

We used soft X-ray absorption spectroscopy (XAS) and magnetic circular dichroism (MCD) at the Co  $L_{2,3}$  edge. Figure 113 shows the XAS and MCD spectra taken at 60, 110 and 300 K, i.e. in the paramagnetic phase, using a 6 Tesla magnet. The MCD signal is only in the order of 1%,

but can nevertheless be measured very reliably due to the good signal to noise ratio, stability of the beam, and the accurate photon energy referencing. In the figure, the experimental MCD curves are compared to theoretical spectra calculated for a  $\text{CoO}_6$  cluster. We are able to obtain good agreement for an inhomogeneously mixed LS-HS scenario (see **Figure 113**), but not for a mixed LS-IS.

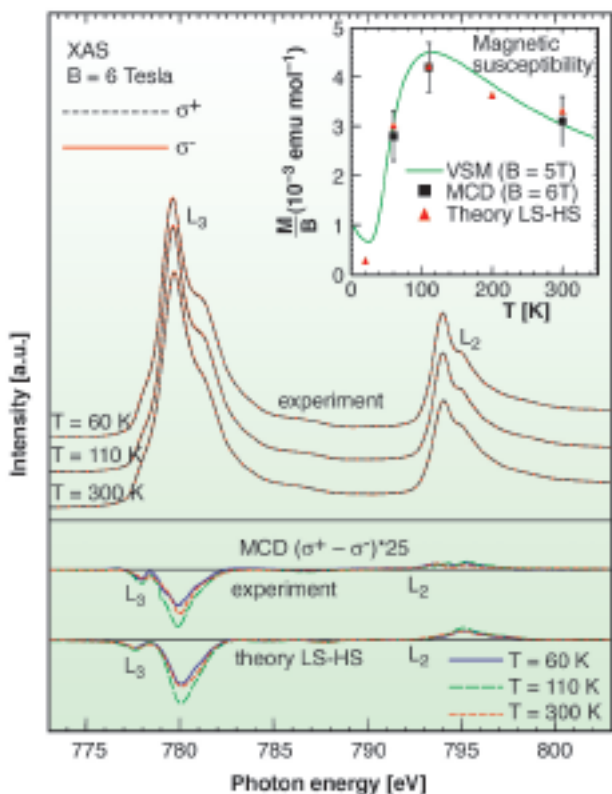


**Fig. 113:** Top: experimental  $\text{Co-L}_{2,3}$  XAS spectra taken from  $\text{LaCoO}_3$  at 60, 110, and 300 K using circularly polarised X-rays with the photon spin aligned parallel ( $\sigma^+$ ) and antiparallel ( $\sigma^-$ ) to the 6 Tesla magnetic field. Middle: experimental MCD spectra. Bottom: theoretical MCD spectra calculated in the LS-HS scenario. Inset: Magnetic susceptibility measured by VSM (solid line), calculated from the cluster (triangles) using the HS population obtained from the XAS spectra and extracted from MCD data (squares).

To check our data, we use the MCD sum-rules to extract the values for the orbital ( $L_z$ ) and spin ( $2S_z$ ) contributions to the induced moments. These results normalised to the magnetic field are plotted in the inset of **Figure 113**. They are in close agreement with the magnetic susceptibility as measured using a vibrating sample magnetometer (VSM).

An important aspect that emerges directly from the MCD experiments is the presence of a very large induced orbital moment: we find that  $L_z/S_z \sim 1/2$ . This means first of all that the spin-orbit coupling must be considered in evaluating the energy level diagram, as is done in **Figure 114**. Second, and crucial for the spin-state issue, this large  $L_z/S_z$  ratio allows us to directly verify the LS-HS scenario and falsify the LS-IS. One should realise that a

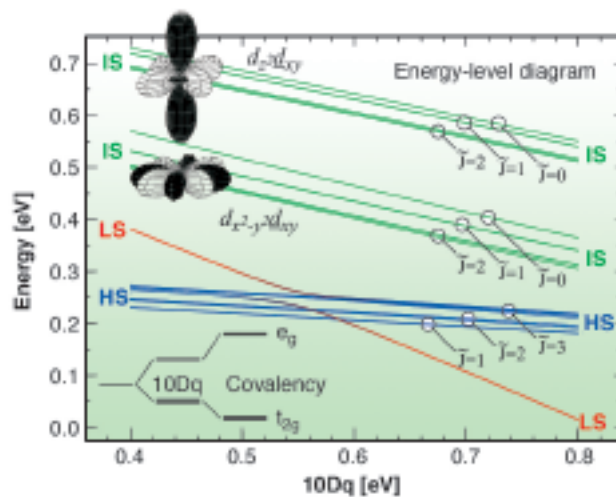


**Fig. 114:** Energy level diagram of a  $\text{CoO}_6$  cluster as a function of the ionic part of the crystal field splitting  $10Dq$ .

$t_{2g}$  electron has a pseudo orbital momentum of 1, which couples with the spin. For the HS state we find a lowest state that is a triplet, with  $L_z = 0.6$ ,  $S_z = 1.3$  and a  $g$ -factor of 3.2, in good agreement also with ESR experiments. For the IS state, the hole in the  $t_{2g}$  shell couples with the electron in the  $e_g$  shell due to the strong orbital dependent Coulomb interactions leading to a  $d_{x^2-y^2}d_{xy}$  state plus their  $x, y, z$ -cyclic permutations (see **Figure 114**). The  $e_g$  electron in turn, couples to the lattice and this leads, according to LDA+U [1], to the formation of an orbital ordered state. This ‘real-space’ state, however, does not carry a large orbital momentum and is therefore not compatible with the values observed in our MCD measurements.

To summarise, we find spectroscopic evidence that the spin-state transition in  $\text{LaCoO}_3$  can be well described by a LS ground state and a triply degenerate HS excited state, and that at elevated temperatures an inhomogeneous mixed-spin state system is formed. The large orbital momentum revealed by the MCD measurements invalidates existing LS-IS scenarios. Consequently, the spin-state issue for the new class of the layered cobaltates needs to be reinvestigated.

## References

- [1] M. A. Korotin *et al.*, *Phys. Rev. B* **54**, 5309 (1996).

## Principal Publication and Authors

M.W. Haverkort (a), Z. Hu (a), J.C. Cezar (b), T. Burnus (a), H. Hartmann (a), M. Reuther (a), C. Zobel (a), T. Lorenz (a), A. Tanaka (c), N.B. Brookes (b), H.H. Hsieh (d,e), H.-J. Lin (e), C.T. Chen (e), and L.H. Tjeng (a), *Phys. Rev. Lett.* **97**, 176405 (2006).

(a) *II. Physikalisches Institut, Universität zu Köln (Germany)*

(b) *ESRF*

(c) *ADSM, Hiroshima University (Japan)*

(d) *CCIT, National Defense University (Taiwan)*

(e) *NSRRC (Taiwan)*

## Element-selective X-ray detected magnetic resonance

X-ray Detected Magnetic Resonance (XDMR) is a new spectroscopic technique in which X-ray Magnetic Circular Dichroism (XMCD) is used to *probe* the resonant precession of the magnetisation when a strong microwave *pump* field  $h_p$  is applied perpendicularly to the static bias field  $H_0$ . Like XMCD, XDMR is element- and edge-selective and is expected to become a unique tool to investigate how precessional dynamics can affect the spin and orbital magnetisation densities of states (DOS) *locally* with p- or d- like symmetry [1, 2]. To illustrate this point, we have used XDMR to determine the precession angle  $\theta$  at the iron K-edge and at the yttrium  $L_{II,III}$  edges in yttrium-iron-garnet (YIG:  $Y_3Fe_5O_{12}$ ) thin films.

The first sample that was investigated was a high quality YIG film grown by liquid phase epitaxy on a (111) gadolinium gallium garnet substrate; the normal to the film was tilted by  $6^\circ$  with respect to the direction of  $H_0$ . XDMR measurements were performed in the longitudinal geometry [3] with an incident microwave power of typically 28 dBm corresponding to a pump field of *ca.* 0.75 Oe. Resonant pumping occurred in the *non-linear* foldover regime of magnetic resonance in which the lineshapes are heavily distorted [1]. This led us to tune systematically the bias field near the critical instability field  $H_{C2}$  where the largest precession angle  $\theta_{C2}$  can be obtained [1]. Since the microwave power was amplitude modulated at a low triggering frequency (*i.e.*  $f_{MW} = 3.5504298$  kHz at the Fe K-edge or  $f_{MW} = 7.1008596$  kHz at the Y L-edges), the XDMR signatures appear as modulation side-bands with respect to the macrobunch repetition frequency of the ESRF ring ( $F_2 = 710.0859611$  kHz in the  $2^{*}1/3$  filling mode). The spectacular dynamic range of our detection system is illustrated by Figure 115 in which the XDMR

signal peaks 34 dB (17 dB) above the noise floor at the Fe K-edge (Y L-edges) [3]. To further improve the sensitivity of our measurements, cross-correlated spectral densities of the two side-bands were exploited. Note that the experiments at the Y L-edges were challenging because the fluorescence intensity was typically 27 dB lower than at the Fe K-edge and the circular polarisation rates were also lower than at the Fe K-edge. For brevity, we have shown only a few typical XDMR spectra in Figure 115: these spectra were obtained on tuning the X-ray excitation energy to the first extremum of the XMCD spectrum.

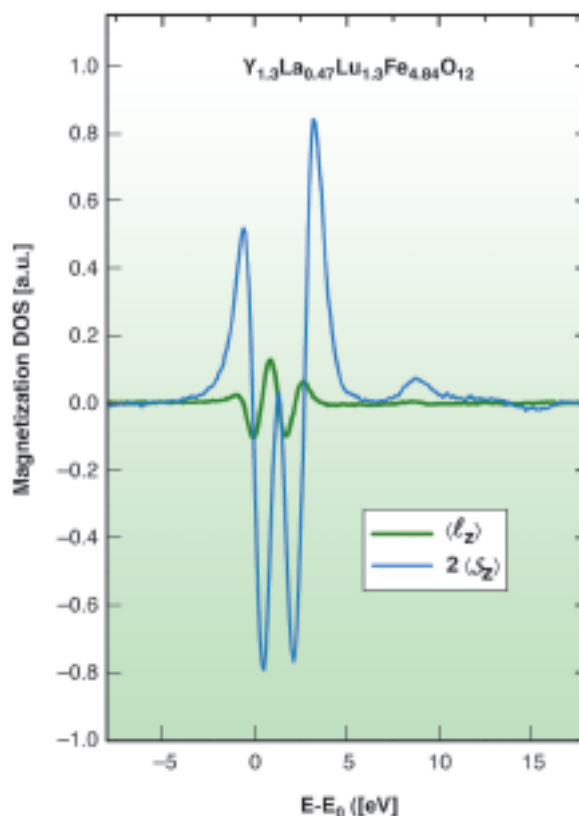


Fig. 116: Orbital and Spin magnetisation of d-projected DOS at the Y site in rare earth doped YIG film. Strictly the same generic spectrum was obtained for the undoped YIG film.

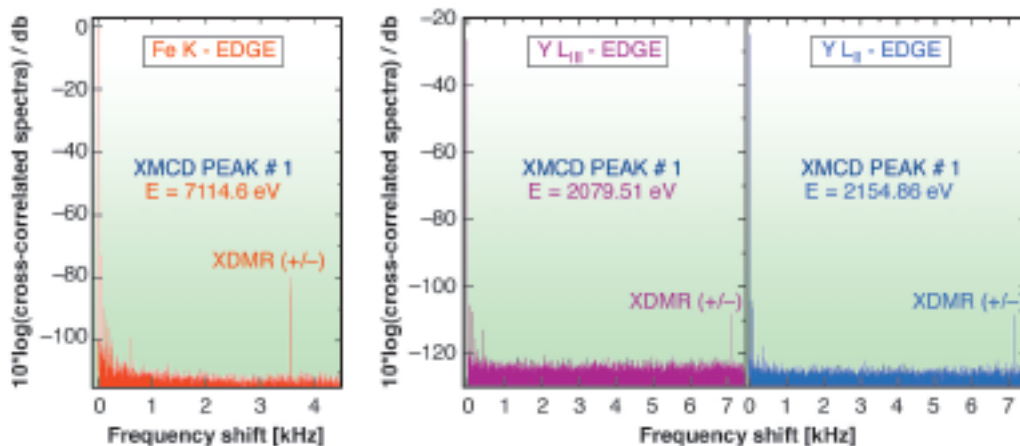


Fig. 115: XDMR spectra measured with a Vector Spectrum Analyser (VSA) at the Fe K-edge and Y  $L_{II,III}$  edges. Cross correlated spectra of the low frequency (-) and high (+) frequency side-bands are shown. The strong signal at  $\Delta F = 0$ , that is proportional to the X-ray excited fluorescence intensity, is used for data normalisation purposes.

The most significant finding in these experiments is that the precession angles  $\theta_{C2}$  measured at the Fe K-edge and Y L-edges were nearly identical:  $\theta_{C2}$  (Fe K-edge) = 5.55°;  $\theta_{C2}$  (Y L<sub>III</sub> edge) = 5.63°;  $\theta_{C2}$  (Y L<sub>II</sub> edge) = 5.59°. What makes this result particularly remarkable is that XDMR measurements at a K-edge describe the precession dynamics of magnetisation components that are exclusively of *orbital* nature [1,2]. Furthermore, it is worth emphasising that in YIG, and other rare earth doped films (e.g. Y<sub>1.3</sub>La<sub>0.47</sub>Lu<sub>1.3</sub>Fe<sub>4.84</sub>O<sub>12</sub>), the Y (La, Lu) atoms are most often considered as *diamagnetic* atoms and, therefore, they are not supposed to contribute to standard FMR spectra. However, this presumption is incorrect because rather intense XMCD signatures were measured at the L-edges of Y (La, Lu) and the respective contributions of the relevant orbital and spin moments can be disentangled by using the XMCD sum rules. As illustrated by **Figure 116**, the XMCD spectra at the Y L-edges are dominated by *induced spin* moments, especially at the energy of the first XMCD peak. Moreover, from the sign of the XMCD signatures, it appears that these induced spin moments are parallel to H<sub>0</sub>. Consequently, they should be *ferromagnetically* coupled to the total Fe spins. The most probable explanation is super-exchange interactions mediated by the oxygen lattice. Our XDMR experiment thus produces clear evidence that the *precession of the orbital component* measured at the iron atom is strongly coupled to the precession of the spin components at both the Fe and Y sites, the same as for acoustic modes.

### References

- [1] J. Goulon, A. Rogalev, F. Wilhelm, N. Jaouen, C. Goulon-Ginet and Ch. Brouder, *Eur. Phys. J. B* **53**, 169-184 (2006).  
 [2] J. Goulon, A. Rogalev, F. Wilhelm, N. Jaouen, C. Goulon-Ginet, G. Goujon, J. Ben Youssef and M.V. Indenbom, *JETP Lett.* **82**, 791-796 (2005).  
 [3] J. Goulon, A. Rogalev, F. Wilhelm, N. Jaouen, C. Goulon-Ginet, G. Goujon, J. Ben Youssef and M.V. Indenbom, *J. Electron Spectr. & Relat. Phenom.* (2006) *in press* (doi:10.1016/j.elspec.2006.11.047) .

### Principal Publication and Authors

J. Goulon (a), A. Rogalev (a), F. Wilhelm (a), N. Jaouen (a), C. Goulon-Ginet (a), G. Goujon (a), J. Ben Youssef (b) and M.V. Indenbom (b), *JMMM* (2006), *submitted*.  
 (a) ESRF  
 (b) Laboratoire de Magnétisme de Bretagne, CNRS FRE 2697, UFR Sciences & Techniques, Brest (France)

## Disentangling multipole resonances through a full X-ray polarisation analysis

In the last 10 years resonant X-ray scattering (RXS) has developed into a powerful technique to obtain direct information about charge, magnetic, and orbital degrees of freedom. It combines the resolution in the determination of long-range ordered structures of X-ray diffraction with the sensitivity to local electronic configurations of X-ray absorption spectroscopy. The development of third generation synchrotron radiation sources has made possible the detection of small effects in electronic distribution: a new interpretation of RXS experiments in terms of electromagnetic multipoles has led to the detection of phase transitions characterised by order parameters of exotic symmetry. However, in several cases the assignment of the multipolar origin to an RXS signal was not clear. The characteristic variation of the intensity and polarisation as the sample is rotated about the scattering vector during an azimuthal scan may allow a clearer identification of the order of the multipole. However, an azimuthal scan cannot be realised in the case of restrictive sample environments such as a cryomagnet or a high pressure cell. Moreover, it is very difficult to identify and separate two resonances of different multipolar origin when they are separated by less than 1 eV. This situation frequently occurs in oxides at the pre-edge region of transition metal K-edges, or at L<sub>2,3</sub> edges of rare-earth compounds, where E1 and E2 transitions can have similar magnitudes.

These problems can be addressed by the experimental technique developed at beamline ID20, based on the combination of a diamond phase plate to rotate the incident linear X-ray polarisation with respect to the plane of the synchrotron and a linear polarisation analysis of the diffracted beam (so called polarisation scans). The technique allows the determination of the Pointcarè-Stokes' parameters P<sub>1</sub> (degree of horizontal-vertical linearly polarised light) and P<sub>2</sub> (degree of polarised light inclined at 45°-135°) as a function of the angle of rotation  $\eta$  of the incoming linearly polarised beam. P<sub>3</sub> (degree of right-left circularly polarised light) is not directly accessible in this setup. For fully polarised light  $P_1^2 + P_2^2 + P_3^2 = 1$ , where  $-1 < P_i < 1$ ,  $i = \{1,2,3\}$ . The polarisation analysis of the diffracted beam can resolve resonances determined by multipolar tensors of different order that are very close in energy, playing on their different relative phase shifts. Polarisation scans were performed at the pre-edge region of the Cr K-edge (E = 5994 eV) in K<sub>2</sub>CrO<sub>4</sub>. In this compound an electric quadrupole tensor (E1-E1 channel) and an electric hexadecapole tensor (E2-E2 channel) are responsible for the strong resonance in the (130) glide-plane forbidden

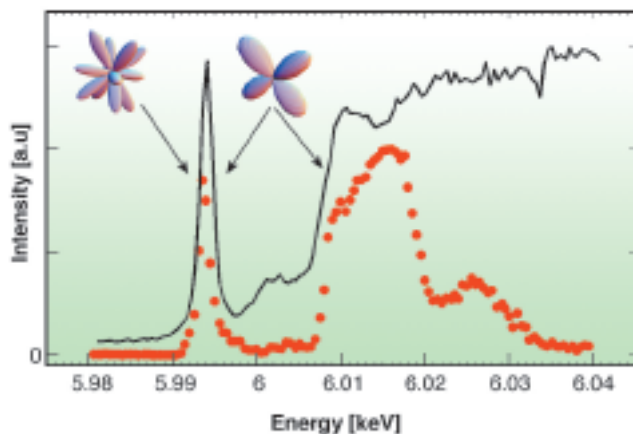


**Fig. 117:**  $K_2CrO_4$  absorption coefficient and  $(130)_{\pi G}$  energy scan (continuous lines and symbols, respectively).

reflection (Figure 117; cartoon pictures show the shape of the two tensors involved in the scattering while the black arrows indicate the energy ranges of the respective contributions). Figure 118 shows the measured results: we discovered a degree of linear polarisation very different from 1 in a wide angular range (bottom panel). *Ab-initio* calculation fit the data nicely (Figure 118, dashed lines), indicating that the missing linear polarisation is fully converted into a circular one. A “time reversed” experiment indeed confirmed that this was the case: by impinging on the sample with a

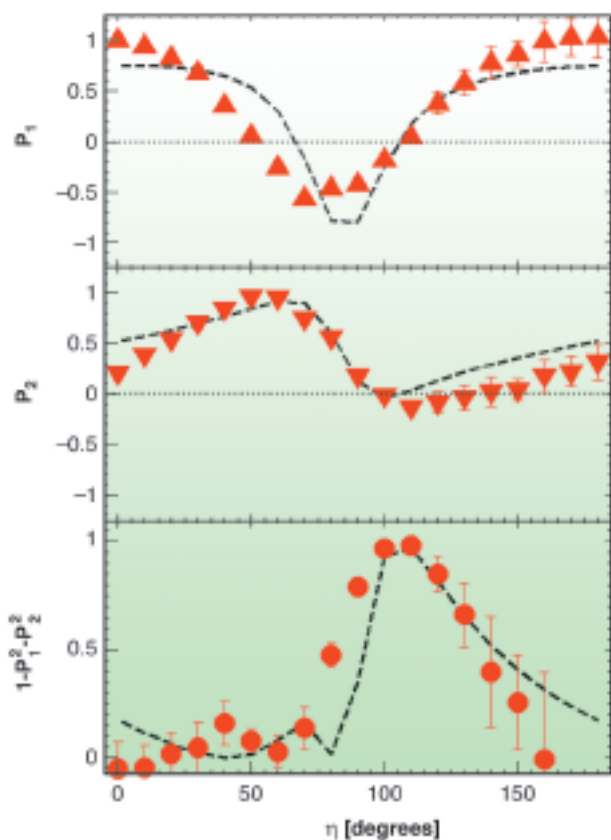


**Fig. 118:** Polarisation scan on the  $(130)$  reflection at  $E = 5994$  eV measured with linearly polarised incident beam.

circularly polarised beam we obtained a diffracted beam fully linearly polarised. Polarisation scans performed at the Cr K-edge energy ( $E = 6010$  and  $6018$  eV), where only the E1-E1 channel is expected to contribute, detected a complete linearly polarised ( $P_1^2 + P_2^2 = 1$ ) scattered beam.

Polarisation analysis of RXS experiments has developed greatly in the last few years, helping our understanding of characteristic order parameters in transition metal oxides, rare-earth based compounds, and actinides. However, a full investigation of Pointcarè-Stokes’ parameters had never been carried out, most likely because linear polarisation analysis was considered sufficient. While linear polarisation analysis may be sufficient when just one excitation channel is involved, several dephasing phenomena may appear when two different excitations close in energy contribute to the transition. As described above, these phenomena may lead to a situation where a scattering process converts an incoming linear polarisation into a circular one due to an interference between two multipolar tensors. The use of phase plates and of a complete polarisation analysis is the key to disentangling multi-resonance structures in those situations where just an energy scan (see Figure 117) is not sufficient. This technique allows a sensitive determination of the relative strength of the multipoles involved and a deeper insight into complex phase transitions and ordering phenomena, being in turn a powerful tool to finely investigate electronic configurations of solid state materials.

#### Principal Publication and Authors

C. Mazzoli (a), S.B. Wilkins (a,b), S. Di Matteo (c), B. Detlefs (a,d), C. Detlefs (a), V. Scagnoli (a), L. Paolasini (a) and P. Ghigna (e), *Phys. Rev. Lett.*, submitted.

(a) ESRF

(b) Brookhaven National Laboratory, Upton (USA)

(c) INFN, Lab. Naz. di Frascati (Italy)

(d) Institute for Transuranium Elements, Karlsruhe (Germany)

(e) Dip.to di Chimica Fisica, Univ. di Pavia, Pavia (Italy)

## Determination of the antiferroquadrupolar order parameters in $UPd_3$

The highly degenerate *f*-electron shells in actinide and rare-earth systems provide a wealth of interesting physical phenomena, with the local degrees of freedom leading to complex phase diagrams. Whilst the order associated with *magnetic dipole moments* has been studied extensively for decades, more recently the

importance of *electric quadrupole moments* has been recognised. It is now clear that the interactions between quadrupoles may be as large as the more familiar dipolar interactions, leading to novel types of ordering in *f*-electron systems.

UPd<sub>3</sub> is particularly interesting because it is one of the small number of metallic materials that exhibit long range quadrupolar ordering. Four phase transitions between 7.8 K and 4.4 K have been detected by microscopic and macroscopic measurement techniques, and attributed to a succession of antiferroquadrupolar (AFQ) ordered phases. Despite intensive effort over the past 25 years, an understanding of these transitions, and the exact nature of the ordering in UPd<sub>3</sub>, has proved highly challenging. Whilst we deduced, some years ago, indirect evidence of quadrupolar order from polarised neutron diffraction measurements in a magnetic field, the first direct microscopic evidence for quadrupolar ordering was obtained in earlier X-ray resonant scattering studies on ID20, with the appearance of new superlattice peaks below  $T_0 = 7.8$  K. The measurements were carried out at the uranium  $M_{IV}$  edge (3.726 keV), confirming that the ordering arises from the U 5*f* electrons.

The unit cell below  $T_0$  is orthorhombic, with the ordered quadrupole moments on the quasi-cubic sites, stacked in antiphase along the *c*-axis. Our results were consistent with polarised neutron data that implied the order parameter below  $T_0$  was  $Q_{x^2-y^2}$ . However, at that time, we could not uniquely identify the order parameter as we were unable to perform the necessary azimuthal scans. We subsequently developed a new model that explained why there are four phase transitions in UPd<sub>3</sub>, and made predictions for the possible order parameters.

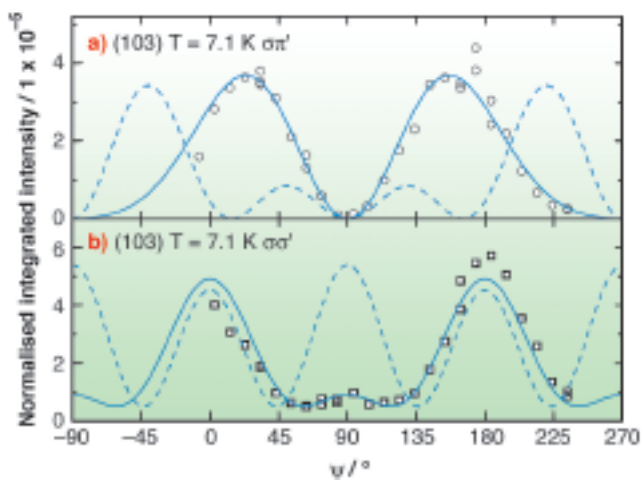


**Fig. 119:** The azimuthal dependence of a) the  $\sigma$ - $\pi'$  and b)  $\sigma$ - $\sigma'$  scattering intensities of the (103) superlattice peak in UPd<sub>3</sub> at the U  $M_{IV}$  edge, at  $T = 7.1$  K. The dashed line shows the calculation for the  $Q_{x^2-y^2}$  order parameter, whilst the full line shows the calculation for  $Q_{zx}$  admixed with 15%  $Q_{x^2-y^2}$  contribution, as discussed in the text.

Advances in cryostat technology on ID20 have now allowed us to make azimuthal ( $\psi$ ) scans in the AFQ ordered phases of UPd<sub>3</sub>. **Figure 119** shows our results for the  $\psi$ -dependence of the  $\sigma$ - $\pi'$  and  $\sigma$ - $\sigma'$  scattering intensities of the (103) superlattice peak at  $T = 7.1$  K. To our surprise, in both the  $\sigma$ - $\pi'$  and  $\sigma$ - $\sigma'$  channels, the data were in clear conflict with our calculations for the  $\psi$ -dependence of the  $Q_{x^2-y^2}$  order parameter (dashed lines in **Figure 119**). Moreover, calculations of the scattering intensity for the  $Q_{xy}$  and  $Q_{yz}$  order parameters do not agree with the data (see [1] for details). However, our results were in good qualitative agreement with calculations for the  $Q_{zx}$  order parameter. The challenge was to reconcile this finding with the polarised neutron  $Q_{x^2-y^2}$  result. Investigation of our theoretical model for the crystal field states of UPd<sub>3</sub> revealed that the onset of  $Q_{zx}$  order leads, from symmetry considerations, to an accompanying small contribution of  $Q_{x^2-y^2}$  order. It is this latter contribution that was detected in our polarised neutron experiments: due to the direction of our applied magnetic field, we were insensitive to antiferromagnetic moments arising from  $Q_{zx}$  order.

The solid line in **Figure 119** shows that our data is fitted extremely well by a calculation for  $Q_{zx}$  order with a small (~15%) contribution of  $Q_{x^2-y^2}$  order. The intensity from  $Q_{zx}$  order is zero at  $\psi = 90^\circ$  in both channels: the finite intensity in the  $\sigma$ - $\sigma'$  channel around this azimuthal angle arises from the small  $Q_{x^2-y^2}$  contribution (see [2] for details).

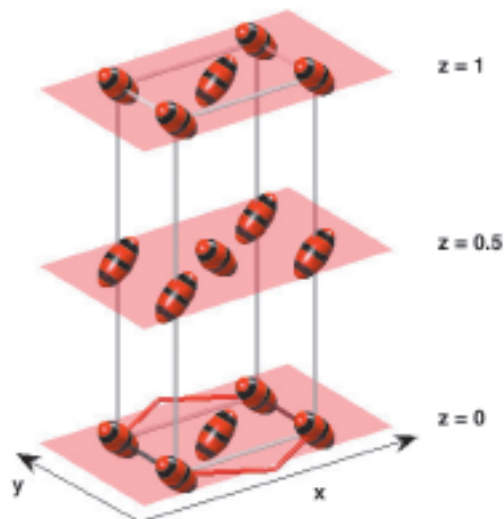


**Fig. 120:** The  $Q_{zx}$  AFQ structure in UPd<sub>3</sub> below  $T_0 = 7.8$  K, with antiphase stacking along the *z*-axis in an orthorhombic unit cell. The quadrupole moments of the uranium 5*f* electrons on the quasi-cubic sites are represented by ellipsoids.

In conclusion, the unique properties of X-ray resonant scattering have enabled us to distinguish the order parameter associated with the highest temperature antiferroquadrupolar phase in UPd<sub>3</sub> between 7.8 K and the next transition at 6.9 K. It is primarily  $Q_{zx}$  with an antiphase stacking along the *c*-axis, as illustrated in **Figure 120**, together with an accompanying  $Q_{x^2-y^2}$

contribution. We now plan to analyse the azimuthal dependence of the superlattice reflections in the lower temperature phases of  $\text{UPd}_3$  where we expect the order parameters are combinations of  $Q_{zx}$ ,  $Q_{x^2-y^2}$ ,  $Q_{xy}$  and  $Q_{yz}$ .

## References

- [1] H.C. Walker, K.A. McEwen, D.F. McMorrow, S.B. Wilkins, F. Wastin, E. Colineau, D. Fort, *Phys. Rev. Lett.* **97**, 137203 (2006).  
 [2] K.A. McEwen, H.C. Walker, M.D. Le, D.F. McMorrow, E. Colineau, F. Wastin, S.B. Wilkins, J-G. Park, R.I. Bewley, D. Fort, Invited paper presented at ICM2006, to be published in *J. Mag. Mag. Mater.*

## Authors

K.A. McEwen (a), H.C. Walker (a), D.F. McMorrow (a), S.B. Wilkins (b).  
 (a) University College London (UK)  
 (b) ESRF, now at Brookhaven National Laboratory (USA)

# Beyond the impurity model in Cerium compounds

The low temperature resistivity minimum, together with the overall reduction of the magnetic moment, are two of the main macroscopic identifiers of the Kondo effect. The effect occurs when a localised impurity is found close to the Fermi surface of a non-magnetic host. For temperatures that are lower than the Kondo temperature,  $T_K$ , the spin of the impurity is compensated by the conduction electrons and the resulting magnetic moment is reduced. Whereas above the Kondo temperature, Kondo systems behave as local moment systems. According to the prevailing single impurity Anderson model, it is the hybridisation between the impurities and the conduction states that results, for  $T < T_K$ , in a non-magnetic ground state. The fingerprint of this state in the photoemission spectrum is the Kondo resonance. The cross-over from low temperature ( $T < T_K$ ) to high temperature ( $T > T_K$ ) is associated with a decrease of the resonance's intensity, as the ground state is destroyed by thermally activated spin fluctuations. Whether or not a description in terms of this model is appropriate has been strongly debated. For cerium (Ce) compounds, the surface sensitivity of most of the previous photoemission investigations, together with an often uncertain identification of the 4f contribution to the photoemitted intensity, are the underlying causes of the conflicting results. Hence, 4f spectra that are more representative of the bulk are needed.

Soft X-ray resonant photoemission spectroscopy performed at the ID08 beamline has allowed us to identify bulk-representative 4f spectral features for

$\text{CeCo}_2\text{Ge}_2$ , a single-crystalline compound whose Kondo temperature is  $T_K \sim 120$  K. In fact, by tuning the photon energy to the Ce  $M_5$  absorption edge ( $h\nu \sim 880$  eV), both bulk and orbital selectivity are obtained; the first due to the increase of the inelastic mean free path for incoming energies belonging to the soft X-ray range, the second due to the enhancement of the 4f intensity by more than one order of magnitude if compared to off-resonance conditions.

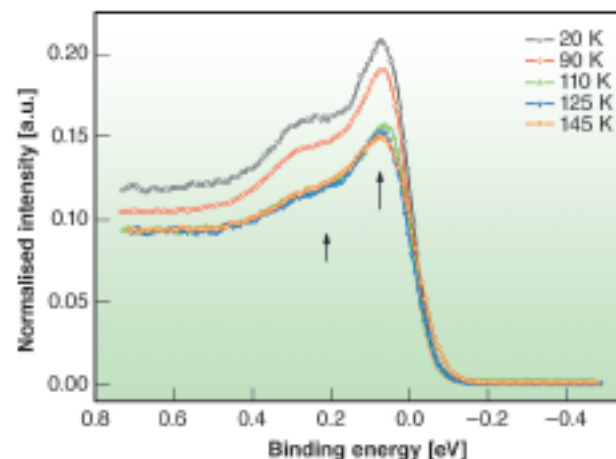


**Fig. 121:** Temperature-dependent, resonant, angle-integrated valence band spectra.  $h\nu \sim 880$  eV. The arrows indicate the position of the Kondo resonance and the spin-orbit partner respectively.  $E_F = 0$  eV.

**Figure 121** shows the angle-integrated valence band of  $\text{CeCo}_2\text{Ge}_2$  measured at several temperatures ranging from  $T = 20$  K to  $T = 145$  K. Despite the fact that the intensity is strongest at 20 K, the shape of the two low temperature spectra is very similar. In particular, two features are observed: the most intense, found at approximately 70 meV binding energy, is the Kondo resonance, whereas the other, positioned at approximately 270 meV, is the spin-orbit partner. As the temperature is raised from 90 K to 110 K, a decrease is observed in the overall intensity, together with a smearing out of the spin-orbit partner. By increasing the temperature further, the signal below 350 meV remains unchanged whereas the intensity of the Kondo resonance continues to decrease. In agreement with the impurity model, we therefore observe a temperature dependence that reflects the progressive breakdown of the singlet ground state.

**Figure 122** shows the angle-resolved valence band of  $\text{CeCo}_2\text{Ge}_2$  for  $T = 20$  K. These data fail to confirm the applicability of the impurity model in its simplest form as, at the heart of the model, is the postulate that both the intensity and the binding energy of the Kondo resonance are constant functions of the momentum component parallel to the surface,  $k_{\text{par}}$ . **Figure 122** indicates the contrary, that the nature of this feature varies. Indeed, the spectral weight is mostly

concentrated within  $\pm 0.7 \text{ \AA}^{-1}$  from the centre of the Brillouin zone ( $k_{\text{par}} = 0 \text{ \AA}^{-1}$ ) and a clear intensity modulation of the Kondo resonance is observed. Most intriguingly, a weak but visible spin-orbit-partner-like feature is seen dispersing towards higher binding energies.

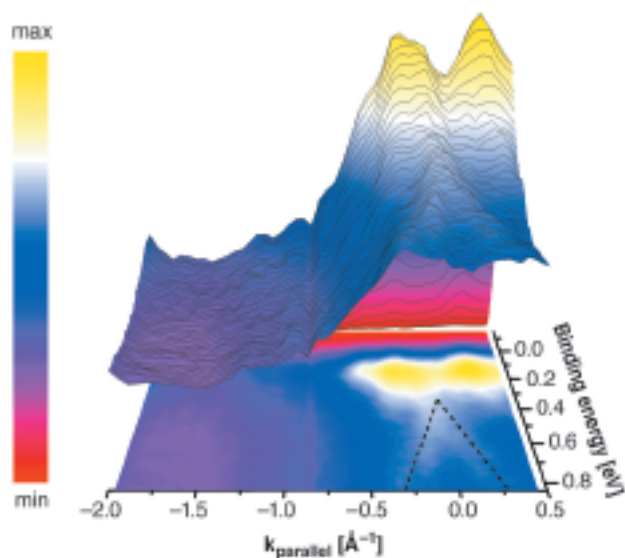


**Fig. 122:** Resonant, angle-resolved, valence band spectrum.  $h\nu \sim 880 \text{ eV}$  and  $T = 20 \text{ K}$ . The binding energy is plotted as a function of  $k_{\text{par}}$  and the colour map indicates the intensity. Top: three dimensional representation. Bottom: two dimensional projection. The dispersing feature is shown by the dashed line.  $E_{\text{F}} = 0 \text{ eV}$ .

The data reveal clear 4f bulk-like features whose temperature dependence is in agreement with the predictions of the impurity model. The major exceptions to this scenario are given by the localisation of the 4f intensity close to the centre of the Brillouin zone and the dispersion of what may be the spin-orbit partner, as observed in **Figure 122**. We refer to a renormalised f-d mixing model, that retains the underlying physics of the impurity approach but is further complicated by a more sophisticated screening mechanism, as a candidate for explaining both the temperature dependence of the Kondo resonance's intensity and its observed directional character.

*In memory of Kenneth Larsson.*

#### Principal Publication and Authors

F. Venturini (a), J.C. Cezar (a), C. De Nadaï (a), P.C. Canfield (b), N.B. Brookes (a), *J. Phys.: Condens. Matter* **18**, 9221 (2006).

(a) ESRF

(b) Ames Laboratory and Department of Physics and Astronomy, Iowa State University, Ames, Iowa 50011, U.S.A.

# X-ray Imaging and Optics

## Introduction

X-ray imaging and microanalysis techniques cover a wide variety of scientific topics ranging from materials science and engineering to life sciences and cultural heritage. The evolution of these techniques is science-driven: a good example is the success achieved when establishing a link with paleontological research, and adapting the techniques to the needs of this community [1,2]. Their results are exemplified by the three-dimensional images of a fossil shown in **Figure 123**.

The present chapter clearly shows the variety of scientific subjects investigated in connection with imaging and microanalysis techniques: it goes from preclinical radiotherapy studies to optics for nanofocussing, and includes applications to biomedical and biological science, materials science, environmental and cultural heritage topics.

The selected **biomedical research** articles comprise both radiotherapy and X-ray imaging. The present number of treatments for cancerous

brain tumours, and their efficiency, is unfortunately quite poor. It is therefore particularly important to develop synchrotron radiation based research aimed at treating brain tumours. Two contributions, one on survival curves using synchrotron stereotactic radiotherapy (SSR), and another on the sparing of healthy tissues when using microbeam radiation therapy (MRT), go in this direction. A report on the time response to inhaled histamine, studied by synchrotron radiation computed tomography (CT) using Xe as a contrast agent and the K-edge subtraction method, provide information on the complex changes in conductance of the respiratory system, important for the understanding and treatment of asthma.

Intense research is being performed using imaging techniques on **biological materials**. Holotomography with very high spatial resolution allowed the investigation of an *Arabidopsis* seed, and showed the existence of a three-dimensional air

space network, which may play a key role in the germination process. In the second article, spatially-resolved diffraction was used to map the texture of human dental enamel.

Application of these techniques to **materials science** continues to provide many original results. Microstructure formed during the growth process controls a substantial fraction of a material's properties. The observation of the solid-liquid interface during directional solidification is essential for studying the dynamical phenomena involved in microstructure formation under controlled conditions. A unique experimental setup, allowing the combination of synchrotron X-ray radiography (SXR) and synchrotron white beam X-ray topography (SWBXT), has been developed. These two imaging techniques provide complementary information on the growth of Al-based alloys: both the evolution of the microstructure morphology and the orientation and strain field within the growing solid are accessible in this way. The final materials-related contribution is a  $\mu\text{m}$ -

scale spatially-resolved investigation of Co impurities in ZnO which allows an identification of the mechanism inducing ferromagnetism in this material.

Imaging and microspectroscopy are being increasingly used to investigate **environment and cultural heritage** subjects. The highlighted contributions start with a note explaining the mechanism of blackening of the red paintings of Pompeii. The evolution from Fe<sup>3+</sup> to Fe<sup>2+</sup> under conditions close to those in magmas during their ascent from the Earth's mantle to the surface, before volcanic eruption, furthers our knowledge of the whole process. Finally the importance of the use of phase contrast to identify insects or plants within opaque fossil amber is pointed out, and three-dimensional images of the fossils identified in this way are shown.

This chapter also includes a note on **X-ray optics metrology**, which shows the present achievements and

emphasises the importance of refined metrology to meet future requirements of nanofocussing optics.

X-ray imaging plays a key role within the planned ESRF **Upgrade Programme**. The present work on X-ray imaging shows the importance of responding to the increasing demand from new scientific communities and gains from the continuous improvements to the techniques. A further effort to improve the spatial resolution to reach the few tens of nm range, for both biological (such as micro-vascularisation of the brain, trace elements in cells) and materials science (such as initiation of cracks) topics, is crucial. It implies building a new, devoted and optimised, long nanoimaging beamline to complement the set of techniques already established within the X-ray Imaging group.

**J. Baruchel**

## References

- [1] J.-Y. Chen *et al.*, *Science* **312**, 1644-1646 (2006).
- [2] R. Macchiarelli *et al.*, *Nature* **444**, 748 - 751 (2006).
- [3] L. Marivaux *et al.*, *Am. J. Phys. Anthropol.* **130**, 425 (2006).

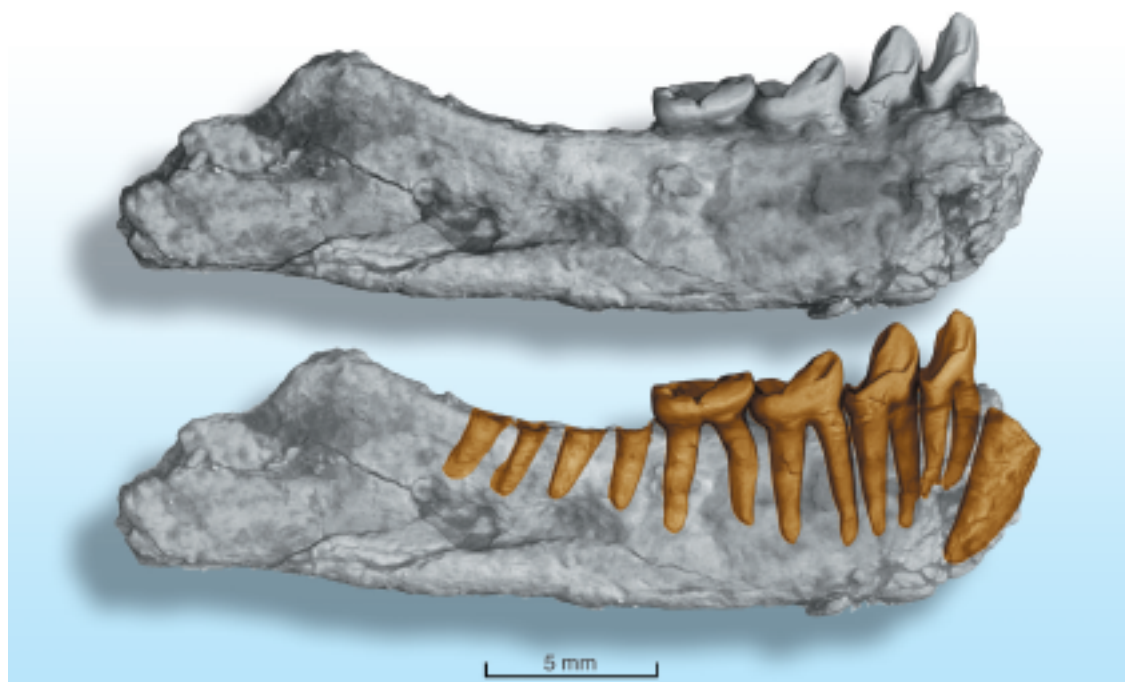


**Fig. 123:** Mandible of a small fossil strepsirrhine primate from the Late Eocene of Thailand, *Muangthanhinius siami*. Non-destructive three-dimensional observation of the teeth roots (ID19, pixel size 10  $\mu\text{m}$ ) gave clues that let us better understand the morphology of the teeth crown. The image analysis allowed a modification of the attribution of this fossil, originally considered as a putative ancestor of lemurs, and now reattributed to an extinct group of primates, the Adapiforms [3]. Image courtesy P. Tafforeau.

## Preclinical Radiotherapy Studies

### *Prolonged survival of Fischer rats bearing F98 glioma after iodine-enhanced synchrotron stereotactic radiotherapy*

Primary brain tumours are one of the ten main causes of death from cancer. Despite aggressive treatment with surgery, radiation and chemotherapy, most patients with these tumours have a less than 2-year survival time after diagnosis. A fundamental goal of radiation therapy is to deliver a high therapeutic dose of ionising radiation to the tumour without exceeding the tolerance of normal tissues surrounding the lesion. Various techniques have been proposed in clinics for producing highly-localised dose distribution. None has given outstanding results so far. Synchrotron stereotactic radiotherapy (SSR) is an innovative radiation therapy technique, where the tumour is loaded with a high-Z element (iodinated contrast agents or platinated chemotherapeutic drugs) and irradiated in stereotactic conditions with monochromatic X-rays from a synchrotron source (tens of eV energy bandwidth), tuned to the optimal energy [1, 2]. The irradiation geometry, the fluorescent X-rays, photoelectrons, and Auger electrons generated on iodine atoms, produce a localised dose enhancement. The purpose of this study was to determine whether the efficacy of iodine-enhanced-SSR could be further improved by using a concomitant injection of an iodinated contrast agent and a transient blood brain barrier opener (mannitol).

Fourteen days after intracerebral inoculations of F98 cells, the animals were irradiated with 50 keV monochromatic X-rays (0, 5, 15 or 25 Gy in a single fraction) while receiving an infusion of hyperosmotic mannitol with iodine, either intravenously or via the carotid (9 to 15 rats per group, 117 rats total). The experiments were performed at the Biomedical Beamline ID17.

A theoretical iodine dose enhancement factor (DEF) was calculated as the ratio of the radiation dose absorbed by the tumour when it is loaded with contrast media (CM) to the dose absorbed without CM. The radiation dose is the energy (J) deposited by the radiation beam per kg of tissue, with no assumption concerning the probability for a given particle to have a lethal effect at the cellular level. The possible biological damage follows after the physical interactions between radiation and atoms or molecules of the cells. Another index, the “iodine biological enhancement factor” (IBEF) was defined. It corresponds to the apparent biological enhancement with iodine and reflects the overall consequences of the treatment, which includes the effects of an increased physical energy

absorption, as well as other radiobiological factors, due to the presence of the high-Z element.

The endpoint of the study was the survival time of the rats after tumour implantation, for a given treatment. The mean survival times, median survival times and increased life spans (ILS = percentage of survival increase relative to the mean or median survival of untreated controls) were calculated for each group.

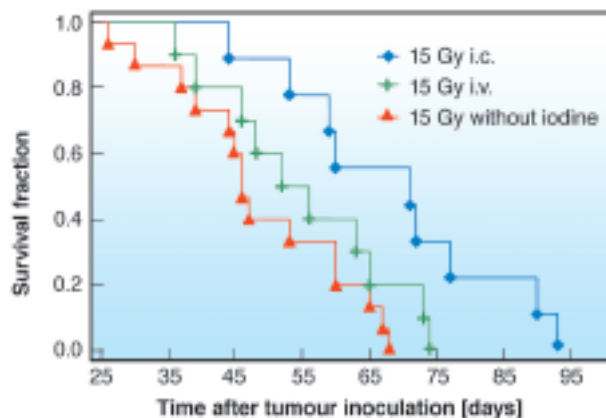


**Fig. 124:** Kaplan-Meier survival curves of F98 glioma-bearing rats treated with stereotactic synchrotron radiation therapy (15 Gy) without contrast agent injection or with iodinated contrast agent (Iomeron) and mannitol injection during irradiation (intravenous and intra-arterial). The irradiation was performed with 50 keV monochromatic X-rays. The untreated controls (curve not shown) had a mean survival time of  $25.6 \pm 2.4$  days (range: 21 – 28 days, median: 26 days).

In the absence of iodine, the mean and median survival times were found to increase with radiation dose. The ILS relative to the median increases exponentially ( $R^2 = 0.999$ ) within the X-ray dose range 5 to 25 Gy. For tumour X-ray doses inferior to 25 Gy, the intracarotid (i.c.) infusion of mannitol and iodine during SSR improved the survival of rats compared to intravenous injection (i.v.) or irradiation alone (Figure 124). Mean survival times (mean  $\pm$  SD) were  $25.6 \pm 2.4$ ,  $48.9 \pm 13.1$  (ILS = 91%), and  $55.2 \pm 13.4$  (ILS = 116%),  $68.8 \pm 16.4$  days (ILS = 169%) for untreated controls, irradiated without iodine, irradiated after infusion of iodine and mannitol i.v. and i.c., respectively (15 Gy). For X-ray doses of 25 Gy, the rats irradiated without iodine had the longest survival (ILS = 607%), but no additional benefit was obtained when iodine and mannitol were injected (ILS = 113% and 78%, after i.v. and i.c. injection respectively). The IBEF was found equal to be 1.69 and 1.13 for 5 and 15 Gy, respectively (i.v. route, theoretical DEF = 1.68). For the i.c. route, we obtained 1.85 and 1.30 for 5 and 15 Gy, respectively (theoretical DEF = 4.11).

These preclinical findings demonstrate that the efficacy of iodine-enhanced-SSR is significantly improved with the concomitant intracarotid infusion of iodine and mannitol for radiation doses less or equal to 15 Gy.

## References

- [1] Adam JF, Elleaume H, Joubert A, *et al.* *Int J Radiat Oncol Biol Phys.* **57**, 1413-1426 (2003).  
 [2] Biston MC, Joubert A, Adam JF, *et al.* *Cancer Res.* **64** 2317-2323 (2004).

## Principal Publication and Authors

JF. Adam (a,b), A. Joubert (a), M.C. Biston, A.M. Charvet, M. Peoc'h (c), J.F. Le Bas (a,b,d), J. Balosso (a,b,e), F. Estève (a,b,d) and H. Elleaume (a), *Int J Radiat Oncol Biol Phys* **64**(2), 603-611 (2006).

- a) INSERM U647, Medical Beamline ID17, ESRF  
 b) Université Joseph Fourier, Grenoble (France)  
 c) Centre Hospitalier Bellevue, Département de pathologie, Saint Etienne (France)  
 d) CHRU Grenoble, Hôpital Michallon, Unité IRM, Grenoble (France)  
 e) CHRU Grenoble, Hôpital Michallon, Département de Cancérologie et d'Hématologie, Grenoble (France)

## Short-term effects of microbeam irradiation on the normal mouse brain microvasculature

Demyelination, vascular damage, dementia, white matter radionecrosis, pituitary diseases and hormone depletion occur regularly after high-dose brain irradiation. Such lesions are likely to be the main cause of cognitive dysfunction observed after conventional cerebral tumor radiation treatment with high cumulative doses. The formation of a vasogenic edema following blood brain barrier (BBB) breakdown is thought to contribute to acute radiation damage.

Microbeam radiation therapy (MRT) is an innovative pre-clinical radiation therapy which uses low energetic and non divergent synchrotron wiggler-generated X-rays which are spatially microfractionated to be delivered to the target volume. High flux synchrotron light allows extremely short irradiation times, which avoids broadening of the collimation due to micro-movement of the target. Previous studies have shown that normal cerebral tissues presented particular high resistance to radiation delivered in microbeams [1,2] and that MRT has a curative effect on cerebral tumors implanted in rat brain [2,3]. To explain the sparing effect of microbeam irradiation on normal tissue adjacent to the tumor, it has been hypothesised that non-irradiated endothelial cells between the irradiated zones are able to rapidly repair the damaged microvessels and/or the BBB in the irradiated zones [1,2].

The aim of this study was to determine MRT-induced vascular damage. We focused on the analysis of early effects (12 h – 3 months) of microbeam irradiation on BBB permeability, cerebral blood volume and capillary density for two different MRT-delivered doses: 312 and 1000 Gy.

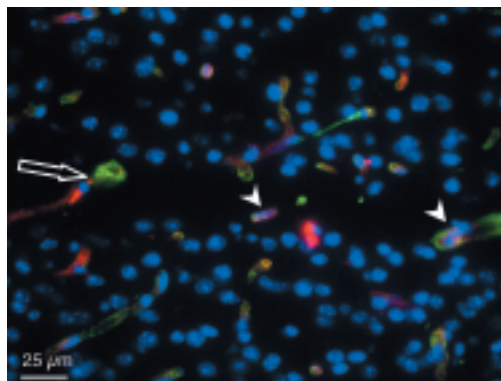


**Fig. 125:** Type IV collagen (green) and platelet endothelial cell adhesion molecule I (red) immunostaining. Horizontal section of a left parietal cortex mouse brain three months after microbeam irradiation with 25 µm-wide microbeams, 211 µm centre-to-centre spacing, skin entrance dose of 1000 Gy. The arrow shows a microbeam path in the motor cortex. An important loss of cell nuclei (blue) can be observed in the microbeam path but immunoreactivity for endothelial cells (arrowhead) remains detectable in the irradiated microslice.

From 12 hours to 3 months after exposure and whatever the dose deposited, there was no difference in the vessel density and in the cerebral blood volume between irradiated and non irradiated cortices. Endothelial cells remained detectable in the irradiated tissue microslices while neurons and glial cells disappeared during the first week after exposure (Figure 125).

For all time intervals after microbeam exposure and whatever the radiation dose, the FITC-dextran remained in the functional capillary network. From 12 hours to 12 days after irradiation, a diffusion of sulforhodamine B in microbeam stripes was observed for a radiation dose of 1000 Gy. No diffusion was detected 1 month after MRT. For a 312 Gy dose, no leakage of sulforhodamine B in the microbeam stripes of normal brain tissue was detected at any time after MRT (Figure 126).

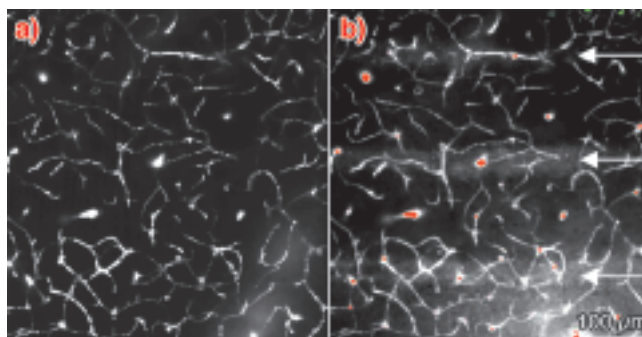


**Fig. 126:** Z-projection of images acquired *in vivo* by multiphoton microscopy, 50 to 100 µm below the dura (2 µm steps) in the left parietal cortex of a nude mouse 12 h after 1000 Gy entrance dose exposure. The mouse was injected intravenously with a) 100 µl FITC-dextran (70 kDa) solution and b) 50 µl of a Sulforhodamine B (0.58 kDa) solution, approximately 2 min before microscopy.

In conclusion, this study shows that microbeam irradiation does not induce severe damage to normal vascular brain tissue. The absence of secondary effects, *i.e.* weak edema formation, rapid BBB repair and absence of significant changes in cerebral blood volume, indicate that microbeam radiation therapy could be a promising tool in the treatment of malignant brain tumors while preserving healthy tissue.

### References

- [1] D.N. Slatkin, P. Spanne, F.A. Dilmanian, *et al.*, *Proc Natl Acad Sci U S A*, 92, 8783-7 (1995).  
 [2] J.A. Laissue, G. Geiser, P.O. Spanne, *et al.*, *Int J Cancer*, 78, 654-60 (1998).  
 [3] F.A. Dilmanian, T.M. Button, G. Le Duc, *et al.*, *Neuro-oncol*, 4, 26-38 (2002).

### Principal publication and authors

R. Serduc (a), P. Vérant (b), J.C. Vial (b), C. Rémy (a), E. Brauer (c), A. Bravin (c), J. Laissue (d), B. van der Sanden (a).

(a) INSERM U 594, Grenoble (France)

(b) CNRS UMR 5588, Grenoble (France)

(c) ESRF

(d) Institute of pathology, Bern (Switzerland)

## Biomedical and Biological Applications of X-ray Imaging

### *Differences in the time course of proximal and distal airway response to inhaled histamine studied by synchrotron radiation CT*

Quantitative study of lung function with synchrotron radiation is a long-term project conducted at the Biomedical Beamline, **ID17**. The goal of the project is to understand the effects of drugs and air pollutants in healthy and diseased lung, and find optimal medication for such common diseases as asthma. The project is based on collaboration between teams working at the ESRF, University of Helsinki, Université de Picardie, Szeged University (Hungary), and Geneva University Hospital.

Stable Xe gas is used as the inhaled contrast agent for imaging the airspaces of an animal model (rabbit). Two simultaneous images are recorded using two X-ray energies that bracket the K-absorption edge of Xe, and the difference image in a logarithmic scale yields the distribution of the contrast gas. The spatial resolution determined by the beam height and detector resolution is 0.1 mm<sup>3</sup>, which is more than an order of magnitude better

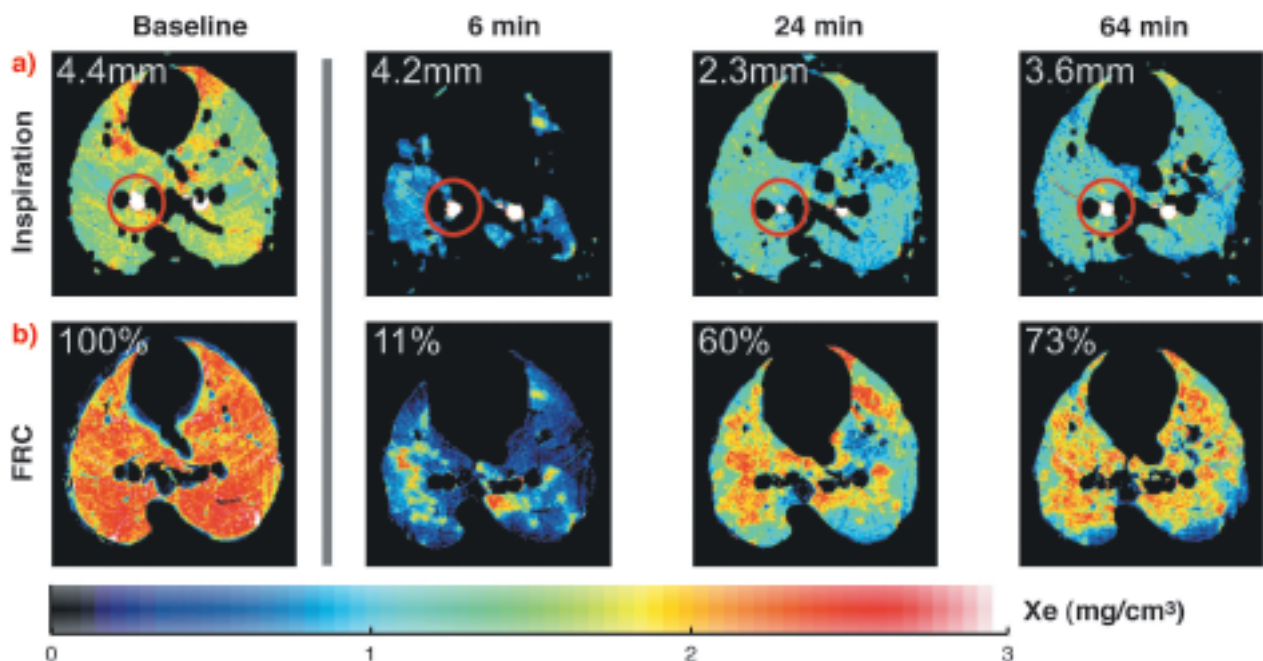


**Fig. 127:** Xe distribution in the middle lung cross-section level at baseline and 6, 24, and 64 minutes after histamine inhalation in a rabbit. **a)** changes in proximal airway caliber. One bronchus in the inspiration images is marked with a circle. The diameter of this bronchus is 4.4 mm in the baseline image; 6 minutes after histamine the diameter is 4.2 mm. The minimal diameter value of 2.3 mm is reached 24 minutes after the histamine inhalation, and recovery to 4.2 mm value is observed 64 minutes later. **b)** changes in the ventilated alveolar area at FRC, functional residual capacity. At 6 minutes after histamine inhalation the ventilated alveolar area is reduced to 11% of the baseline value with significant heterogeneity. The ventilated alveolar area recovered in 24 minutes to 60% of the baseline value and in 64 min to 73% of the baseline values.

than the resolution achieved by any other method for lung imaging. In addition, the noise level is strongly reduced, as the signal from other parts of the object is eliminated.

Although airway hyperreactivity is the hallmark of bronchial asthma, little is known about the differences in the regional kinetics of airway narrowing in the tracheo-bronchial tree during an asthma attack. Previous studies in this project showed that inhaled histamine induces large patchy defects in Xe wash-in in the peripheral lung air spaces with rapid spontaneous reversal, suggesting that the *in vivo* reactivity and kinetics of airway response to histamine inhalation could be different in distal vs. proximal airways [1]. In this study the narrowing of proximal airways was imaged directly, while the distal airway obstruction was indirectly quantified by measuring changes in the regional ventilated area on the basis of the densities of Xe gas.

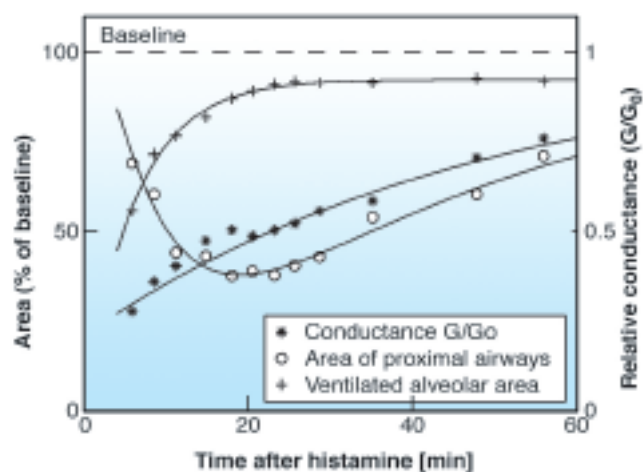


**Fig. 128:** Relative changes in respiratory system conductance  $G/G_0$ , luminal area of proximal airways at the lower cross-section level where the largest response to histamine was observed, and ventilated alveolar area after inhalation of histamine aerosol.

Results of the study are shown in **Figure 127** and **128**. The CT images show the slow contraction of a large airway, the immediate constriction of distal airways based on the reduction of the ventilated alveolar area, and the very non-uniform distribution of the ventilated air spaces in the lungs. The subsequent time course of lung response in **Figure 128** shows the rapid recovery of the distal airways, and the slow recuperation of the main bronchi. A plausible explanation is that of different airway wall structures, as the relative cartilage content decreases and the smooth muscle content increases in distal airways. There are also indications that the delayed maximal response to histamine and the slow recovery observed in the main bronchi may be due to sub-mucosal edema formation followed by gradual removal.

One of the most important overall indicators of lung function is the conductance (inverse of resistance) of the respiratory system. The findings of this study suggest that the changes in conductance result from combined

reactions of proximal and distal airways. However, the relative contribution of these components seems very unequal in time after an asthma attack provoked by histamine. These findings are potentially important for studies of the patho-physiology and treatment of asthma.

## References

[1] S. Monfraix, S. Bayat, L. Porra, G. Berruyer, C. Nemoz, W. Thomlinson, P. Suortti, A.R.A. Sovijärvi, *Phys. Med. Biol.*, **50**, 1-11 (2005).

## Principal Publication and Authors

S. Bayat (a), L. Porra (b), H. Suhonen (b), C. Nemoz (c), P. Suortti (b,c), A.R.A. Sovijärvi (d), *J. Appl. Physiol.*, **100**, 1964-1973 (2006).

(a) *Université de Picardie, Amiens (France)*

(b) *University of Helsinki (Finland)*

(c) *ESRF*

(d) *Helsinki University Central Hospital (Finland)*

## Holotomography reveals new features in seed structure

Seeds are central to the world's wildlife as well as to its agriculture, in the latter case both in the form of cereals and as the mediator for the renewal of crops. Seeds of the botanical geneticist's favourite test plant, the weed-like, unassuming *Arabidopsis thaliana* (wall cress or mouse-ear cress) were investigated using holotomography, an approach developed at the ESRF [1]. This technique is quantitative phase tomography with micrometre resolution using hard synchrotron radiation X-rays. It is a variant of microtomography, the microscopy-scale version of medical computed tomography (CT). Many images are taken for different orientations of a given sample and then digitally combined to provide either three-dimensional (3D) renditions or virtual slices along any direction. Tomography usually relies on attenuation or absorption contrast, *i.e.* to the local variations in its *amplitude* or intensity, with respect to the average beam intensity, due to the inhomogeneous distribution of absorption in the sample. For holotomography, an essential contribution to the image is due to the effect of the sample on the *phase* of the X-ray beam going through it. This is due to inhomogeneous refractive index and/or thickness distributions in the sample. At a third-generation synchrotron radiation source such as ESRF, these relative phase variations can be turned very simply into contrast and thus produce an image. Thanks to the spatial coherence in the beam, especially on a long beamline such as the Imaging Beamline ID19, Fresnel diffraction turns local variations in phase into changes in intensity, and thus into an image. This requires no lens, but the detector must be placed some distance from the sample. The images recorded at more than one distance must then be processed to provide quantitative phase maps.

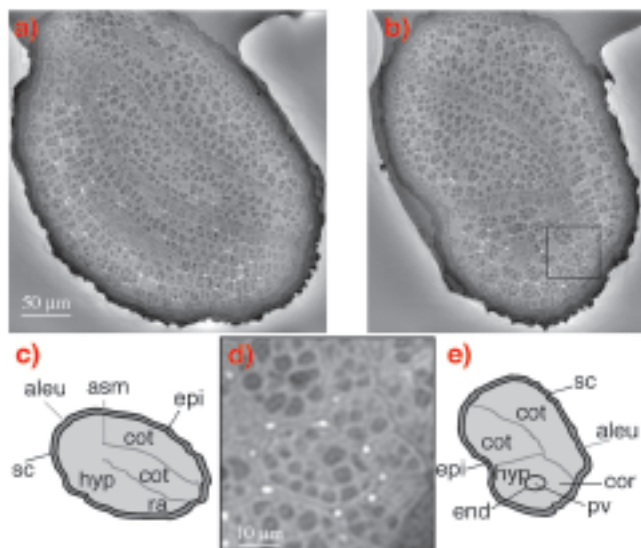


**Fig. 129:** a) and b) two virtual slices, one pixel (0.3  $\mu\text{m}$ ) thick, of an *Arabidopsis thaliana* seed, corresponding to two perpendicular orientations; c) and e) schematic representation (among the designations: cot = cotyledon; hyp = hypocotyls; sc = seed coat); d) magnified image corresponding to the square in (b).

Phase maps corresponding to different sample orientations are then combined, using the same software as for absorption tomography. This provides quantitative 3D information about the local density – strictly speaking, the electron density. **Figure 129** shows a virtual slice and the corresponding schematic drawings. Individual cells and organelles inside the cells are clearly visible in the enlargement of a section (**Figure 129d**). In the reproduction scheme used, darker corresponds to higher density. The white dots showing up at the junction of cells correspond to essentially zero density, *i.e.* to gas. More detailed 3D scrutiny, as in **Figure 130** [2] shows that the voids form a network. This network of air space is the major finding of this investigation. It may be an important actor in plant life, by first storing and then, at the onset of the germination process, quickly distributing oxygen. In addition, it could serve for rapid water transport to the various seed tissues and organs during imbibition. A noteworthy aspect is that this air space network could not be reliably identified using the standard approach of fixation, dehydration, embedding, microtome slicing, colouring, and optical microscope observation. The

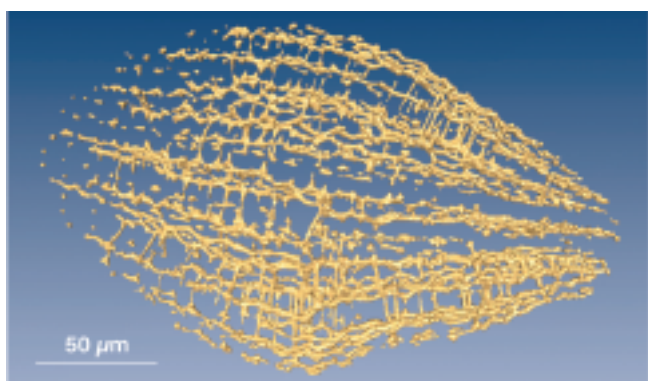


**Fig. 130:** Network of voids in the seed.

reason is that slicing requires the various liquids, in particular the polymer embedding agent, to permeate the sample. Due to the imperviousness of the seed coat, this is impossible unless incisions are deliberately made. In contrast, the X-ray tomography approach is completely non-destructive. Another question worth addressing is whether high energy (typically 21 keV) X-rays are the right probe for investigating a minute (0.4 mm), low-absorption object such as this seed. The answer is that they provide a unique combination of the desired resolution (0.3  $\mu\text{m}$  pixel size was used here), field of view (2000 x 2000 pixels) and depth investigation capacity (the whole sample). While the irradiation dose involved in this phase tomography investigation is high, it is less high than in attenuation contrast tomography. The investigation was made possible by the fact that no visible change in the morphology of the seed occurred, whereas irradiation usually leads to distortion in wet samples.

In conclusion, holotomography has made it possible to obtain the first 3D images and renditions of an autonomous living object, a small seed, at the sub-micrometre scale and in a non-destructive manner. The air-space network evidenced for the first time in this study may play a central role in the germination process.

## References

- [1] P. Cloetens, W. Ludwig, J. Baruchel, D. Van Dyck, J. Van Landuyt, J. P. Guigay, and M. Schlenker, *Appl. Phys. Lett.* **75**, 2912 (1999).
- [2] The image can be rotated in the supporting material to the original publication, <http://www.pnas.org/cgi/content/full/0603490103/DC1>.

## Principal Publication and Authors

P. Cloetens (a), R. Mache (b), M. Schlenker (c), and S. Lerbs-Mache (b), *Proc. National Acad. Sci., (USA)*, **103**, 14626-14630 (2006).

(a) ESRF

(b) Laboratoire Plastiques et Différentiation Cellulaire, UJF/CNRS, Grenoble (France)

(c) Département Nanosciences, Institut Néel, CNRS/UJF/INPG, Grenoble (France)

## 2D mapping of texture in human dental enamel

Dental enamel is the most highly mineralised and strongest biological hard tissue. It comprises 95% hydroxyapatite (HA) mineral, 4% water, and 1% organic matter (non-collagenous protein). The hydroxyapatite crystal structure of dental enamel has been determined previously by several workers. It has space group  $P6_3/m$  with lattice parameters  $a = 9.513 \text{ \AA}$  and  $c = 6.943 \text{ \AA}$  [1,2]. However the measurements were made on powdered enamel collected from many teeth, therefore any texture

information regarding the growth of the HA crystallites was lost. Information on texture is extremely valuable both for understanding the formation of dental enamel, and also to be able to increase the longevity of restorations by improving their clinical placement. In an earlier study Hirota examined the tilting of the enamel-prism orientation at twelve points in a human canine using laboratory 2D X-ray diffraction [3]. In our study, we have mapped, for the first time, the texture distribution as a function of position within entire slices of intact enamel using position-sensitive synchrotron X-ray diffraction. Here we present the preliminary results.

High-resolution synchrotron X-ray diffraction was used to collect 2D diffraction images at 150  $\mu\text{m}$  spatial resolution over the entire tooth crown. Each diffraction image had an exposure time of 5s meaning that by moving the sample relative to the beam in an x and y direction a 150  $\mu\text{m}$ -resolution map of the tooth on a grid of 10 mm x 7 mm could be collected in approximately eight hours. A 2D Mar CCD detector was used so that the change in texture around full diffraction rings could be observed. Basic texture distribution maps were generated by performing Rietveld refinement analysis of 1095 diffraction patterns, using an inhouse batch processing program and the GSAS software [4], and extracting the intensity (texture) coefficients. A composite map of CCD images of an adult second premolar is shown in **Figure 131** where diffraction patterns were collected every 150  $\mu\text{m}$ . Each point on the image is one 2D diffraction pattern, and these images have been arranged to form the whole image for illustration. The shape of the tooth can clearly be seen from this composite image. The lighter patterns around the edge are formed by the strongly textured enamel, and the darker patterns in the middle are the dentine. Below this image are four individual diffraction patterns from different parts of the tooth. Scans a), c) and d) illustrate the change in texture direction at difference positions within the enamel. Scan b) shows that dentine is nanocrystalline (broader peaks) and less textured.

The strongest degree of preferred orientation was found in the 002 reflection, and areas of high crystallite alignment on the tooth cusps are found on the expected biting surfaces of the teeth. The texture direction of enamel is perpendicular to and follows the shape of the enamel-dentine junction. Additionally, it can be seen that below the groove between the two cusps (the fissure), there is a circular region of enamel which is less textured than the

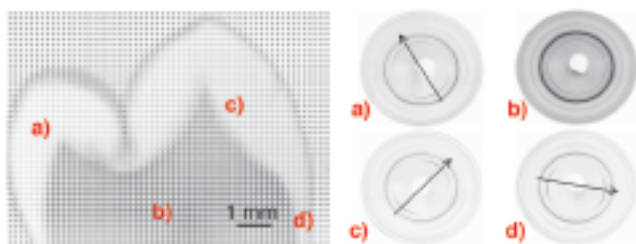


**Fig. 131:** 2D images of whole tooth section with different regions highlighted. a), c), d) enamel ; b) dentine.

surrounding structure. We believe this to be caused by a fissure lesion in the enamel which has demineralised the enamel and possibly affected it's crystalline structure.

By using spatially-resolved synchrotron X-ray diffraction, in a few hours of data collection, we have quantified the change in texture in dental enamel as a function of position within the tooth. Our study has been possible due to the high flux and energy (15keV) of the synchrotron X-rays allowing counting times of a few seconds per image, and the use of a relatively thick sample to give us results representative of the bulk material. This has given detailed quantitative information on the degree of crystallite alignment in different regions of tooth enamel not previously reported. Our results bring novel insight on the texture distribution and crystallinity within teeth and have the potential to optimise the clinical placement of dental composite materials in restorations.

### References

- [1] R.A. Young, P.E. Mackie, *Materials Research Bulletin* **15**, 17 (1980).
- [2] R.M. Wilson, J.C. Elliott, S.E.P. Dowker, *American Mineralogist* **84**, 1406 (1999).
- [3] F. Hirota, *Archives of Oral Biology* **27**, 931 (1982).
- [4] A.C. Larson, R.B. Von Dreele, General Structure Analysis System (GSAS) Los Alamos National Laboratory Report, LAUR 86-748 (2004).

### Principal Publication and Authors

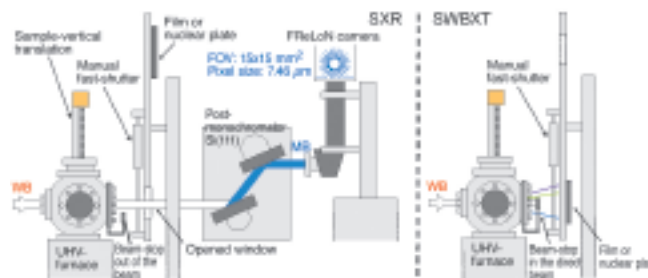
M. Al-Jawad (a), R. Cywinski (a), S.H. Kilcoyne (b), D.J. Wood (c), R.C. Shore (c), L. Bouchenoire (d), A. Steuwer (e), Fifth International Conference on Synchrotron Radiation in Materials Science, Chicago July 30- Aug 2 (2006), SRMS5- 203. Conference Proceedings (full publication submitted to Biomaterials).  
 (a) School of Physics and Astronomy, Univ. of Leeds (UK)  
 (b) Institute for Materials Research, Univ. of Salford (UK)  
 (c) Leeds Dental Institute (UK)  
 (d) XMaS beamline, ESRF (France)  
 (e) FaME38, ILL-ESRF (France)

## Imaging and Microanalysis Applied to Materials Science

### *A new setup combining radiography and diffraction topography to study the solidification of Al-based alloys in situ*

Material properties are primarily controlled by the microstructure built during the growth process. Beside their technological interest, understanding pattern formation at the solid-liquid interface is also a model case of self-organisation in systems out of thermodynamic

**Fig. 132:** Schematic drawing of the experimental set-up developed at ID19 for the combined SXR-SWBXT investigation of Al-based alloy solidification.



equilibrium. Directional solidification is the key technique for studying the dynamical phenomena involved in microstructure formation under controlled conditions. *In situ* and real-time investigations are crucial to the clarification of the pattern dynamics. A unique experimental setup, allowing the combination of synchrotron X-ray radiography (SXR) and synchrotron white beam X-ray topography (SWBXT), has been developed at beamline **ID19**. These two imaging techniques provide complementary information. While radiography captures the evolution of microstructure morphology (shape, velocity of the growing interface) and solute segregation, topography provides crystallographic insight into the growing solid (orientation, strain field) and, in favourable cases, enables defect characterisation.

Upward solidification is performed inside a Bridgman furnace placed in an Ultra High Vacuum (UHV) chamber [1]. The thin Al-based alloy sample ( $37 \times 6 \times 0.2 \text{ mm}^3$ ) is placed in a graphite crucible, mounted in a holder connected to a motorised translation stage. For *in situ* and real-time X-ray imaging (Figure 132), the main surface of the sample ( $37 \times 6 \text{ mm}^2$ ) is set perpendicular to the incident synchrotron X-ray white beam (WB). The transmitted beam is used for radiography. Radiographs are recorded using the FReLoN CGD-camera developed at the ESRF. Diffracted beams are used for topography. Topographs are recorded at will, discontinuously on high-resolution films (resolution  $5 \mu\text{m}$ ) or nuclear plates (resolution  $1 \mu\text{m}$ ) stored on a wheel placed after the UHV-chamber.

Alloy solidification from the melt often results in the growth of branching structures known as dendrites. Dendritic patterns play a critical role in the engineering of finished products with optimum properties by a wide range of solidification processes, such as casting

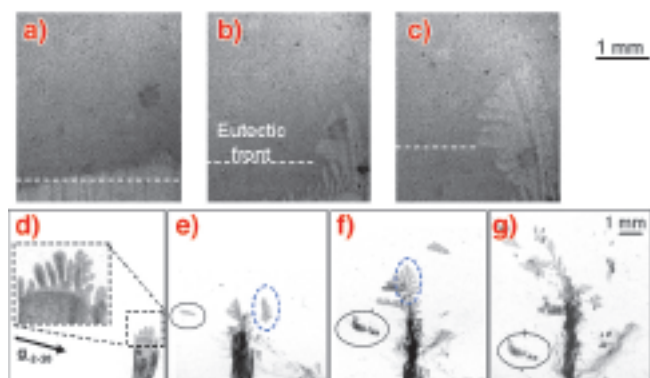


**Fig. 133:** Radiographs (a-c) and (-2-2 0)-topographs (d-g) recorded during the formation of a dendritic columnar microstructure.  $V = 1 \mu\text{m/s}$ ,  $G \approx 30 \text{ K/cm}$ . (a, d)  $t = t_0 + 1574\text{s}$ , (b, e)  $t = t_0 + 2461\text{s}$ , (c, f)  $t = t_0 + 3253\text{s}$ .

[2] and welding. Therefore, dedicated experiments are timely. Microstructure formation and quality during the directional solidification of a model metallic alloy, Al - 3.5 wt% Ni, were analysed simultaneously for the first time (Figure 133). The radiographs (Figure 133a-c) show the development of the dendritic microstructure following the morphological instability of the smooth solid – liquid interface. We can see from the topograph in Figure 133d that the dendrites are of high quality in the early stage of their growth. Indeed, the equal-thickness fringes (see close-up) attest the absence of defects (dislocations: less than  $10 \text{ cm/cm}^3$ ) in the solid. Then, although nothing can be anticipated from the continuous evolution of the dendrite morphology in the radiographs, disorienting of dendrite parts begins (Figure 133e) and becomes exacerbated with time in the topographs (Figure 133f and g). In Figure 133e and f, the image of the secondary dendrite arm (circled in black) stays separated from the main stem due to mechanical bending, whereas the image of the dendrite top (circled in dashed blue), which moves away to the right following a rotation of about  $0.1^\circ$  around the dendrite axis, later comes back into position, which suggests an elastic behaviour. At later times (Figure 133g), the distortion field splits the image into many pieces, which makes the dendrite hardly recognisable.

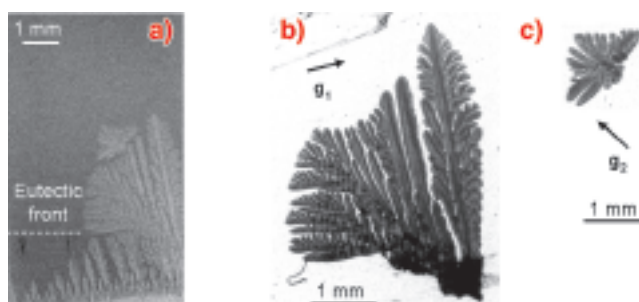


**Fig. 134:** Al-3.5wt%Ni solidification: Radiograph of the sample (a), topographs of the columnar dendritic structure (b) and of the equiaxed grain (c). Images recorded 59 min 54s after the start of cooling.

The strain level depends on the solidification process. For instance, in the case of dendritic growth by cooling the same sample at a rate of  $0.5 \text{ K/min}$  (Figure 134), high quality dendrites are observed even at sizes comparable to the largest in Figure 133 (see equal-thickness fringes in Figure 134b). Figure 134c shows that the equiaxed grain growing just above the columnar dendrite in the radiograph is equally perfect.

It is worth noticing that this grain stopped the growth of the dendritic microstructure below it.

## References

- [1] H. Nguyen-Thi *et al*, *J. Phys. D: Appl. Phys.* **36**, A83 (2003).  
 [2] J.A. Spittle, *Int. Mater. Rev.* **51**, 247 (2006).  
 [3] B. Billia *et al*, *Phys. Rev. Lett.* **93**, 126105 (2004).

## Principal Publication and Authors

A. Buffet (a), G. Reinhart (b), T. Schenk (c), H. Nguyen-Thi (b), J. Gastaldi (d), N. Mangelinck-Noël (b), H. Jung (b), J. Härtwig (a), J. Baruchel (a), B. Billia (b), *J. Phys. D: Appl. Phys.*, *in press*.

(a) ESRF

(b) L2MP, Université Paul Cézanne– Aix-Marseille III, Marseille (France)

(c) Ecole des Mines de Nancy (France)

(d) CRMCN, Campus Luminy, Marseille (France)

## Cobalt puts uniform spin distributions into ZnO

There is growing interest in the use of the spin degree of freedom in semiconductor quantum structures as a medium for the manipulation and storage of classical and quantum information. The confluence of both semiconductor and magnetic storage concepts is expected to have many advantages such as non-volatility, increased data processing speed, decreased electric power consumption, and increased integration densities compared to standard semiconductor devices. In all novel spin devices, diluted magnetic semiconductors (DMSs) play a key role. As one example, it has been suggested during the last few years that Co impurities in ZnO introduce exceptional magnetic properties, this may even lead to ferromagnetism with high Curie temperatures [1]. However, one of the key unanswered questions is whether the resulting material is indeed an alloy of (Zn,Co)O or whether it remains as ZnO with clusters, background impurities or second phases responsible for the magnetism. To clarify the mechanism by which ferromagnetism is produced, it is crucial to study the retention of single-phase elemental traces as well as local atomic distortions around Co sites, issues analysed in detail by the present work.

We have studied the Co incorporation on pulsed laser deposited (PLD) ZnO films with micrometre resolution at beamline ID22. Thin films were prepared at 400°C on sapphire substrates with a controlled atmosphere of 5N oxygen at  $2 \times 10^{-4}$  mbar. The monochromatic beam was focused using Kirkpatrick-Baez mirrors (at Co K-edge  $\sim 10^{10}$  photons/second in the focused beam:  $1.5 \times 3.5 \mu\text{m}^2$  size). The X-ray fluorescence (XRF) data are shown in Figure 135. Co concentrations, ranging from 5% up to about 26%, were estimated from the Co and Zn  $K_{\alpha}$  line

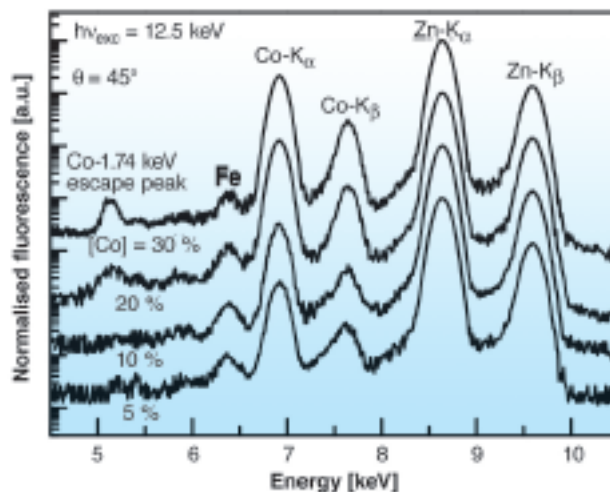


Fig. 135: XRF spectra of ZnO samples with different Co content taken at 12.5 keV.

intensity ratio [2]. The presence of residual Fe atoms could play a key role in the resulting magnetism. Elemental maps of Co and Zn were also obtained by measuring their  $K_{\alpha}$  line intensities over the sample surface. Uniform patterns with no intensity changes ( $< 0.02\%$ ) were observed for all samples, showing a homogeneous distribution of both elements at the length scale of the beam size.

XANES spectra around the Zn and Co K edges are shown in Figure 136a, shifted horizontally for clarity. Our results strongly suggest a substitutional Co incorporation into the Zn sites. A direct comparison to the XANES data around Co K edge for several model compounds confirmed predominant tetrahedral coordination of Co atoms in ZnO. Finally, Figure 136b shows the magnitude of the Fourier transforms of the Co K-edge EXAFS functions for low and high Co concentrated ZnO. Within experimental accuracy, there is no significant change of the first and second neighbour distances as a function of the Co content. The spectra look very similar, except for an apparent reduced magnitude of the nearest O-neighbour peak. This

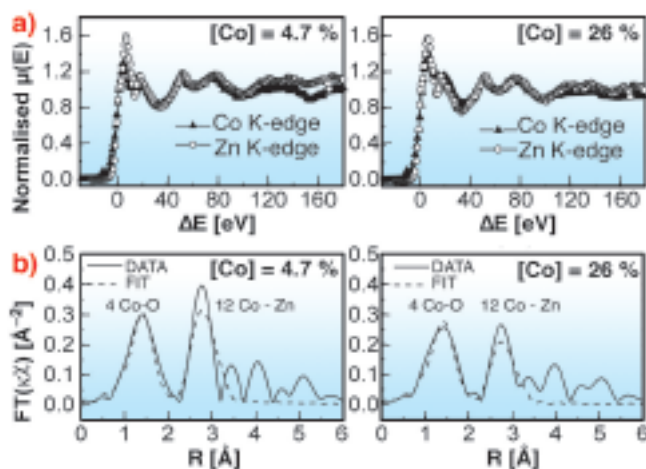


Fig. 136: a) Comparison of the Co and Zn K-edge XANES for low and high Co content in ZnO. b) Comparison of the Fourier transforms of the Co K-edge EXAFS functions. The dashed lines correspond to the data fits using FEFFIT program.

amplitude reduction is accounted for by the increase of the nearest O-neighbour Debye-Waller (DW) factor  $\sigma^2_{\text{Co-O}}$  at higher Co concentration. The small decrease in the Co-Zn distance, on the other hand, might be attributed to the competing effects of the lattice parameter reduction induced by Co incorporation and the tensile strain due to the pseudomorphic growth on sapphire (lattice mismatch  $\sim 16\%$ ). The increase in the DW factor as a function of the Co concentration can be understood because the higher static disorder induced on the Co-Zn distance by the strong Co-O interaction.

In summary, the Co concentration was estimated for all ZnO samples by XRF analysis. XANES spectra around both Co and Zn K-edges retained their main characteristics with the Co content (*i.e.* the number and energy positions of the principal resonances), strongly indicating Co on substitutional Zn sites. Chemical analysis revealed predominant tetrahedral coordination geometry of Co atoms in ZnO. Within the resolution of the hard X-ray microprobe, uniform spatial distributions of Co and Zn sites were detected on the micrometre scale. Finally, the EXAFS results provided direct evidence for the substitution of Co atoms in Zn sites.

## References

- [1] T. Dietl, H. Ohno, F. Matsukura, J. Cibert, D. Ferrand, *Science*, **287**, 1019-1022 (2000).  
 [2] G. Martinez-Criado, A. Somogyi, S. Ramos, J. Campo, R. Tucoulou, M. Salome, J. Susini, M. Hermann, M. Eickhoff, M. Stutzmann, *Appl. Phys. Lett.*, **86**, 131927 (2005).

## Principal Publication and Authors

G. Martinez-Criado (a), A. Segura (b), J.A. Sans (b), A. Homs (a), J. Pellicer-Porres (b), J. Susini (a), *Appl. Phys. Lett.*, **89**, 061906 (2006).  
 (a) ESRF  
 (b) Applied Physics Department, Valencia University (Spain)

# Imaging and Microspectroscopy for Environment and Cultural Heritage Studies

## ***Blackening of Pompeian cinnabar paintings elucidated using X-ray microfluorescence***

Pompeii and surrounding cities are a valuable treasure of our cultural heritage as they give a frozen image of the every-day life in the Roman Empire at the beginning of the 1<sup>st</sup> century. Unfortunately, some of the beautiful wall

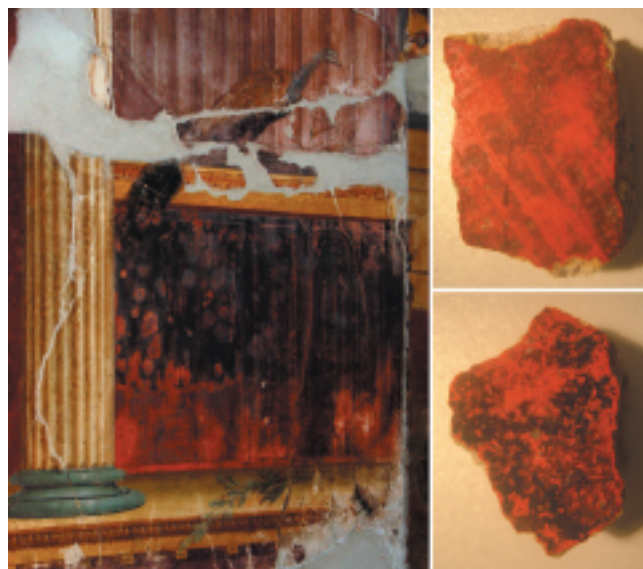


**Fig. 137:** Left, photo of a degraded wall painting in Villa di Poppea, Oplonti. Right, photos of the studied samples.

paintings that contribute to the Pompeian reputation are suffering badly from degradation. Mercury sulfide (HgS), commonly named cinnabar, is a deep red pigment, extensively used to cover the background of paintings. It participates in the highly-coloured rendering of the decoration. Yet, in certain circumstances, it can become unstable, turning into dull grey-black shades (**Figure 137**). Several samples of wall painting were taken from both altered and unaltered areas and submitted to microanalyses in order to shed light on this dramatic blackening (**Figure 137**).

The common assumption proposed to explain this phenomenon is the phase transformation of red cinnabar into black meta-cinnabar by the action of light. Different analyses were performed at the **ID21** beamline to tackle this problem.

The elements present in both well preserved and altered samples were identified. In addition to the sulphur and mercury originating from the pigment, and the calcium present as calcite in the mortar, minor exogenous elements were detected. Among them, aluminium, silicon, potassium and more interestingly chlorine. Micro X-ray fluorescence signals were then mapped over pink, grey or black surfaces. Thus, the elemental distributions were directly correlated to the visible appearance of paintings. In particular, the chlorine map matched a grey alteration perfectly. X-ray absorption spectroscopy at the chlorine K-edge was performed to assess its chemical environment. Chlorine was found to be associated with sodium and mercury. Indeed, chlorine is known to foster the cinnabar sensitivity to light and its consecutive darkening [1]. Two sources of NaCl have been suggested: the vicinity of the sea (samples studied here come from “Villa Sora” in Torre del Greco which is at the seashore) and the probable use of a particular protective mixture – the so-called “Punic Wax” – which, according to Plinius the Elder, was made by the use of seawater.

All these observations explain the deep lilac-grey aspect observed on some samples. Yet, analyses performed on another part of the painting, with a darker appearance, show a high accumulation of sulphur without chlorine. X-ray absorption spectroscopy at the sulphur K-edge revealed the speciation of sulphur and refutes the hypothesis of a phase transformation into meta-cinnabar. Amazingly, instead of this suspected phase, another compound was identified: calcium sulphate, namely gypsum. So, instead of a “simple” phase transition, sulphur was subject to a real oxidation going from a reduced sulphide ( $S^{(-II)}$ ) to an oxidised sulphate ( $S^{(+VI)}$ ) state. Most presumably, this gypsum ( $CaSO_4 \cdot 2H_2O$ ) results from the reaction of  $SO_2$  with the calcite ( $CaCO_3$ ) present in the mortar. This assumption is supported by the fact that, chlorine, whose role has already been mentioned in the darkening process, can also catalyse the linkage reaction  $HgS \rightarrow Hg + S$ , thus providing a source of sulphur for further reactions with the oxygen of air and the final formation of  $SO_2$ .

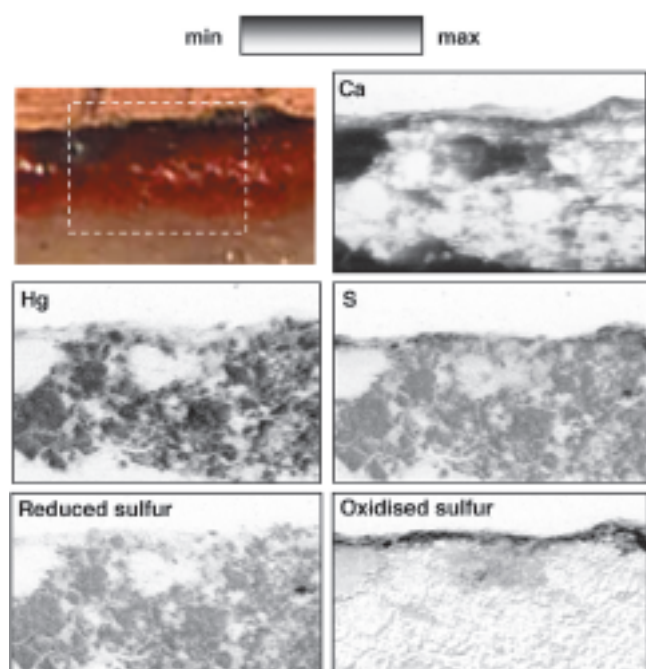


**Fig. 138:** Elemental and chemical maps in a cross-section of a degraded fragment. Map size  $95 \times 60 \mu m^2$ .

Having identified the various sulphur compounds as markers of degradation, an additional in-depth analysis was performed. A sample was embedded in resin and polished perpendicularly to the painted layer. In this way, all the painting stratigraphy was accessible from the mortar to the surface. The pigmented layer was of only  $100 \mu m$  deep rendering the use of the micro-probe essential. Micro-X-ray fluorescence was recorded with several exciting energies. **Figure 138** shows that oxidised sulphur species, sulphates, are present in a very thin superficial layer of about  $5 \mu m$ . Below this, a thick layer of intact cinnabar is still present.

In conclusion, this experiment refutes the classical explanation proposed for cinnabar blackening. Instead,

a complex pathway involving the reaction of both chlorine and sulphur dioxide has been demonstrated. This study exploits the high spatial resolution, low detection limit and high chemical sensitivity provided at the ID21 X-ray microscope. A complete elucidation of this phenomenon will require the analysis of a wider range of samples originating from various environmental situations, for example inside or outside, exposed to various climates and with or without a protecting overlayer. In particular, the possible action of micro-organisms in this set of complex chemical reactions has to be addressed.

#### Reference

[1] J.K. McCormack, *Miner. Deposita*, **35**, 796-798, (2000).

#### Principal Publication and Authors

M. Cotte (a), J. Susini (a), N. Metrich (b), A. Moscato (c), C. Gratzu (c), A. Bertagnini (d), M. Pagano (e), *Anal. Chem.*, (2006).

(a) ESRF

(b) Laboratoire Pierre Süe, CEA-CNRS, Saclay (France)

(c) Dipartimento di Scienze della Terra, Pisa (Italy)

(d) Istituto Nazionale di Geofisica e Vulcanologia, Pisa (Italy)

(e) Soprintendenza per i Beni Archeologici del Molise, Campobasso (Italy)

### Probing the redox state of iron in silicate melt/glass

Iron buffers the redox state of magmas during their ascent from the Earth's mantle to the surface as it is the most concentrated element having variable oxidation states over the range of natural oxygen fugacities. Assessing the ( $[Fe^{3+}/(Fe^{3+}+Fe^{2+})]$ ) ratio of water-rich melts and those of magmas prior to eruption remains an experimental challenge.

Here we address this problem by *in situ* measurements of the chemical environment of Fe in natural melt/glass inclusions using micro X-ray absorption near edge structure spectroscopy (XANES) at the Fe-edge. The pre-edge features of  $Fe^{2+}$  and  $Fe^{3+}$  are located on the tail of the main absorption edge in XANES spectra, and they may be discriminated in natural or experimental glasses. Melt/glass inclusions trapped in natural volcanic crystals are suitable experimental systems that give us a snapshot of the magmatic conditions at their time of entrapment, prior to eruption. The melt inclusions studied here were trapped at high temperature ( $750^\circ C$ ) and preserved as glassy inclusions in natural quartz crystals (**Figure 139a**) which act as a pressure cell avoiding outgassing during heating. They represent the typical low viscosity peralkaline rhyolitic magma, rich in both  $H_2O$  (2.5 wt%) and  $FeO$  (7 wt%), producing the so-called pantellerite lava, of which Pantelleria island is the type locality.

Various series of *in situ*  $\mu$ XANES spectra at the iron K-edge were collected between 800 and 20°C on melt inclusions, using the X-ray microscopy beamline ID21. The quartz hosting the glass inclusions were prepared as double-face polished, 150-190  $\mu\text{m}$  thick lamella in order to preserve the inclusion nearly in the centre of the mineral. They were heated in a water-cooled furnace. The XANES spectra were also acquired for reference glasses, and all were in transmission mode. The energy scan was performed in the so-called continuous mode for which the silicon (220) double crystal monochromator scanned the energy on-the-fly (non stop between two energy points) and the undulator gap and focal distance of the lens were both tuned accordingly. This dead-time free operation mode allows quick energy scans (30 s) with optimum scan reproducibility. The synchrotron X-ray source was demagnified in order to obtain a spot of  $2 \times 2 \mu\text{m}^2$ .

The main points that arise from the  $\mu$ XANES experiments are: 1) the position of the Fe pre-edge centroid of the  $1s \rightarrow 3d$  transition correlates with the  $\text{Fe}^{3+}/\Sigma\text{Fe}$  ratios in reference glasses; 2)  ${}^4\text{Fe}^{3+}$  prevails in highly oxidised peralkaline glasses, using alkalis for charge balance; 3) the ferrous iron predominates in the melt inclusions at high temperature whereas the intensity of the  $\text{Fe}^{3+}$  peak increases upon cooling. Iterative  $\mu$ XANES experiments performed on the same samples show that the process is reversible. The slower the cooling rate, the higher the ferric iron contribution (Figure 139b).

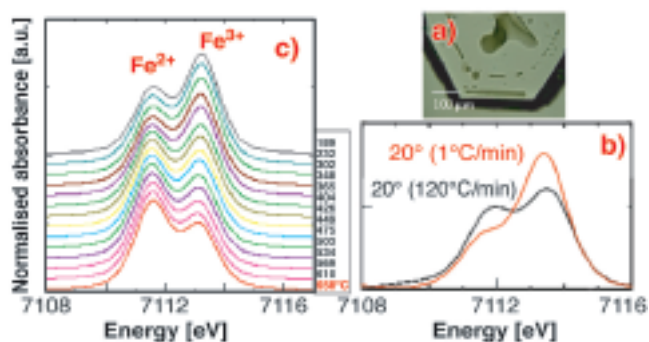


**Fig. 139:** Quartz-hosted melt inclusions from Pantelleria island a);  $\mu$ XANES spectra collected on ID21 b) and ID24 c) showing the influence of the cooling rate on the pre-edge features.

We also carried out kinetic  $\mu$ XANES experiments on the same series of quartz crystals and inclusions, in dispersion mode, on the XAS beamline ID24 [1]. The  $\mu$ XANES spectra were collected over a range of temperature from 740 to 20°C, with cooling rates varying from  $\sim 130$  to 10 °C/min. Fast acquisition times (7.9 s per spectra) allowed real time monitoring of the chemical environment of iron. These experiments evidence similar variations in the relative intensity of  $\text{Fe}^{2+}$  and  $\text{Fe}^{3+}$  pre-edges with temperature within a short time span (Figure 139c), involving rather fast kinetics [2].

Upon cooling to 20°C, the contrasting behaviour of  $\text{Fe}^{2+}$  and  $\text{Fe}^{3+}$  pre-edge is accompanied by a variation in the site geometry, with a predominance of  ${}^4\text{Fe}^{3+}$  at low temperature, compared to high temperature melts. It results in an anomalous apparent redox state of iron (Figure 140), when determined against glass standards, rapidly quenched, and where Fe is thus in a different coordination. This apparent oxidation of iron upon cooling is an artefact of changes in Fe coordination. It implies that the  $[\text{Fe}^{3+}/\Sigma\text{Fe}]$  ratio of glassy samples, measured at 20°C, may be significantly overestimated. This ratio is difficult to retrieve by probing naturally cooled glass inclusions, and most silicate glasses, unless the cooling rate is known. We show here that high temperature  $\mu$ XANES experiments led to an assessment of the ferric-ferrous ratio in the water-rich peralkaline melt in pre-eruptive magmatic conditions.

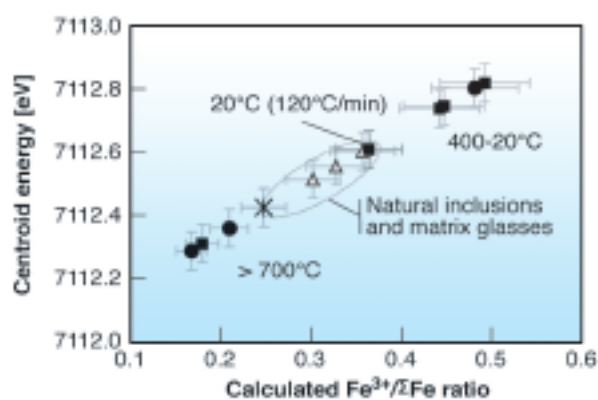


**Fig. 140:** Variation of the calculated  $\text{Fe}^{3+}/\Sigma\text{Fe}$  ratio in melt/glass inclusions with temperature and cooling rate in comparison to those of naturally cooled glass inclusions and matrix glasses.

## References

- [1] S. Pascarelli, O. Mathon and G. Aquilanti, *J. of Alloys and Compounds* 362, 33 (2004).
- [2] N. Métrich, J. Susini, M. Munoz, S. Pascarelli and D. Massare, *Geophysical Research Abstract* 7, 08840 (2005).

## Principal Publication and Authors

- N. Métrich (a), J. Susini (b), E. Foy (a), D. Massare (a), F. Farges (c), S. Lequien (a), L. Sylla (a) and M. Bonnin-Mosbah (d), *Chemical Geology* 231, 350-363 (2006).
- (a) *Laboratoire Pierre Süe, CNRS-CEA, CE-Saclay, Gif sur Yvette (France)*  
 (b) *ESRF*  
 (c) *Laboratoire de Géosciences, Université de Marne La Vallée (France)*  
 (d) *INSTN, CEA, CE-Saclay (France)*

## ***Non-destructive study of fossil inclusions in opaque amber using phase contrast X-ray synchrotron imaging***

Amber is a plant fossil resin that dates from the Carboniferous period (~ 300/350 million years ago) to the present day. It sometimes contain fossil organisms that are generally in an excellent state of preservation. The study of these organisms permits a reconstitution of paleoenvironments and allows us to obtain pieces of information about the evolution of groups that are relatively rare in the fossil record, such as insects and spiders. Most well-known ambers originate from the Baltic Sea (Eocene, ~ 30-50 My) and from the Dominican Republic (Miocene, ~ 15-20 My).

During the last ten years, some sites with especially rich fossiliferous amber from lower Cretaceous (~ 100 My) have been discovered in Charente-Maritime (South-western France). These sites are studied intensively since lower Cretaceous sites containing amber are relatively rare. This period is also a key one in the Earth's history with the explosion of phanerogams (plants with flowers), the maximum level of oceans and the maximum temperatures. Nevertheless, about 80% of the amber collected on these sites is opaque and cannot be investigated with classical optical methods, such as the optical microscope and binocular microscope, even after polishing.

Finding the precise location of organisms embedded in the opaque amber was the first major problem encountered in this study. It was impossible to see anything using classical methods (Figure 141a), so synchrotron X-ray imaging was proposed as a solution for detecting the inclusions in amber [1]. Absorption radiography (Figure 141b) failed to reveal fossils in most cases due to their tiny volume, too small with respect to the volume of their containing amber blocs. Fortunately, propagation phase contrast was found to reveal the organisms very clearly (Figure 141c). This was initially demonstrated on isolated amber blocs [1], then the experimental protocol was optimised to permit a rapid survey of numerous amber blocs to find many fossil inclusions [2]. In only 48 hours, we succeeded in imaging about 2 kg of amber (corresponding roughly to a surface of 4000 cm<sup>2</sup>) with a pixel size of 5 µm, using propagation phase contrast radiography at beamline ID19. More than 350 well-preserved fossil organisms have been located and roughly identified (up to the family taxonomic level). This first survey showed a biological diversity as rich as the one observed in the small amount of transparent amber from the same sites.

Some specimens were chosen for their preservation state and scientific interest, and scanned using phase contrast microtomography at beamlines ID19 and BM05 with

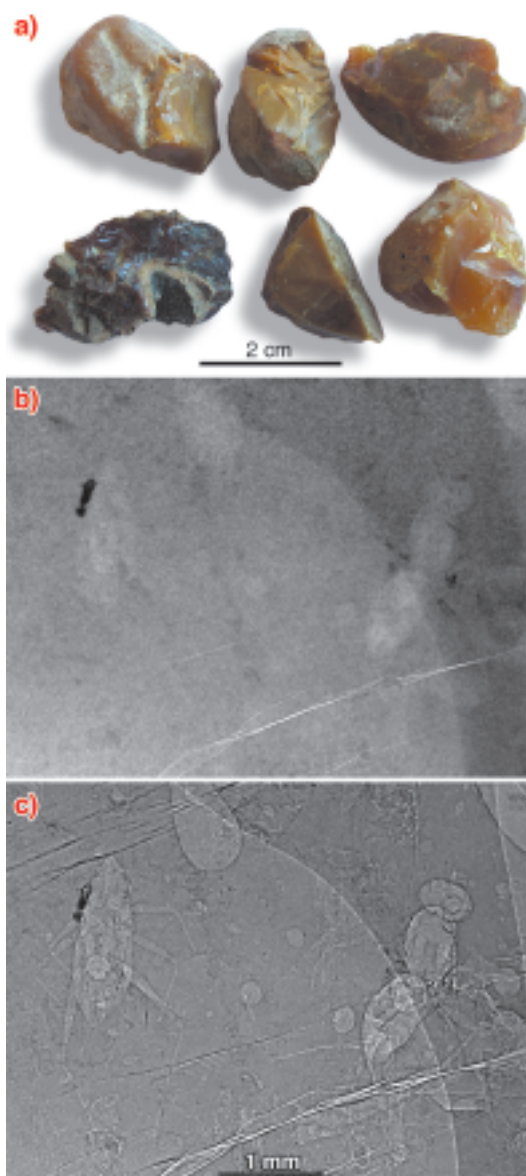


**Fig. 141:** a) Opaque amber blocs from Charente-Maritime. b) radiography of a bloc with inclusions in absorption mode. c) the same radiograph in propagation phase contrast mode with 990 mm of propagation distance (pixel size: 5 µm).

various voxel sizes from 0.7 to 15 µm. Preliminary experiments demonstrated that that technique can reveal fossil insects in opaque amber in 3D with plenty of details [1]. 3D segmentation of the data allowed us to virtually extract the selected fossil organisms from resin in order to describe them in detail and to make a taxonomic identification of the species. More than 40 specimens have been scanned to date, and a diverse range of organisms has been discovered using this technique (Figure 142). The observation of microtomographic slices showed that most of the inclusions are empty. The original organism has completely disappeared, leaving an empty cast with all of the details, or, for some arthropods, an empty envelop corresponding to the original cuticle (exoskeleton). Sometimes, pyrite has crystallised in these cavities creating a replica of the organism. In a few rare cases, some internal organic structures are still preserved. For these particular specimens, we used

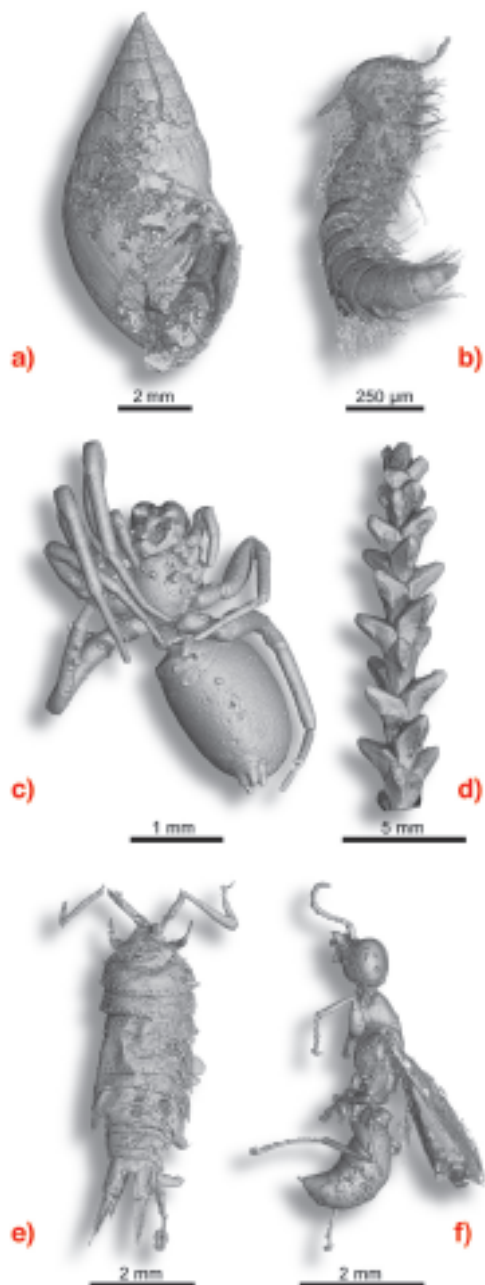


**Fig. 142:** Examples of virtual 3D extraction of organisms embedded in opaque amber. **a)** Gastropod *Ellobiidae*. **b)** Myriapod *Polyxenidae*. **c)** Arachnid. **d)** conifer branch (*Glenrosa*). **e)** Isopod crustacean *Ligia*. **f)** Insect hymenopteran *Bethyliidae*.

holotomography (quantitative phase tomography) to enhance the visibility and contrast of preserved organic structures that are sometimes extremely tiny. For example, this technique permitted us to see cellular structures (cell walls and in some cases even the preservation of inner cell structures) on a small branch of a fossil conifer (**Figure 143**).

This large survey of fossil organisms in opaque amber brings precious information about both the organisms and their ecosystem. The small gastropod (**Figure 142a**) indicates a close proximity of warm brackish water, the small isopod crustacean (**Figure 142e**) would have lived in a littoral area. These indications are in accordance with the hypothesis of a littoral environment like a lagoon

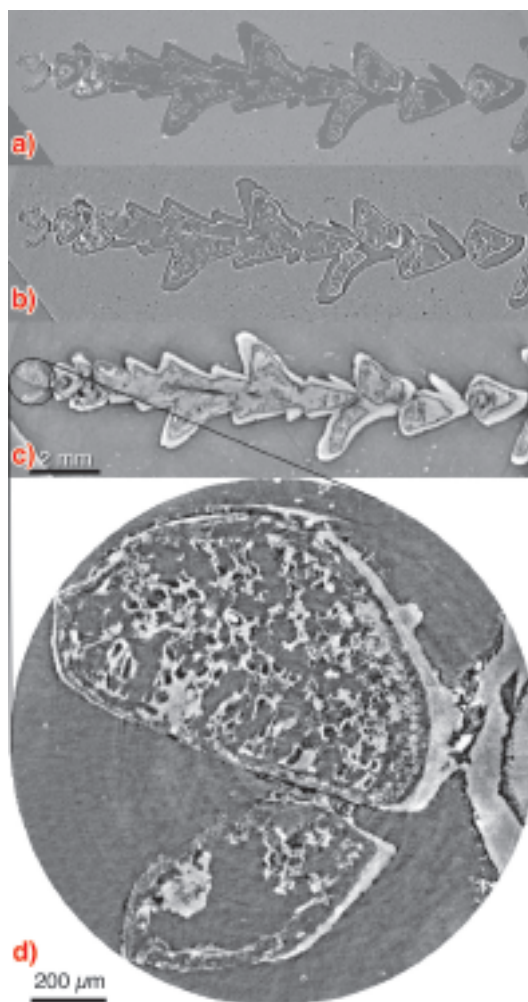


**Fig. 143:** Comparison between scans in **a)** absorption mode, **b)** propagation phase contrast and **c)** holotomography, on the conifer branch (*Glenrosa*) with a voxel size of 15  $\mu\text{m}$ . **d)** result of a high resolution holotomography (voxel size 1.4  $\mu\text{m}$ ) on the terminal burgeon showing clear cellular and tissue structures.

or a mangrove swamp. Nevertheless, data are still insufficient from a statistical point of view to be able to obtain a reliable paleoenvironmental interpretation. This preliminary study was undertaken during a masters degree and concerned only 2 kg of opaque amber. There remains more than 80 kg to study, which should result in a very busy PhD thesis.

#### References

- [1] P. Tafforeau *et al.*, *Applied Physics A*, 195-202 (2006).
- [2] M. Lak, Master2 dissertation (2006).

#### Authors

M. Lak (a,b), P. Tafforeau (b,c), D. Néraudeau (a), V. Perrichot (d) et A. Nél (e).

(a) Géosciences Rennes, UMR 6118, Rennes (France)

(b) ESRF

(c) LGBPH Poitiers, UMR 6046, Poitiers (France)

(d) Museum für Naturkunde, Berlin (Germany)

(e) MNHN Paris (France)

# Optics for Nanofocussing

## Status of the ESRF long trace profiler

The ESRF mirror metrology laboratory houses a home made Long Trace Profiler (LTP) and several other commercial interferometers. It is basically a double pencil slope-measuring interferometer, able to give the slope error, radius of curvature, and through integration, the height profile for optical surfaces larger than one metre in length. The repeatability of the ESRF LTP is better than  $0.05 \mu\text{rad}$ . To characterise its absolute precision, the ESRF metrology lab has been involved in two round-robin campaigns one at a European level and the second with the APS and SPring-8. These campaigns consist of an inter-comparison of standard X-ray mirrors measured with various LTPs and also with the BESSY N.O.M (Nanometre Optical component Measuring Machine).

The agreement for flat mirrors is better than  $0.1 \mu\text{rad}$  even for the state-of-the-art flat mirror (100 mm long) provided by the Osaka University whose figure error, measured by micro-stitching interferometry [1], is  $0.4 \text{ nm rms}$ . For spherical mirrors, the radius of curvature (down to 44 m) conformity is better than 0.3% and the residual slope profiles agree impressively well - in particular between BESSY and the ESRF, although the BESSY measurement is done with an autocollimator sensor (Figure 144).

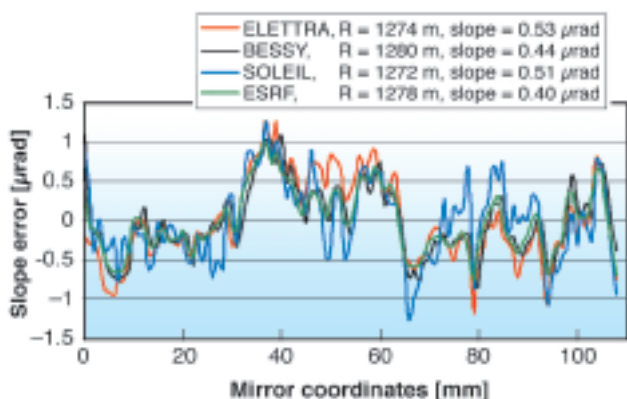


Fig. 144: spherical mirror ( $R = 1.3 \text{ km}$ ) residual slopes after best sphere subtraction.

The new generation of X-ray optics used in elliptical KB configuration, which are required for nanofocussing, is challenging for LTP metrology due to their strong slope variations. Another issue is the new concept of fixed curvature optics where LTP metrology is mandatory for deterministic surface correction. Efforts to improve the LTP performance have been made with these goals in mind. New measurement procedures have been developed to considerably reduce systematic errors induced by internal LTP optical elements. They consist of averaging profiles at various tilt angles and after a mirror rotation by 180 degrees.

The slope registration in respect to the mirror edges has also been improved to reach a repeatability better than  $5 \mu\text{m}$ . Finally new mathematical tools have been implemented resulting in a new approach to the slope error calculation, where the ideal parameters of incidence angle and focussing distance are evaluated in order to minimise the residual slope errors of the mirror. Tests were carried out on an elliptical KB focussing mirror made by elastic emission machining at the Osaka University and characterised by micro-stitching interferometry presenting a residual shape error below  $1 \text{ nm rms}$ .

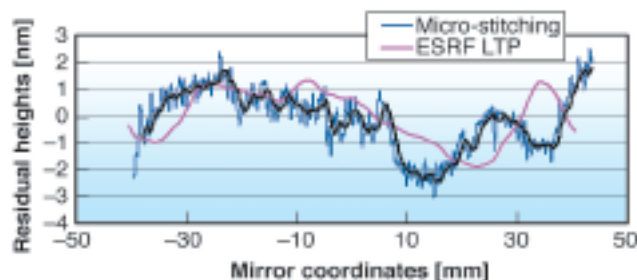


Fig. 145: OSAKA mirror residual heights after best ellipse subtraction.

With the given elliptical parameters ( $\theta = 3.26 \text{ mrad}$  and  $q = 128 \text{ mm}$  for the focussing distance) the residual errors measured with LTP are  $5.4 \mu\text{rad}$  for slopes and  $55 \text{ nm}$  for heights, these values drop down to  $0.21 \mu\text{rad}$  and  $0.98 \text{ nm}$  with the ideal parameters ( $\theta = 3.233 \text{ mrad}$  and  $q = 128.96 \text{ mm}$ ). The deviation in respect to the OSAKA metrology is  $2 \text{ nm PV}$ , and  $0.12 \text{ nm rms}$  (Figure 145). This excellent agreement suggest that a refined LTP metrology should be able to meet future requirements of nanofocussing optics.

### Reference

[1] K. Yamauchi, K. Yamamura, H. Mimura, Y. Sano, A. Saito, K. Ueno, K. Endo, A. Souvorov, M. Yabashi, K. Tamasaku, T. Ishikawa, Y. Mori, *Rev. Sci. Instrum.* **74**, 2894-2898 (2003).

### Principal Publications and Authors

A. Rommeveaux (a), M. Thomasset (b), D. Cocco (c), F. Siewert (d), *SPIE Proc.* 5921-20, 117-128 (2005); L. Assoufid (e), A. Rommeveaux (a), H. Ohashi (f), K. Yamauchi (g), H. Mimura (g), J. Qian (e), O. Hignette (a), T. Ishikawa (f,h), C. Morawe (a), A.T. Macrander (e), S. Goto (f), *SPIE Proc.* 5921-21, 129-140 (2005).

(a) ESRF

(b) Synchrotron Soleil (France)

(c) Sincrotrone Trieste (Italy)

(d) BESSY GmbH (Germany)

(e) APS (USA)

(f) SPring-8/JASRI (Japan)

(g) Osaka University (Japan)

(h) SPring-8/RIKEN (Japan)



Highlights 2006

# The X-ray Source

## Introduction

Throughout 2006, the Machine Division continued its efforts to improve performance whilst carrying out a number of developments, which are described hereunder.

## Machine parameters

**Table 2** presents a summary of the characteristics of the storage ring's electron beam.

Energy	[GeV]	6.03
Maximum current	[mA]	200
Horizontal emittance	[nm]	4
Vertical emittance (minimum achieved)	[nm]	0.03
Revolution frequency	[kHz]	355
Number of bunches		1 to 992
Time between bunches	[ns]	2816 to 2.82

**Table 2: Principal characteristics of the electron beam.**

**Table 3** gives the main optics functions, electron beam sizes and divergences at the various source points. For insertion device source points, the beta functions, dispersion, sizes and divergences are computed in the middle of the straight section. Two representative source points of bending magnet radiation have been selected, corresponding to observation angles of 3 and 9 mrad from the exit, which correspond to two distinct magnetic fields. Electron beam profiles are Gaussian and the size and divergence are presented in terms of rms quantities.

		Even ID Section (ID2, ID6 ...)	Odd ID Section (ID1, ID3 ...)	Bending Magnet 3 mrad	Bending Magnet 9 mrad
Field	[T]	Depends on ID	Depends on ID	0.4	0.85
Horiz. beta functions	[m]	35.2	0.5	1.41	0.99
Horiz. dispersion	[m]	0.137	0.037	0.061	0.045
Horiz. rms e- beam size	[ $\mu\text{m}$ ]	402	59	100	77
Horiz rms e- divergence	[ $\mu\text{rad}$ ]	10.7	90	116	111
Vert. beta functions	[m]	2.52	2.73	34.9	34.9
Vert. rms e- beam size	[ $\mu\text{m}$ ]	7.9	8.3	29.5	29.5
Vert. rms e- divergence	[ $\mu\text{rad}$ ]	3.2	3	0.85	0.85

**Table 3: Beta functions, dispersion, rms beam size and divergence for various source points.**

Filling pattern		Uniform	Hybrid	16-b	4-b
Number of bunches		992	24x8+1	16	4
Maximum current	[mA]	200	200	90	40
Lifetime	[h]	75	30	11	6
Rms energy spread	[%]	0.11	0.11	0.12	0.16
Rms bunch length	[ps]	20	25	48	55

**Table 4: Current, lifetime, bunch length and energy spread in various representative filling modes.**

The associated full width half maximum sizes and divergences are 2.35 times larger. Horizontal electron beam sizes and divergences are given for the uniform filling modes and apply to almost all filling patterns except for the single bunch, for which a slightly larger size and divergence is attained due to the increased energy spread of the electron beam. Vertical electron beam sizes and divergences apply to the uniform, 2 x 1/3 and hybrid filling modes only. To increase the lifetime of the stored beam, the vertical beam sizes and divergences are increased typically by 50% in the 16 and 4 bunch filling patterns.

The lifetime, bunch length and energy spread depend, to a large extent, on the filling pattern. These are given in **Table 4** for a few representative patterns. Note that in both the 16 bunch and 4 bunch filling patterns, the energy spread and bunch length decay with the current (the value indicated in the table corresponds to the maximum current). The bunch lengths are given for the usual radio frequency (RF) accelerating voltage of 9 MV (8 MV for 16-b and 4-b).

## Summary of machine operation

In 2006, 687 shifts (5496 hours) of beam were initially scheduled. However, following an investigation made by an external company, the ESRF was informed in November 2005 that the Litaflex material used in the baking jackets installed during the early commissioning period contained asbestos. A detailed investigation revealed that Litaflex was present in about 60 different places inside the ring tunnel. Measurements were

RUN NUMBER	TOTAL 2005	2006-01	2006-02	2006-03	2006-04	2006-05	TOTAL 2006
Start		03/02/06	31/03/06	09/06/06	18/08/06	27/10/06	
End		22/03/06	31/05/06	26/07/06	18/10/06	18/12/06	
Total number of shifts	846	141	183	141	183	156	804
Number of USM shifts	683	115.9	149.1	113.8	149.5	124.9	653.16
Beam available for users (h)	5296	910.9	1172.9	886.6	1179	969.5	5118.9
Availability	97.61%	98.88%	99.19%	98.08%	99.40%	97.45%	98.66%
Dead time for failures	2.39%	1.1%	0.8%	1.9%	0.6%	2.6%	1.3%
Dead time for refills	0.72%	0.6%	0.9%	0.7%	0.8%	0.4%	0.7%
Average intensity (mA)	153	164	136	142	122	177	146.6
Number of failures	123	11	15	16	22	21	85
Mean time between failures (h)	44.4	84.3	79.5	56.9	54.4	47.6	61.5
Mean duration of a failure (h)	1.1	0.9	0.6	1.1	0.3	1.2	0.82

Table 5: Summary of the machine operation in 2006.

immediately performed to quantify the amount of asbestos fibres in the air of the ring tunnel. The results showed that no traces were present. Nevertheless, the presence of asbestos inside the foam of the material, even in low quantities, would have significantly complicated further interventions in the ring tunnel. The ESRF management decided to remove all pieces of Litaflex as soon as possible and in a single exercise. This was possible during the winter shutdown. Preparation work started early December 2005, immediately after the discovery. Due to constraints set by legal requirements, the removal of the litaflex by a specialised company could only be started on 3<sup>rd</sup> January 2006. It took four weeks to equip the tunnel and fully complete this operation, delaying the accelerator restart by two weeks. User service mode (USM) resumed on 6<sup>th</sup> February instead of 24<sup>th</sup> January, thus reducing the scheduled USM time over the year to 5248 hours, of which 23 hours were dedicated to radiation tests, so that 5225 hours remained for USM. Out of these scheduled 5225 USM hours, 5155 hours of beam were effectively delivered (including 36 hours of refill). This represents a beam availability of 98.66%. Dead time due to failures accounts for the remaining 1.34% (Table 5). This is the highest availability figure recorded since the construction of the ESRF.

The mean time between failures (MTBF) reached 61.5 hours, which is an excellent figure, higher than the 2005 score. Fourteen long delivery periods (*i.e.* more than 100 hours) without a single interruption took place in 2006, the longest of those was 177 hours (7 days)!

As an example, we highlight the 8<sup>th</sup> week of run 2006-04, when the beam was delivered in 4 times 10 mA filling mode for 168 hours without a single hitch despite the 42 refills (Figure 146).

## Filling patterns

No significant changes in the distribution of the modes are to be noted for 2006 compared to the previous year. The multibunch modes remain dominant, making up 63% of the shifts. Figure 147 shows the distribution of the various filling modes in 2006.

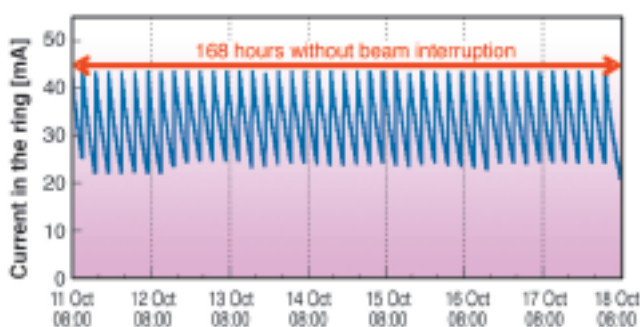


Fig. 146: 168 hours of beam delivery without interruption.

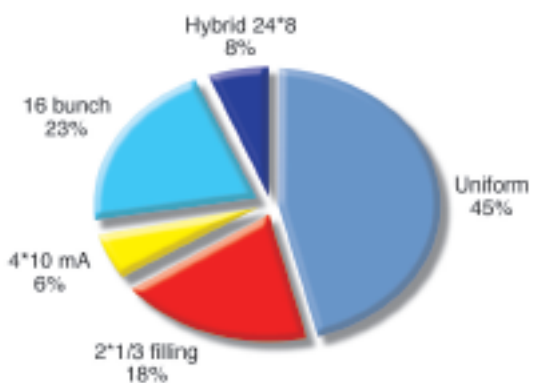
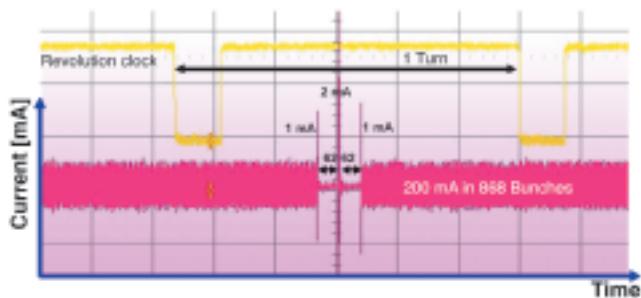


Fig. 147: Distribution of the filling modes in 2006.

The increasing demand for time structure led to the development of a new multibunch filling pattern: the so-called “7/8 + 1 filling mode”. The overall lifetime is in the order of 72 hours at 200 mA. The presence of a gap (1/8 of the circumference) avoids beam-ion instabilities, thus maintaining the vertical emittance at the lowest value,



**Fig. 148:** Current versus time of the new 7/8+1 filling mode. A high current per bunch with 62 empty bunches on both sides (at  $10^{-9}$  level) allows time-resolved beamlines to select a single bunch with a very high contrast ratio.

around 25 pm-rad. A single bunch of 2 mA, placed in the middle of the gap, is delivered with a contrast ratio of  $10^{-9}$  between filled and unfilled bunches. To satisfy Users' requests such as achieving a sharp contrast between the bunch trains and the nearly empty buckets, the first and the last bunch of the train are filled at 1 mA.

**Figure 148** presents the time structure of the beam around the ring circumference.

## Vacuum activities

In 2005 there was an in vacuum water leak located in the crotch absorber of cell 15. It resulted in a 5-day loss of USM. Soon afterwards, we realised that all other crotches were developing the same type of damage and were expected to break over the coming years. The problem is linked to the presence of a high flux of X-rays in the water producing very active radicals that combine with the copper and slowly erode the copper tube walls.

A modified version was quickly developed with twice the copper thickness in order to reduce the X-ray flux. A new series of crotch absorbers was ordered making use of glidcop (dispersion strengthened copper) in order to keep good mechanical resistance at high temperatures. Seven out of the thirty-two cells of the ring were let to atmospheric pressure in 2006 to replace the older crotches with new ones. The work was performed during the scheduled shutdown and there were no consequences for the user programme. The systematic replacement will continue throughout 2007 and should be completed in early 2008. Other activities of the vacuum group included the installation of another set of four narrow aperture ID vessels equipped with a non-evaporable getter (NEG) coating, a new in-vacuum undulator in cell 9 as well as the replacement of a few other chambers.

## Bunch by bunch feedback and 300 mA stored beam

A broadband bunch-by-bunch feedback system has been developed for the longitudinal, the vertical and the horizontal plane to combat coupled bunch instabilities. Our initial motivation was to allow ramping of the stored current up to 300 mA. To achieve this goal, a longitudinal feedback (LFB) system is required to damp longitudinal oscillations caused by the interaction of the beam with the higher order modes (HOM) of the accelerating radio frequency (RF) cavities.

The transverse feedback system (TFB) uses similar processing and was therefore easily derived from the LFB. It will damp horizontal and vertical instabilities arising from the interaction of the beam with the resistive wall impedance of the vacuum chamber and with the ions remaining in the UHV system. This damping will allow operation at reduced chromaticity, *i.e.* with relaxed sextupole settings. It is expected to provide a larger dynamical aperture of the lattice and a corresponding longer lifetime.

## Longitudinal feedback system

The strongest longitudinal HOM of the RF cavities interacts with longitudinal coherent coupled bunch oscillations of the beam. When the frequency of such an HOM precisely coincides with the upper synchrotron sideband of a revolution harmonic, the resonant exchange of energy between the beam and the cavities may result in an oscillation that increases exponentially. Its growth time decreases with the beam current and when it becomes smaller than the natural synchrotron damping time of 3.5 ms, the beam explodes longitudinally. Even in cases where the instability is contained through non linear effects, the undulator radiation becomes unusable because of the strongly increased energy spread. Such instabilities have been recorded at currents as low as 40 mA. So far, the strongest HOM of the cavities are kept off such destructive resonances by means of a dedicated temperature regulation of the cavities to  $\pm 0.05^\circ\text{C}$ . With increasing current, however, more and more of the weaker HOMs become unstable and experience has confirmed that there are no temperature settings which allow us to escape from HOM driven instabilities above 250 mA. To damp such HOM driven longitudinal instabilities, we have designed and implemented a bunch by bunch longitudinal feedback system. This feedback system measures the deviation of the arrival time in a phase pick up with respect to the nominal bunch phase for each bunch, at a rate of 352.2 MHz. A fast digital signal processor then computes the value of

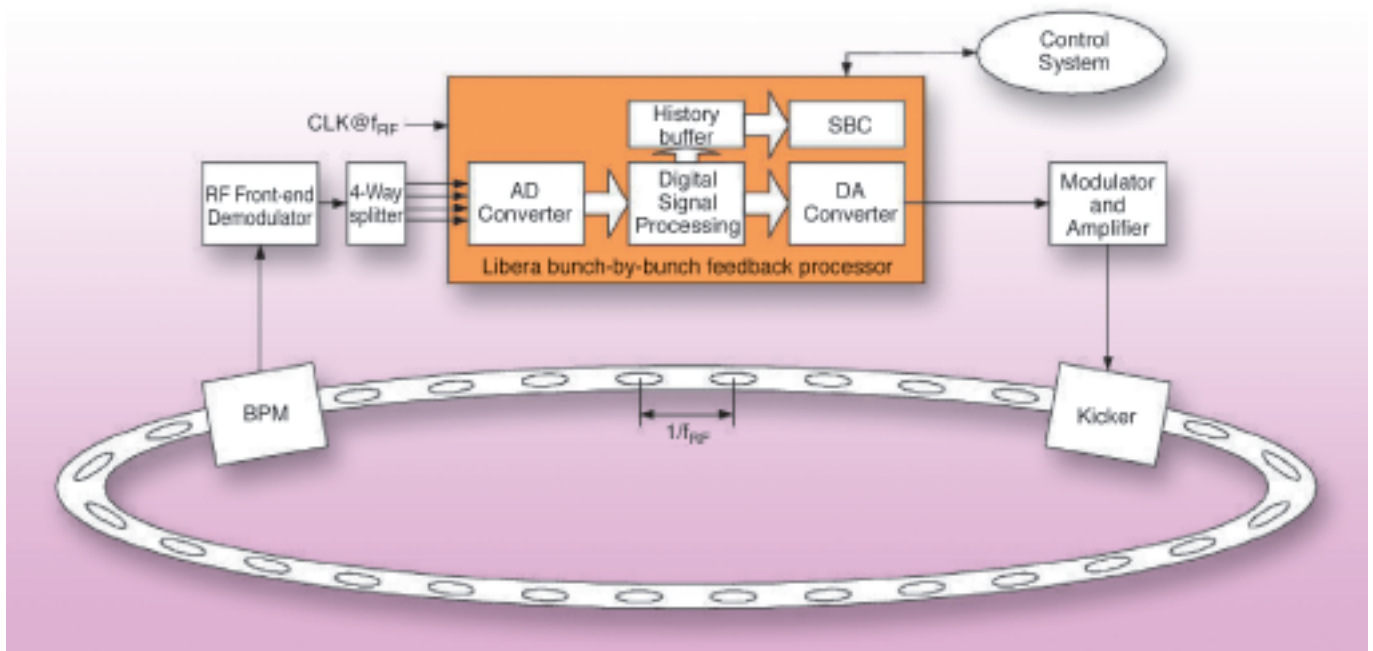


**Fig. 149:** Bunch-by-bunch feedback system for the damping of coupled bunch beam instabilities (from: [www.i-tech.si](http://www.i-tech.si)).

a correction kick (acceleration or deceleration) which is applied to the same bunch but at another place around the ring circumference. The layout of the feedback system is shown in **Figure 149**.

The components of this system have either been built at the ESRF (beam pick ups, RF front ends, kicker cavity) or subcontracted (kicker amplifier, digital signal processor). The procurement of the digital signal processor was done through a technical collaboration with the company Instrument Technology. This company customised electronics initially developed for the processing of BPM signals, called the Libera system, and turned it into a bunch by bunch signal processor. The new system has suitable data acquisition and processing rates, does data logging and has a high level programming environment for the coding of the feedback algorithm into the field programmable gate array (FPGA).

Thanks to this newly developed feedback system and to further tuning of the RF cavity working point, the target current of 300 mA was achieved in December 2006 for the first time, in uniform filling mode (the most challenging in terms of beam instability) without any sign of feedback saturation. The feedback sensitivity is such that the remaining oscillation of the damped instability has an amplitude less than one thousandth of the bunch length.

## Transverse feedback system: in commissioning

A horizontal and vertical bunch by bunch system has also been developed. The interaction of the beam with the vacuum chamber can cause unstable oscillations of the beam in the vertical or horizontal plane. These instabilities are currently avoided by tuning the sextupoles to obtain a positive value of the machine chromaticity. However, large chromaticity values have detrimental effects on beam lifetime and the injection efficiency, so it is desirable to use a transverse feedback system to allow operation with a reduced value for the chromaticity. The effect of the spurious oscillations of the beam caused by the imperfect closure of the injection bump will also be reduced by the horizontal feedback, which is also beneficial for operation with frequent topping up. These transverse feedback systems are based on the scheme shown in **Figure 149**. We made initial tests of the vertical feedback system with encouraging results and have already obtained a damping time of the vertical oscillations of 100  $\mu$ s (or 30 turns) instead of the natural betatron damping time of 7 ms. This fast damping is obtained without spoiling the vertical emittance, showing that the noise of the electronics detecting the position error signal is low. We tested a first application of the vertical feedback on a 200 mA beam stored with uniform filling. With such a filling pattern the emittance is usually spoiled by small vertical oscillations due to the interaction of the beam with positive ions trapped in the vicinity of the beam orbit. The application of the feedback reduced the vertical emittance from 27 pm to 21 pm.

## Developments of in-air X-ray diagnostics

Only 10% of the X-rays generated in the bending magnets are delivered to the beamline's front-end. The other 90% are mainly dissipated inside the crotch absorber (Figure 150). However, ~ 2 ppm of this power (i.e. 300 uW/mRad horizontal) is not absorbed and traverses the complete structure (of ~ 40 mm Cu) into the air behind. This leakage power is carried by the very high energy photons. The spectrum of this signal presents a

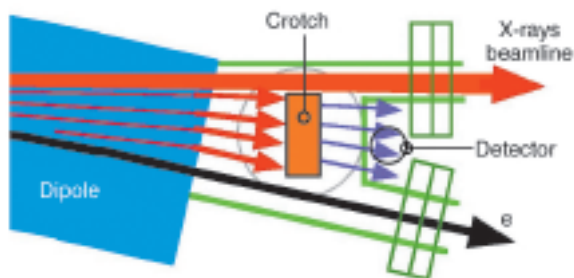


Fig. 150: Position of the IAX-detector just behind a crotch absorber.

peak at ~ 170 KeV. At this high energy the natural photon beam's vertical divergence is small. The in-air X-ray (IAX) detector is located at ~ 1 m from the source point in the bending magnet and the observed vertical spot size essentially results from the projected natural divergence of the synchrotron radiation convoluted by the vertical size of the electron beam at the source. The imaging IAX detector uses a High-Z scintillator, such as CdWO<sub>4</sub> or LuAg:Ce, with a simple optical system to focus an image onto a CCD camera (Figure 151). The assembly is compact since space is limited between the crotch chamber and the flanges, just a few cm further downstream. Lead shielding (not shown) was applied to protect the components against degradation from the hostile environment at this location.

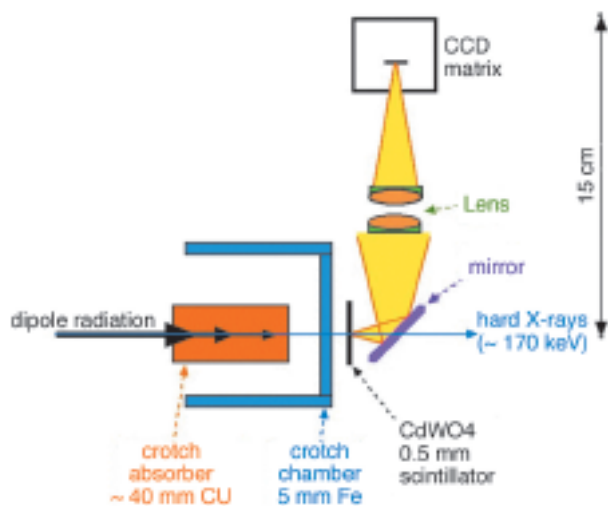


Fig. 151: Schematic side-view of the imaging IAX detector.

The image that the X-rays project onto the screen is essentially a wide horizontal line with a vertical profile of small dimensions. (Figure 152). The electron beam size is obtained from the measured beam size following a deconvolution with the natural divergence of the synchrotron radiation.

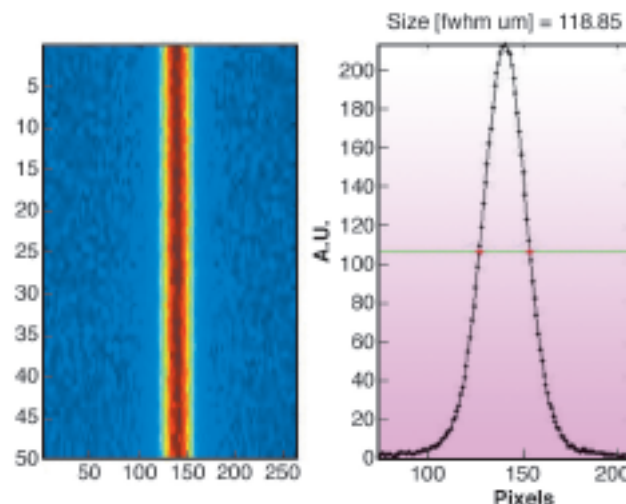


Fig. 152: Example of image and profile-plot obtained with the imaging IAX detector.

The relative precision of the electron beam size measurement is estimated at better than 2%, taking into account the precision with distance and photon divergence. Comparative measurements (Figure 153) of the ring's vertical emittance were carried-out with this device together with the two independent emittance measurement systems based on X-ray pinhole cameras. The current in a single skew-quadrupole was varied over a certain range and at each point the resulting vertical emittance measurements of the three devices were recorded. The apparent discrepancy between the three results (with each device at a different physical location

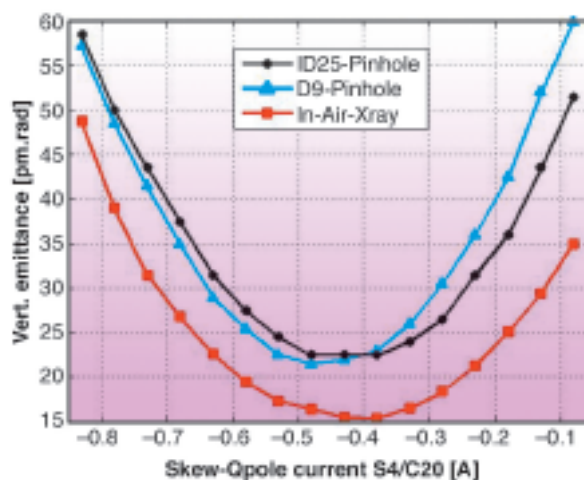
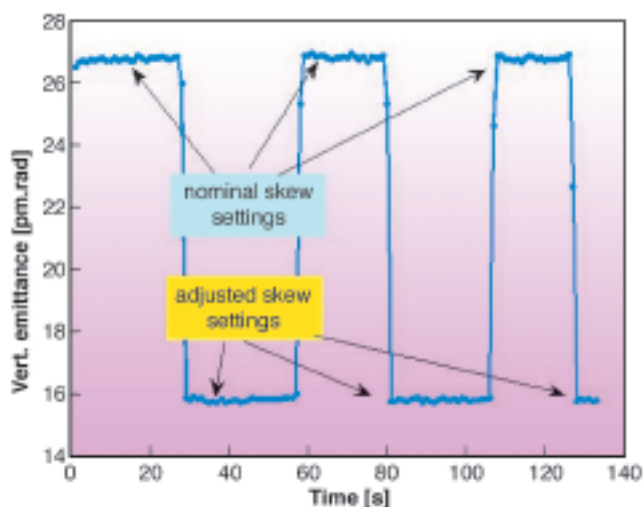


Fig 153: Results of vertical emittance measurements with the imaging IAX and the two X-ray pinhole camera systems versus varying current in a skew-quadrupole.

in the ESRF ring) is expected with the applied method. The high resolution (estimated at < 0.05 pm for 1 second measurement & averaging time) is also shown in

**Figure 154** when the currents in the skew quadrupoles are switched a few times between two different settings (nominal and ultra-small emittance).



**Fig. 154:** Vertical emittances measured by the imaging IAX camera C5 for two different settings of the skew quadrupoles.

In 2006, five IAX Imaging devices were commissioned. Such detectors will later be used to develop a vertical emittance stabilisation system that will maintain a small unchanged vertical emittance over long periods for any gap settings of the insertion devices.

## Electric IAX detector

The same leakage X-rays can also be detected more directly by the use of a high-Z blade in combination with a small in-air ionisation volume. This 'electric version' of an IAX detector consists of two parallel plates (or blades of 23 x 23 mm) separated by a small distance (typically 1 mm) in air. One of the blades is connected to a DC bias voltage (type 50V), while the other blade is connected via a short coaxial cable to a high impedance electric measurement device.

Interaction of the high energy X-rays with the high-Z material causes ionisation of the air molecules in the small volume between the two blades. This conductive state together with the applied DC bias voltage allows measurement of a strong voltage signal.

With the detector positioned on the slope of a  $\sim 100$   $\mu\text{m}$  fwhm vertical profile the recorded voltage signal is extremely sensitive to vertical beam position variations. The linearity is acceptable for beam displacements of  $\pm 20$   $\mu\text{m}$ .

The performance in the AC range up to 400 Hz is shown in recordings with the global feedback system either active or off (**Figure 155**). Extensive tests have been

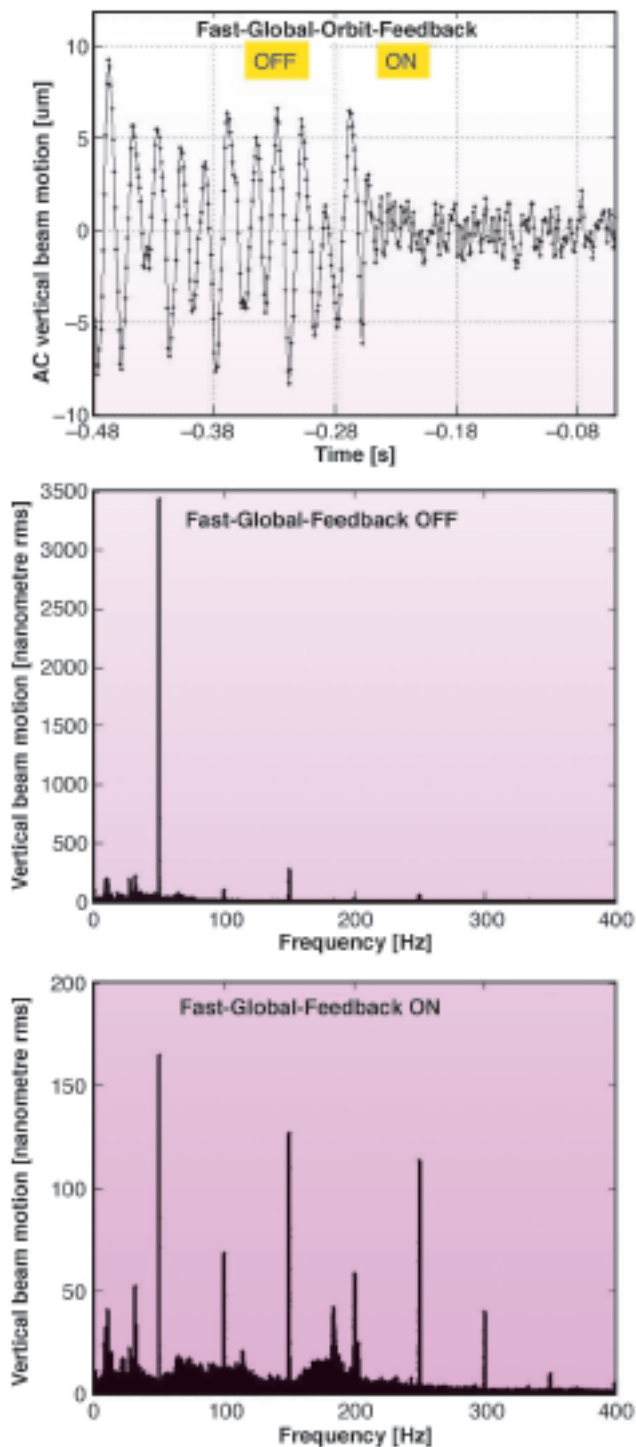


**Fig. 155:** Vertical beam positioning [ $\mu\text{m}$ ] vs time and associated FFT observed through an electric IAX monitor with or without the position feedback in operation.

carried out to assess the resolution and to compare with other diagnostic methods. The in-air blade monitor, that benefits from its location on a high vertical beta in the machine lattice, demonstrates a superior resolution to both the fast electron beam position monitors (BPMs) and the classical X-ray beam position monitors using blades sensitive to UHV. Eight of these devices are scheduled for installation in 2007. The interest of such monitors is in the further stabilisation of the orbit in the vertical plane beyond the present state limited by the noise in electron BPMs.

## Storage ring magnet lattice

The installation of canted undulators in some of the straight sections of the ESRF storage ring is envisaged in the future. In order to minimise the reduction in flux / brilliance induced by the splitting of the straight sections and the chicane magnet setup, the possibility of increasing the available space for insertion devices in straight sections beyond the 5 m currently available has been investigated.

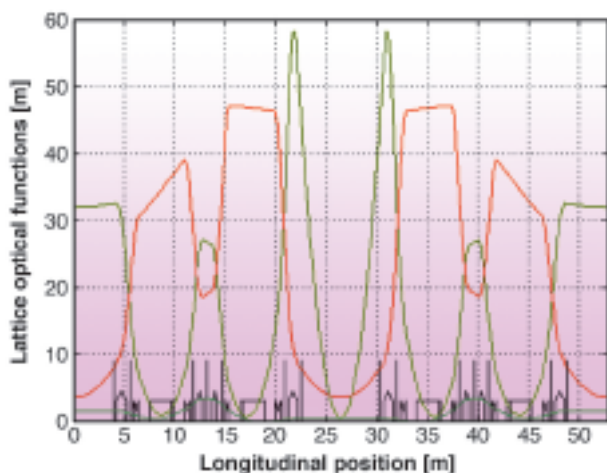


**Fig. 156:** New lattice functions allowing the implementation of 6 m long IDs.

The ESRF storage ring's double bend achromat lattice type was designed with quadrupole triplets in the straight sections to provide maximum flexibility and allow the possibility of setting a wide range of  $\beta$  values in the straight sections. This flexibility has never been used

and replacing the quadrupole triplets by doublets is attractive with regards to free space. Indeed the removal of the last quadrupole adjacent to the ID allows an increase in the ID length from 5 to 6 m. In 2006, a new current setting for all quadrupoles and sextupoles of the lattice that do not power the QD1 and QD8 family (located on both sides of the undulators) was defined. This was tested and implemented in User Service Mode in October 2006. Minor changes in beam parameters were induced by this change of lattice functions. In order to anticipate a longer-term evolution of the lattice where the available space for IDs could be further increased to 7 m by shortening the long quadrupoles of the doublets, the vertical  $\beta$  in the straight section has been increased from 2.5 m to 3.5 m, thus leading to a reduction of the vertical tune by 2 integers. The lattice functions are shown in **Figure 156**.

As of December 2006, the lifetime in uniform filling mode is about 55 h compared to 75 h for the previous lattice. A further optimisation of the non linear lattice is required and this will be done in 2007. This should restore the original lifetime.

The new lattice has a nominal horizontal emittance of 3.7 nm and an energy spread of 0.11 % (against 3.8 nm and 0.11% for the one in used so far). **Table 6** gives the beta functions, dispersion and beam size in both horizontal and vertical planes for the new lattice. There are small variations such as a 20% increase of the vertical beam size and a similar decrease in divergence. There is also a reduction of the horizontal source size in both high and low beta ID source points by 6 and 11% respectively.

		Even ID Section (ID2, ID6 ...)	Odd ID Section (ID1, ID3 ...)	Bending Magnet 3 mrad	Bending Magnet 9 mrad
Field	[T]	Depends on ID	Depends on ID	0.4	0.85
Horiz. beta functions	[m]	31.9	0.34	1.09	0.79
Horiz. dispersion	[m]	0.150	0.037	0.054	0.038
Horiz. rms e- beam size	[ $\mu\text{m}$ ]	379	53	86	67
Horiz rms e- divergence	[ $\mu\text{rad}$ ]	10.8	105	112	108
Vert. beta functions	[m]	3.5	3.6	46.6	46.6
Vert. rms e- beam size	[ $\mu\text{m}$ ]	9.1	9.1	34	34
Vert. rms e- divergence	[ $\mu\text{rad}$ ]	2.6	2.6	0.74	0.74

**Table 6:** Beta functions, dispersion, rms beam size and divergence for the various source points of the ring operated with the new lattice settings.



**ESRF**

Highlights 2006

# Facts and Figures



# Member and Associate Countries

(as of January 2007)

## Members' share in contribution to the annual budget:

27.5%	France
25.5%	Germany
15%	Italy
14%	United Kingdom
4%	Spain
4%	Switzerland
6%	Benesync (Belgium, The Netherlands)
4%	Nordsync (Denmark, Finland, Norway, Sweden)

## Additional contributions

(percentages refer to Members' total contribution):

1%	Portugal
1%	Israel
1%	Austria
1%	Poland
0.47%	Czech Republic
0.2%	Hungary



# The Beamlines

Details of the public ESRF beamlines as well as those operated by Collaborating Research Groups (CRG) are given in **Tables 7** and **8**. **Figure 157** shows the location of the beamlines in the experimental hall.

The recently refurbished beamlines ID03 and ID26 became operational in 2006. The Machine Division beamline ID06 is currently being moved to ID30, while ID06 will become a beamline for instrumentation development. Both beamlines will become operational during the year 2007.

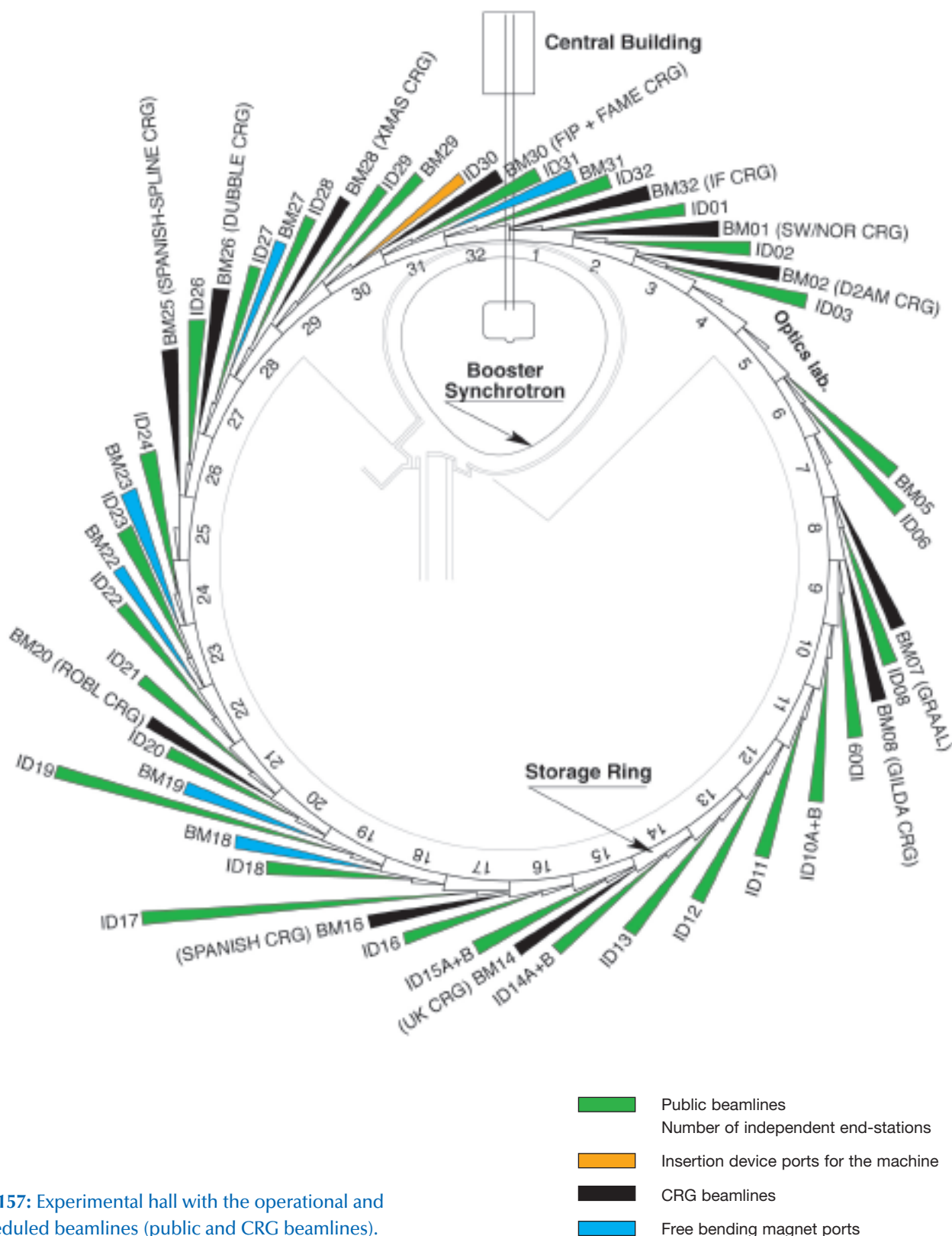


**Fig. 157:** Experimental hall with the operational and scheduled beamlines (public and CRG beamlines).

SOURCE POSITION	NUMBER OF INDEPENDENT END-STATIONS	BEAMLINE NAME	STATUS
ID01	1	Anomalous scattering	Operational since 07/97
ID02	1	High brilliance	Operational since 09/94
ID03	1	Surface diffraction	Operational since 09/94
ID06	1	Instrumentation development	Operational in 2007
ID08	1	Dragon	Operational since 02/00
ID09	1	White beam	Operational since 09/94
ID10A	1	Troika I + III	Operational since 09/94
ID10B	1	Troika II	Operational since 04/98
ID11	1	Materials science	Operational since 09/94
ID12	1	Circular polarisation	Operational since 01/95
ID13	1	Microfocus	Operational since 09/94
ID14A	2	Protein crystallography EH 1	Operational since 07/99
		Protein crystallography EH 2	Operational since 12/97
ID14B	2	Protein crystallography EH 3	Operational since 12/98
		Protein crystallography EH 4	Operational since 07/99
ID15A	1	High energy diffraction	Operational since 09/94
ID15B	1	High energy inelastic scattering	Operational since 09/94
ID16	1	Inelastic scattering I	Operational since 09/95
ID17	1	Medical	Operational since 05/97
ID18	1	Nuclear scattering	Operational since 01/96
ID19	1	Topography	Operational since 06/96
ID20	1	Magnetic scattering	Operational since 05/96
ID21	1	X-ray microscopy	Operational since 12/97
ID22	1	Microfluorescence	Operational since 12/97
ID23	2	Macromolecular crystallography MAD	Operational since 06/04
		Macromolecular crystallography microfocus	Operational since 09/05
ID24	1	Dispersive EXAFS	Operational since 02/96
ID26	1	X-ray absorption and emission	Operational since 11/97
ID27	1	High pressure	Operational since 02/05
ID28	1	Inelastic scattering II	Operational since 12/98
ID29	1	Multiwavelength anomalous diffraction	Operational since 01/00
ID30	1	Machine division beamline	Operational in 2007
ID31	1	Powder diffraction	Operational since 05/96
ID32	1	SEXAFS	Operational since 11/95
BM05	1	Optics - Open Bending Magnet	Operational since 09/95
BM29	1	X-ray absorption spectroscopy	Operational since 12/95

**Table 7:** List of the ESRF public beamlines in operation and under construction.

SOURCE POSITION	NUMBER OF INDEPENDENT END-STATIONS	BEAMLINE NAME	FIELD OF RESEARCH	STATUS
BM01	2	Swiss-Norwegian BL	X-ray absorption & diffraction	Operational since 01/95
BM02	1	D2AM (French)	Materials science	Operational since 09/94
BM07	1	GRAAL (Italian / French)	Gamma ray spectroscopy	Operational since 06/95
BM08	1	Gilda (Italian)	X-ray absorption & diffraction	Operational since 09/94
BM14	1	UK CRG	Macromolecular crystallography (MAD)	Operational since 01/01
BM16	1	SPANISH CRG	Structural biology (MAD, SAX)	Operational since 01/03
BM20	1	ROBL (German)	Radiochemistry & ion beam physics	Operational since 09/98
BM25	2	SPLINE (Spanish)	X-ray absorption & diffraction	Operational since 04/05
BM26	2	DUBBLE (Dutch/Belgian)	Small-angle scattering & interface diffraction Protein crystallography + EXAFS	Operational since 12/98 Operational since 06/01
BM28	1	XMAS (British)	Magnetic scattering	Operational since 04/98
BM30	2	FIP (French) FAME (French)	Protein crystallography EXAFS	Operational since 02/99 Operational since 08/02
BM32	1	IF (French)	Interfaces	Operational since 09/94

**Table 8:** List of the Collaborating Research Group beamlines in operation and under construction.

## User Operation

After more than 10 years of successful operation of the facility for scientific Users, the year 2006 saw the full complement of 31 public beamlines, together with 11 additional beamlines operated by Collaborating Research Groups (CRGs) available for experiments by visiting research teams. **Figure 158** shows the increase in the number of applications for beamtime since 1999, and confirms that although the main beamline construction effort was complete by 1999, the number of applications for beamtime continues to increase steadily.

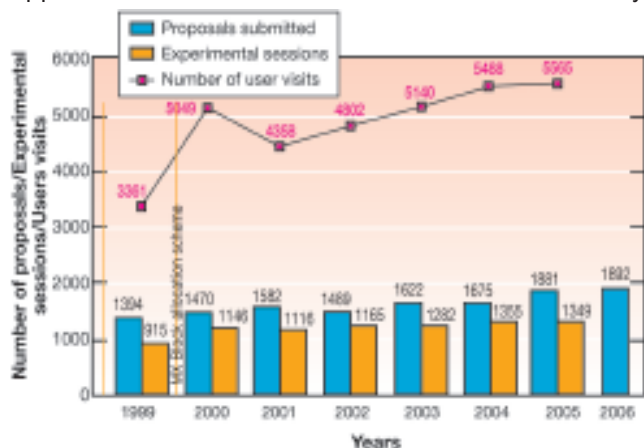


**Fig. 158 :** Numbers of applications for beamtime, experimental sessions and user visits, 1999 to 2006. N.B. Final numbers of experiments and user visits for 2006 were not available at the time of going to press.

Proposals for experiments are selected and beamtime allocations are made through peer review. Review Committees of specialists for the most part from European countries and Israel, have been set up in the following scientific areas:

- chemistry
- hard condensed matter: electronic and magnetic properties
- hard condensed matter: crystals and ordered systems
- hard condensed matter: disordered systems and liquids
- applied materials and engineering
- environmental and cultural heritage matters
- macromolecular crystallography
- medicine
- methods and instrumentation
- soft condensed matter
- surfaces and interfaces.

The Review Committees met twice during the year, some six weeks after the deadlines for submission of proposals (1 March and 1 September). They reviewed a record number of 1892 applications for beamtime, and selected 828 (43.8 %), which were then scheduled for experiments.

Features of this period:

- in view of the increasing numbers of proposals

received overall, and of emerging areas of research in the areas of the environment and cultural heritage, two new Review Committees were created, viz, a hard condensed matter: disordered systems & liquids Committee, and a Committee in environmental and cultural heritage matters.

- the continued successful operation of the Block Allocation Group (BAG) scheme for macromolecular crystallography users. This scheme, designed to encourage groups of users to block together their multiple requests for beamtime, and the scheduling of their experiments, encompassed 45 groups from Europe and Israel in 2006.

Scientific field	Total shifts requested	Total shifts allocated
Chemistry	3 421	1 036
Hard condensed matter:		
• Electronic and magnetic prop.	4 624	2 055
• Crystals and ordered structures	3 800	1 657
• Disordered systems	2 159	630
Applied materials and engineering	3 350	1 428
Environmental and cultural heritage matters	1 843	666
Macromolecular crystallography	3 139	2 341
Medicine	997	423
Methods & instrumentation	886	342
Soft condensed matter	2 811	1 358
Surfaces & interfaces	2 893	1 146
<b>Totals</b>	<b>29 923</b>	<b>13 082</b>

**Table 9:** Number of shifts of beamtime requested and allocated for user experiments, year 2006.

Requests for beamtime, which is scheduled in shifts of 8 hours, totalled 29 923 shifts or 239 384 hours in 2006, of which 13 082 shifts or 104 656 hours (43.7%) were allocated. The distribution of shifts requested and allocated, by scientific area, is shown in **Table 9**.

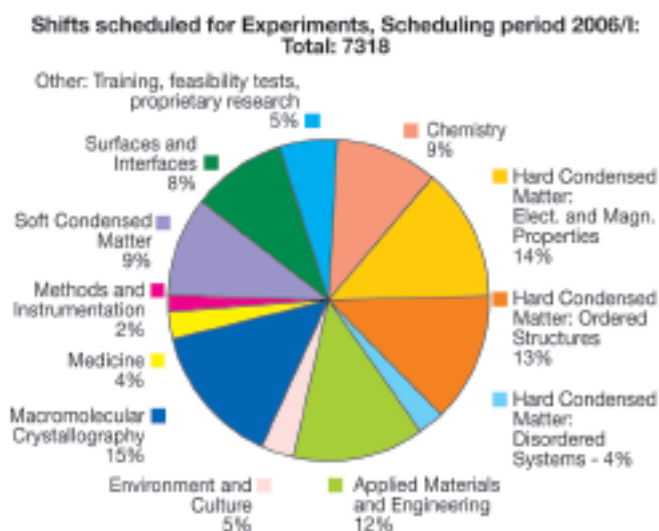


**Fig. 159:** Shifts scheduled for experiments, March to July 2006, by scientific area.

The breakdown of shifts scheduled for experiments by scientific area in the first half of 2006 is shown in **Figure 159**. This period saw 2978 visits by scientists to the ESRF under the user programme, to carry out 712 experiments. **Figure 158** shows the rapid rise in the number of user visits since 1999, the higher numbers in recent years reflecting in part the multiple visits made by macromolecular crystallography BAG teams. The peak in 2000 is due to a somewhat longer scheduling period, and correspondingly higher overall number of experimental sessions, and visits by users.

Overall, the number of users in each experimental team averaged 4.2 persons, and they stayed for some 4 days. Users responding to questionnaires indicate that they particularly appreciate the assistance they receive from scientists and support staff on beamlines, and smooth administrative arrangements, in addition to the quality both of the beam and of the experimental stations. Facilities on site, such as preparation laboratories, the Guesthouse and a canteen open 7 days a week, also make an important contribution to the quality of user support.

## Administration and Finance

Expenditure and income 2005				
	kEuro		kEuro	
Expenditure			Income	
Machine			2005 Members' contributions	67 081.3
Personnel		4 982.5	Funds carried forward from 2004	6.0
Recurrent		2 444.4		
<i>Operating costs</i>	2 000.3		Other income	
<i>Other recurrent costs</i>	444.1		Scientific Associates	3 768.7
Capital		3 156.3	Sale of beamtime	2 373.2
<i>Machine developments</i>	3 156.3		Other sales	397.6
Beamlines, experiments and in-house research			Compensatory funds	1 157.0
Personnel		21 837.1	Scientific collaboration and Special projects	1 735.6
Recurrent		6 645.8	Other	1 308.4
<i>Operating costs</i>	3 767.4			
<i>Other Recurrent costs</i>	2 878.4			
Capital		7 255.0		
<i>Beamline developments</i>	4 638.1			
<i>Beamline refurbishment</i>	2 616.9			
Technical and administrative supports				
Personnel		15 776.1		
Recurrent		9 493.8		
Capital		4 920.8		
Personnel costs provision		1 301.0		
Unexpended committed funds				
Funds carried forward to 2006		15.0		
<b>Total</b>		<b>77 827.8</b>	<b>Total</b>	<b>77 827.8</b>

Revised expenditure and income budget for 2006				
	kEuro		kEuro	
Expenditure			Income	
Machine			2006 Members' contributions	68 449
Personnel		5 025	Funds carried forward from 2005	15
Recurrent		2 200		
<i>Operating costs</i>	1 806		Other income	
<i>Other recurrent costs</i>	394		Scientific Associates	3 821
Capital		3 060	Sale of beamtime	2 420
<i>Machine developments</i>	3 060		Other sales	525
Beamlines, experiments and in-house research			Compensatory funds	68
Personnel		23 335	Scientific collaboration and Special projects	1 380
Recurrent		6 455	Other	1 690
<i>Operating costs</i>	3 345			
<i>Other Recurrent costs</i>	3 110			
Capital		7 330		
<i>Beamline developments</i>	2 800			
<i>Beamline refurbishment</i>	4 530			
Technical and administrative supports				
Personnel		16 220		
Recurrent		10 100		
Capital		3 993		
Industrial and commercial activity				
Personnel		440		
Recurrent		210		
Personnel costs provision				
<b>Total</b>		<b>78 368</b>	<b>Total</b>	<b>78 368</b>

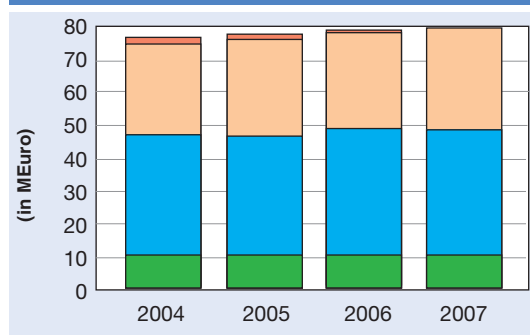
Expenditure 2005 by nature of expenditure		kEuro
<b>PERSONNEL</b>		
ESRF staff		40 975.0
External temporary staff		25.1
Other personnel costs		1 595.0
<b>RECURRENT</b>		
Consumables		6 795.0
Services		9 581.1
Other recurrent costs		2 208.0
<b>CAPITAL</b>		
Buildings, infrastructure		3 156.8
Lab. and Workshops		249.4
Machine incl. ID's and Fes		3 156.2
Beamlines, Experiments		7 255.0
Computing Infrastructure		1 385.8
Other Capital costs		128.7
Personnel costs provision		1 301.0
<b>Unexpended committed funds</b>		
Funds carried forward to 2006		15.0
<b>Total</b>		<b>77 827.8</b>

Revised budget for 2006 by nature of expenditure		kEuro
<b>PERSONNEL</b>		
ESRF staff		43 105
External temporary staff		85
Other personnel costs		1 830
<b>RECURRENT</b>		
Consumables		7 295
Services		9 355
Other recurrent costs		2 315
<b>CAPITAL</b>		
Buildings, infrastructure		2 007
Lab. and Workshops		455
Machine incl. ID's and Fes		3 060
Beamlines, Experiments		7 330
Computing Infrastructure		885
Other Capital costs		646
Personnel costs provision		
<b>Total</b>		<b>78 368</b>

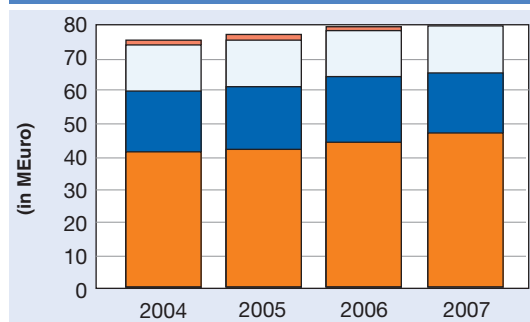
2006 manpower (posts filled on 31/12/2006)				
	Scientists, Engineers, Senior Administrators	Technicians and Administrative Staff	PhD students	Total
<b>Staff on regular positions</b>				
Machine	25	38	2	65
Beamlines, instruments and experiments*	197	64.2	29	290.2
General technical services	51.6	64.6		116.1
Directorate, administration and central services	30.3	52.8		83.2
<i>Sub-total</i>	<i>303.9</i>	<i>219.5</i>	<i>31</i>	<i>554.4</i>
<b>Other positions</b>				
Short term contracts	8	13.8		21.8
Scientific collaborators	7			7
Staff under "contrats de qualification" (apprentices)		17		17
European Union grants	7		3	10
<b>Total</b>	<b>325.9</b>	<b>250.3</b>	<b>34</b>	<b>610.2</b>
Absences of staff (equivalent full time posts)				24.9
<i>Total with absences</i>				<i>585.4</i>
<i>External funded research fellows</i>	<i>4</i>		<i>14</i>	<i>18</i>

\* Including scientific staff on time limited contract.

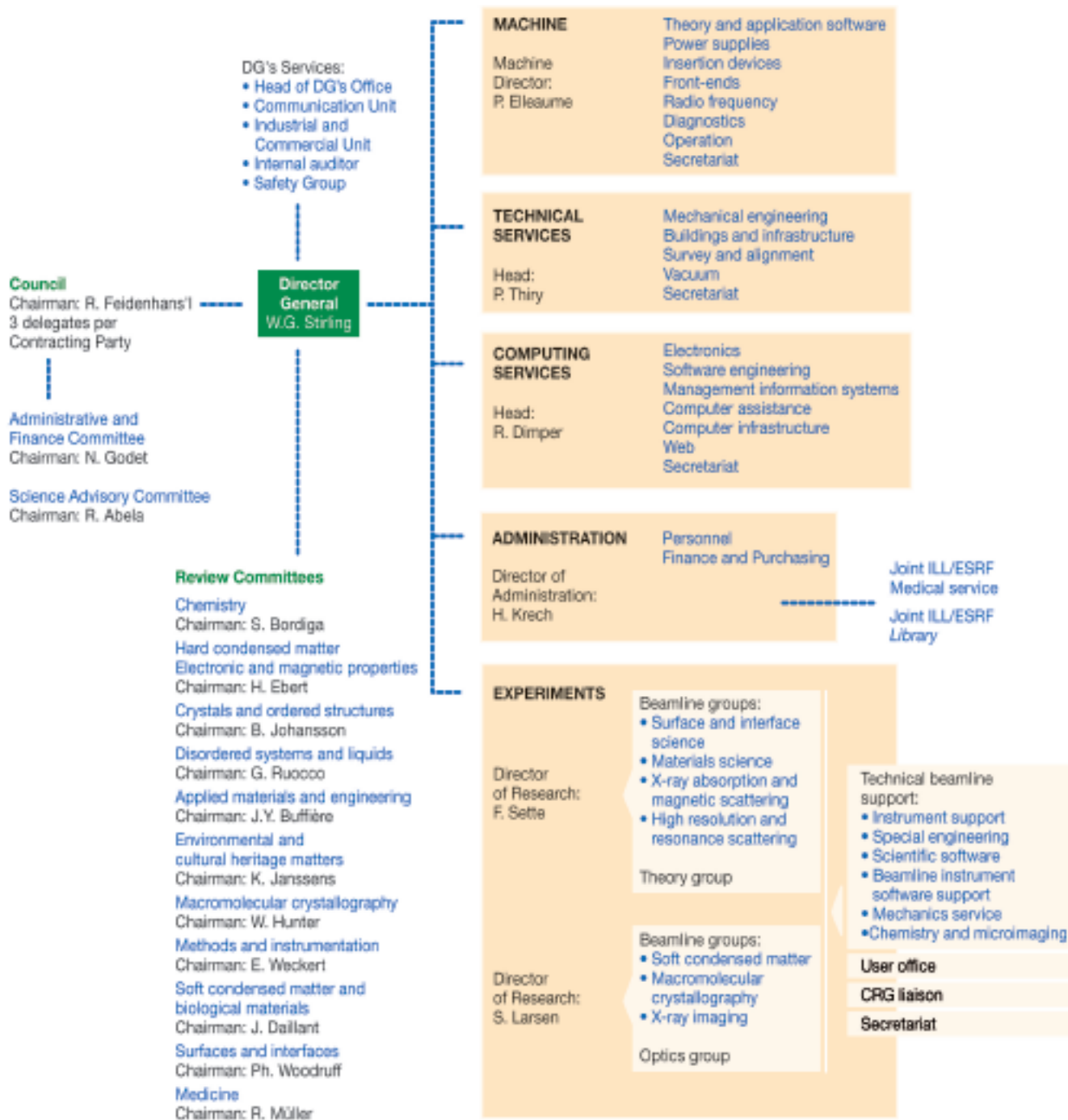
Financial resources in 2004, 2005, 2006 and 2007, by major programme  
(current prices in MEuro for the respective years)

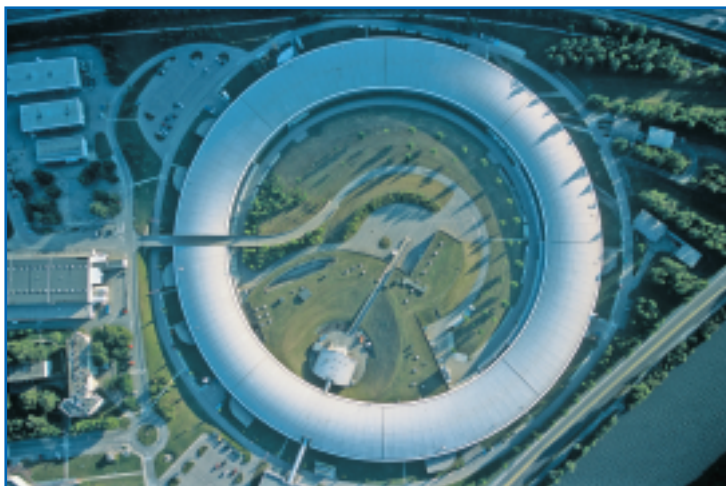


Financial resources in 2004, 2005, 2006 and 2007, by nature of expenditure  
(current prices in MEuro for the respective years)



# Organisation Chart of the ESRF (as of January 2007)





Cover photo: aerial vue of the ESRF, 2002. Credit: D. Morel.  
Other photos credits: P. Ginter (pages 112 and 120) and C. Argoud (page 3).

*We gratefully acknowledge the help of:  
C. Argoud, J. Baruchel, N. Brookes, D. Cornuéjols,  
P. Elleaume, A. Kaprolat, Å. Kvik, S. Larsen, G. Leonard,  
R. Mason, C. Riekkel, M. Rodriguez Castellano, R. Rüffer,  
F. Sette, W.G. Stirling, S. McSweeney, J. Zegenhagen,  
and all the users and staff who have contributed to this  
edition of the Highlights.*

**Editor**

G. Admans

**Layout**

Pixel Project

**Printing**

Imprimerie du Pont de Claix

© ESRF • February 2007

**Communication Unit**

**ESRF**

BP220 • 38043 Grenoble • France

Tel. (33) 4 38 88 19 46 • Fax. (33) 4 76 88 25 42

<http://www.esrf.eu>